N°d'ordre NNT:2021LYSEI111

THESE de DOCTORAT DE L'UNIVERSITE DE LYON
opérée au sein de
l'INSA LYON

Ecole Doctorale N° 34
Matériaux de Lyon

Spécialité de doctorat : Matériaux Polymères

Soutenue publiquement le 17/12/2021 à 14h, par :
Ibtissam TOUIL

Multi-micro/nanolayers of highly mismatched viscoelastic polymers based on polyethylene with varying macromolecular architectures: Multiscale investigations towards better control of their structuration and recycling by coextrusion

---

Devant le jury composé de :

DUQUESNE Sophie	Professeur (Université de Lille)	Rapporteur
AJJI Abdellah	Professeur (École Polytechnique de Montréal)	Rapporteur
EL KISSI Nadia	Directrice de Recherche CNRS (Université Grenoble Alpes)	Examinateur
DUCHET Jannick	Professeur (INSA LYON)	Examinateur
LAMNAWAR Khalid	Professeur (Associate, HDR) (INSA Lyon)	Directeur de thèse
MAAZOUZ Abderrahim	Professeur (INSA Lyon)	Directeur de thèse
DA CRUZ-BOISSON Fernande	Ingénieure de Recherche CNRS (INSA Lyon)	Invitée
LU Bo	Docteur (Université de Zhengzhou, Chine)	Invité

Département FEDORA – INSA Lyon - Ecoles Doctorales

SIGLE	ECOLE DOCTORALE	NOM ET COORDONNEES DU RESPONSABLE
CHIMIE	**CHIMIE DE LYON** https://www.edchimie-lyon.fr Sec. : Renée EL MELHEM Bât. Blaise PASCAL, 3e étage secretariat@edchimie-lyon.fr	**M. Stéphane DANIELE** C2P2-CPE LYON-UMR 5265 Bâtiment F308, BP 2077 43 Boulevard du 11 novembre 1918 69616 Villeurbanne directeur@edchimie-lyon.fr
E.E.A.	**ÉLECTRONIQUE, ÉLECTROTECHNIQUE, AUTOMATIQUE** https://edeea.universite-lyon.fr Sec. : Stéphanie CAUVIN Bâtiment Direction INSA Lyon Tél : 04.72.43.71.70 secretariat.edeea@insa-lyon.fr	**M. Philippe DELACHARTRE** INSA LYON Laboratoire CREATIS Bâtiment Blaise Pascal, 7 avenue Jean Capelle 69621 Villeurbanne CEDEX Tél : 04.72.43.88.63 philippe.delachartre@insa-lyon.fr
E2M2	**ÉVOLUTION, ÉCOSYSTÈME, MICROBIOLOGIE, MODÉLISATION** http://e2m2.universite-lyon.fr Sec. : Sylvie ROBERJOT Bât. Atrium, UCB Lyon 1 Tél : 04.72.44.83.62 secretariat.e2m2@univ-lyon1.fr	**M. Philippe NORMAND** Université Claude Bernard Lyon 1 UMR 5557 Lab. d'Ecologie Microbienne Bâtiment Mendel 43, boulevard du 11 Novembre 1918 69 622 Villeurbanne CEDEX philippe.normand@univ-lyon1.fr
EDISS	**INTERDISCIPLINAIRE SCIENCES-SANTÉ** http://ediss.universite-lyon.fr Sec. : Sylvie ROBERJOT Bât. Atrium, UCB Lyon 1 Tél : 04.72.44.83.62 secretariat.ediss@univ-lyon1.fr	**Mme Sylvie RICARD-BLUM** Institut de Chimie et Biochimie Moléculaires et Supramoléculaires (ICBMS) - UMR 5246 CNRS - Université Lyon 1 Bâtiment Raulin - 2ème étage Nord 43 Boulevard du 11 novembre 1918 69622 Villeurbanne Cedex Tél : +33(0)4 72 44 82 32 sylvie.ricard-blum@univ-lyon1.fr
INFOMATHS	**INFORMATIQUE ET MATHÉMATIQUES** http://edinfomaths.universite-lyon.fr Sec. : Renée EL MELHEM Bât. Blaise PASCAL, 3e étage Tél : 04.72.43.80.46 infomaths@univ-lyon1.fr	**M. Hamamache KHEDDOUCI** Université Claude Bernard Lyon 1 Bât. Nautibus 43, Boulevard du 11 novembre 1918 69 622 Villeurbanne Cedex France Tél : 04.72.44.83.69 hamamache.kheddouci@univ-lyon1.fr
Matériaux	**MATÉRIAUX DE LYON** http://ed34.universite-lyon.fr Sec. : Yann DE ORDENANA Tél : 04.72.18.62.44 yann.de-ordenana@ec-lyon.fr	**M. Stéphane BENAYOUN** Ecole Centrale de Lyon Laboratoire LTDS 36 avenue Guy de Collongue 69134 Ecully CEDEX Tél : 04.72.18.64.37 stephane.benayoun@ec-lyon.fr
MEGA	**MÉCANIQUE, ÉNERGÉTIQUE, GÉNIE CIVIL, ACOUSTIQUE** http://edmega.universite-lyon.fr Sec. : Stéphanie CAUVIN Tél : 04.72.43.71.70 Bâtiment Direction INSA Lyon mega@insa-lyon.fr	**M. Jocelyn BONJOUR** INSA Lyon Laboratoire CETHIL Bâtiment Sadi-Carnot 9, rue de la Physique 69621 Villeurbanne CEDEX jocelyn.bonjour@insa-lyon.fr
ScSo	**ScSo*** https://edsciencessociales.universite-lyon.fr Sec. : Mélina FAVETON INSA : J.Y. TOUSSAINT Tél : 04.78.69.77.79 melina.faveton@univ-lyon2.fr	**M. Christian MONTES** Université Lumière Lyon 2 86 Rue Pasteur 69365 Lyon CEDEX 07 christian.montes@univ-lyon2.fr

*ScSo : Histoire, Géographie, Aménagement, Urbanisme, Archéologie, Science politique, Sociologie, Anthropologie

Résumé

L'objectif de la présente thèse consiste en l'étude fondamentale pour la compréhension de l'ultra-confinement des polymères sur les propriétés rhéologiques et la dynamique des chaines lors de l'élaboration des multi-micro/nanocouches par le procédé de coextrusion. Pour ce faire, les travaux ont été menés sur des couples modèles à base de polyéthylènes (PE) et de polymères confineurs de type (PS et PC). L'originalité de notre approche concerne la coextrusion de ces polymères ayant un fort contraste des propriétés rhéologiques. Dans ce cadre, différents grades de PEs ayant des architectures macromoléculaires avec des ramifications courtes (SCB) et des ramifications longues (LCB) ont été utilisés. Outre l'étude rhéologique, les systèmes élaborés ont été analysés par diverses techniques de caractérisation telles que le MEB, MET et 2D-WAXS, afin de sonder les propriétés morphologiques, la structure cristalline et la dynamique des chaînes PEs à différentes échelles. Des instabilités ont été observées en fonction du contraste viscoélastique des polymères stratifiés et de la tension interfaciale. Des cartes de stabilités ont été établies. Dans certaines conditions, différentes structures multi-nano-couches nano-architecturées présentant un écoulement stable et ayant une architecture complexe ont été alors obtenues. Lors de la mise en œuvre, la démultiplication des couches influence fortement la microstructure/morphologie et l'orientation cristalline des PE. En outre, nous avons constaté que le confinement moléculaire des PE présente un effet notoire sur la morphologie et la microstructure des multicouches, en fonction de la nature du polymère confineurs. De surcroit, le comportement la rhéologique et de ces PE se révélait être influencé en fonction du type et la longueur de branchements. Quant au comportement rhéologique en élongation, le phénomène de Strain hardening dépend fortement du nombre de couches, de l'architecture et de la composition. Des mécanismes moléculaires ont été proposés pour élucider les manifestations observées. Parallèlement et malgré le fort contraste rhéologique, nous avons pu modéliser à partir des mesures élongationnelles les propriétés de la tension interfaciale, en particulier dans le cas des nanocouches. Par ailleurs, ce travail démontre clairement comment l'évolution structurelle multi-échelle au cours du processus de coextrusion micro-/nano-couche peut contrôler les propriétés finales et notamment le processus de « Strain-hardening ». En outre, les résultats obtenus visent à une meilleure compréhension des propriétés interfaciales pour contrôler l'interface/les interphases dans ces polymères multicouches modèles, tout en intégrant leur recyclabilité. A cet égard, et dans le contexte de l'économie circulaire, une approche prospective allant de l'éco-design à l'élaboration des systèmes multi-micro/nano couches facilement recyclable a été étudiée. Par conséquent, une nouvelle voie est proposée. Elle consiste à proposer une approche innovante pour diminuer le nombre de constituants, réduire l'épaisseur des couches et en évitant d'utiliser des liants en vue d'améliorer la recyclabilité mécanique des systèmes étudiés.

MOTS-CLÉS : Coextrusion multinanocouches, interface, instabilités, rhéologie, recyclage, éco-conception, mélanges de polymères, morphologie, modélisation.

Abstract

This study aims to understand the effects of confinement on the rheology and molecular dynamics in multilayer polymeric structures fabricated by the forced-assembly multilayer coextrusion of polyethylenes (PE) and confined polymers (PS and PC). The originality of our approach deals with coextrusion of these high mismatched viscoelastic systems. Through this work, PEs with varying macromolecular architectures, with short-chain branching (SCB) and long-chain branching (LCB), were used. Various nano-structured multilayer structures with stable flow and layered architecture were then obtained. Hitherto, various characterization techniques such as WAXS, SEM or TEM, and rheology were used to probe the structure and molecular dynamics of the PE chains. Micro and nanolayered instabilities were observed depending on the viscoelastic mismatched properties and interfacial tensions. The layer multiplication strongly affects the crystallization microstructure/morphology and molecular orientations of PEs. Interestingly, we found that macromolecular and geometrical confinements further influence the final morphology. Subsequently, they remarkably influence the rheology and molecular dynamics of PEs depending on the amount of LCB. From micro- to nanolayers, strain hardening properties in the extensional measurements are strongly dependent on the number of layers, architecture, compositions and confinement. Relevant mechanisms involving molecular rheology theories are proposed to elucidate the reasons underlying the changes. Meanwhile, we were able to model interfacial tension properties especially in the case of nanolayered polymeric systems. Hence, this work clearly demonstrates how the multiscale structural evolution during the micro-/nano-layer coextrusion process can control the final properties of multilayered products. Our findings are aimed at a better understanding of the interfacial properties towards controlling the interface/interphases in the present micro-nanostructured model multilayers polymers including their recyclability for advanced applications ranging from ultra-barrier films from cast extrusion to flexible and high transparency sheets for thermoforming process. Finally, and in the context of circular economy, a future-oriented approach from eco-design to a recycling strategy of the studied multi-micro/nanolayered systems was investigated. Therefore, a novel route is purposed to decrease the number of constituents, control the thickness of the layers, avoid using tie layers, and enhance the recyclability of the studied systems.

Keywords: Multi micro-/nanolayered polymers, interface, coextrusion, instabilities, rheology, recycling, eco-design, polymer blends, morphology, elongation rheology, modelling.

Contents

List of Figures

List of Tables

Introduction générale

Les multinanocouches mis en œuvre par le procédé de coextrusion sont extrêmement importants pour des applications dans des domaines aussi variés que stratégiques tels que la plastronique, l'énergie, l'optique et films à propriétés Ultra-barrière pour l'emballage alimentaire. Une innovation récente de ce procédé consiste à démultiplier le nombre de couches au moyen d'une nouvelle génération de groupes multiplicateurs développés au sein de notre laboratoire (Forced Assembly Layer Coextrusion). Il s'agit d'une technologie versatile puisqu'elle permet d'obtenir une architecture spécifique des films stratifiés en fonction des applications visées. Il est établi que les approches classiques permettent de stratifier au moins cinq couches micrométriques de polymères. Actuellement, le gain en haute valeur ajoutée nécessite le développement de nouveaux matériaux fonctionnels pouvant être constitués par une centaine à des milliers de couches. L'épaisseur des couches obtenues peut-être de l'ordre de dizaines de nanomètres. Ce projet de thèse porte sur une étude fondamentale du confinement des polymères dans les structures multicouches mis en œuvre par le procédé de coextrusion. L'objectif ultime est d'obtenir des matériaux fonctionnels ayant des structures multi-nano-couches nano-architecturées et présentant un écoulement stable. Les travaux de recherche consistent en la compréhension des phénomènes multiphysiques mis en jeu lors de l'élaboration de multinanocouches avec des études multi-échelles. On vise en particulier une meilleure compréhension des mécanismes sous-jacents qui sont à l'origine de l'apparition des morphologies singulières (twist, 2D, 1D, etc.). Toutefois, les phénomènes mis en jeu lors de l'élaboration de ces matériaux sont particulièrement complexes car ils impliquent de façon couplée des aspects hydrodynamiques avec des cinématiques d'écoulement en cisaillement et en élongation.

Dans ce travail, nous cherchons à répondre aux questions suivantes :

- Quel est l'effet de la structure des matériaux sur les propriétés rhéologiques ?
- Quel est l'effet du contraste des propriétés rhéologiques sur les morphologies induites aux échelles nanométriques (stabilité d'écoulement, répartition des épaisseurs ?)
- Quelle est l'incidence de l'ultra-confinement sur les propriétés microstructurales (cristallinité) ?

Ce manuscrit va s'articuler autour de cinq chapitres :

Le **premier chapitre** décrit l'état de l'art des différentes méthodes d'obtention de film multicouches avec un accent particulier sur le procédé de coextrusion multinanocouche. Nous décrivons par la suite l'effet du confinement géométrique induit par ce procédé et ces diverses propriétés (optique, diélectrique, etc.). Les aspects fondamentaux liés à l'interdiffusion des chaînes macromoléculaires aux interfaces sont quant à eux présentés dans ce chapitre. De plus, les défauts et instabilités d'écoulement rencontrés lors de la mise en œuvre sont enfin présentés. L'originalité de notre démarche consiste en la compréhension des phénomènes multiphysiques mis en jeu lors de l'élaboration de multinanocouches avec des études multi-échelles.

Le **deuxième chapitre** vise à effectuer une caractérisation très fine des matériaux utilisés (LDPEs et LLDPEs) d'un point de vue physico-chimique et rhéologique en termes de viscoélasticité linéaire et non linéaire. Le but de ce chapitre est de mieux comprendre les propriétés structurelles et architecturales de ces PEs en relation avec leurs propriétés rhéologiques en cisaillement et en élongation. Ces PEs seront coextrudés avec du PS et du PC en tant que polymères confineurs. Pour la clarté de ce manuscrit, les propriétés rhéologiques des polymères confineurs seront données, à titre comparatif, dans le chapitre suivant.

Le **troisième chapitre** se focalise sur la mise en forme des différentes structures multi-micro/nanocouches ayant une architecture complexe au moyen de groupes multiplicateurs développés au laboratoire. Il s'agit, dans un premier temps, d'associer différents matériaux confineurs amorphes de type (PS et PC) de différentes Tg avec un PE ayant des branchements courts et longs. L'originalité de notre approche concerne la coextrusion de ces polymères ayant un fort contraste rhéologique. Une étude de comportement rhéologique des polymères seuls en viscoélasticité linéaire a été réalisée dans des conditions réelles représentatives de la mise en forme des polymères. Ensuite, différentes structures multi-micro/nanocouches allant de 32 à 16380 couches de différentes compositions sont obtenues. Dans un second temps, la rhéologie en cisaillement et en élongation de nos différents films multicouches est effectuée. Parallèlement, la modélisation de la tension interfaciale des systèmes multi-miro/nanocouches en cisaillement et en élongation est ensuite réalisée. Les résultats de ce chapitre visent à une meilleure compréhension des propriétés interfaciales pour contrôler l'interface/les interphases dans ces polymères multicouches modèles.

Le **quatrième chapitre** porte sur la compréhension de l'effet du confinement de nos systèmes multi-micro/nanocouches sur les propriétés morphologiques et structurales induites. Les systèmes élaborés ont été analysés par diverses techniques de caractérisation telles que le MEB, TEM, AFM et 2D-WAXS, afin de sonder les propriétés morphologiques, la structure cristalline et la dynamique des chaines PEs à différentes échelles.

Enfin, le **dernier chapitre** s'attache à mettre en place une nouvelle démarche allant de l'éco-design à l'élaboration des systèmes multi-micro/nanocouches facilement recyclable. Tout d'abord, nos systèmes multicouches sont recyclés mécaniquement en utilisant deux différentes méthodes de recyclage. Nous avons ensuite étudié l'effet du confinement de nos systèmes sur les propriétés mécaniques. Enfin, nous avons évalué l'impact du procédé de recyclage sur les propriétés mécaniques et morphologiques.

Chapter 1. Literature Review-A journey on processing and interfacial phenomena in multi-micro/nanolayers

1. Introduction

In nature, a diverse range of multi-layered structures with varying functional scales exist and may serve as a biomimetic model for the development of new materials. These architectural materials show distinct characteristics as of multiscale, function system design, and interfacial impact. Among the various examples are butterfly wings, whose bright color is determined by the multiscale structure; mother-of-pearl, which is very rigid; and wood, which has high mechanical performances. This chapter presents the research findings that have been reported in academia over the last several years on multilayered polymers derived from the co-extrusion techniques, which is critical for the further research developed in this thesis. To begin, the various techniques for manufacturing multilayered polymers are described and compared. Second, more details are given on interfacial phenomena that occur in multilayer co-extruded polymers. Third, the rheological phenomena that occur in multilayer coextruded polymers, such as flow instabilities and interfacial defects, are thoroughly described. A special attention is given to the research findings on this topic of our group in the two past decades. Finally, a summary of the uses of multilayer coextruded polymers with advanced properties is included in this study.

2. Multilayered polymers

Recently, flexible, and lightweight functional multilayer films have been used more often in applications such as printed electronics, energy, nanomedicine, automotive, and construction, among others. Numerous methods exist for combining various polymers to produce multilayered films. This section provides an overview of the most frequently used techniques to produce multilayer films. Layer-by-layer assembly, lamination, multilayer coextrusion, solvent casting, and spin coating are all common manufacturing methods.

2.1. Layer-by-Layer Assembly

Layer-by-layer assembly (LbL) is a commonly used method for fabricating multilayer thin films with controlled thicknesses and properties at the nanoscale [1]. Numerous materials, such as polymers, proteins, and nanoparticles that could be dispersed or dissolved in aqueous solutions and form ionic or hydrogen bonds, may be utilized in multilayer construction using the LbL technique, as shown in **Figure 1.1**. The multilayer structures are constructed by laying down alternating layers with opposite charge components and by adding wash processes in between. This may be done via a variety of methods, including

immersion, spinning, spraying, electromagnetic, and fluidics. Therefore, the LBL technology has been widely used to produce multilayered functional materials, polyelectrolyte films, and tissue repair with nanoscale controllable thicknesses, physicochemical properties, and confined crystallization [1]. Additionally, LBL has been performed by dipping treated substrates into the desired solutions, washing with deionized water to remove unbound materials, and then drying using filtered air. This procedure is repeated until the desired number of layers is achieved to create a multilayer nanofilm.

Over the past two decades, significant theoretical and experimental advancements have been achieved on this topic. Layer-by-layer assembly has proved to be a very effective technique, with surprisingly deep multidisciplinary implications for scientific investigation.

Nonetheless, scaling up this technology is critical for real-world applications and daily life advancements. Otherwise, the development of other relevant methods for the industrial production of multilayer films with controlled characteristics is still in the early stages.

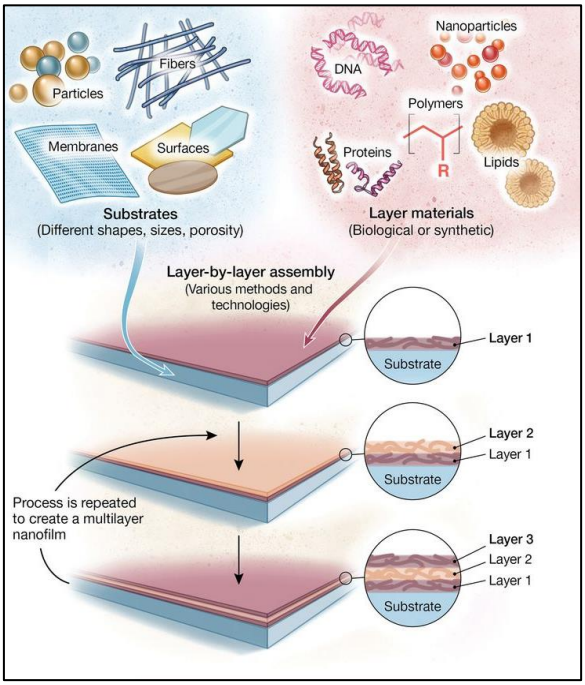

Figure 1.1 A schematic view of layer-by-layer assembly [2].

2.2. Lamination

The lamination technique may combine two or more materials, including non-polymeric materials such as aluminum foils or papers. Melt extrusion is the most frequently used with lamination technique. In this methodology, the molten polymer is first extruded between the

two substrates and then compressed against a chilled roller that can solidify the molten polymers. The bonding strength of extruded material to the primary polymers is strongly dependent on the physico-chemical compatibility and extrusion conditions. Furthermore, adhesive lamination can be used to fabricate polymer film-based structures such as laminated epoxy/fiber composites [2]. Moreover, lamination may be accomplished by heating and compressing two films, one of which is heat-sealed. Thus, the laminates are formed at an increased temperature. In sum, this technique is widely used for complex multicomponent systems with limited number of layers including the non-polymeric supports.

2.3. Solution casting and spin-coating

Solution casting is another straightforward method for fabricating multilayer films. In this process, the polymer solution is first deposited on a substrate, which is then sprayed to create a film with a thickness varying from micro- to nanoscale based on the viscosity of the polymer solution and the solvent evaporation rate. Other factors can sometimes affect the thickness of the resulting films.

The spin-coating technique has been used for several decades for the fabrication of thin and uniform films. This process consists in four stages: deposition, spin up, spin-off, and evaporation, as described in **Figure 1.2**. First, a small drop of the polymer solution is placed on the center of a substrate, which is then rotated at a controlled high speed to spread the fluid via centrifugal force until the required thickness is reached. Generally, the volatile solvent used in this technique ensure its simultaneous evaporation during spinning. This technique is often used to produce multifunctional films, especially photoresists, lithography resists, and protective coatings [3]. Unfortunately, this laboratory method is limited to small samples. One of the drawbacks of this approach is the inability to control polymer solubility with non-conventional solvents at high temperatures.

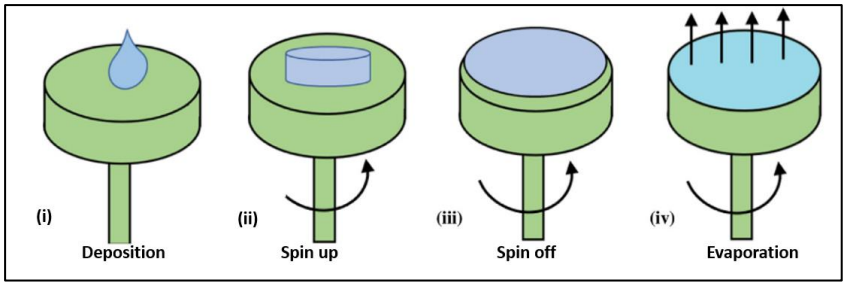

Figure 1.2 Spin-coating steps on the substrate [3].

2.4. Multilayer coextrusion

Over the past years, there has been a significant increase in industrial demand to create and produce new and continuous multifunctional organic materials with extremely enhanced characteristics, namely in terms of optical properties [4][5][6], mechanical properties [7], gas barrier properties [8], and dielectric properties [9], especially in the domains of packaging (bottles, food packaging, cosmetics, pharmaceutics, etc.) and transport (vehicles and aeronautics). For the clarity purpose of this state of the art, the readers can refer to our first review in this topic regarding multi-microlayered coextrusion [10]. One way to make more high-performing materials is to use multilayer polymeric structures by applying an innovative technique, named the forced-assembly multilayer coextrusion process to move from micro to nanolayered polymers. This layer multiplication process was initially developed by Dow 40 years ago [11] and more recently updated by Baer's group at Case Western Reserve University. In our group, we have upgraded this first generation of multiplier elements to high mismatched viscoelastic polymers based on different couples (PVDF/PMMA, PVDF-HFP/PC, PP/PE, …). This process allows the fabrication of architectural structures by controlling the structuration at the micro-/nanoscale of multiphase polymer systems. The layer thickness of multilayer coextruded films ranges from microns down to around 10 nm and is obtained by increasing the layer number from two to thousands of alternating layers of the two polymers [12]. In comparison to earlier techniques such as LbL assembly and spin coating, which have low productivity, this technology enables easy control of polymer crystal growth in a confined space.

As illustrated in **Figure 1.3**, two extruders feed the melt into a feedblock, followed by a series of layer-multiplying components (or multipliers) with cast film die. Each multiplier divides the initial melt stream vertically into two, spreads it, and then stacks the layered melt while keeping the total melt thickness constant. Therefore, the thickness of each layer $h_{nomA \text{ or } B}$ is decreased, and the number of layers multiplied after each multiplier (Eq. (1) for A/B bilayer multiplication). Multilayer coextrusion is the chosen technique for multilayer fabrication in this thesis. Following there is more information about multilayer coextrusion and its use. The final number of layers is determined as a function of the number of multiplications dies, which are placed in series between the feedblock and final film or sheet exit dies. For example, it is $2*2^n$ for A/B or $3*2^n$ for A/B/C systems (A, B and C are the extruded polymer components).

$$h_{nomA,B} = \varphi_{A,B} \frac{h_{total}}{2^n} \quad (1)$$

where φ_A and φ_B represent the volume fraction of A and B, respectively, h_{total} the total film thickness, and n the number of multipliers.

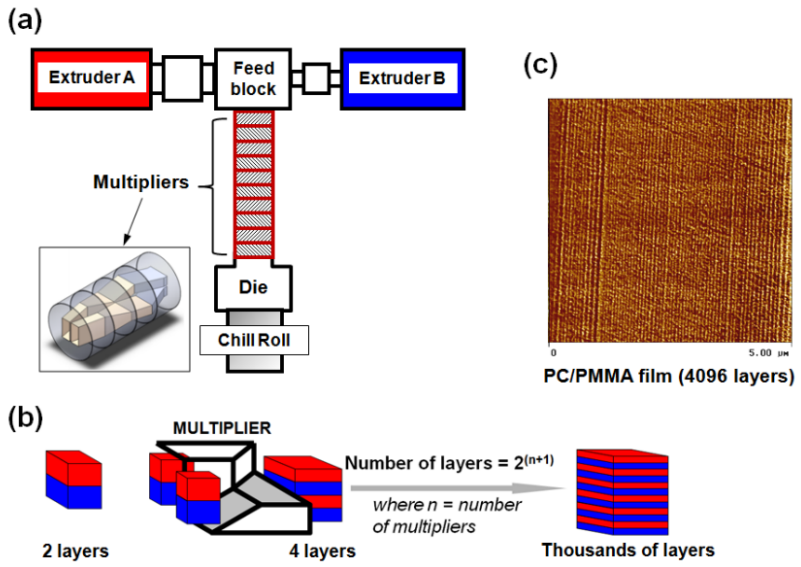

Figure 1.3 Schematic illustration of (a) a two-component coextrusion process equipped with (b) the multiplying-element device. (c) AFM phase image for cross section of 4096-layered PC/PMMA multilayer with nominal layer thickness of 30 nm [13].

3. Confinement phenomena in multilayer coextruded polymers

3.1. Confined crystallization

Nanolayered polymeric materials created via the forced assembly coextrusion process are widely known to be potential candidates to provide synergistic effects, offering enhanced properties compared to those of pure components. This process can easily control the growth of polymer lamellar crystals in confined spaces. The spatial confinement in multilayered films results in a change in crystallization behavior, structure, and morphology. When the layer thickness of the confined polymer becomes comparable to the thickness of polymeric crystal lamella, unique crystalline morphologies and orientations can be produced. For example, poly(ethylene oxide) (PEO) confined against amorphous polymer PS in multilayer systems has revealed an in-plane orientation of crystalline lamellae [14] due to geometrical/spatial confinement, as illustrated in **Figure 1.4**. The impact of PS confinement can already be evident at 1 μm thick microscale PEO layers, with a change from isotropic spherulitic structure (3D) to truncated spherulites (2D) nucleating at the PS/PEO interface. Upon reducing the PEO layer thickness to 300 nm, stacks of oriented PEO in-plane lamellas are seen. As the confined PEO layer thickness approaches 75 nm, the orientation of in-plane lamellas is significantly increased. Further decreasing the PEO layer thickness to 25 nm, the PEO crystallizes into long single-layered PEO lamellae with a large aspect ratio. Wide-angle X-ray scattering (WAXS) has been used to confirm the 1D lamellae structure of PEO under nanolayer confinement **Figure 1.4 (b)**.

Similar to the PEO/PS system, PCL/PS co-extruded films exhibit the same behavior as the PCL layer thickness decreases from microns to nanometers and crystallize as in-plane lamellae [15]. **Figure 1.5** illustrates the evolution of the crystalline structure of both the PEO and PCL when they are confining in micro- to nano-layers by a hard-confining layer, which indicates the formation of a single crystal morphology for PEO. As a result of confinement, the effective oxygen permeability decreases by approximately two orders of magnitude in this direction [14]. This is due to the increased tortuosity of the diffusion pathway that passes through the highly oriented lamellae. Furthermore, it has been observed that confinement can result in the formation of other crystal morphologies and lamellar orientations in other

polymers. For example, the crystal structure of high-density polyethylene (HDPE) is confined by high Tg confining polymers, polycarbonate (PC), and polysulfone (PSF) [16] in the nanolayered coextrusion process, revealing a twisted morphology in extremely thin layers. Changes in morphology have led to an increase in crystallinity and enhanced both the oxygen and water vapor barrier properties of the multilayer systems. A systematic study of HDPE nanolayers sandwiched between thicker polystyrene (PS) in multilayer coextruded systems has been studied [17]. Interestingly, as the layer thickness of HDPE decreased from the microscale to the nanoscale, a significant reduction in crystallinity was observed from 60 to 30% [18]. This result was associated with discoidal morphologies in microscale (>100 nm) that transformed into long bundles of edge-on lamellae in HDPE nanolayers (<100 nm). Therefore, changes in morphology led to an increase in oxygen permeability of the multilayer systems by a factor of three [18]. For certain cases, it is possible to obtain this crystal orientation and enhance barrier properties by biaxially stretching multilayer films during melt coextrusion. For PCL/PS nanolayered systems, it is shown that barrier properties are increased by the factor 200 (See the following section)[19].

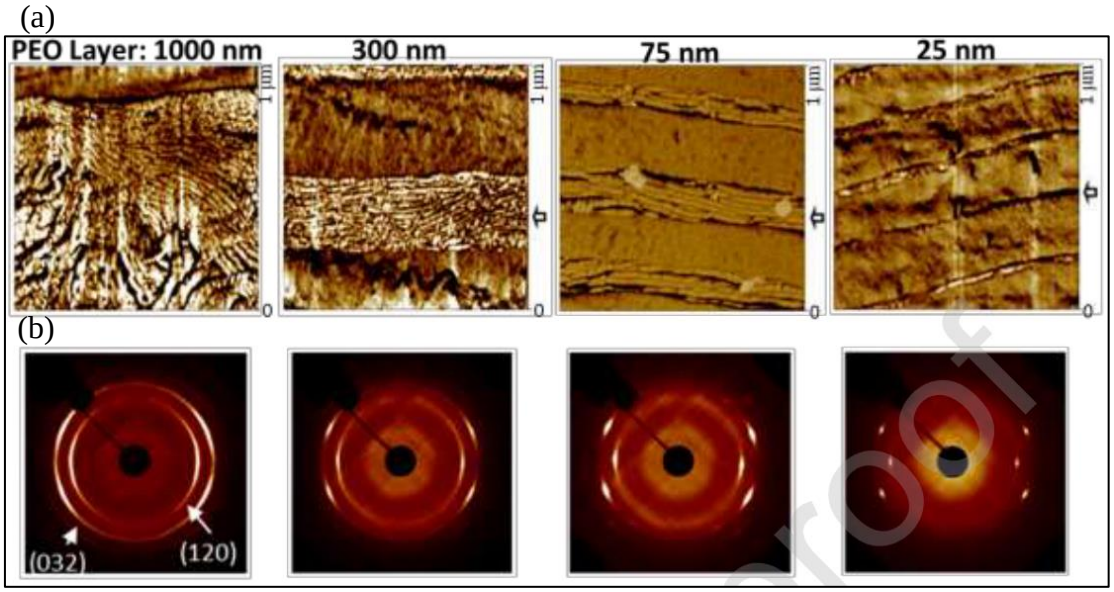

Figure 1.4 (a) Atomic force microscopy (AFM) phase images of cross sections and (b) extrusion direction wide-angle x-ray scattering (ED WAXS) patterns of PS/PEO multilayer films with 1000 nm, 75 nm and 25 nm PEO layers (arrows) [4].

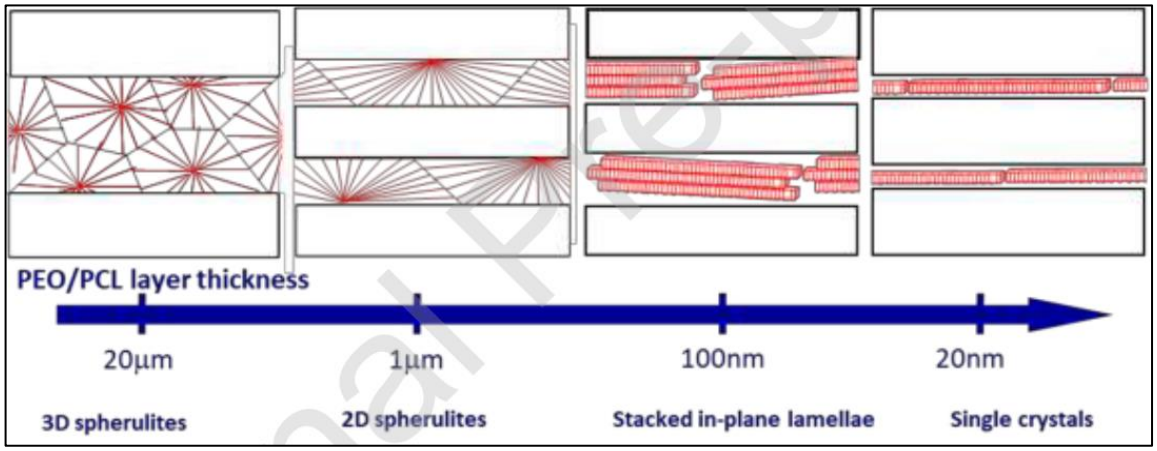

Figure 1.5 Evolution of the crystalline structure of both the PEO and PCL when they are confining from micro- to nano-layers.

3.2. Glass transition dynamics

For semi-crystalline layered polymers, the confined crystallization induced through nanolayer confinement can also affect the glass transition temperature (Tg) of the multilayer films. For amorphous layered based couples, one specific example uses PMMA polymer coextruded with PC [20], with thickness ranging from several microns to several nanometers. This study aimed to investigate the molecular mobility at the glass transition evolution in multi micro-nano-layered PC/PMMA films, as well as the cooperatively rearranging region (CRR) size and the glass transition temperature (Tg). The molecular mobility of each polymer is observed to change dramatically when the layer thickness approaches 125 nm, indicating that the constituent polymers exist as two-dimensional layers under these conditions. For PC, a drastic decrease in the cooperatively rearranging region at the glass transition was observed under the multilayer confinement effect. This is due to changes in the conformation of the macromolecular chain. For PMMA, a slight evolution of the cooperatively rearranging region was noted, due to the lower intermolecular interactions and lower monomeric friction in the main chains as compared to the PC (i.e.: PMMA Tg is lower than PC Tg). Another recent work studied similar multilayers of PC/PMMA, and no change was observed on the dynamic correlation (CCR size) of PMMA under geometric confinement, especially as the layer thickness approaches or equals the correlation length scale (**Figure 1.6 (a)**) [21]. Additionally, both the fragility and the width of relaxation dispersion were not influenced by the geometric confinement (**Figure 1.6 (b)**). However, the dynamic correlation volume/length, which represents the cooperativity of the

dynamics, remained unchanged (Figure 1.6 **(c)**). Moreover, it was discovered that the intermixing of PMMA with the high-Tg component (PC) at the extended interfacial area was the primary cause of the rise in the local segmental relaxation time and glass transition temperature of PMMA with decreasing layer thickness.

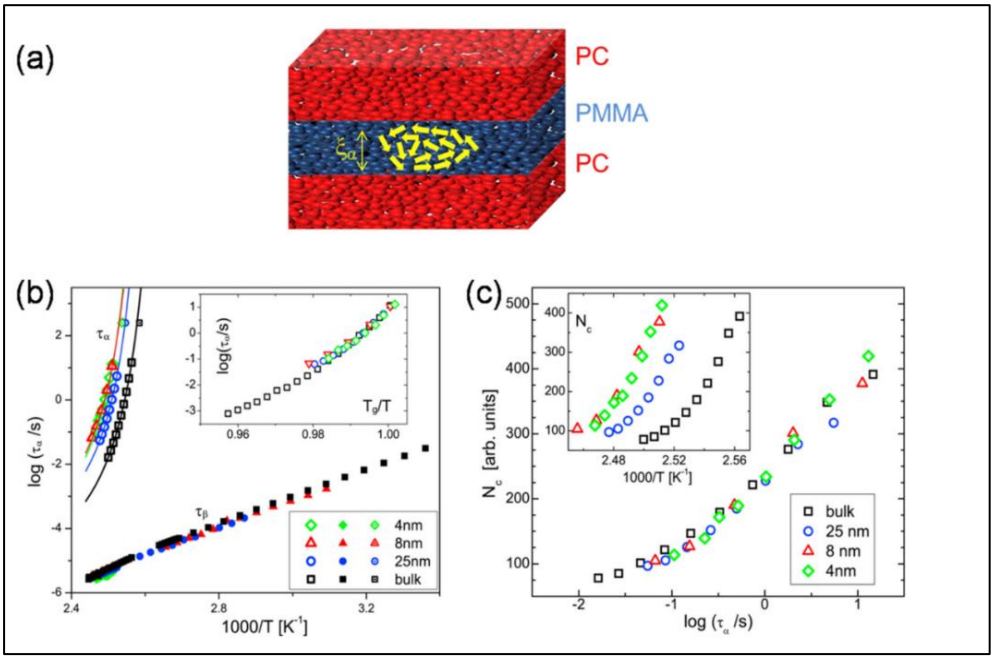

Figure 1.6 (a) In PC/PMMA multilayers, the confinement length scale is compared to the correction length of confining PMMA. (b) Segmental α-relaxation time activation graphs (τ_α) for PC/PMMA multilayers and bulk PMMA. (c) The number of correlated units (Nc) as a function of the α-relaxation time for bulk and nanoconfined PMMA samples. Despite the significant variations in Nc caused by confinement (inset), the dependency of Nc onτ_α is the same as for bulk PMMA [18] [17].

4. Properties and applications of multi-micro/nanolayer coextruded polymers

By using a forced assembly layer coextrusion process, it was possible to create films of alternating layers with well-controlled hierarchical structures down to the nanoscale. Over the last decade, advances in material characterization methods have enabled a better understanding of the structure-property relationships. The results demonstrate that layer thickness affects the functional properties of the bulk material.

4.1. Gas barrier properties

The multilayer coextrusion process is now widely used to fabricate films with high barrier properties, such as those used in packaging [22] [23] or electronic devices. Many packaging applications require the use of materials with a good barrier to oxygen and water vapor, to protect the products from degrading in an atmospheric environment [22]. The gas barrier properties of polymers are largely dependent on their solid-state structures, including crystal orientation, crystallinity, and free volume. However, the crystalline structure of polymers has a strong impact on their gas barrier properties, since the free volume for the transport of gas molecules is controlled by the polymer chain-packing distribution. Note that semi-crystalline polymer is a bi-phase system. It has a crystalline and amorphous phases, where the amorphous phase is assumed to be permeable to gas transport and the crystalline part is assumed to be impermeable [24]. One efficient way of achieving the required gas barrier properties is to control the polymer's solid state and increase the layer number and architecture. By confined crystallization at the nanoscale, the lamellar orientation of semi-crystalline polymer is significantly affected, resulting in a considerable increase in gas barrier performance by two to three orders of magnitude [25]. Many studies have investigated the effect of geometrical/spatial confinement of semi-crystalline polymer in multilayer coextrusion on the gas barrier property of multilayer films, especially at the nanoscale. As discussed in the previous section, most of these studies use a semi-crystalline polymer as the confined polymer, such as poly(ethylene oxide) (PEO), high density polyethylene (HDPE), or polycaprolactone (PCL). The amorphous polymer used as the confining one can, for example, be polystyrene (PS), polycarbonate (PC), or poly(methyl methacrylate) (PMMA). Generally, the chosen confining polymer has a crystallization temperature (Tc) or a glass transition temperature (Tg) higher than that of the confined semi-

crystalline polymer, in order to ensure “hard confinement” during a cooling process from multilayer coextrusion [4].

Baer and coworkers [26] studied the effect of lamellar orientation of highly crystalline PEO on gas barrier properties in EAA/PEO and PS/PEO nanolayered films. The PEO/EAA system exhibited a single-crystal morphology as the PEO layer thickness was reduced to the nanoscale, resulting in a two-order reduction of the magnitude of the effective gas permeability (**Figure 1.7(a)**). Another multilayer film system with PEO confinement against amorphous polystyrene (PS) showed a stacked “in-plane” lamellar structure, leading to a significant decrease in oxygen permeability. Similarly to the PEO/PS system, the PCL/PS system showed a single crystal structure, resulting in a 200-fold improvement in the barrier properties at the nanoscale by increasing the tortuosity[19], as illustrated in **Figure 1.7**(b).

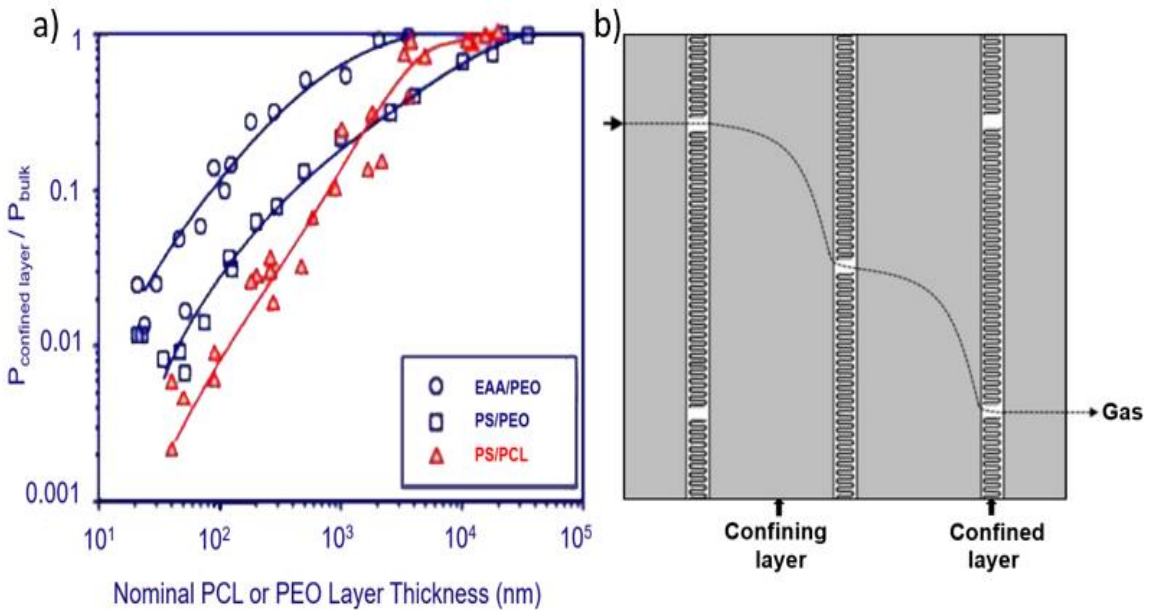

Figure 1.7 (a) The oxygen permeability of the PEO layers in EEA/PEO multilayer films of different layer thickness. The arrows indicate the EAA and PEO layers. (b) A schematic depicting the gas diffusion route via the layered structure with PEO layers 20 nm thick [4].

4.2. Dielectric properties

The layer-multiplying coextrusion technology has proved to be the most effective method for producing polymeric dielectric films with significantly high energy density, high dielectric breakdown strength, low hysteresis, and lower dielectric losses[27] [28]. Among the various strategies adopted for fabricating films with both high dielectric constant and low loss polymers, multilayered films have attracted increasing attention owing to their ability to control the number of layers, structure/morphology, layer thicknesses, and interfaces [29]. It is well documented that these layered films are generally composed of one high dielectric constant dipolar polymer, such as PVDF homopolymer or one of its copolymers, and one high breakdown strength polymer, such as PC, PMMA or PET, with low dielectric loss. This shows that when the PVDF layer thickness is reduced to the nanometer scale owing to the nanoconfinement effect on ion-hopping polarization transport, both dielectric and hysteresis loop decreases (**Figure 1.8a,d**) [30]. Another benefit is that the multilayer film decreases ferroelectric switching from the crystalline phase of PVDF, resulting in lower hysteresis loop loss, because of the local electric field in PVDF layers being efficiently decreased in multilayers with a high permittivity contrast **(Figure 1.8c**) [31][32][33][34]. Moreover, the local electric field in multilayer films may also be altered or diminished by interfacial polarization originating from both ions and electrons. Therefore, the dielectric breakdown mechanism highlights the importance of interfaces in enhancing breakdown properties and lifetime characteristics [25] [28]. This enhancement in these multilayered materials was attributed to a unique treeing pattern around the failure site, facilitated by the layer interfaces. Layers and interfaces act as barriers to the propagation of a breakdown channel through the film thickness. Further studies have shown that changes in interfacial adhesion (adding a tie layer) and/or biaxial orientation [36] may improve the ultimate dielectric performance of multilayer films. The high contribution of interfaces/interphases is also proved for dielectric and piezo-electric properties in the recent papers of our group. To improve future polymeric film capacitor dielectrics, multilayer films may be made with less unfavorable polarization (i.e., ionic conduction or ferroelectric switching) and more favorable polarization (i.e., dipolar polarization or electronic/atomic polarization).

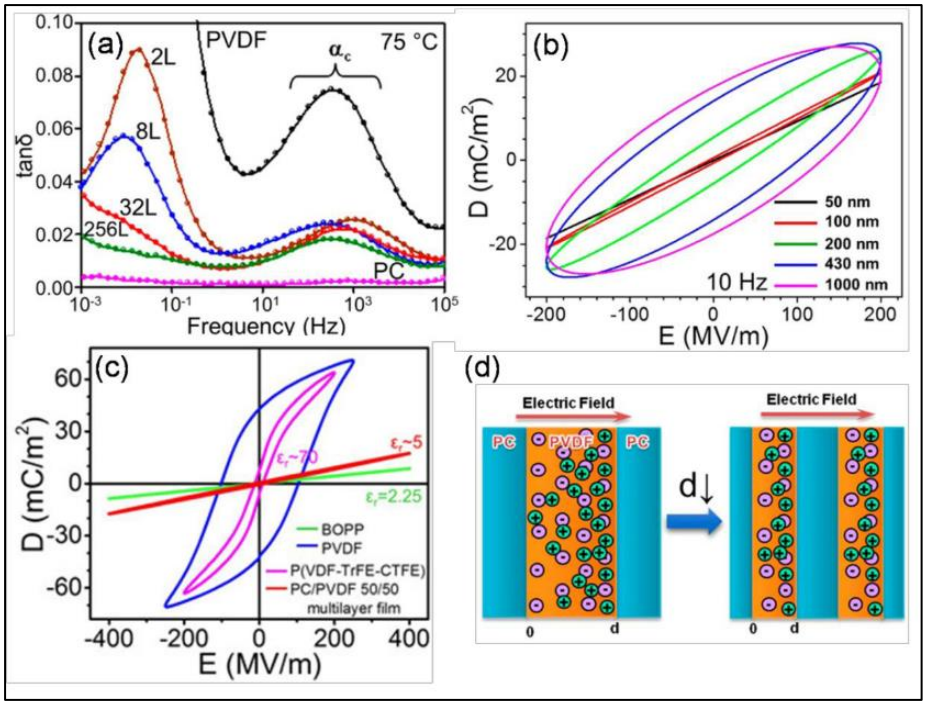

Figure 1.8 (a) Dielectric dissipation factor (tanδ) as a function of frequency for the PC/PVDF (50/50) multilayers, and PVDF and PC control films at 75 °C. (b) Simulated D-E loops for the monolithic slab of various thicknesses at 100 °C. (c) Comparison of D-E loops for commercially biaxially oriented polypropylene (BOPP), PVDF homopolymers, PVDF terpolymers, and PC/PVDF multilayers. (d) Schematic of the nanoconfinement effect on ion-hopping polarization in PVDF layers of different thicknesses.

4.3. Optical properties

For optical applications, the nanolayered materials produced by the coextrusion method offer significantly enhanced optical properties that are not attainable with a conventional polymer blend [4]. Optically iridescent films, for example, can be produced by alternating layers of controlled thickness, each of them having different refractive indices (such as polystyrene (PS) and poly (methyl methacrylate) (PMMA), or polycarbonate (PC) and polypropylene (PP)) (**Figure 1.9a-b**) [37] [38]. Modifying the polymer pair selection, volume composition, and the number of layers allows the production of 1D photonic crystals with different reflection bandgaps that exist in the visible, infrared, and ultraviolet ranges (**Figure 1.9(c)**) [4] [5] [32]. In contrast, when the individual layer thickness reaches one-quarter wavelength of light, the multilayer films exhibit excellent transparency and provide high-quality light reflection. Additionally, nanolayered films with gradient layer thicknesses have enabled the production of films with high reflectivity in the visible range [4]. This

research has allowed the production of a synthetic human eye lens utilizing nano-layered film systems with a refractive index gradient. Using multilayered films, other properties were shown, such as brightness-increasing optical films for LCD display monitors [40].

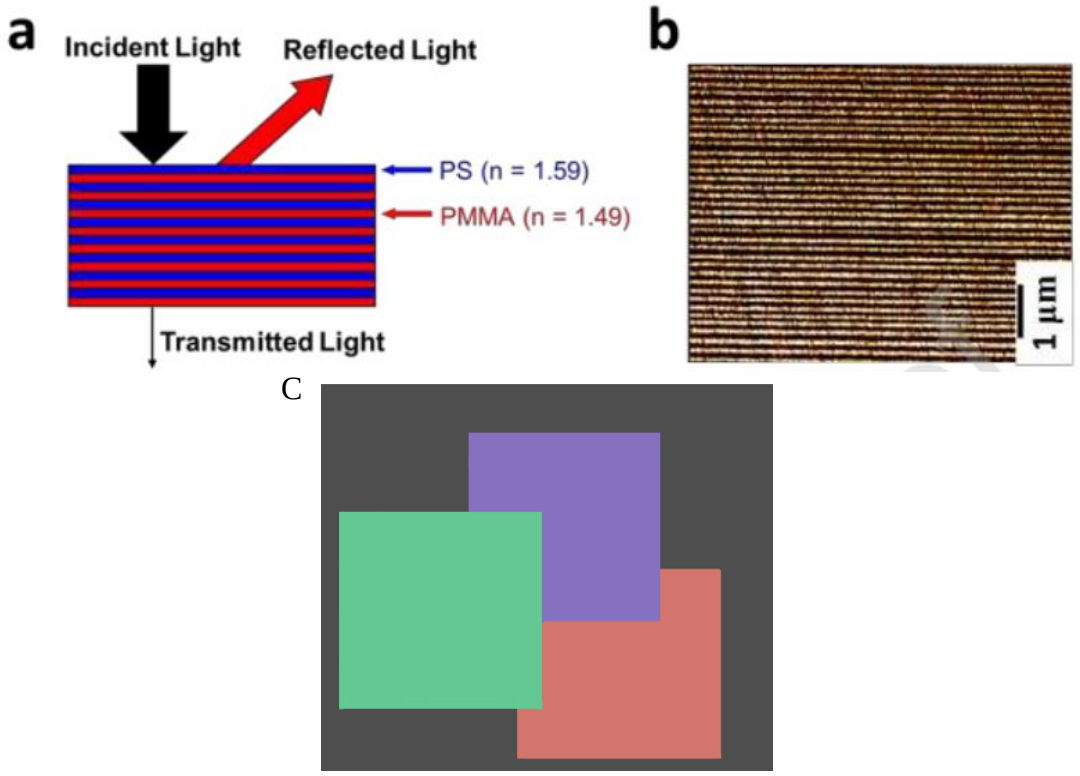

Figure 1.9 a) 128 alternating layers of PS and PMMA with equal volume compositions and an overall film thickness of 10.1 µm by the two-component multilayer coextrusion system b) AFM image of the 128 layer PS/PMMA multilayer film cross-section, revealing the relative uniform layer structure with an average layer thickness of 86 nm with a standard deviation of 24% c) Example of PS/PMMA 1D photonic films presenting various colors [5].

Besides conventional packaging and optical properties, multilayered coextrusion is a promising method for a wide range of applications as well as shape memory polymers, porous materials, multilayered micro- and nanofibers, multilayered foams, and composites. These improvements are the result of well-controlled architectural structures.

5. Interfacial phenomena in multilayer coextruded polymers

In multiphase systems: including polymer blends, multi micro- and nano-layered polymer structures, the interfaces dividing polymer pairs acquire an important interest in defining the resulting macroscopic properties of multicomponent products. A better understanding of the structures and properties of interface/interphase is critical to attain the required properties. Most of polymer pairs are immiscible, and the interfaces dividing polymers are mechanically thin and weak, due to the weaker entanglement and interpenetration in the interfacial area. This weak interfaces between polymer pairs can result to a very brittle material. In this section, the interfacial phenomena including the theoretical aspects of interfaces, interfacial diffusion, and their underlying mechanisms during multilayer coextrusion process are discussed.

5.1. Theoretical aspects

A self-consistent-field (SCF) approach is used to predict the interfacial properties between two immiscible polymers. This theory was introduced by Helfand and Tagami [34] [35]. According to this approach, the density profile of the two polymers (ρ_A and ρ_B) exhibits an exponential decay:

$$\rho_A = \frac{1}{2} + \frac{1}{2} tanh\left(\frac{x\sqrt{6\chi}}{b}\right) \quad (2)$$

Here the parameter χ represents the Flory Huggins thermodynamic interaction between the polymer segments of A and B, b designates the statistical segment length, and x corresponds to the distance from the interface. The hyperbolic tangent is used to describe the probability distribution function of A-B segments, as shown in **Figure 1.10.** The intersection of the steepest tangential line with the horizontal lines defines the volume portion of each of the polymeric components in the interfacial region (i.e. interphase). The thickness Δl of the latter is therefore given by:

$$\Delta l = \frac{2b}{\sqrt{6\chi}} = 2\left(\frac{{b_A}^2 + {b_B}^2}{12\chi}\right)^{1/2} \quad (3)$$

It is obvious that as the interaction parameter χ decreases, the density profile widens, and the interfacial thickness Δl increments with $\chi^{-1/2}$. As χ approaches zero, the width of the interfacial region approaches infinity, the interfacial region becomes indistinguishable, and the system becomes a single phase.

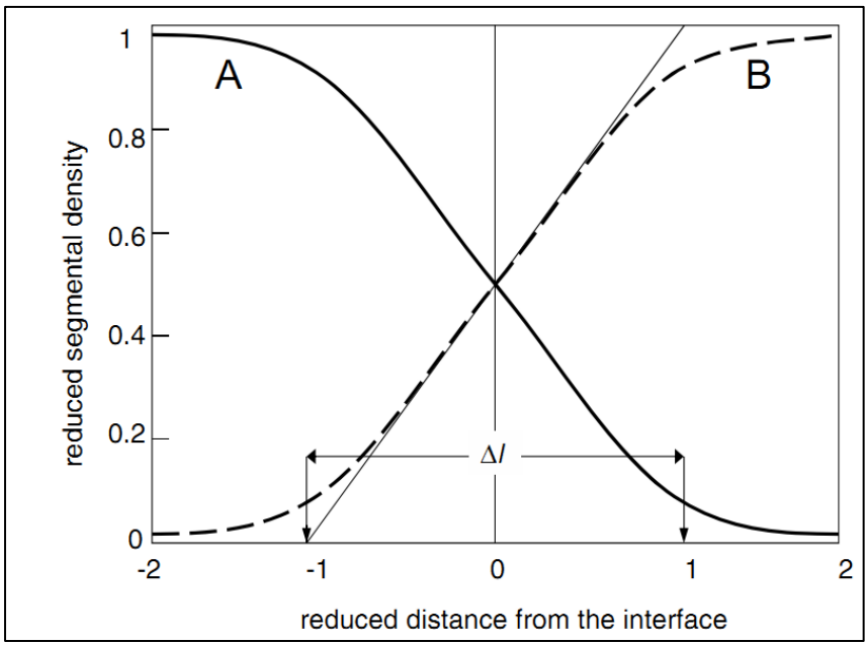

Figure 1.10 Segmental density profiles through the interface [43].

Moreover, the interfacial tension may be calculated by using the following equation:

$$\Gamma_{AB} = b\rho_0 kT\sqrt{\frac{\chi}{6}} \tag{4}$$

The Helfand-Tagami theory suggests that for the high molecular weight binary blend:

- ✓ the surface free energy (interfacial tension) varies only as $\chi^{1/2}$;
- ✓ the interfacial tension is inversely related to interfacial thickness;
- ✓ the chain ends of both component polymers concentrate at the interface;
- ✓ the third component, which has a lower molecular weight, is repelled to the interface;

Broseta and colleagues developed the Helfand-Tagami [44] theory for the interface of polymer with finite molecular weights (chain lengths). The terms N_A and N_B are the respective number of segments per chain of polymer A and B.

$$\Delta l = \frac{2b}{\sqrt{6\chi}}\left[1 + \frac{\ln 2}{\chi}\left(\frac{1}{N_A} + \frac{1}{N_B}\right)\right] \quad (5)$$

For lower molecular weight polymers, the interfacial thickness is much wider, approaching the Helfand-Tagami model for the higher molecular weight limit Eq. (3). **Table 1-1** summarizes typical interphase thickness values for polymer blends.

Table 1-1 Typical interphase thickness values for polymer blends [43].

Blend	Δl (nm)
Immiscible	2
Immiscible blends with block copolymer	5-15
Homopolymer/copolymer	30
Reactively compatibilized	30-60
Partially miscible	300

The majority of polymers are immiscible, and the interfaces dividing polymer pairs are mechanically thin and weak as predicted by the Helfand-Tagami theory, due to the weaker entanglement and interpenetration in the interfacial area. Furthermore, as indicated by Eq. (4), the interfacial tension between dissimilar polymers is significant. Generally, adding a third polymeric component as a compatibilizer, indeed a block or a graft copolymer, was the most common technique for compatibilization. It was expected that the compatibilizer

would tend to migrate to the interface and widen the segmental concentration profile. Several studies have found that adding a block or graft copolymer reduces interfacial tension and changes the molecular structure at the interface. Moreover, the addition method presents another problem, in which a copolymer tends to migrate to various locations, producing saturated solutions and mesophases or micelles in both phases and the interlayer. Thus, the additional copolymer compatibilizer should have:

a) good miscibility between components.

b) each block's molecular weight is just slightly greater than the molecular weight.

c) concentration slightly over the critical micelle concentration.

5.2. Interfacial diffusion

5.2.1. Basic interdiffusion theories

Mutual diffusion (also termed interdiffusion) occurs when two polymers come into intimate contact during melt processing, due to the migration of polymer chains across the interface. The interdiffusion process improves polymer-polymer adhesion and interface stability.

However, the mutual diffusion coefficient (D_m) is the parameter that controls the rate of disappearance of the concentration gradient and is governed by the system's composition, excess enthalpy, and entropy of segment-segment mixing [45] [39] [40]. It is determined using the following equation:

$$D_m = 2(\chi_S - \chi)\phi_A\phi_B D_T \tag{6}$$

here $\phi_A\phi_B D_T$ denotes an Onsager transport coefficient and is related to the mobility of segments or the monomeric friction coefficient of the components involved. The χ_S represents the interaction parameter at the spinodal

$$\chi_S = \frac{1}{2}\left(\frac{1}{\phi_A N_A} + \frac{1}{\phi_B N_B}\right) \tag{7}$$

where N_A and N_B are the degrees of polymerization for polymers A and B, respectively.

The transport coefficient D_T is related to the individual mobility of the components involved. Note that this coefficient was predicted by two distinct theories: the slow theory

with a slower moving component [48] and the fast theory [49] with a faster-moving one. Hence, both theories evolved from the Flory-Huggins lattice theory through Onsager syntax. It should be mentioned that the chemical potential gradient is the main factor behind interdiffusion.

The following equations illustrate the relationship between the flux J_i and the chemical potential gradient:

$$J_A = -\Lambda_A \nabla(\mu_A - \mu_V) \tag{8}$$

$$J_B = -\Lambda_B \nabla(\mu_B - \mu_V) \tag{9}$$

$$J_V = \Lambda_A \nabla(\mu_A - \mu_V) + \Lambda_B \nabla(\mu_B - \mu_V) \tag{10}$$

where Λ_i denotes the Onsager coefficient of lattice i. A, B, and V are the respective subscripts for molecule A, molecule B, and vacancy. The Flory-Huggins theory was used to derive the chemical potential gradient:

$$\nabla\mu_i = \frac{k_B T}{\phi_i}\left(\frac{\phi_B}{N_A} + \frac{\phi_A}{N_B} - 2\chi\phi_A\phi_B\right)\nabla\phi_i \tag{11}$$

where T corresponds to the temperature and k_B denotes the Boltzmann constant.

The slow theory assumed no vacancy flux $J_V = 0$, resulting in:

$$J_A = -J_B = \frac{-\Lambda_A\Lambda_B}{\Lambda_A + \Lambda_B}\nabla(\mu_A - \mu_B) \tag{12}$$

Combining Eqs. (11), (12) and the continuity Eq. (13) for molecule A

$$\frac{1}{\Omega}\frac{\partial\phi}{\partial t} = \nabla(-J_A) \tag{13}$$

yields:

$$\frac{\partial \phi}{\partial t} = \nabla(D_m \nabla \phi) = \nabla(-\Omega J_A) \\ = \nabla\left[\frac{\Omega k_B T}{\phi_A \phi_B}\left(\frac{\Lambda_A \Lambda_B}{\Lambda_A + \Lambda_B}\right)\left(\frac{\phi_B}{N_A} + \frac{\phi_A}{N_B} - 2\chi\phi_A\phi_B\right)\nabla\phi_i\right] \tag{14}$$

and D_m can be generated as follows:

$$D_m = \frac{\Omega k_B T}{\phi_A \phi_B}\left(\frac{\Lambda_A \Lambda_B}{\Lambda_A + \Lambda_B}\right)\left(\frac{\phi_B}{N_A} + \frac{\phi_A}{N_B} - 2\chi\phi_A\phi_B\right) \tag{15}$$

where Ω denotes the volume of a quasi-lattice site.

On the other hand, the fast theory considers $J_A \neq 0$ but rather $\nabla\mu_i = 0$, resulting in the total flux J_A^T of A:

$$J_A^T = -\Lambda_A \phi_B \nabla\mu_A + \Lambda_B \phi_A \nabla\mu_B \tag{16}$$

An identical expression of D_m can be derived:

$$D_m = \Omega k_B T\left(\frac{\phi_B}{\phi_A}\Lambda_A + \frac{\phi_A}{\phi_B}\Lambda_B\right)\left(\frac{\phi_B}{N_A} + \frac{\phi_A}{N_B} - 2\chi\phi_A\phi_B\right) \tag{17}$$

By comparing Eq. (17) to Eq. (16), we may determine:

$$D_T = \phi_B N_A D_A^* + \phi_A N_B D_B^* \tag{18}$$

The tracer diffusion coefficient D_i^* can be given:

$$D_i^* = \frac{\Omega k_B T}{N_i \phi_i}\Lambda_i \tag{19}$$

The Onsager coefficient Λ_i may be expressed as a function of Rouse mobility $B_{0,i}$, or as a function of the monomeric friction coefficient ξ_i of the lattice i:

$$\Lambda_i = \frac{B_{0,i} N_i^e}{\Omega N_i}\phi_i = \frac{N_i^e}{\xi_i \Omega N_i} \tag{20}$$

with N_i^e denoting the repeat unit number between entanglement length of composition i.

Since the interface remains symmetrical throughout interdiffusion, the slow-mode theory implies equal and opposing fluxes of both polymers. In comparison, the fast-mode theory explains interdiffusion with a moving interface as uneven fluxes balanced by a net flow of vacancies through the interface. It indicates a shift in the interface to the faster-diffusion component and a widening of the concentration profile in the slower component.

5.2.2. Interdiffusion in multilayer coextrusion

Polymer-polymer interdiffusion can also occur during coextrusion owing to the intermixing of component layers, resulting in the development of an interphase [29] [43]. This process offers an unusual opportunity to study the kinetics of interdiffusion, especially for miscible systems. A schematic illustration of interdiffusion behavior occurring in the layer multiplying coextrusion process for a miscible (nylon/EVOH) pair is highlighted in **Figure 1.11**. Due to the miscibility of the nylon and EVOH melts, the layers begin to interdiffuse as soon as they are coupled in the feedblock, then flow through a series of layer-multiplying die elements until the melt is quenched after exiting the film die. This process results in a rise in the number of layer interfaces, increases the melt contact time, and reduces layer thickness. As a result, the amount of interlayer interdiffusion quickly rises and eventually forces the whole melt into a homogenous blend after many multiplications.

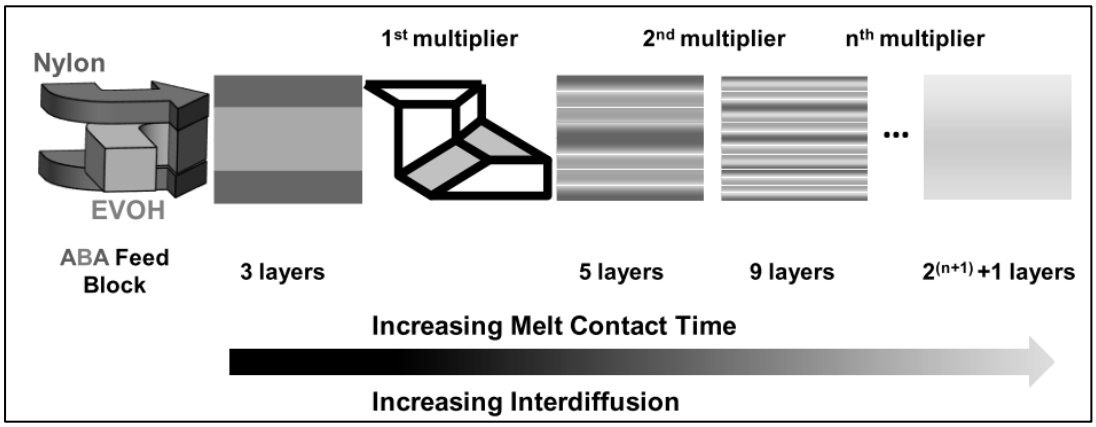

Figure 1.11 Schematic illustration of the interdiffusion of nylon and EVOH during the layer multiplying coextrusion process [51].

Khariwala and co-workers [51] investigated the kinetics of interdiffusion of two miscible polymers, nylon-6 and EVOH, during the multiplying coextrusion process (see **Figure 1.12**). As can be seen, the 17-layered films exhibit clear layer boundaries with smooth interfaces, and the 129-layered films exhibit a diffused interphase, but the two polymer constituents still appear in this sample. Whereas when the layer number increases to 1025, fully interdiffused nylon/EVOH layers are observed. This clearly demonstrates the interdiffusion behavior produced during the coextrusion process by the intermixing of component layers. Moreover, few studies have yet been presented about modeling interdiffusion during the coextrusion process. Baer *et al.* [50] studied the interdiffusion process in micro-layered structuresusing polycarbonate (PC) and copolyester (KODAR), and they developed a model to describe the interdiffusion that occurs during the coextrusion process. The composition profile can be obtained from Fick's equation for one-dimensional, nonsteady state diffusion:

$$\frac{\partial W_i}{\partial t} = D_m \frac{\partial^2 W_i}{\partial x^2} \tag{21}$$

where Wi denotes the weight fraction of species i, D_m indicates the mutual diffusion coefficient, t represents the diffusion time, and x defines the position. From the symmetry of the micro-layered structure, only one-half layers of the two components were considered. Furthermore, several assumptions of weakly interacting polymer were made in order to simplify the analysis:

a) the mutual diffusion coefficient D_m is independent of the composition and varies only with the temperature.

b) the interface between neighboring layers is assumed to be constant.

c) the first interface is neat, and the boundaries of the interdiffusion elements have a composition gradient of zero:

$$\left(\frac{\partial W_{PC}}{\partial t}\right)_{x=0} = \left(\frac{\partial W_{PC}}{\partial t}\right)_{x=(L_{PC}+L_k)/2} = 0 \tag{22}$$

where L_{PC} and L_k are respectively the layer thickness of PC and KODAR.

Following that, the partial differential Eq. (21) may be resolved using the variable separation method, resulting in:

$$W_{PC}(x,t) = \frac{L_{PC}}{L_{PC}+L_k} + \sum_{n=1}^{\infty} \frac{2}{n\pi} \sin\left(\frac{n\pi L_{PC}}{L_{PC}+L_k}\right) \times \cos\left(\frac{2\pi n x}{L_{PC}+L_k}\right) \exp\left(\frac{-4n^2\pi^2 Dt}{(L_{PC}+L_k)^2}\right) \quad (23)$$

By correlating the mutual diffusion coefficient to the gas permeability, we can calculate the concentration gradient across the interface. To conclude, this model is based on the slow-mode mechanism, in which the mutual diffusion coefficient is independent of the composition. As a result, it may be unable to explain fast-controlled diffusion, particularly in situations when the mutual diffusion coefficient is significantly influenced by the compositions [45] [46].

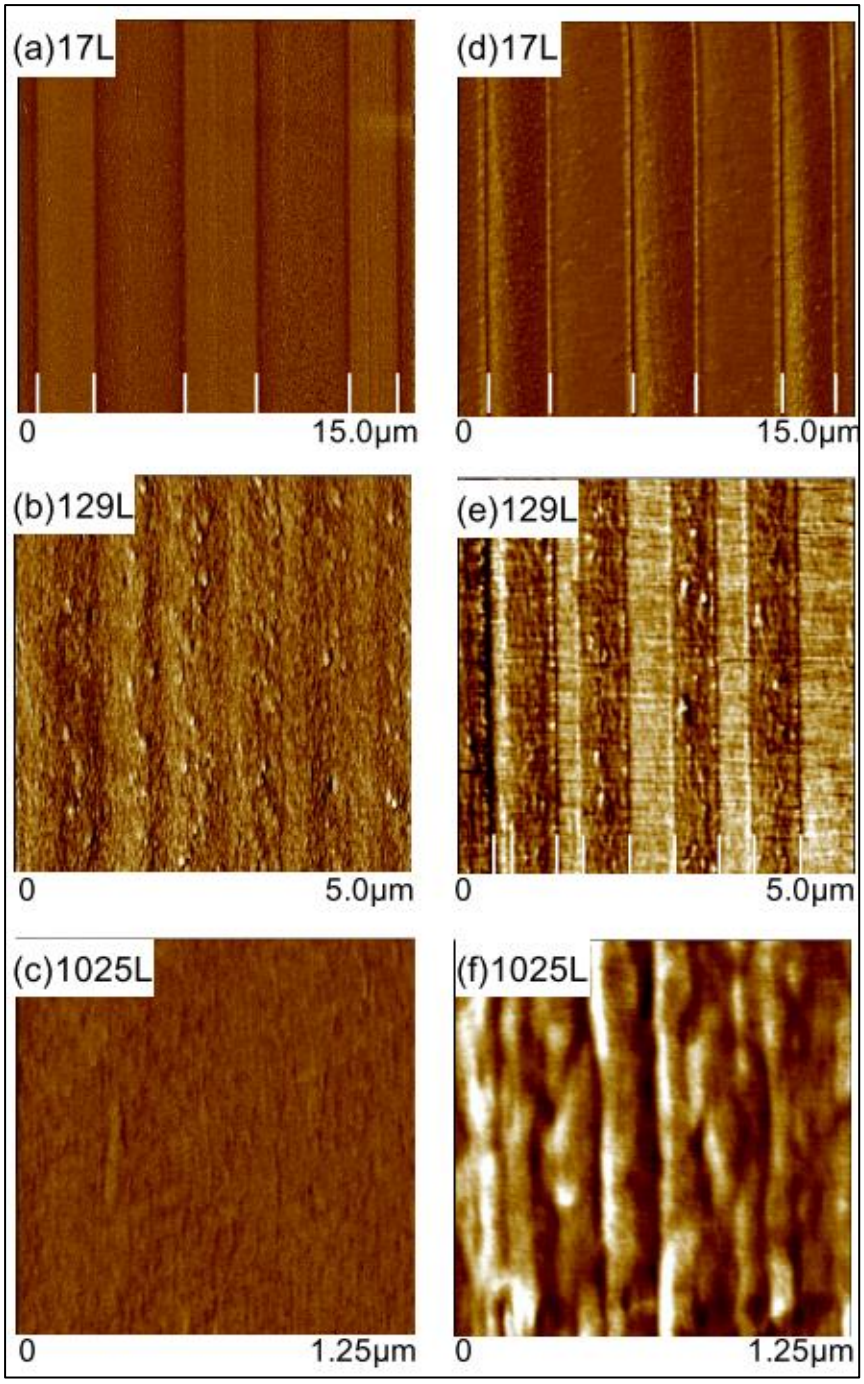

Figure 1.12 AFM phase images revealing the layer morphology of nylon/EVOH multilayers with an increasing number of layers for (a-c) nylon / EVOH44 multilayers and (d- f) nylon / EVOH24 multilayers. (a,d) 17 layers with a nominal layer thickness of 3.2 μm, (b,e) 129 layers with a nominal layer thickness of 400 nm, and (c,f) 1025 layers with a nominal layer thickness of 50 nm [51].

A more recent analysis based on the fast-controlled mode theory was proposed by Lamnawar et al, describing interdiffusion in a practical coextrusion process [53]–[55]. They developed a modified rheological model based on a primitive Qiu-Bousmina model [52], in order to compute the mutual diffusion coefficient with composition dependence, and then mapped the interfacial diffusion profile in the coextruded layers following the theory of polymer dynamics and fast-mode theory.

Considering the apparent coefficient of friction (ζ_b) for the mixture, the Onsager coefficient (Λ_i) has the following form:

$$\Lambda_i = \frac{N_b^e}{\zeta_b \Omega N_i} \phi_i \tag{24}$$

where (N) represents the average number of repeat units between entanglements for a polymer pair, and $(\zeta_{b)}$ denotes the monomeric friction coefficient that is strongly composition dependent. Thus, D_m can be linked to the structural properties of a binary A/B mixture as follows:

$$D_m = \frac{k_B T N_b^e}{\zeta_b}\left(\frac{\phi_B}{N_A} + \frac{\phi_A}{N_B}\right)\left(\frac{\phi_B}{N_A} + \frac{\phi_A}{N_B} - 2\chi\phi_A\phi_B\right) \tag{25}$$

Experimentally, the mutual diffusion coefficient (Dm) can be measured by relating it to the interphase's rheological behavior and using a planar polymer A/B sandwich assembly with a healing time:

$$\frac{1}{G_I^*(t)} = \frac{H}{2(D_m t)^{1/2}}\left(\frac{1}{G_{s,t}^*} - \frac{1}{G_{s,0}^*}\right) + \left(\frac{\phi_A}{G_{A,0}^*} + \frac{\phi_B}{G_{B,0}^*}\right) \tag{26}$$

where $G_{s,t}^*$and $G_{s,0}^*$ represent the respective complex moduli of sandwich assembly at healing times of t and 0, $G_{A,0}^*$ and $G_{B,0}^*$ designate the complex modulus of polymer A and B at t = 0, $G_I^*(t)$ defines the complex modulus of the interphase at the healing time t, and H denotes the total thickness. The mutual diffusion coefficient D_m is given by:

$$\zeta_b = \frac{\pi^2 k_B e_b^{'2} T}{N_b^3 b^4}\frac{1}{\omega}\left[\left(\frac{8G_{N,b}^0}{\pi^2 G_I^*(t)}\right)^2 - 1\right]^2 \tag{27}$$

In the Eq. (27), $G_{N,b}^0$ represents the average plateau modulus of the interphase/blend; N_b is the number of the repeat unit of the blend; e_b is the stem length on the order of the gyration radius of entanglements; b represents the effective bond length; and ω is the angular frequency. D_m is expressed as follows:

$$D_m = \left[\frac{(2/3)^{1/3} p}{\left(9q + \sqrt{3} \times \sqrt{-4p^3 + 27q^2}\right)^{1/3}} + \frac{\left(9q + \sqrt{3} \times \sqrt{-4p^3 + 27q^2}\right)^{1/3}}{2^{1/3} \times 3^{2/3}} \right]^2 \quad (28)$$

With

$$p = \frac{8\delta\omega G_{N,b}^0}{\pi^2} \left(\frac{\phi_A}{G_{A,0}^*} + \frac{\phi_B}{G_{B,0}^*} \right) \quad (29)$$

$$q = \frac{8\delta\omega G_{N,b}^0}{\pi^2} \frac{H}{2t^{1/2}} \left(\frac{1}{G_{s,t}^*} - \frac{1}{G_{s,0}^*} \right) \quad (30)$$

$$\delta = \frac{N_b^e {N_b}^3 {N_b}^4}{\pi^2 {e_b}^2} \left(\frac{\phi_B}{N_A} + \frac{\phi_A}{N_B} \right) \left(\frac{\phi_B}{N_A} + \frac{\phi_A}{N_B} - 2\chi\phi_A\phi_B \right) \quad (31)$$

The resulting interphase thickness may be calculated using the following formula:

$$h_I' = 2(D_m)^{1/2} \quad (32)$$

The basic Fickian solution may also be used to estimate the concentration profile of diffuse species across the interface:

$$\phi(z,t) = \frac{1}{2} \left[erf\left(\frac{h - z}{2(D_m t)^{1/2}} \right) + \text{erf}\left(\frac{h + z}{2(D_m t)^{1/2}} \right) \right] \quad (33)$$

where h denotes the layer thickness, and z represents the spatial axis along the diffusion direction with z = 0, and erf indicates the error function.

According to the proposed interdiffusion model above, it is possible to plot the evolution of the apparent mutual diffusion coefficient and the interphase thickness with time, as shown in **Figure 1.13**, for a PMMA/PVDF bilayer. X-ray analysis (EDX) was used to measure the concentration profile, and also the rheological model was applied to determine the mutual diffusion coefficient and interphase thickness of a PMMA/PVDF multilayers [55].

Interestingly, the predicted interphase thicknesses quantitatively match those found by X-ray analysis (EDX), suggesting that the interdiffusion model has been validated.

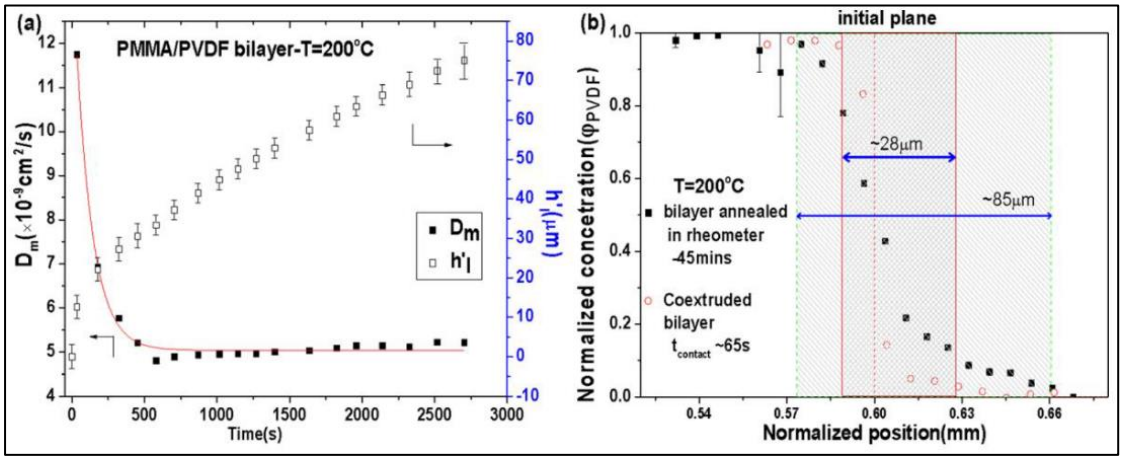

Figure 1.13 (a) Time evolution of the mutual diffusion coefficient and interphase thickness of a PMMA/PVDF bilayer healed at 200°C: (b) Normalized PVDF concentration profile versus normalized position determined from SEM-EDX in the cross-section of the bilayer after being healed for 45 min (solid black squares) and the coextruded bilayer (open red circles). [43].

5.3. Interphase materials

Some coextruded nanolayered materials with immiscible or weakly interacting pairs are referred to as interphase materials [50] [51]. Using the multilayer coextrusion technique, it is possible to produce films with thousands of layers, with individual layer thicknesses ranging from micro- to nanoscale. The amount of interphase generated by intermixing at the interface increases as the layer thicknesses fall below the interphase thickness (a few nanometers for immiscible pairs).

In research completed by Hiltner and colleagues, the glass transition temperatures of multilayered immiscible PC/PMMA (50/50 v/v) films were evaluated, with layer thickness ranging from 25 mm to 5 nm [58]. According to **Figure 1.14(a)** the observed glass transition temperature varied from bulk component values as the layer thickness dropped to 10 nm or less, or even combined into an intermediate value.

The unexpected crossing of the glass transition (as in miscible blends) is attributed to the finite interphase of mixed component chains. This suggests that the interphase fraction becomes much larger and eventually dominates the total systems, as shown in **Figure**

1.14(b). Moreover, it was observed that when the layer thickness is decreased below 10 nm, the permeability drastically increases. As a result, it is established that PC/PMMA nanolayered films are composed of three constituents: PC, PMMA, and interphase layers, as shown in **Figure 1.14(c)** [51] [52][59], [60].

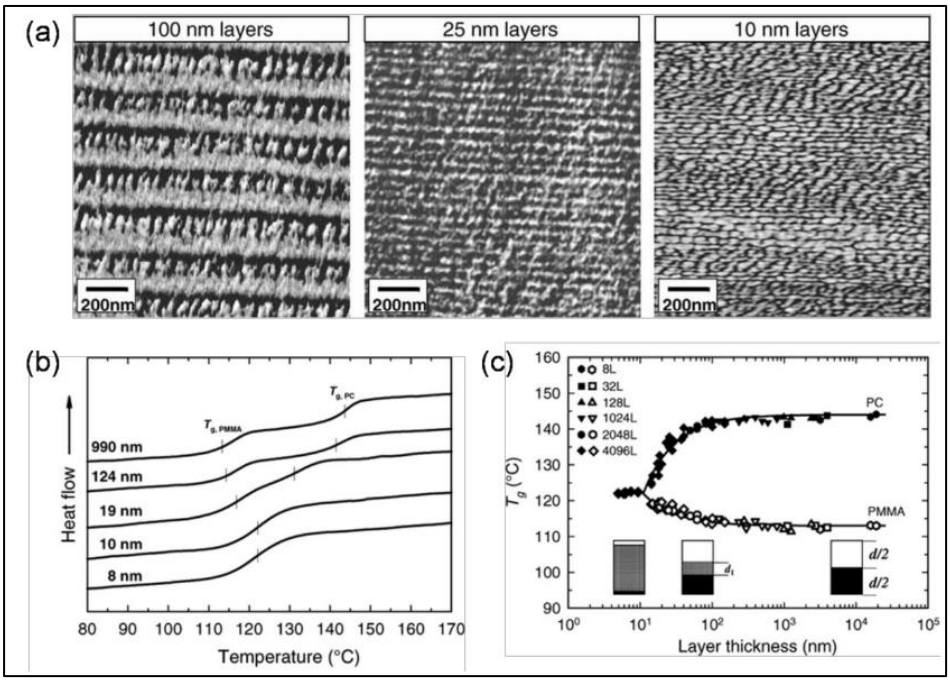

Figure 1.14 (a) AFM phase images for cross-sections of PC/PMMA nanolayer films. (b) DSC thermographs of multilayered PC/PMMA films. (c) Dependence of glass transition temperatures on the layer thickness of multilayered PC/PMMA films.

6. Rheological phenomena in multi-micro/nanolayer coextruded polymers

6.1. Melt flow instability in the coextrusion process

In coextrusion, melt flow instabilities are produced as a result of differences in the non-Newtonian and viscoelastic melt flow properties of the constituent polymers. These melt flow instabilities cause irregularities at the interfaces, non-uniform thickness, polymer intermixing, layer thickness variation, and film thickness variation [61]. The flow instability, viscosity, and viscoelastic differences between the constituent polymers can all contribute to the interfacial distortions that are observed. **Figure 1.15** depicts the surface conditions for three types of flow conditions: stable flow, moderately unstable flow, and highly unstable flow. This instability may be produced by an improperly matched viscosity ratios during co-extrusion process. At low melt flow rates, a smooth interface between layers

is observed, indicating that the flow is stable (**Figure 1.15 (a)**). As the melt flow rate increases gradually, some minor waviness may develop at the layer's interface, which may not affect the overall film quality. Extremely high melt flow rates, on the other hand, can result in very strong layer distortions in the film structure (**Figure 1.15 (c)**).

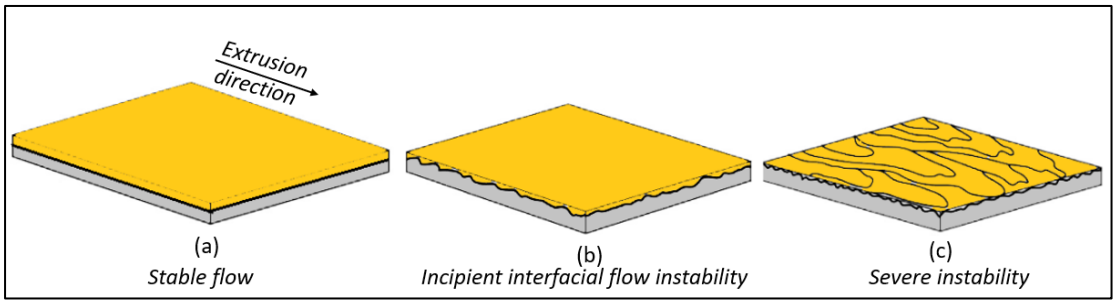

Figure 1.15 Illustration of film or sheet appearance. In (a) stable flow conditions, (b) incipient interfacial flow instability, and (c) severe instability.

Among the most common interfacial instabilities, we can mention the zigzag and wave type patterns (see **Figure 1.16**). They are both correlated to viscous instabilities.

When the critical shear stress is exceeded, zigzag patterns are produced. In this case, the instability occurs in the direction of the flow. This instability can be solved by decreasing the shear stress below the critical value. Other parameters could be adjusted to reduce zigzag instability, such as increasing the die gap, reducing the extrusion rate, and decreasing the skin layer viscosity.

Wave-type instability, on the other hand, manifests as parabola shapes spanning the film's width. This instability is also viewable in the flow direction. Unlike the zigzag pattern, the wave pattern is more closely related to the geometric shapes of the feed block and dies. To prevent this kind of instability, the feed block and die designs must be adjusted. These shortcomings may result in the material degradation of the final properties in some cases, especially those that require a regular, homogeneous structure (optical properties, for example).

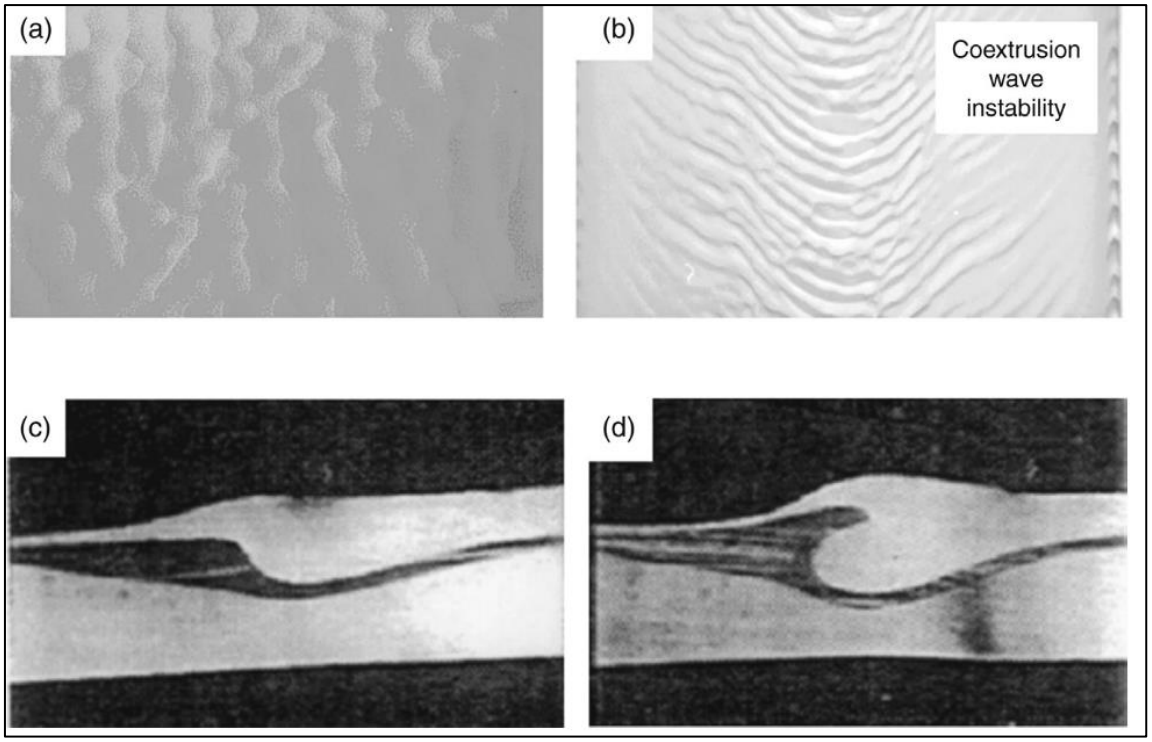

Figure 1.16 Interlayer instability patterns (a) zigzag, (b) wave, and (c,d) cross-section image of wave pattern evolution in a three-layered film

6.2. Effects of rheological mismatch on the layer structure

Adapting the rheological properties is a critical step in producing a high-quality multilayer structure. This section will discuss the impact of insufficient adaptation and inappropriate selection of rheological parameters. The viscoelastic couple defines a polymer's rheological properties. In addition to elastic instabilities, the mismatch in the viscosities of the two polymers results in the encapsulation phenomenon. This phenomenon occurs in the direction of extrusion, as the less viscous polymer A migrates toward the wall and encapsulates the viscous polymer B (see **Figure 1.17**).

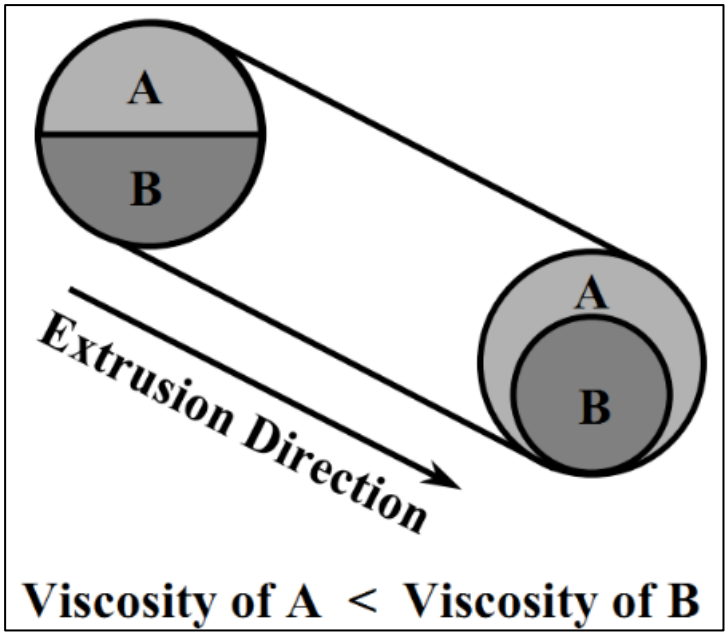

Figure 1.17 Viscous encapsulation in the layered A/B system.

Encapsulation is one of the most frequently observed interfacial distortions in multilayer coextrusion. Moreover, encapsulation is dependent on shear rate and residence time. The greater the shear rate, the more the encapsulation phenomenon becomes visible. The residence time is the duration over which the less viscous polymer approaches the walls. The effect of residence time on the final deformation caused by the encapsulation phenomenon is illustrated in **Figure 1.18.** The presence of encapsulation-induced deformation becomes more palpable as the residence time (Z cm) increases.

The encapsulation phenomenon may occur by second flow motion, even with matched viscosities. In [62], very explicit experimental and numerical demonstrations have been made to show the encapsulation phenomenon generated by the second normal stress difference. The experimentations were performed using low-density polyethylene (LDPE) with a different pigmentation (black/white) and a square-section die channel, see **Figure 1.18**. This highlights the gradual development of white lobes that are slightly smaller at a high melt flow index. As described below, the encapsulation phenomenon becomes more pronounced as the distance Z between the feedblock's output and the die’s wall grows.

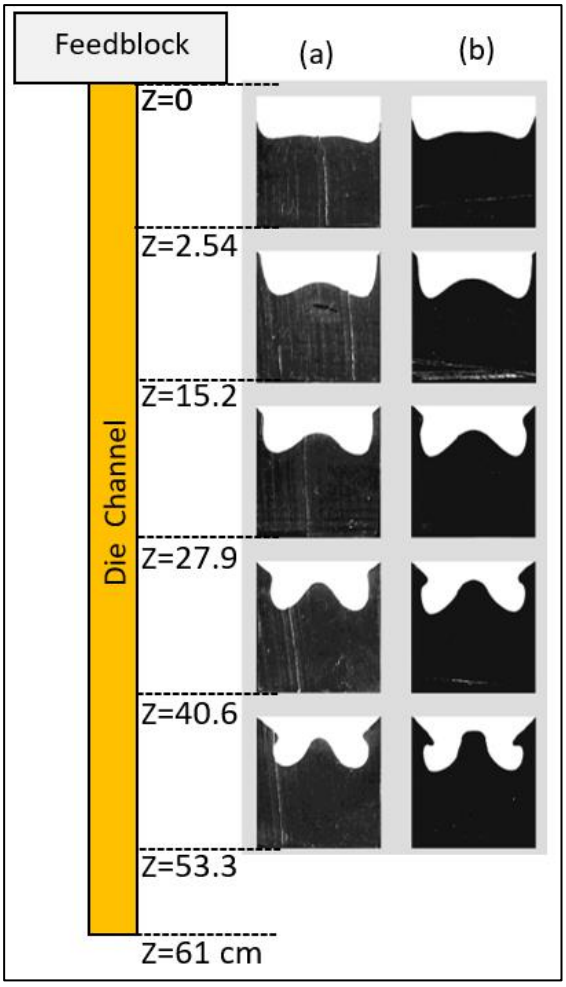

Figure 1.18 (a) Low flow rate and (b) high flow rate, with Z as the distance between the feedblock's output and the die channel's output [62].

In the same article [62], Debbaut and Dooley numerically drew the profiles of the second normal stress (N2) difference along the median and diagonal lines on a square cross-section of the straight channel at a total flow rate of 2.5 kg/h. The LDPE properties were used for computing. This simulation was performed using a mathematical multimode differential viscoelastic fluid model. N2 is more pronounced near the channel's lateral surfaces and is completely absent in the channel's center. The model matches the experimental findings, as shown in **Figure 1.19**. Based on the profiles, the researchers believed that the secondary movements were initiated by the nature of the boundary conditions on the lateral surfaces. As previously stated, the speed gradient indicates that the speed is zero at the lateral surfaces' edges and maximum in the middle. Additionally, the closer the particles are to the walls, the

greater the resistance to flow; as a result, the particles gravitate toward the center, which fuels the secondary movement.

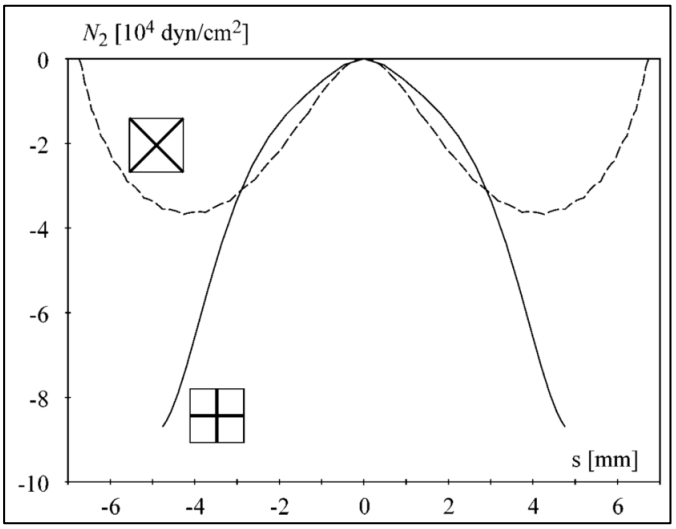

Figure 1.19 Profiles of the second normal stress difference along the median (-) and diagonal lines (- - -) in a square cross-section with a total flow rate of 2.5 kg/h [62].

The second flow motion depends on the geometry of the die and the elasticities of the polymers coextruded. Concerning the impact of the die geometry, experiments were carried out in [63], using the same polymer(polyethylene) with different pigmentation (black/white), showing the difference between film coextruded through the circular die and through the square die (see **Figure 1.20** and **Figure1.21**). We notice that the secondary flows caused by second normal stress differences in elastic polymers are more significant in the square die channel. Secondary flows in a circular die are very weak because of their radial symmetry. To summarize, to achieve a layer with good uniformity and to avoid distortion caused by poor adaptation of rheological properties, it is necessary to choose viscosities that are close between coextruded polymers. Similarly, careful selection of the polymer's elasticity and die geometry is critical for minimizing secondary flow motion.

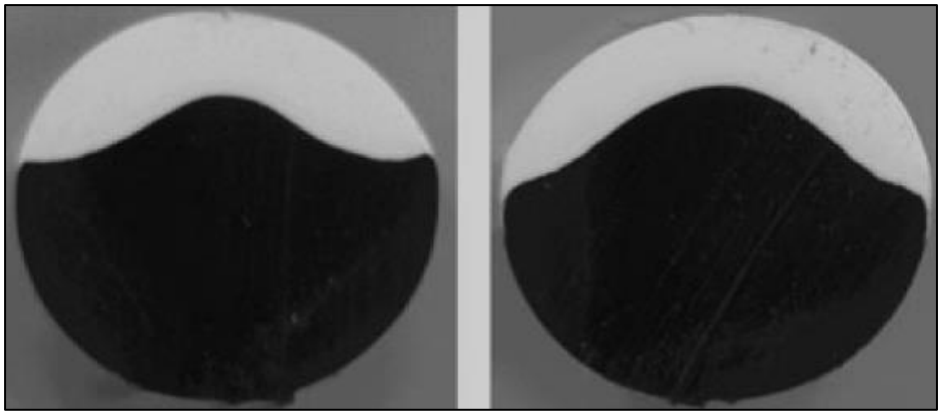

Figure 1.20 Layer interface deformation for a coextruded structure of polyethylene D resin in both layers flowing through a circular channel with (a) a position near the entry and (b) a position near the exit of the channel [63].

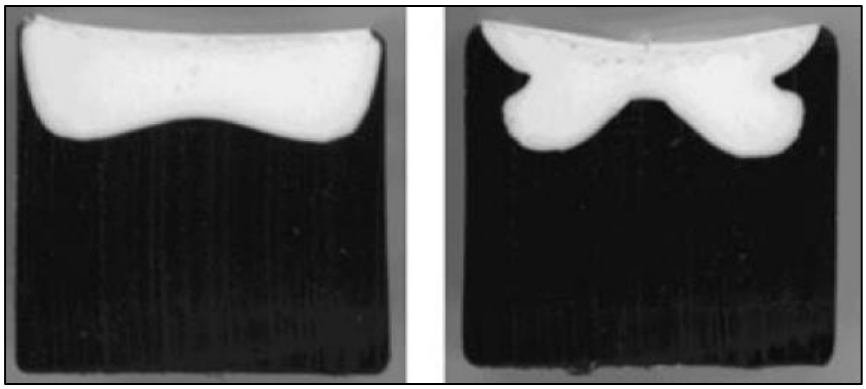

Figure 1.21 Layer interface deformation for a coextruded structure of polyethylene D resin in both layers flowing through a square channel with (a) a position near the entry and (b) a position near the exit of the channel [63]

6.3. Interfacial slip in nanolayers

Interfacial slip is a phenomenon that occurs when polymer chains become disentangled at interfaces under high shear rates (**Figure 1.22(a)**). As is well known, the majority of commercial polymers are thermodynamically immiscible, and their interfacial area between them may have a lower density than their constituent bulk materials. As a result of decreased entanglements at their interface, a considerable slip may occur at the interface throughout the flow. Interestingly, when A/B layered materials exhibit low chemical compatibility or

adhesion, densitometry differences within layered films with large numbers of layer interfaces may result in nontrivial interphase volumes [61]. At high shear rates, low chain entanglement in interphases exhibits interfacial instability, leading to an interfacial slip mechanism.

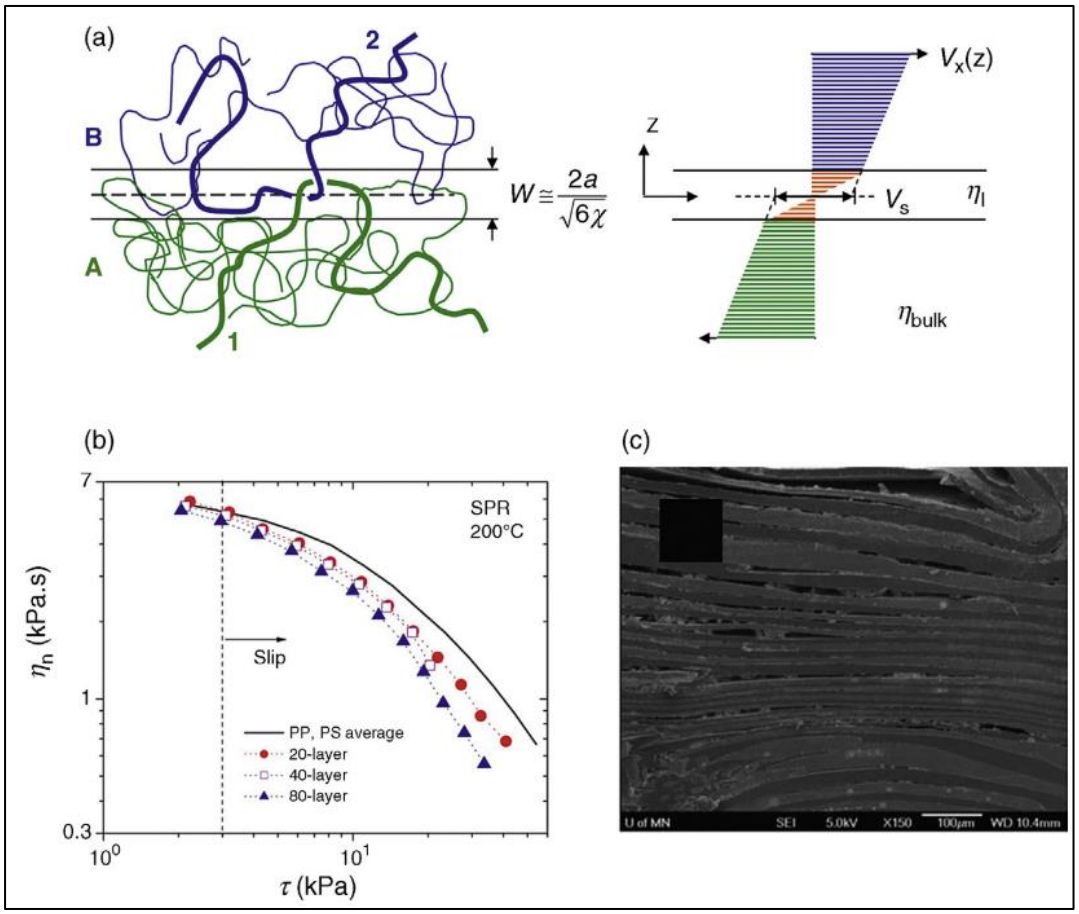

Figure 1.22 (a) The interface between entangled melts of two incompatible polymers A and B. Chains are less entangled in the interfacial region than in the bulk, although some pairs of A and B chains (such as the chains 1 and 2 shown) nonetheless form entanglements across the interface. The result is a lower interfacial viscosity, ηI, when a shear stress, τ, is applied. The fluid velocity appears, at a macroscopic level, to be discontinuous across the interfacial region, with an apparent slip velocity Vslip; (b) nominal viscosity of multilayer samples and the harmonic average solid lines of the neat components, as measured in the sliding plate rheometer by steady shear experiments, namely PP and PS, with deviations from the average viscosity observed above approximately 3 kPa; and (c) SEM micrographs of 80-layered PP/PS samples after steady simple shear in the rotational parallel-disk [61].

The presence of interfacial slip phenomena in several-layered polymeric film systems has been thoroughly investigated by Macosko and colleagues, as a function of the number of layer interfaces, material compatibility, and applied shear. For example, PP/PS multilayer films with closely matched viscosities were used to determine the pressure drop via a slit die, and the normal viscosity in a shear rheometer [64]–[66]. At a high shear rate, an obvious deviation was observed between the measured pressure drops of multilayer samples and the normal viscosity (**Figure 1.22(b)**) when compared to homopolymers. The authors noticed a considerable slip between the PP and PS interfaces as the flow rate was increased. As shown in **Figure 1.22(c)**, severe film layer instability manifested as layer breakup and/or delamination in nanolayered materials. This may have been caused by interfacial slip. In another example, PS/PMMA multilayer films with a lower Flory–Huggins parameter χ than PP/PS were used to study coextrusion effects on interfacial adhesion. They found a slight pressure drop, and slip velocity decreased with the interfacial width [64]. Additionally, the incorporation of a premade polystyrene-block-ethyl-ethylene-diblock copolymer P(S-b-EE) to the PP/PS system could suppress the interfacial slip [64]. The interfacial slip phenomena indicate that, in addition to the usual assumption of matching viscosities, interfacial interactions and sufficient adhesion in multilayered polymers during processing are very important to reduce or even suppress this phenomenon.

6.4. Layer breakup

The layer breakup phenomenon is a defect that affects the uniformity and continuity of the layers that are formed, resulting in irregularities at the interface [67]. This occurrence often leads to a deterioration of the final properties of the film, particularly those requiring a regular and uniform structure, such as transparency (optical properties, for example). However, considerable layer breakup was seen for many nanolayered systems during the coextrusion process, suggesting that the layer-continuity limit is system-dependent. For example, continuous layers of polycarbonate (PC) and poly(methyl methacrylate) (PMMA) have been achieved at a thickness of 5 nm [57], while nothing thinner than 25 nm has been observed for polypropylene (PP) and polystyrene (PS) [68] **(Figure 1.23**). Unfortunately, for PP/PC systems, only layers thicker than 500 nm can be obtained [69]. In another study, Hiltner and colleagues found that the layer breakup phenomena reduce the barrier property

of a PP/poly(ethylene oxide) (PEO) nanolayer film when the PEO layer thickness is below 25 nm [70].

For the development of new nanolayered polymeric materials with enhanced properties, it is critical to better understand the processes that govern the breakup of these layers. Currently, information about the mechanism controlling the layer breakup in nanolayers, and also the physical mechanisms governing them, is still lacking in the literature. However, some authors have suggested that layer breakup phenomena during coextrusion might be produced by a distorted interface or instabilities in coextrusion (viscous encapsulation or secondary flows), which are mainly encountered when rheologically mismatched polymers are coextruded. The interfacial instabilities started initiated by a minor perturbation at the interfaces that can be amplified along with the flow in the die, particularly when the layer thicknesses are reduced below a critical value. It has been shown that elastic and viscosity jumps at interfaces enhance instability.

Additionally, it has been shown that material properties contribute to layer breakup. Bironeau et al. recently demonstrated that a critical layer thickness of about 10 nm exists in another PS/PMMA multilayer system, below which the layers deteriorate. This is explained by small interfacial perturbations that are exacerbated by van der Waals disjoining forces. The critical layer thickness seems to be solely dependent on material properties, and completely independent of the processing parameters. In another PVDF/PC system with a significant rheological mismatch, the layers break up into micro sheets and droplets when the nominal layer thickness is less than 160 nm. This is caused by viscoelastic differences between the component melts, and the resulting dielectric properties are dramatically altered [60]. This is similar to the dewetting phenomenon, which occurs when thin polymer layers spontaneously break into nanosheets and nanodroplets, resulting in the appearance of morphologies that are similar to those seen in polymer mixtures [67].

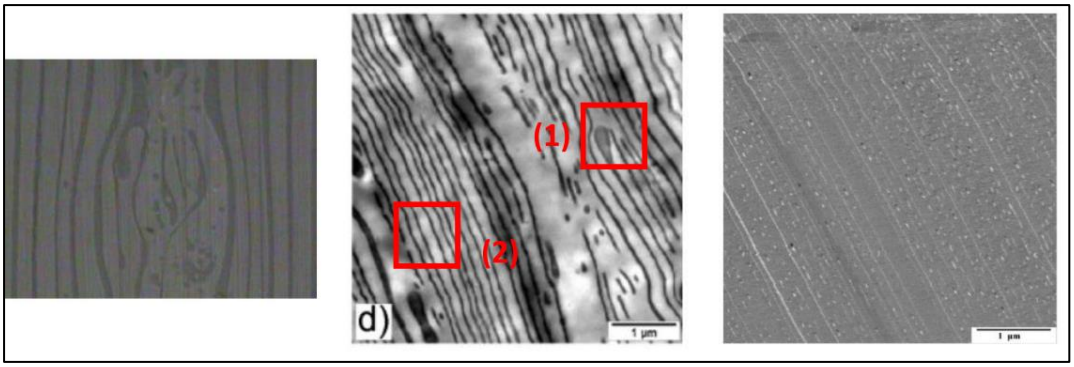

Figure 1.23 Micrographs showing the existence of layer breakup induced by the coextrusion process for different systems, including: (a) PP/PC (optical microscopy), (b) PP/PS (TEM), and (c) PET/PC (AFM).

7. Concluding remarks and originality of our approach

Multilayer coextrusion has become a significant manufacturing process that has expanded the application and usage potential of multilayer structures by combining thousands of alternating layers of two or three polymers. This technical advancement has enabled an improved understanding of polymer structures, physicochemical properties, interactions at the micro and nanoscale, rheology, and dynamics at the polymer-polymer interfaces. This chapter investigated systematically the interfacial phenomena involved in multi-micro-/nanolayered polymer coextrusion from a fundamental science and an engineering perspective. These phenomena, including interlayer diffusion, interfacial instabilities, and interfacial geometrical confinement, frequently occur at the layer-layer interfaces of multilayered polymers produced by multilayer coextrusion processing. The origins and basic theories of these interfacial phenomena are described, as well as how they can affect microstructural development and macroscopic properties that result. In particular, these interfacial phenomena have a notable role in determining the interlayer adhesive strength, glass transitions, mechanical and other physicochemical properties of coextruded multilayer polymers. These processes of multilayer systems show strong dependences on the compositions, thicknesses and numbers of layers, processing conditions (such as flow fields and temperature), and the inherent properties of constituent polymers as well. An understanding of the rheology and dynamics at the polymer-polymer interface is essential for establishing the processing-structure-property relationship of multilayered polymers in coextrusion process. Moreover, this chapter provides some suggestions influencing the interfaces and microstructure in multilayered polymer systems intended for advanced applications. Despite the interesting research papers published recently to this filed, there a few investigations to tackle coextrusion of high mismatched viscoelastic polymers. Moreover, this thesis will contribute to better understanding the relationships between molecular structure, processing, and properties in various scales ranging from micro to nanoscale. Hence, a multi-scale investigation of interfacial phenomena in micro-nanolayered polymers will be addressed. Another originality of our approach is dealing on how forced assembly layer coextrusion can be used for the eco-design by recycling to help recyclability of the developed structures.

Chapter 2. Structure-rheology properties of polyethylenes with different macromolecular architecture

This chapter deals with the studied four polyethylenes to be coextruded with PS or PC as confined polymers. The main objective is to gain a better understanding of the structure and architecture properties of these PE in relationship with their shear and elongation properties. For the clarity of this manuscript, the rheological properties of the confined polymers will be given, for comparison, in the following chapters.

1. Introduction

Polyethylene is one of the most widely used polymers in the packaging industry. It is classified into three main categories: high-density polyethylene (HDPE), linear low-density polyethylene (LLDPE), and low-density polyethylene (LDPE), as illustrated in **Figure 2.1**. HDPE has a linear structure with few or no small branches, which results in a high degree of crystallinity and a low-strain hardening in the melt state [71]. High-density polyethylene (HDPE) and linear low-density polyethylene (LLDPE) are polymerized using ethylene and α-olefins, which are commonly 1-butene, 1-hexene, and 1-octene [72] [73]. Single-site catalysts (SSC) even enable the incorporation of a small number of long-chain branching (LCB) structures into linear polyethylene (PE), thus enhancing processing characteristics. As a result, their molecular structure, physical properties, and applications are very different. LDPE, on the other hand, is often made by a free-radical process at high temperatures and pressure [74]. This process results in a polymer with a very large molecular weight distribution and a complex structure containing a wide range of branching structures leading to irregular packing. LDPE contains both short-chain branches (SCBs) and long-chain branches (LCBs) that can be as long as the main chain.

The molecular weight distribution, degree of branching, branch length as well as nature of branching existing in polymers have a significant effect on their processing behavior and rheological properties in both shear and elongational regimes [75]. The issue is to understand the relationship between structural changes in polyethylene chains and melt rheological properties, since rheological performances are very sensitive to molecular structures.

It is widely known that short-chain branches suppress crystallinity, which accounts for the low density in the solid phase and the high flexibility [74]. Besides that, long-chain branches allow the viscosity to drop significantly when the shear rate is raised, which facilitates the processing of this material in the molten state. Increased LCB enhances zero shear rate viscosity, but it is difficult to obtain a correct measurement of this viscosity using rheological

methods, according to its higher pronounced shear thinning behavior [76]. Moreover, homogeneous LCB distribution is known to show strain hardening during elongational flow and to alter crystallization and phase behavior in the solid state, resulting in changed mechanical properties when compared to linear structures [77] [76] [75][78].

Different characterization techniques have been used to characterize the types of branching, degree, and branch length of LDPE and LLDPE using techniques such as ^{13}C NMR spectroscopy, triple detection GPC, and rheological methods [76] [79] [80] [81] [82]. Shear-thinning and melt strength can all be used to estimate the amount of LCB present in a sample, but they are unable to directly determine the amount of LCB. Although ^{13}C NMR spectroscopy has been widely used to measure LCB, it is difficult for this technique to provide an intrinsically quantitative LCB quantification, because all branches longer than six carbons provide the same result.

The goal of the present chapter is two-fold: the first part is devoted to giving a very detailed characterization of the molecular structure of linear and branched polyethylene. Next, the second section is dedicated to investigating the linear and nonlinear rheology of the PEs at the molten state. These findings will contribute to better understanding the relationships between the molecular structure of linear and branched PEs and their rheological properties (both linear and non-linear viscoelastic properties).

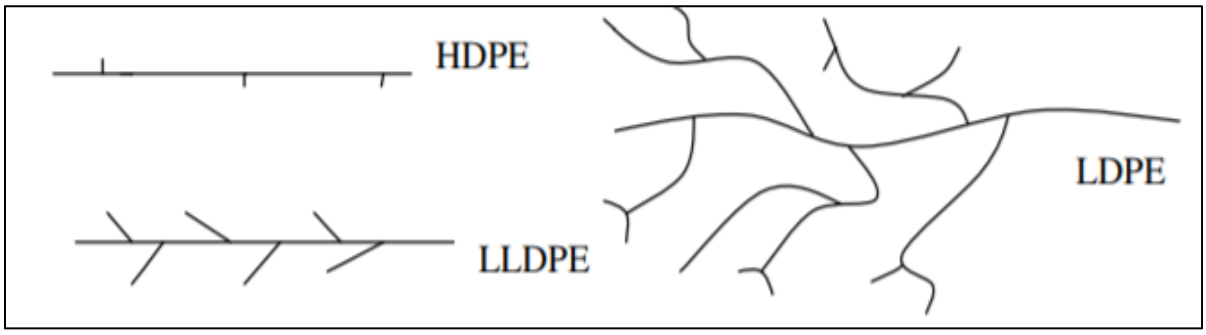

Figure 2.1 HDPE, LDPE, and LLDPE molecular structures.

2. Experimental section

2.1. Materials and sample preparation

Two sets of samples were selected in view of our goals: a set of two low-density polyethylenes (ExxonMobil 165 and LyondellBasell 3020D) and two linear low-density polyethylenes (INEOS 6910 and MarlexD139) with different molecular weights and branching architectures. The LLDPE used was an ethylene-1-hexene copolymer produced by a metallocene catalyst (**Table 2.1**).

Table 2-1 Summary of polyethylenes selected in this work.

Polymer	**Manufacturer**	**Comonomer type**	**Density (g/cm3)**	**MFI** (190°C/2.16 kg) (g/10min)
LDPE-L1	ExxonMobil 165	-----	0.922	0.33
LDPE-L2	LyondellBasell 3020D	------	0.928	0.3
LLDPE-LL1	Ineos 6910	1-Hexene	0.936	1
LLDPE-LL2	MarlexD139	1-Hexene	0.918	1

2.2. Small-amplitude oscillatory shear measurements (SAOS)

Rheological measurements of the neat polymers were performed by a stress-controlled DHR-2 (Discovery Hybrid Rheometer, TA Instruments), using 25 mm parallel-plate geometry with a gap of 1 mm. The experiments were conducted at temperatures ranging from 150 to 250°C under nitrogen atmosphere. The specimens for rheological measurements were compression-molded for 5 min to reduce any residual stress with a pressure of 200 bars between two Teflon films to obtain a smooth surface. The first test was a dynamic strain sweep with a maximum angular frequency of 628 rad/s [43]. Thus, the strain value is fixed to 5% to ensure the linear viscoelastic domain.

Moreover, the following rheological tests were performed:

1) A dynamic time sweep test was performed to verify the thermal stability of the neat polymers at different molten temperatures at a set angular frequency of 1 rad/s.

2) A dynamic frequency sweep tests with frequencies ranging from 628 to 0.01 rad/s at fixed strain amplitude of 5% from 150 to 250°C.

2.3. Start-up uniaxial extensional rheology

Extensional rheology was performed to probe the effect of long-chain branching (LCB) and short-chain branching (SCB) of the selected PEs and to understand the effect of molecular structures on their rheological properties. More recently, it has been proved that the elongational experiments are more sensitive to long-chain branching than classic characterization methods (SEC-MALLS, etc.) [83].

In our study, uniaxial extensional rheology measurements were carried out by a Sentmanat Extensional Rheometer fixture (SER-2, Xpansion Instruments, LLC) mounted on a DHR-2 TA instrument. The neat polymers were split into strips with dimensions of 20 mm x 10 mm x 0.8 mm (length x width x thickness). Then, the extremities of the sample were mounted on the dual rotating windup drums, to ensure a uniform extensional deformation. Therein, the extensional flow data were collected at different Hencky strain rates at a constant temperature of (150°C,190°C, and 240°C) under a nitrogen atmosphere. Strain validation and continuous visual access were performed during the measurements by a built-in camera to monitor the evolution of a specimen's width dimension at the constant Hencky rate [55]. This allowed us to ensure that we are in pure uniaxial deformation if the slop is the half of the applied strain rate. **Figure 2.2** shows an example of the real recorded camera evolution of neat polymer LLDPE-LL2 undergoing stretching at a constant Hencky strain rate of 0.1 s^{-1}, while **Figure 2.3** shows an example of calculated width dimension from pictures and its comparison theoretical values. The evolution of the actual sample width was compared with theoretical ones by using Eq. (34):

$$W(t) = W_0[\exp\left(-\frac{\dot{\varepsilon}_H(t)}{2}\right)]^{1/2} \quad (34)$$

, where W_0 is the initial width dimension before stretching.

Excellent superposition of actual and theoretical width evolution values is obtained for all PEs thereby illustrating the agreement between actual and applied strain with the SER over a broad range of extensional rates (0.1 and 10 s^{-1}), which further ensures a truly uniform extensional deformation during uniaxial extension experiments in the whole range of Hencky amplitudes (from 0 to 3.8).

The Hencky strain rate can be expressed as:

$$\dot{\varepsilon}_H = \frac{2\Omega R}{L_0} \tag{35}$$

where R corresponds to the windup drum radius, L_0 is the fixed length of the specimen sample, and Ω represents the angular rotation speed of the cylinders.

For a constant Hencky strain rate, the cross-sectional area of the stretched molten specimen can be expressed as:

$$A(t) = A_0\left(\frac{\rho_s}{\rho_M}\right)^{2/3} \exp(-\dot{\varepsilon}_H t) \tag{36}$$

where ρ_M is the melt density of the polymer, ρ_S is the solid-state density, and A_0 is the initial cross-sectional area at the solid state. Then the tensile stress growth coefficient, $\eta_E^+(t)$, of the stretched sample can be defined as:

$$\eta_E^+(t) = \frac{F(t)}{\dot{\varepsilon}_H A(t)} \tag{37}$$

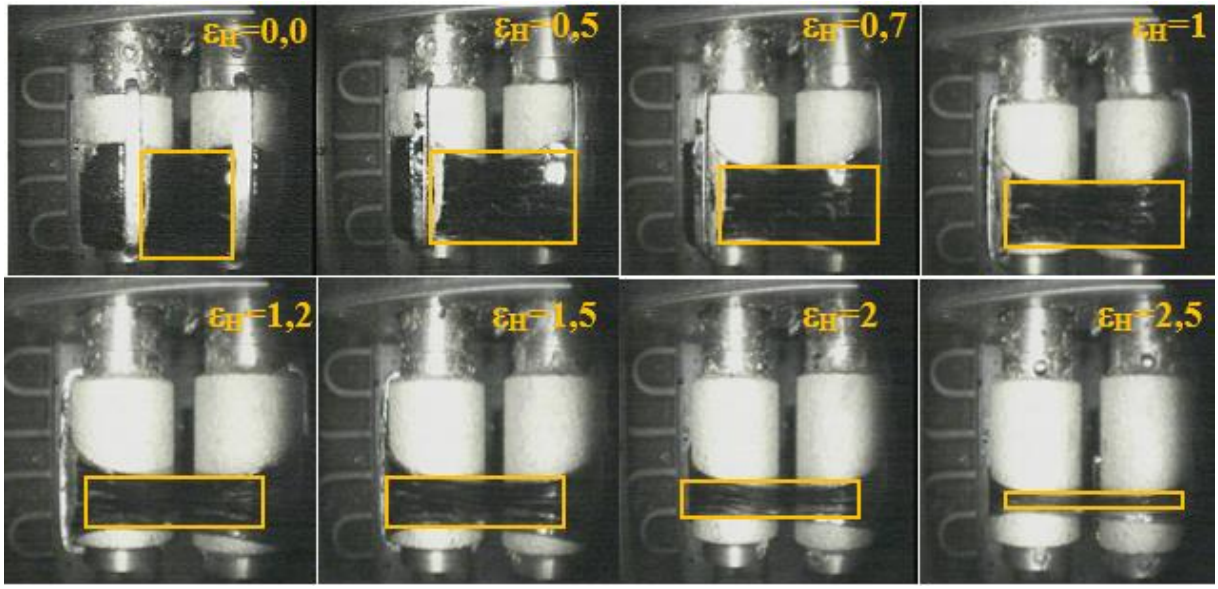

Figure 2.2 Example of sequential images recorded by the built-in camera to show the evolution of actual width dimension of neat polymer LLDPE-LL2 at 190°C undergoing stretching at a constant Hencky strain rate of 0.1 s^{-1}.

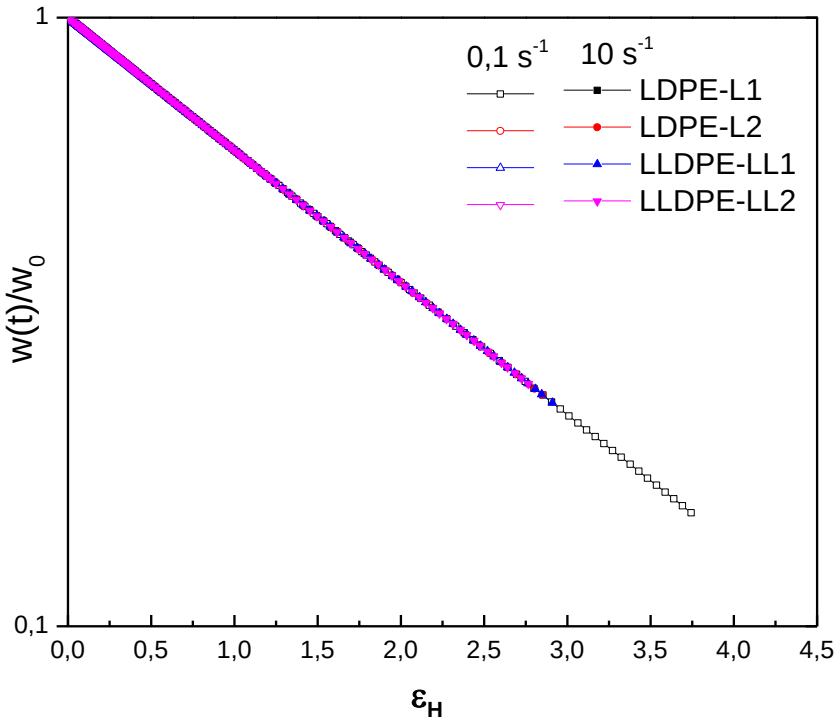

Figure 2.3 Calculated width ratio from sequential recorded image for all PEs against the Hencky strain for two applied strain rates: 0.1 s^{-1} and 10 s^{-1}. The obtained results corroborate the theoretical values and confirm that deformation is uniaxial during measurements.

For each polymer, the linear viscoelastic (LVE) envelopes were determined independently by fitting the oscillatory shear data with a multi-mode Maxwell discrete relaxation spectrum using the following formulas:

$$G'(\omega) = \sum_{i=1}^{N} G_i \frac{(\omega\tau_i)^2}{1+(\omega\tau_i)^2} \tag{38}$$

$$G''(\omega) = \sum_{i=1}^{N} G_i \frac{\omega\tau_i}{1+(\omega\tau_i)^2} \tag{39}$$

where G_i and τ_i are the relaxation strength and the time constant of mode i, respectively. In addition, these parameters were used to calculate the LVE extensional viscosity (zero-rate limit) referred to as the Trouton equation used to normalize extensional viscosity data as follows:

$$\eta^{+}_{E,0} = \lim_{\varepsilon \to 0} \eta^{+}_{E}(t,\dot{\varepsilon}) = 3\sum_{i=1}^{N} G_i\tau_i(1-e^{\frac{t}{\tau_i}}) \tag{40}$$

2.4. Thermal and physicochemical characterization of the PEs

2.4.1. Size-exclusion chromatography and multi-angle laser light scattering (SEC-MALLS)

Size-exclusion chromatography is a method in which molecules are separated according to their hydrodynamic volume and size. The combination of SEC for separation with a multi-angle laser light scattering (MALLS) for analysis provides a versatile and reliable way to characterize the polymer chain microstructure. The separation principle of SEC-MALLS is described in **Figure 2.4**. The stationary phase is a porous gel in which small molecules will remain within the pores and flow more slowly, whereas large, dissolved molecules will stay in the mobile phase and flow quickly because they are too large to penetrate into the pores, thus efficiently sorting the molecules by size. Then, each small fraction of polymer eluted leaving the SEC column is analyzed instantly by the multi-angle laser light scattering MALLS. The MALLS term refers to the amount of light scattered by the samples at each angle detected and is used to study the long-chain branching of PEs. This method is more sensitive to the presence of long-chain branching in high molecular weights than in the low molecular weights [79].

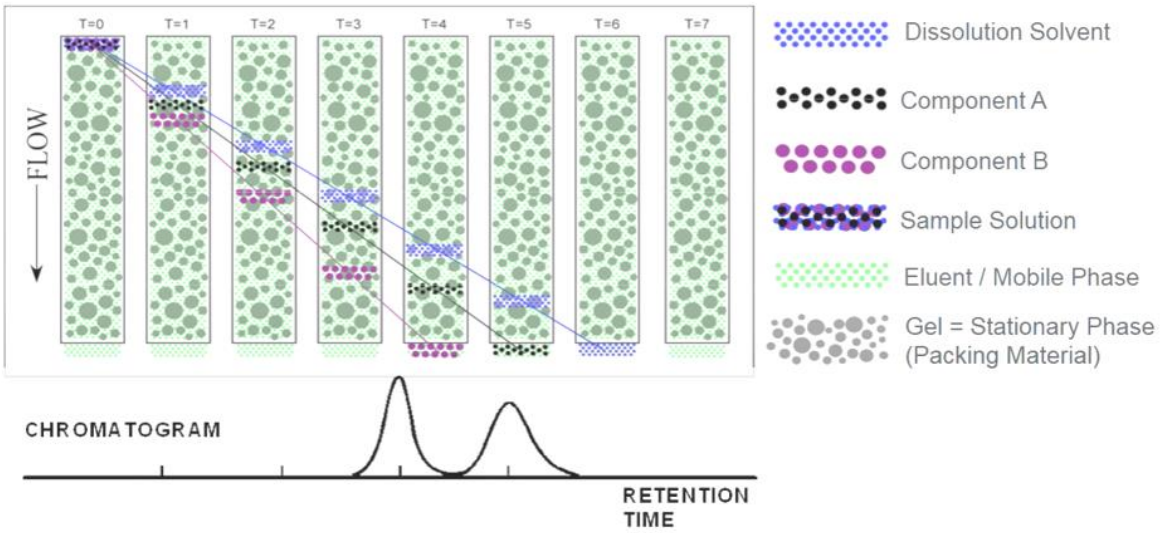

Figure 2.4 The separation principle of SEC.

The absolute molar masses and radius of gyration Rg of all PEs used in this study were measured directly by the SEC-MALLS technique. Therefore, the long-chain branching distribution and content in the PEs were also determined by direct application of the Zimm–Stock approach [84]. The measurement was done at 150°C with 1,2,4-trichlorobenzene (TCB)

solvent and a flow rate of 1 mL/min. The light scattering detector was placed in line between the SEC system and the refractive index detector.

The number average molar masses (M_n) and the weight average molar masses (M_w) were determined following the equations below:

$$\overline{M_n} = \frac{\sum n_i M_i}{\sum n_i} \tag{41}$$

$$\overline{M_w} = \frac{\sum n_i M_i M_i}{\sum n_i M_i} = \sum w_i M_i \tag{42}$$

where w_i is the weight average molar masses and n_i is the fraction of molecules having a molar mass of M_i. The dispersity index, Đ, is the ratio between the weight and number averages as follows:

$$Đ = \frac{\overline{M_w}}{\overline{M_n}} \tag{43}$$

2.4.2. Nuclear magnetic resonance (^{13}C-NMR)

Nuclear magnetic resonance (^{13}C-NMR) is a spectrometric technique used to probe details of molecular structures. The position of a peak in the ^{13}C-NMR spectrum is defined by the local electronic environment of the carbon atom in the molecule [85]. The spectrometer used in this project is a Bruker Advance II spectrometer operating at 400 MHz for 1H and ^{13}C. Spectra were identified with a 5 mm QNP or a PSEX 10 mm probe with the z-gradient coil at 100.6 MHz. A polymer mass of 200 mg was eluted with tetrachloroethylene (TCE) and deuterated benzene (TCE/C6D6 7:3 vol) at 110°C. The deuterated solvent was used to provide the internal lock signal. Chemical shift values (δ) were provided in units of ppm with tetramethylsilane (TMS) as reference. Quantitative spectra were taken with a 70° flip angle and a delay time of 10s [72].

2.4.3. Analytical crystallization elution fractionation

Crystallization elution fractionation (CEF) [86] is a technique that combines the advantages of both processes temperature rising elution fractionation (TREF) with crystallization analysis fractionation (CRYSTAF). In TREF analysis [86][87][88], the sample is first dissolved in a

suitable solvent at a high temperature. The solution is then injected into the TREF column. In CRYSTAF analysis [89], the separation occurs in a stirred crystallization vessels with no support by measuring the polymer solution concentration as the temperature decreases throughout the crystallization process.

The advantage of the CEF method is to increase the physical separation obtained in the crystallization step and to reduce the fractionation time in the elution cycle, leading to a new extended separation as displayed in **Figure 2.5**. In CEF, the first step is loading the sample, followed by pumping a small flow of the solvent through the column over the cooling process [90]. The crystallization occurs at different places in the column and is maintained until the sample reaches its fullest extent of crystallization. Then, a new solvent flow Fe is inserted again as in TREF [86] at an appropriate rate while the temperature is still increased. By raising the temperature of the column, the eluant dissolves the polymer components. A detailed description of this method is reported in the literature [86]. This method was used to support the information regarding the molecular architecture and branching structures of the different PEs as determined by SEC and ^{13}C NMR.

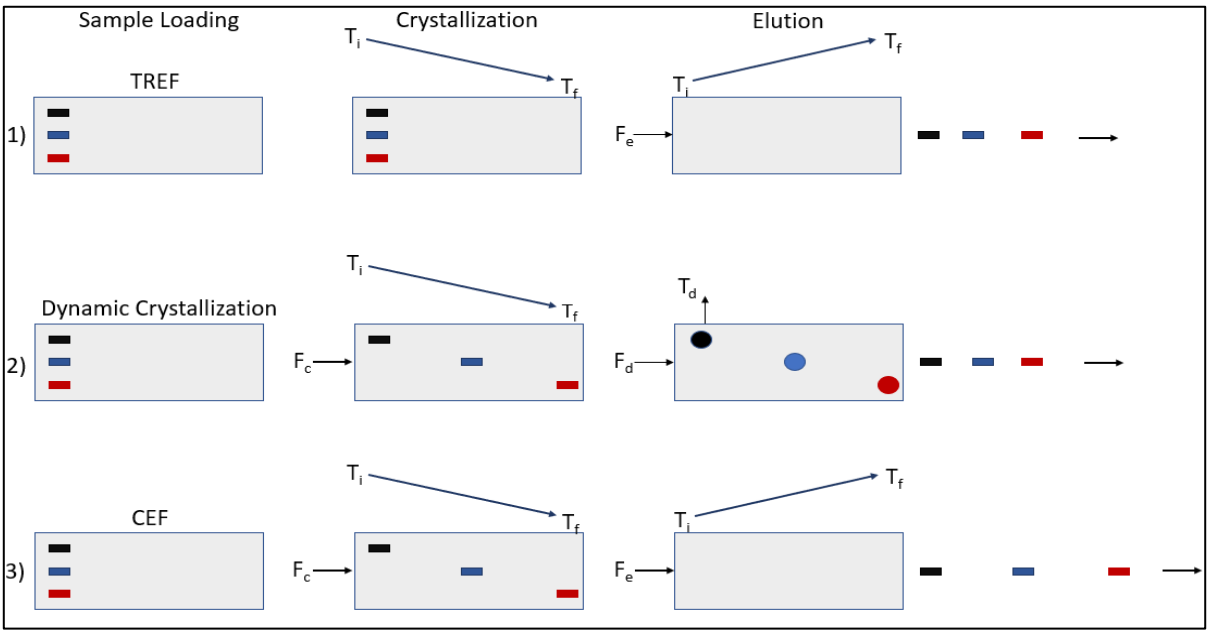

Figure 2.5 Schematic of the separation process by crystallizability with Ti and Tf as the initial and final temperature of each step: 1) TREF separation process; 2) dynamic crystallization, and 3) crystallization elution fractionation [86].

In the present study, the separation of PEs is performed by multidetector CEF. A mass of 4 mg of each PE was dissolved in 8 mL of 1,2,4-trichlorobenzene (TCB) and injected through the column head at a crystallization flow rate of 0.05 mL/min. After the complete crystallization period and temperature reached 35ºC with a percent crystallinity of 2°C/min, the oven started the heating program with a rate of 4°C/min up to 130°C. Fourier transform infrared spectroscopy (FTIR) was used to identify the amount of CH3/1000C of each eluted fraction while neglecting the end groups. Thus, the elution temperature was directly related to the number of short-chain branches/1000 carbon atoms by a linear relationship [91].

2.4.4. Differential scanning calorimetry

Differential scanning calorimetry (DSC) experiments were carried out using a TA Instruments Q20 apparatus to study the influence of the different molecular architectures of the PEs on their crystallinity. A polymer mass of 5-6 mg was weighted and prepared in a low-mass pan. Then, a temperature program was set in which the samples were first heated from -80 to 200°C, then cooled to -80°C followed by a second heating scan to 200°C at a heating/cooling rate of 10°C/min under a nitrogen atmosphere. The melting temperature (Tm) was noted, as the maximum of the melting peak was determined from the second heating scan. The crystallization temperature (Tc) was taken from the maximum of the exothermal peak in the cooling scan. Polymer crystallinity was calculated according to the following equation. The ΔH_m^{∞} used for PEs was 289 kJ/kg [92].

$$X_C = \frac{\Delta H_m}{\Delta H_m^{\infty}} * 100 \quad (44)$$

where X_C is the percentage of crystallinity of the samples.

3. Results and discussion

3.1. Polyethylene microstructural characterizations

3.1.1. Estimation of branching content using SEC-MALLS

The weight average molar mass (M_W), dispersity, and amount of LCB per molecule of each PE chosen in this project were measured by SEC-MALLS. The results are shown in **Figure 2.6** and the corresponding Mw, Mn, and dispersity index are listed in **Table 2.2**. The LLDPEs selected for this study are copolymers of ethylene-1-hexene, with the LLDPE-LL2 prepared by

the use of a metallocene catalyst and the LLDPE-LL1 produced with a Zeigler-Natta catalyst. According to the literature, the LLDPEs obtained with metallocene (single-site catalyst) will lead to a narrower dispersity ranging from 2 to 2.5 [93][94]. This is in good agreement with our results, where the dispersity factor of LLDPE-LL2 is close to 2, as shown in **Table 2.2**. In contrast, the broad dispersity of LLDE-LL1 (Đ =5) is obtained by a Ziegler-Natta (Z-N) catalyst contains a multiplicity of active-sites [89][95].

Therefore, the most remarkable feature of the distributions is the distinct high molecular weight tail of LDPE-L1 in comparison with the others. The branched LDPEs present broader dispersity distribution with a higher polydispersity index ranging from 7 to 9. The reason for this high dispersity is related to the complex LDPE molecular structure, which is formed via free-radical polymerization and at high pressure [96]. The amounts of LCB/1000C for the four kinds of PEs were also determined, and they are listed in **Table 2.2**. As expected, both LDPEs contain a higher amount of LCB/1000C compared to the LLDPEs with values of 2 for the LDPEs and nearly to 1 in the case of LLDPEs, respectively.

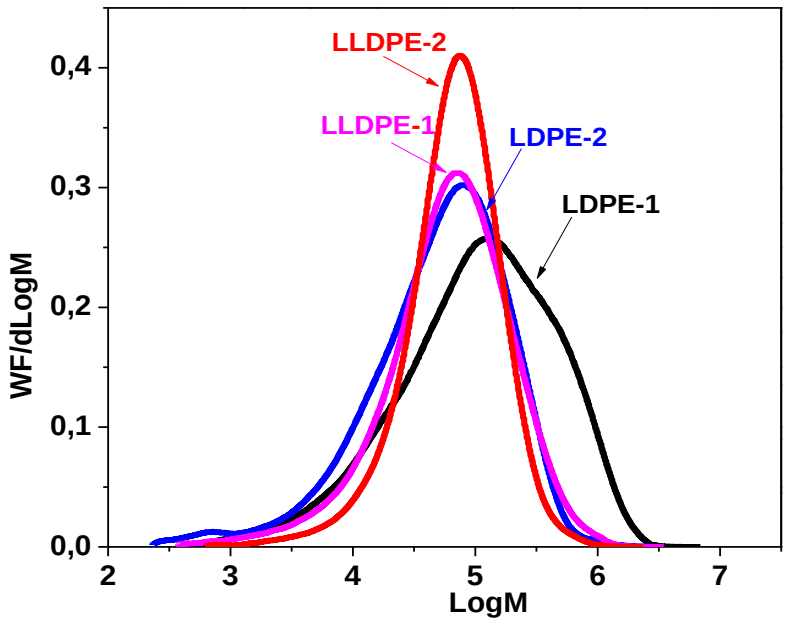

Figure 2.6 Molar mass distributions of the studied four polyethylenes with different degrees of branching.

Table 2-2 Molecular weight characteristics of the investigated polymers.

Sample	Mw (g/mol)	Mn (g/mol)	Đ	LCB/1000C
LDPE-L1	238 600	26 600	9	2
LDPE-L2	95 700	13 660	7	1.5
LLDPE-LL1	107 600	22 900	5	0.7
LLDPE-LL2	93 750	37 300	2.5	0.9

3.1.2. Estimation of branching content by ^{13}C NMR

Qualitative analyses of chain branching in the LDPEs and LLDPEs were carried out by ^{13}C NMR spectroscopy using Randall methods [97]. The molar masses of branched LDPEs is quite complex, containing short-chain (SCB) and long-chain branching (LCB). The LLDPEs were obtained by ethylene-1-hexene copolymerization. According to the literature, copolymerization of ethylene with 1-hexene results in the formation of butyl branches along the polyethylene backbone, providing a good NMR target for creating the butyl branch, which is the most abundant branch seen in LDPE [97].^{13}C-NMR chemical shift assignments for all polyethylenes used in this study were assigned according to Randall's previous work and were referenced by setting the major methylene's backbone carbon resonances to 29.5 ppm, 29.6 ppm, 30 ppm, and 31.1 ppm)[97]. The ^{13}C chemical shifts, peak assignments, and spectral integration of both LDPEs and LLDPEs are presented in the Table 2-3 and the spectrum is displayed in Appendix.

The microstructural determination of both LDPE and LLDPE and the nomenclature utilized to identify the various backbone carbons are shown in **Figure 2.7**. The nomenclature is based on Randall, Usami, and Takayama's previous work [98].

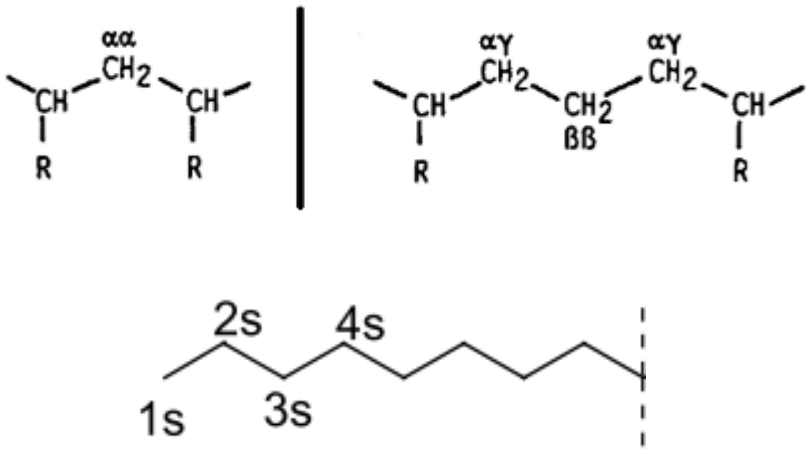

Figure 2.7 Assignment of the polymer backbone and side-chain carbons [10].

The backbone carbons are designated by a pair of Greek letters that indicate the position of the closest methine carbons in each direction. The branch point is denoted by the carbon marked 'br' that can be easily isolated. The Greek symbol α denotes that methine carbon is bonded to a methylene carbon of concern, while two Greek symbols, αα, signify that the given methylene carbon is sandwiched between two methine carbons. Therefore, the β means that a methine carbon is two carbons removed from the carbon of concern, and so on. The saturated end group is correspondingly labeled 1s, 2s, 3s, or 4s. Additionally, the position of each carbon inside the different types of branches is identified by xBn, where x denotes the branch's length and n designates the location of the carbon inside the branch beginning with the methyl group as 1, as demonstrated by **Figure 2.8** [97].

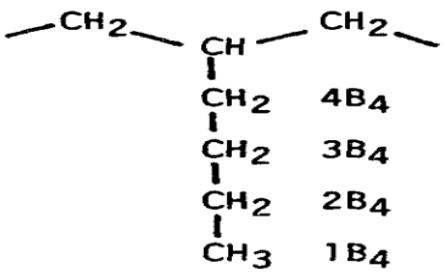

Figure 2.8 An isolated butyl branch.

The presence of short-chain branching (SCB) can be identified from the βBn≥4 + βB2 resonances located at 27.3 ppm and was observed for both the LDPEs and the LLDPEs (Table 2-3). In the case of the LLDPEs, the $\beta\beta_{EHEHE}$ assignment was identified at 24.1 ppm, and was equal to 2.13 for LLDPE-LL1 and 0.53 for LLDPE-LL2. Even weaker resonances indicate the presence of a small amount of short-chain branching. The equation below was used to measure the total number of short-chain branches N_{SCB} per 1000 carbons utilizing spectral integration from ^{13}C-NMR spectra.

$$N_{SCB} = \frac{\left(\left(\frac{I_\beta}{2}\right) + I_{\beta\beta}\right)}{N_C} * 1000 \quad (45)$$

where I_β represents the calculated integral, and N_C corresponds to the total number of carbons (**Table 2-3**).

In addition, the appearance of a 3Bn ≥ 6 assignment at 32.2 ppm indicates that long-chain branching is also present. For the LDPEs, the value of 3Bn ≥ 6 resonance was around 2, while for the LLDPEs it was about 0.5. Even weaker resonances indicate the presence of a small amount of long-chain branching. Moreover, for both LDPEs and LLDPEs, we used the equation below to determine the total number of long-chain branches (NLCB) per 1000C.

$$N_{LCB} = \frac{(I_{Bn\geq 6} * 1000)}{N_C} \quad (46)$$

where $I_{Bn\geq 6}$ denotes the calculated integral at 32.2 ppm and N_C corresponds to the total number of carbons.

It is noteworthy that propyl branches are typically absent in both LDPEs.

$$N_{LCB} = \frac{(I_{Bn\geq 6} * 1000)}{N_C} \quad (47)$$

Table 2-3 ^{13}C chemical shifts, peak assignments, and spectral integration of both LDPEs and LLDPEs.

Chemical shift (ppm)	Assignments	Integral calculation.			
		L1	L2	LL1	LL2
10.9	1B2	4.46	3.21	-	0.32
14	1S+1B4+1B6+1B5	9.98	8.91	17.81	10.25
19.9	1B1	2.72	0.00		
22.9	2S+2B5+2B_6^+	3.74	3.51	0.60	0.37
23.4	2B4	8.69	7.96	21.26	11.50
24.1	$\beta\beta_{EHEHE}$	0	0	2.13	0.52
26.8	2B2+4B5	7.59	7.66	0.00	0.32
27.3	$\beta B_{n>4} + \beta B_2$	27.86	22.71	40.12	27.36
27,48	βB_1	2	0	0	0
29.5	3B4	1000	1000	1000	1038.92
29.6	4S				
30	[CH2]n				
30	$\gamma B_{n>4}$+γB_2				
31.1	$\gamma\gamma_{HEEH}$				
32.2	3S+3B_6^+	2.49	2.27	0.68	0.44
32.7	3B5	2.12	1.94	0.00	0.00
33.2	CHB1	2.59	0.00	0.00	0.00
34	4B4+αB2	40.90	36.28	74.19	50.52
34.4	$\alpha B_{n>4}$				
34.8	4HHH				
35.6	brHHE	1.81	0.98	2.64	0.00
37	CH(1,3-)diB2	1.44	1.21	0.00	
37.5	$\alpha\delta B_1$	5.75	0.00		
38	CHB^+4	11.61	9.58	22.07	15.90
38.8	$\alpha\alpha$	2.08	1.04	1.03	0.37
39.4	xx		0.75	0.00	0.00
Total number of carbons (Nc)		1137.8	1108	1182.5	1156.8

The identities of the various short-chain branches existing in both the LDPEs and LLDPEs are presented in **Table 2.4**. It can be seen that LLDPE-LL1 contains a significant amount of short-chain butyl compared to LLDPE-LL2, with a value of 18 for LLDPE-LL1 and 12 for LLDPE-LL2. These differences are directly related to the polymerization process, which means that the LLDPE-LL1 obtained using the Zeigler-Natta catalyst exhibits broader dispersity and, in consequence, a higher amount of short-chain branching content. Otherwise, the LLDPE-LL2 obtained using the metallocene catalyst presents narrow dispersity and, as a result, a lower

amount of short-chain butyl. In the case of LDPE-L2, both methyl and propyl branches are absent, which is common in low-density polyethylene, contrary to the LDPE-L1. The presence of methyl branches can be explained by the insertion of a propylene monomer as a chain transfer agent to regulate both crystallinity and molar masses as was the case for LDPE-L1. The quantity of long-chain branches per 1000 carbon atoms is presented in **Table 2.4** and is around 0.5 for both LLDPEs and 2 for both LDPEs. Since the end-group and main chain resonances can overlap, we can only estimate the long-chain branch content qualitatively in our NMR study. The **Table 2.5** summarize the calculated LCB/1000C with the two methods. The obtained results with SEC-MALLS corroborate those of ^{13}C-NMR highlighting the accuracy of our procedures.

Table 2-4 Analysis of chain branches in PEs and branching content estimation with the ^{13}C-NMR method.

Sample code	L1	L2	LL1	LL2
B1/1000C	2	0	0	0
B2/1000C	1	1	0	0
B4/1000C	6	6	18	12
B5/1000C	2	2	0	0
Bn≥6/1000C	2	2	0.6	0.5
SCB/1000C	11	9	18	12
LCB /1000C	2	2	0.6	0.5
Total amount of chain branching per 1000C	13	11	18.4	12.5

Table 2-5 LCB/1000C determined using two methods.

Sample	SEC-Malls LCB/1000C	^{13}C-NMR Cn (n>=6)/1000C
LDPE-L1	2	2
LDPE-L2	1.5	2
LLDPE-LL1	0.7	0.6
LLDPE-LL2	0.9	0.5

3.1.3. Estimation of branching content and distribution with CEF

Crystallization elution fractionation (CEF) was used as a complementary tool to ^{13}C-NMR and SEC to investigate the chemical composition distribution (CCD) of both LDPEs and LLDPEs. These samples were eluted and fractionated according to their crystallization temperature. First, the chains with less crystallinity were eluted, followed by the chains with higher crystallinity. **Figure 2.9** shows the effect of the polymerization process on the CCD of ethylene-1-hexene copolymers as measured by CEF, and the results are summarized in **Table 2-6**. The CEF profiles of the studied polymers revealed distinct peaks, with the first peak (F1) is corresponding to the amorphous phase with extremely branched chains. The second and third peaks (F2 and F3) correspond to the crystalline phase of the polymer with relatively few branched chains. The sum of these peak areas gives the total branching content expressed per thousand carbon atoms (/1000C) and is also listed in the **Table 2-6**. Notably, the branching in LDPE is referred to as long-chain branching (LCB), whereas the branching in LLDPE is referred to as short-chain branching (SCB) [91]. As shown in **Figure 2.9**, both LLDPEs exhibit a bimodal branching distribution, showing two peaks in the crystalline phase (F2 and F3). The LLDPE-LL1 has a very broad branching distribution and a less uniform composition distribution (distance between F2 and F3 in **Figure 2.9 (a))** with a total branching content of 22. This behavior is expected from the Ziegler-Natta catalyst, since there are at least two or more active sites used to generate PE chains, with varying comonomer compositions and chain lengths. The incorporation of monomer is not uniform on this catalyst, with a mixture of chains. On the contrary, the LLDPE-LL2 has a more uniform microstructure with a narrow chemical

distribution and a total branching content of 13, which may be ascribed to the presence of only one active site in metallocene catalysts. The single-site catalyst (metallocene catalyst) technology is used to tailor the molecular architecture of polyolefin by adjusting catalyst structures and process parameters. These well-controlled microstructures could be employed to help design polymerization models. From **Figure 2.10**, both LDPEs display a unimodal branching distribution, showing one peak in the crystalline phase (F2) and a narrow CEF profile with a total branching content of 19 for LDPE-L1 and 14 for LDPE-L2, as expected from the free-radical polymerization mechanism.

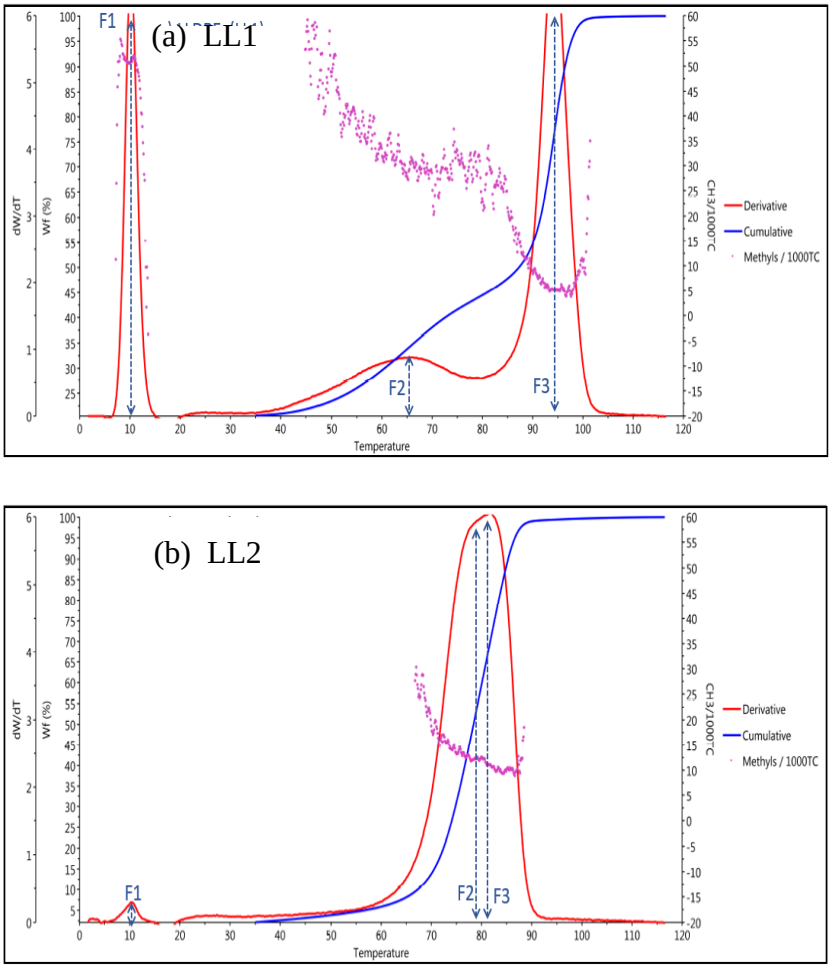

Figure 2.9 Effect of catalyst type on ethylene-1-hexene copolymers determined by CEF: (a) LLDPE-LL1 obtained using a Z-N catalyst and (b) LLDPE-LL2 obtained using a metallocene catalyst.

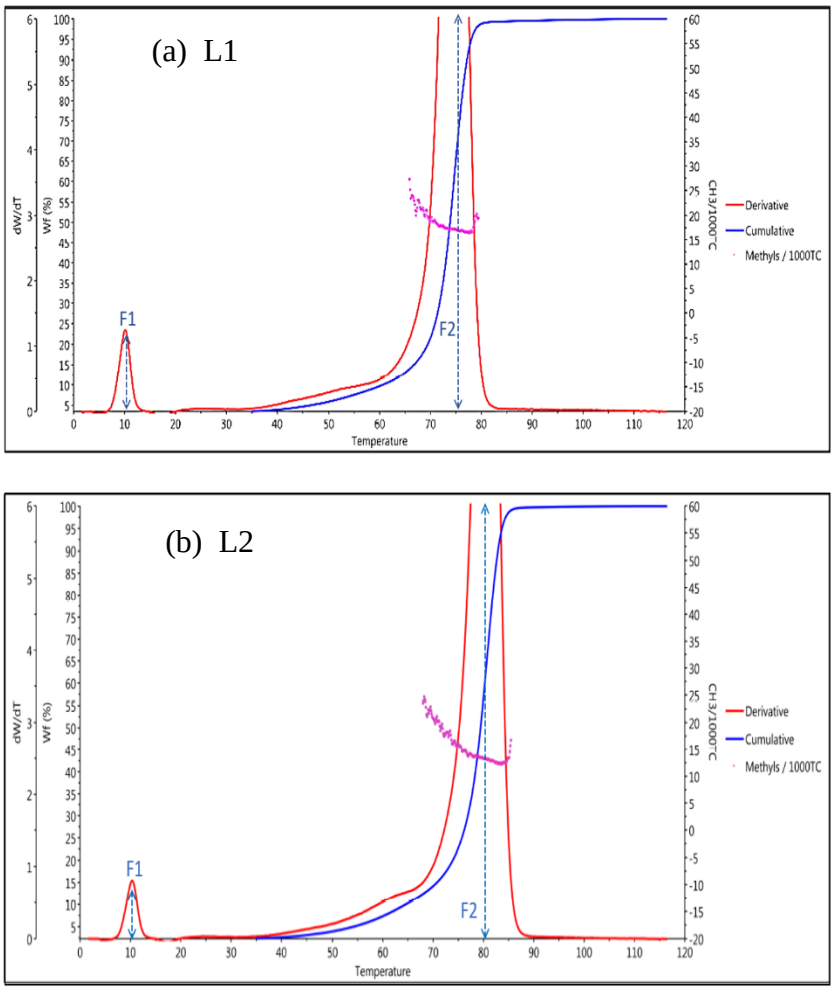

Figure 2.10 CEF profiles of LDPEs produced by free radical polymerization.

To summarize, the CEF analysis was used to obtain information about the branching distribution of the studied PEs that the ^{13}C-NMR method alone cannot provide. As evidenced in **Table 2-6,** the CEF findings were of the same order of magnitude as those obtained using the ^{13}C-NMR analysis, indicating the reliability of both methods. It is interesting to note that the CEF method does not efficiently fractionate LCB existing in the PEs, since the LCB behave like the main chains and thus have some impact on chain crystallinity. On this basis, only findings determined by ^{13}C-NMR can be used to predict the LCB content.

Table 2-6 Characteristics of the CEF fractions of the PEs.

Sample	Peak elution temperature (°C)			CH3/1000C
	F1	F2	F3	
LDPE-L1	10	75	-	19
LDPE-L2	11	81	-	14
LLDPE-LL1	10	66	94	22
LLDPE-LL2	11	78	82	13

3.1.4. Differential scanning calorimetry (DSC)

The thermal fractionation of the studied PEs was measured using DSC as shown in **Figure 2.11** and the detailed results are listed in Table 2-7. It is quite clear, from the melting process, that LLDPE-LL2 with its lower branch content, is rather different from all other studied PEs Owing that it is presenting two different melting peaks of the heat flow, a larger one at 107°C and a narrower one at 118°C. This could indicate the presence of two crystal populations. Comparing these results with those obtained from CEF, it seems that the first melting peak that appears at lower temperature represents the short-branched fractions (F2), while the second narrower peak refers to the more linear components with very low branching content (F3). The formation of a double peak for LLDPE with lower branch content has also been observed by Cabrera et al., 2020 [91]. In this last reference of our group, we hypothesized that the low branching content of LLDPE may result in a segmented intra-chain comonomer distribution that could initiate the segregated crystalline state.

Furthermore, only one melting peak can be viewed for the other PEs in their melting cycle. This single broader peak may be related to the single crystal population. Crystallization temperatures (T_c), melting point (T_m), and the degree of crystallinity (Xc %) of the four types of polyethylene were calculated from the second heating ramp. The values obtained from the DSC curve are reported in **Table 2-7**. It can be seen, that the degree of crystallinity of LLDPE-LL1 is much higher than that of LLDPE-LL2, with values of 46% for LLDPE-LL1 and 35% for LLDPE-LL2, respectively. This trend is expected as the LLDPE-LL1 has a higher melting temperature. Moreover, comparing the crystallinity and the melting temperature of LDPE-L1 and LDPE-L2, they do not change significantly.

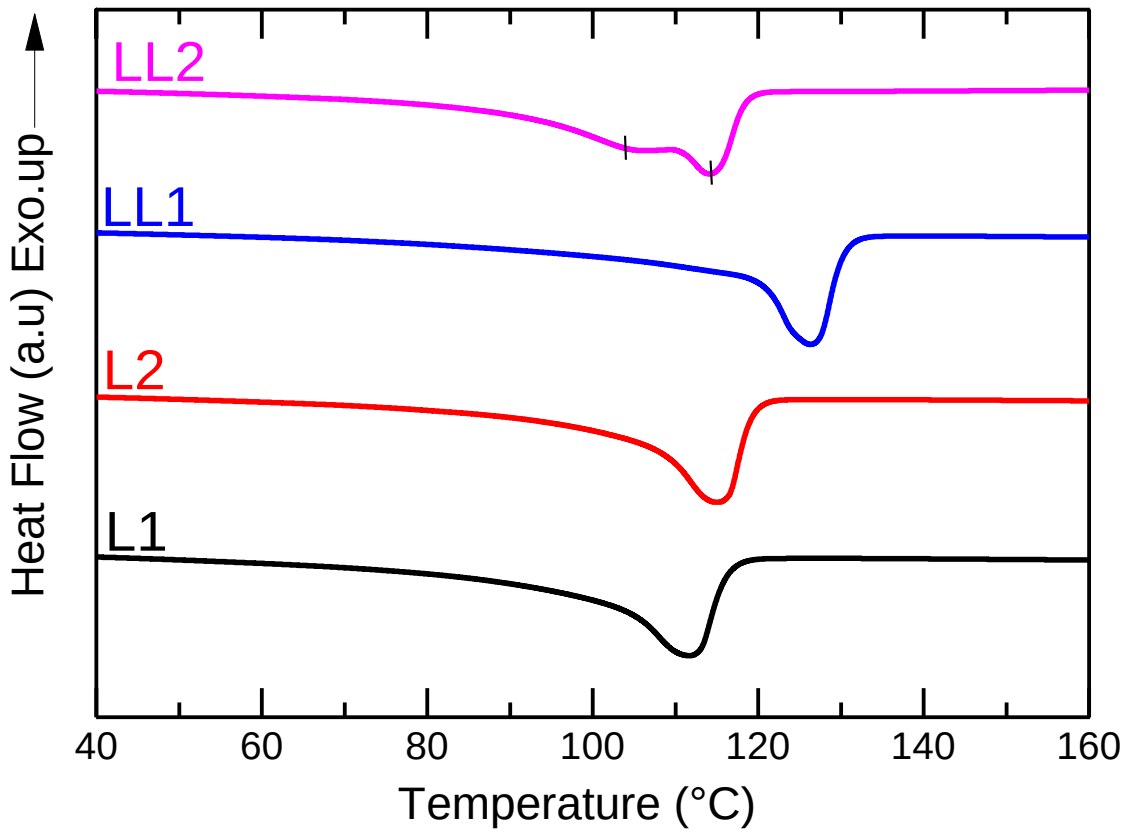

Figure 2.11 DSC thermograms for the different PEs.

Table 2-7 Various crystallization parameters of both sets of polyethylenes measured by DSC.

Samples	T_c (°C)	T_m (°C)	X_c (%)
LDPE-L1	93	112	42
LDPE-L2	98	115	38
LLDPE-LL1	110	126	46
LLDPE-LL2	100	107 - 118	35

3.2. Influence of molecular architectures of PEs on rheological properties

3.2.1. Dynamic time sweep test

In this section, we examine the linear viscoelastic properties of both linear and branched PEs at different temperatures. For the sake of clarity, only the rheological results at 190°C are presented here. Prior to testing, it was necessary to first check that the polymer melt does not degrade during the dynamic shear measurements (Small-Amplitude Oscillatory Shear, SAOS). An example of the normalized viscosity and storage modulus as a function of time is shown in **Figure 2.12** at a reference temperature of 190°C. First, it can be seen that the viscoelastic responses for both LLDPEs do not change over the testing time. This suggests that the molecular structure of the LLDPEs remained relatively unchanged [99]. Likewise, at a shorter time, the thermal stable behavior of the LDPE plots is highlighted. Whereas, at a longer time (t>15 min), the behavior of the LDPEs is different compared with the linear one. A vertical shift was required at a longer time, which could be due to some crosslinking among the LDPE chains or degradation mechanisms occurring over a long period (time).

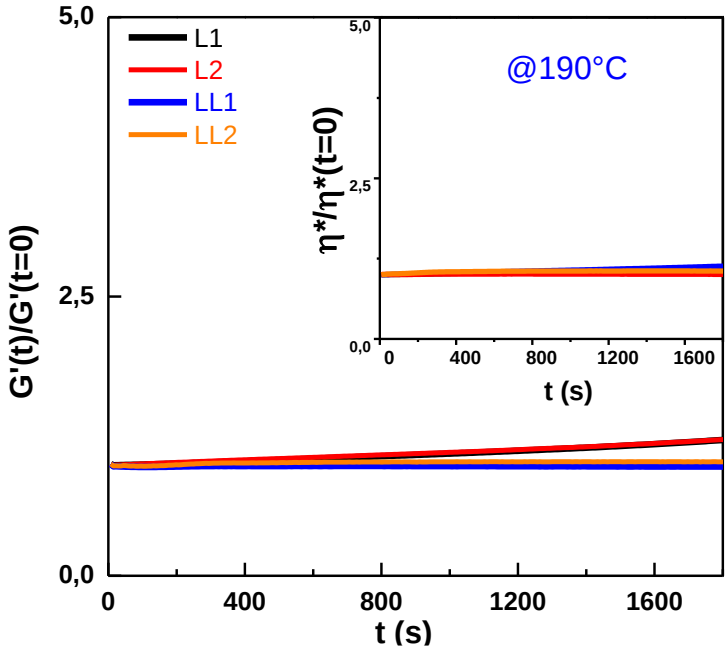

Figure 2.12 Comparison of the evolution of G′/G′(t=0) and η*/η*(t=0) as a function of healing time at 190°C with an angular frequency of 0.1 rad/s for neat PEs.

3.2.2. Dynamic frequency sweep

The viscoelastic properties of polymeric materials are very sensitive to the molecular structure of polyethylene including short/long chain branching and dispersity. **Figure 2.13** depicts the master curve of dynamic complex viscosity (η*) against angular frequency (ω) for all of the neat polymers at a reference temperature of 190°C. First, it can be observed that the rheological behavior of both linear and branched PEs is different with some shear-thinning behaviors, which are more pronounced beyond 10 rad/s. Their zero-shear viscosity can be simply deduced as the $\lim_{\omega \to 0} \eta^* = \eta_0$ in the Newtonian regime, except for the LDPEs, whose zero-shear viscosity values were not reached experimentally. As found in the literature, the presence of long-chain branching causes a significant increase in shear-frequency/thinning behavior [100].

Moreover, it can be clearly seen that LDPEs are more viscous compared to the linear ones at lower angular frequency regions. This behavior was expected since the LDPE contains a high amount of LCB/1000C compared to LLDPE with values of 2 for LDPEs and close 0.5 for LLDPEs, respectively. The presence of long-chain branching created more entanglements density thus resulting in higher molecular weights giving rise to higher viscosities at lower frequencies and exhibit a significant shear thinning at higher frequencies[101]. Herein, the zero-shear viscosity (η_0) was calculated by fitting the experimental data with the Carreau-Yasuda model [1] and then compared with the measured viscosity at 0.01 rad/s.

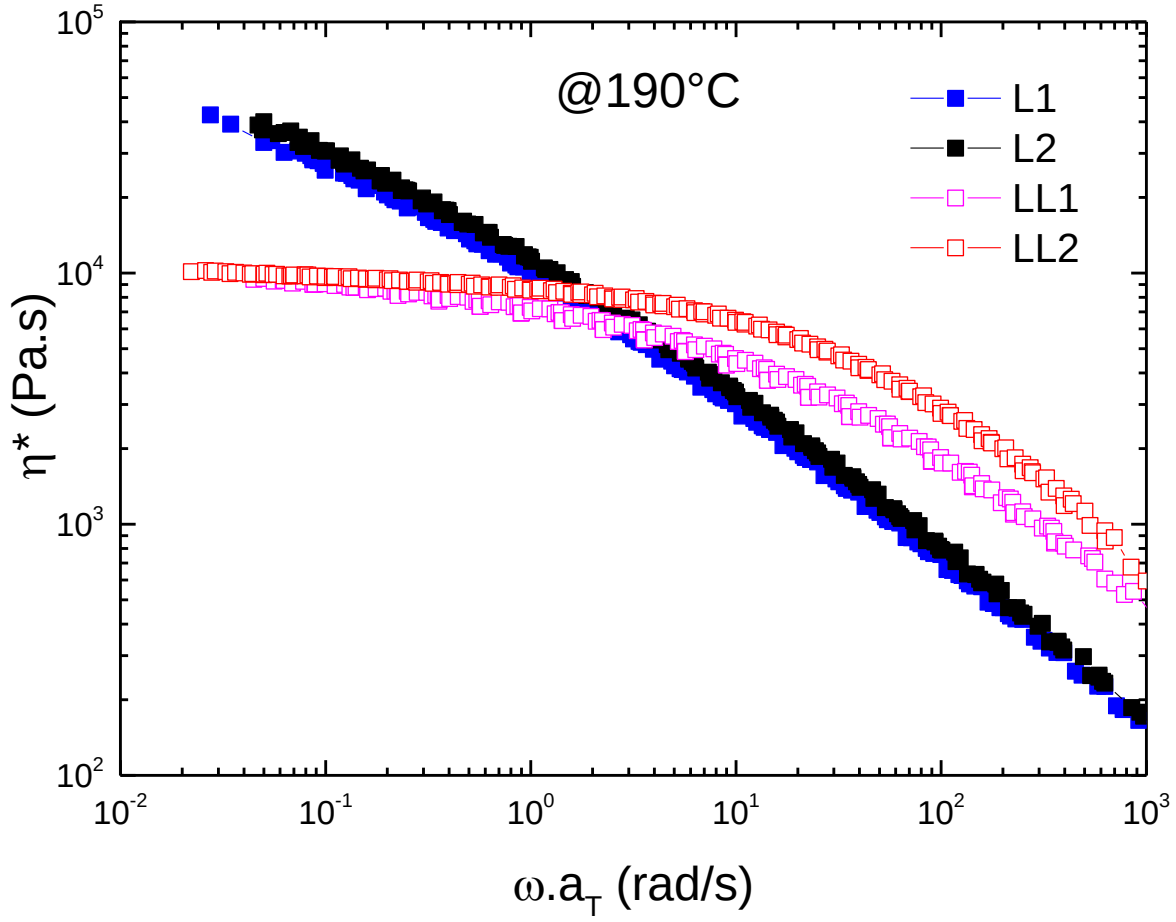

Figure 2.13 Example of master curve of complex viscosity versus angular frequency at a reference temperature of 190°C for all PEs.

Master curves of storage modulus (G′) and loss modulus (G″) reduced at a reference temperature of 190°C for all neat PEs are given in **Figure 2.14**. The rheology at the terminal zone was found to follow the standard relations $G' \sim \omega^2$, $G'' \sim \omega^1$ for the neat polymers. The crossover of G' and G'' allow us to calculate the relaxation time ($\tau_d = \eta_0/G_N^0$). The main characteristics of the selected PEs are summarized in **Table 2-8.** The plateau modulus (G_N^0) was estimated with van Gurp-Palmen plots by extrapolation at the lower limit of δ. The weighted average terminal relaxation time determined from the Cole-Cole plots (η″~η′) was taken as the order of reptation time (τ_{rep}) (See Figures in the following section).

Additionally, the Rouse relaxation time might be calculated using the following equation:

$$\tau_R = \frac{6M_w\eta_0}{\pi^2\rho RT}\left(\frac{M_c}{M_w}\right)^{2.4} \quad (48)$$

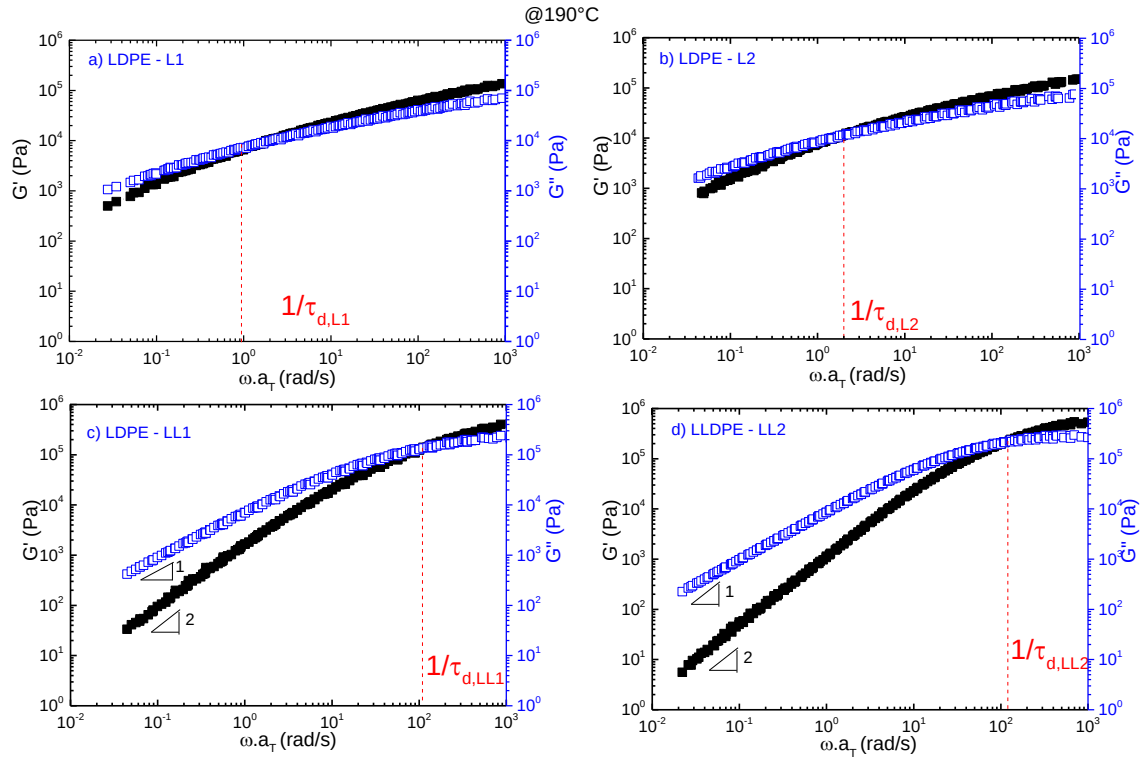

Figure 2.14 Master curves of storage modulus (G′) and loss modulus (G″) reduced at a reference temperature of 190°C for all PEs.

Table 2-8 Material characteristics based on linear viscoelastic measurements at 190°C.

Sample code	L1	L2	LL1	LL2
M_w (g/mol)	238600	95700	107600	93750
Đ	9	7	5	2.5
LCB/1000C (^{13}C NMR)	2	2	0.6	0.5
SCB/1000C (^{13}C NMR)	11	9	18	12
η* (0,01rad/s) at 190°C [Pa.s]	35169	13785	7619	9232
η_0 (Carreau) [Pa.s]	38459	16426	8280	9845
Ea (kJ/mol)	53	51	26	31
G_N^0 (x105Pa)	1.1	1	2.6	6
z	7	3	8	16
τ_d (s)	6.3	3.14	0.06	0.06
τ_R (s)	0.1	0.1	0.005	0.001

The activation energy (Ea) of the selected PEs was obtained from the logη0 plotted versus 1/T within a temperature range of 160°C<T<240°C. Obviously, it can be seen from **Table 2-8** that the activation energy of each LDPE is higher compared to that of the LLDPEs. The corresponding value for the two LDPEs is around 50 kJ/mol, which is typical for LDPEs [23] [27]. This is due to the higher molar masses and the long-chain branches that are obtained using a free-radical mechanism. On the contrary, the flow activation energy values of LLDPEs are 26 kJ/mol for LL1 and 31 kJ/mol for LL2, values that are once again typical for LLDPEs [103]. This is related to the negligible long chain branching in LLDPE.

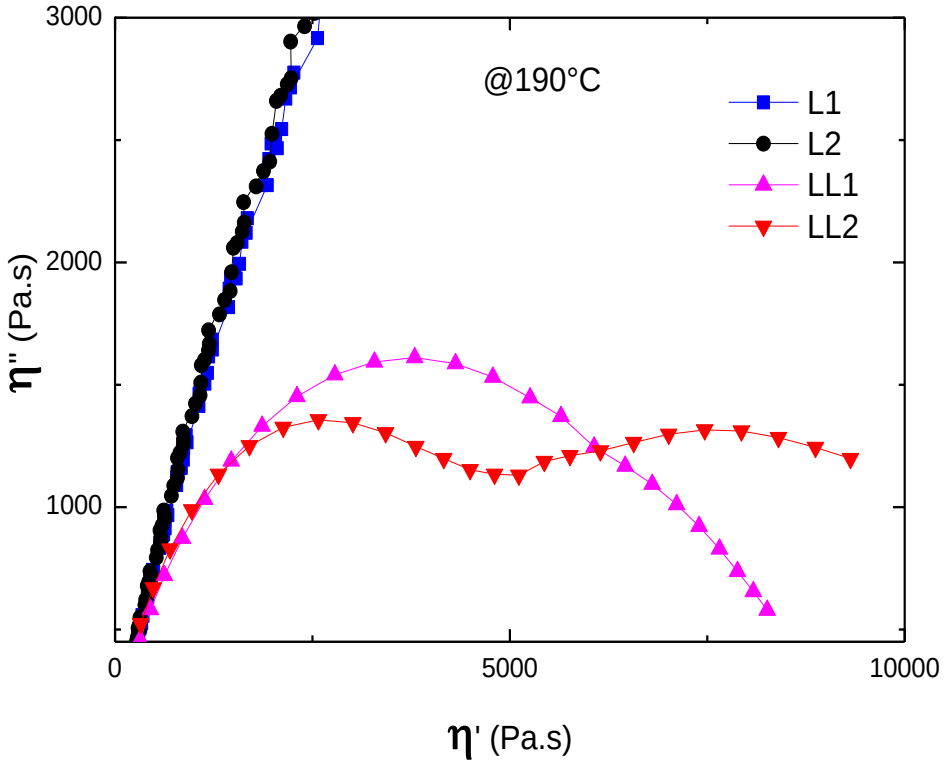

Figure 2.15 Cole-Cole plots for neat PEs at 190°C.

Figure 2.15 presents the plots of η" versus η', which are typical Cole-Cole plots. The LDPEs display a part of arc highlighting the effect of their long relaxation process in comparison to linear LLDPEs. A semicircular shape was obtained for LL1 with a relaxation time of 0.25 s. For LLDPE-LL2, we note the presence of two prominent relaxation peaks. The first, at a shorter time (0.04 s), was related to the relaxation of the short chain, whereas the second one, situated at 16s, could be attributed to the reptation of the backbone. The intensity of the weighted relaxation peak of LLDPE-LL2 is a little weaker, meaning the elasticity is reduced due to the low molar masses and low chain branching. The wide relaxation peak of LLDPE-LL1 indicates a non-uniform chain structure and its sensitivity to higher SCB/LCB density in comparison to LLDPE-LL2.

However, for LDPEs, no arc shape was seen even at low frequencies, indicating a very long relaxation time for this polymer. These differences can be explained by the different PE structures and molecular weight distributions. Hence, the presence of LCB has a more pronounced effect on viscoelastic properties.

The weighted relaxation spectra H(λ)*λ represent the time distribution of the chain relaxation behavior for the neat polymers. The linear relaxation spectrum H (λ) was determined using the dynamic modulus, according to Eq.(49) [104] :

$$G^* = \int_{-\infty}^{+\infty} \frac{H(\lambda) i\omega\lambda}{\lambda(1+i\omega\lambda)} d\,\lambda \tag{49}$$

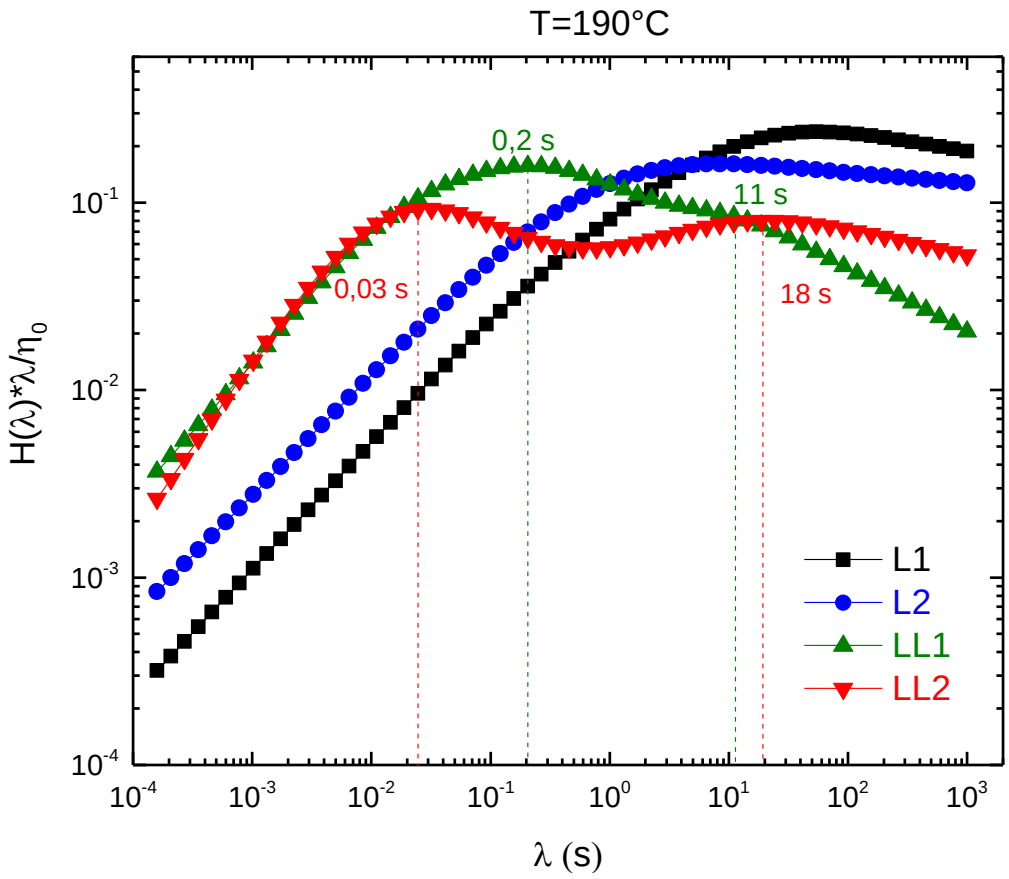

Figure 2.16 Normalized weighted relaxation spectra with zero shear viscosities of the PEs at 190°C.

Figure 2.16 illustrates the weighted relaxation spectra normalized by the zero-shear viscosity as a function of the relaxation time of neat polymers at 190°C. They are normalized to eliminate the effect of viscosity mismatches between polymers. This reflects the continuous time distribution of chain relaxations. As depicted in the same **Figure 2.16,** the PEs show different characteristic relaxation times because of their different structures and molecular weight distributions. For the LLDPEs, two prominent relaxation spectrum peaks can be clearly observed. They are situated at about 0.03 s and 18 s for LLDPE-LL2 and at 0.2 s and 11 s for LL1. The first peak corresponds to the relaxation of short chains due to the reptation of the linear chains (backbone). A second one is related to the existence of a second phase with a longer relaxation time influenced by the presence de LCB despite their small amount. While for LDPEs the relaxation spectrum could not be detected in the present experimentally available range of frequency, according to their high amount of LCB. These results are in agreement with the Cole-Cole plots in **Figure 2.15**. In all, the relaxation times of the studied PE are dominated by the reptation of long chains, which explains why the rheological properties of a polymer are strongly influenced by the longest chains in the system.

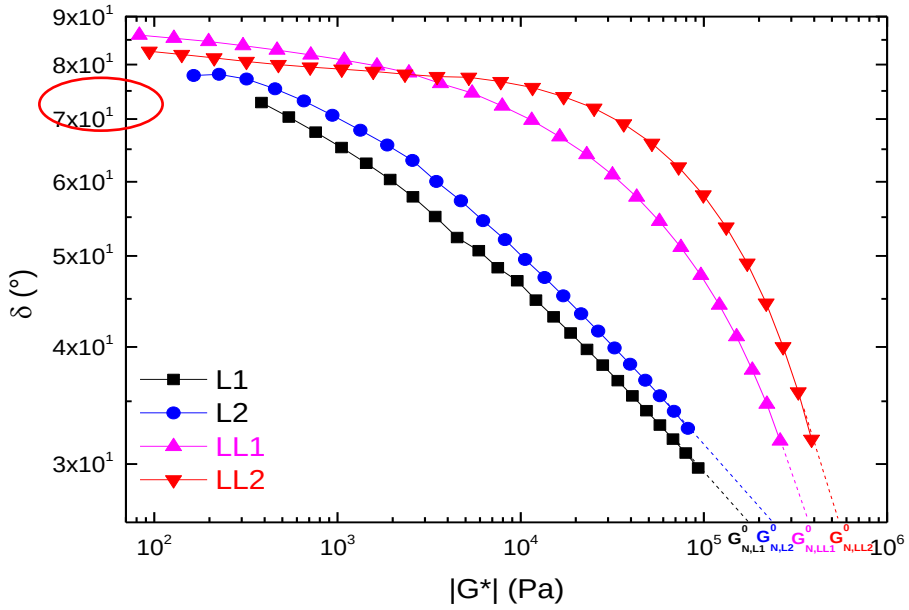

Figure 2.17 Van Gurp-Palmen (vGP) plots of phase angle (δ) versus complex modulus (G*) for all linear and branched PEs at 190°C.

Figure 2.17 depicts the van Gurp-Palmen plots of these PEs at 190°C. The plots show the evolution of the phase angle, in terms of |G*|, for all linear and branched PEs, and were used to estimate the G_N^0, by an extrapolation of these curves at the lower limit of δ. The phase angles are strongly dependent on molecular weight and are very sensitive to polydispersity and the presence of long-chain branching. As the number of LCBs increases, the entire curve shifts to the left of the complex modulus axis. We note that the effect of LCB is similar to that of polydispersity. To sum, the LDPEs display high elastic behaviors than LLDPE polymers. **Figure 2.18** shows the thermorheological behavior found for LLDPEs and LDPEs in terms of a δ-|G*| plot. The LLDPE metallocene ethylene-hexene copolymers with very low levels of long-chain branching are thermorheologically simple, i.e., the superposition appears to be good. We conclude that these linear copolymers exhibit only mild complexity. While long-chainbranching results do not exhibit time-temperature superposability, they are thermorheologically complex.

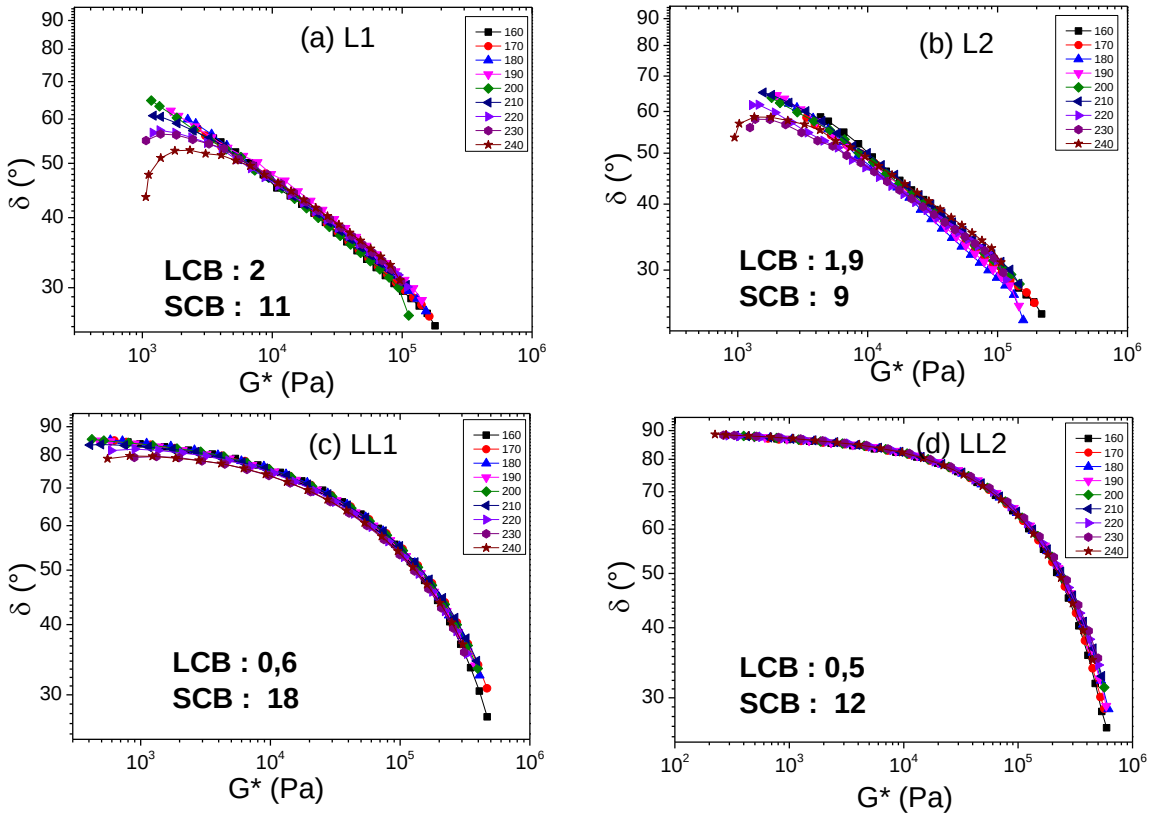

Figure 2.18 Representative vGP curves of linear and short-chain branched PEs over the temperature range from 160 °C to 240°C.

3.2.3. Extensional rheology of all PEs at 190°C

Uniaxial extensional rheology was used to investigate the melt flow properties of the four different types of polyethylenes and to determine their processability under flow conditions simulating the coextrusion system and their stretching in the chill-roll **Figure 2.19** shows the evolution of extensional viscosity (i.e. stress growth coefficient) as a function of time at 190°C with extension Hencky rates varying from 0.1 to 10 s^{-1}. The transient extensional viscosities of neat polymers are in good agreement with the LVE envelope. The latter was determined independently from linear viscoelastic shear rheology measurements and plotted as a dashed black line. It is first seen that the LDPE-L1 seems to exhibit the strongest strain-hardening among the tested polyethylenes. This observed behavior is expected since this polymer is characterized by broader dispersity, molecular weight, and also a high amount of long-chain branching. The number of LCBs per 1000 monomers was found to be 2 for LDPE, which favors the entanglement between chains. As explained by S. Lindeblad et al. [105], the origin of the strain hardening behavior was attributed to the number of branches that increase the monomeric friction between a small molecule and the surrounding molecules, allowing the backbone to be extended more than its linear polymer. Consequently, as the arms with the remainder of the molecule are sufficiently aligned by the elongational flow, friction is reduced, and can be hindered by LCB backbones. Similar behavior was seen in LDPE-L2 and could be correlated again to the amount of short- and long-chain branching as we have demonstrated previously.

Therefore, in terms of LLDPE-LL2, a positive deviation in extensional viscosity from the LVE envelope at larger strains was observed, indicating an enhanced strain hardening. This result was not expected, since this polymer has lower molecular weight and negligible long chain branching (0.5 LCB/1000C). It can be said that extensional rheology is extremely sensitive to even trace amounts of LCB and the homogeneity of its distribution per chain. Whereas this find does not seem to be valid for LLDPE1 which it is more polydisperse. The presence of two distributions in relaxation spectrum can be another key to explain this difference. These results are in correlation with the literature, indicating that even a small amount of LCB may result in significant differences in elongational behavior [105][106].

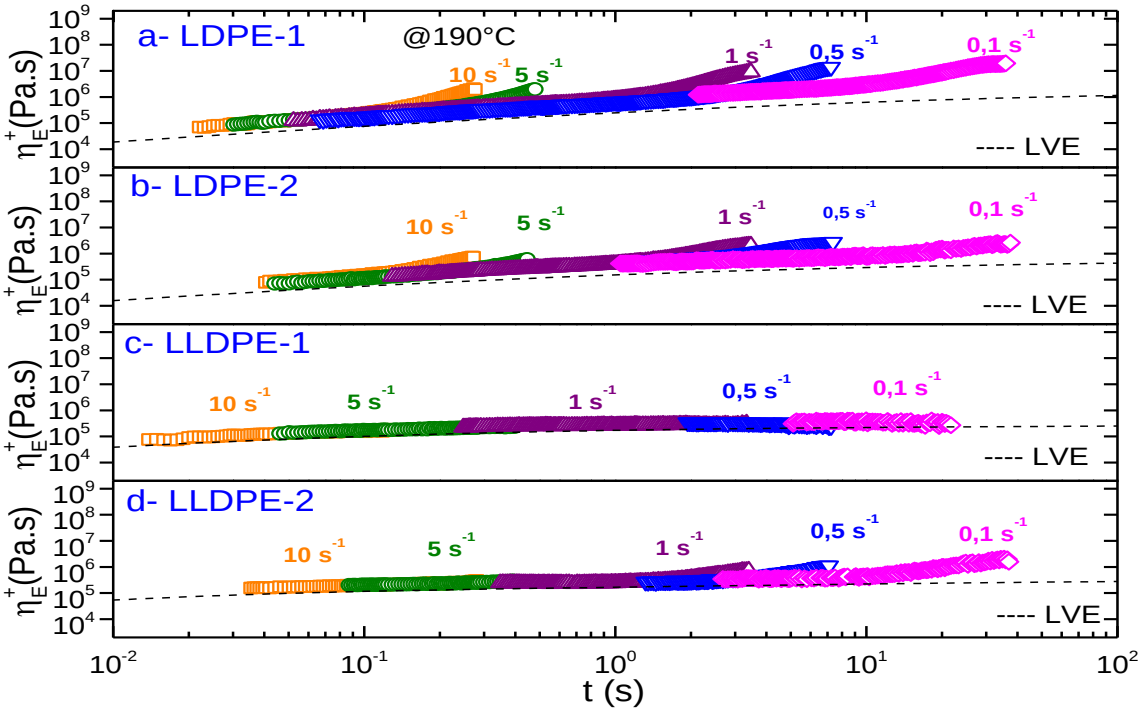

Figure 2.19 Extensional viscosity at the temperature of 190°C with the extensional rate varying from 0.1 to 10 s^{-1} for the different PEs. The dashed lines represent the LVE envelope (i.e., $3\eta_0^+(t)$).

3.2.4. Comparison between the predictions of the HMMSF model and Extensional rheology data

Modeling the shear and extensional rheological behaviors of polymers have been studied extensively to get detailed information on polymer molecular structure and processing behavior. On one hand, the KBKZ integral constitutive equation [107][108], one of the older models, has shown promising results in predicting polymer system shear and extensional rheological behaviors [109]. Samurkas et al. [110], on the other hand, demonstrated that the KBKZ model seems to be unable of simultaneously predicting the strain softening in shear and strain hardening in planar flows. Another research [111] used the Doi-Edwards theory [112] as well as the molecular stress function model [113] [114]to predict the extensional rheological behavior of linear and LCB polyethylene melts.

In a recent research, Wagner et al. [115]–[117] used the MSF model with two nonlinear material parameters to simulate the extensional viscosity growths. Masubuchi et al. [118] studied the molecular mobility in elongational flow by simulating primitive chain networks. They found good agreement between models and experimental data of monodisperse linear and pom-pom branched polystyrene. Narimissa et al. [83], [119], [120]developed a hierarchical multimode stress function (HMMSF) model to predict the rheological behaviors of linear and LCB polymers for different types of flow including uniaxial extensional, multiaxial extensional, and shear deformations. This HMMSF model is based on hierarchical relaxation, dynamic dilution, interchain tube pressure, and convective constraint release[121]. The model's findings match well with those obtained from elongational viscosity data for a variety of LCB polymer melts and present an opportunity for estimating the morphology as well as the crystallization rate of HDPE[122].

The aim of this part is to compare the HMMSF model to the obtained extensional rheological data of both sets of LDPEs and LLDPEs. So far, we've only worked with two types of LDPE at 150°C, and therefore the remainder LLDPEs will be modeled soon. More details about the HMMSF modelling approach can be found in the [121]. **Figure 2.20** compares the measured extensional viscosity of LDPE-L1 and LDPE-L2 at 150°C to the HMMSF model's predictions. As we can observe the HMMSF model and the extensional viscosity data of both LDPEs show good agreement. The slight deviation observed for LDPE-L2 for 0,005 s^{-1} is possibly attributed to a measurement error.

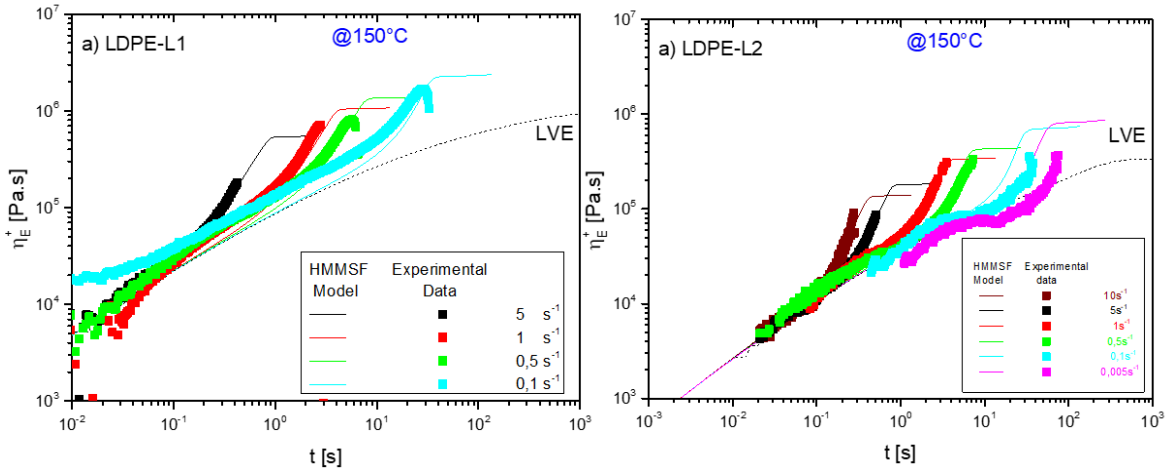

Figure 2.20 Comparison between the predictions of the HMMSF model (continuous lines) and measurements of Extensional rheology (symbols) at 150°C.

4. Conclusion

The physicochemical, thermal, and rheological properties for the four kinds of polyethylenes (LDPEs and LLDPEs) were studied. The LDPEs used were produced by a free-radical catalyst, while the LLDPEs were obtained with different catalyst systems: one with metallocene and one with a Ziegler-Natta catalyst.

Initially, the structure of each sample was obtained from various physicochemical characterization techniques such as nuclear magnetic resonance spectroscopy (^{13}C-NMR), size exclusion chromatography and multi-angle laser light scattering (SEC-MALLS), and crystallization elution fractionation (CEF). It was found by SEC and ^{13}C-NMR that LDPEs of high molecular weight contain a great amount of LCB in comparison with linear ones, which is in good agreement with the dispersity of each sample. The reason for this difference is related to the complex LDPE molecular structure, which is formed via free-radical polymerization and at high pressure.

Therefore, the samples were then analyzed with CEF as a complementary tool to ^{13}C-NMR and SEC to investigate the chemical composition distribution (CCD) of the studied PEs. The findings indicate that the CCD of each sample depends strongly on the catalyst used. The LLDPE-LL1 produced by the Z-N catalyst exhibits a broad branching distribution and a less uniform composition distribution, whereas the LLDPE-LL2 obtained with a metallocene catalyst shows a more uniform microstructure with a narrow chemical composition distribution. Likewise, the two LDPEs display narrow and unimodal distribution, as expected from the free-radical polymerization mechanism used to form them. Moreover, the CEF findings were of the same order of magnitude as those obtained using the ^{13}C-NMR analysis, indicating the reliability of both methods.

Furthermore, the linear and nonlinear rheology were used to probe the structure of the branched and linear polyethylene. The rheological results were strongly influenced by the presence of long-chain branching (LCB). It was found that LDPEs with a higher amount of LCB (2 LCB/1000C) created more entanglements density thus resulting in higher molecular weights giving rise to higher viscosities at lower frequencies and exhibit a significant shear thinning at higher frequencies. Moreover, the activation energy of LDPE is higher when

compared to linear LLDPE . Indeed, the presence of long-chain branching leads to more pronounced strain hardening behavior in the elongational flow. Therefore, in terms of LLDPE-LL2, a positive deviation in extensional viscosity from the LVE envelope at larger strains was observed. This result was not expected since this polymer has lower molecular weight and negligible long chain branching (0.5 LCB/1000C). It can be said that extensional rheology is extremely sensitive to even trace amounts of LCB and the homogeneity of its distribution per chain. Whereas this find does not seem to be valid for LLDPE-L1 which it is more polydisperse. The presence of two distributions in relaxation spectrum can be another key to explain this difference. Lastly, a comparison between the predictions of the HMMSF model and Extensional rheology data was done. A good agreement was found between the HMMSF model and the extensional viscosity data. These findings lead to a better understanding of the relationships between the molecular structure of linear and branched PEs with rheological properties.

Chapter 3. Interfacial shear and elongational rheology of immiscible micro-nanolayered polymers with varying macromolecular architectures and highly mismatched viscoelastic properties: New insight into nanostructure effects and the modeling of interfacial properties

1. Introduction

Shear and extensional flows dominate the multilayer coextrusion process and have been widely studied in the literature to highlight the role of interfaces under large shear [123][65][64] and elongation deformations [124]. For example, Zhang et al. created a compatible multilayer film by combining PMMA and PVDF with a composition of 50% using layer-multiplying coextrusion [55]. The transient extensional viscosity $\eta_E^+(t)$ or tensile stress growth coefficient of the bilayer film was enhanced as a result of the thick interface. In another study from our previous works, Lu et al., Bondon A. et al.investigated the influence of an in situ reactive interphase on the melt shear and extensional rheology using a model multi-micro/nanolayered systems composed of maleic anhydride grafted PVDF or PP (PVDF-g-MAH, PP-g-MAA) and polyamid-6 (PA6) or EVOH [60][46]. The authors were able to quantify interfacial stress from extensional measurements. The presence of graft copolymers entangled at the interface was shown to be responsible for the significant increase in strain hardening behavior that resulted. Levitt et al. amplified the interfacial effects by producing films with 100 alternating layers via manual lamination of reactive and nonreactive polymer pairs [125]. They attributed the observed strain hardening to reactions at the polymer-polymer interface as well as the interfacial tension between immiscible layers. In a recent study, Macosko et al. [124]studied the role of interfacial tension on rheological measurements by combining isotactic polypropylene (PP) and polyethylene (PE) via a coextrusion process. The resulting decrease in shear viscosity during shear deformation was related to chain disentanglement across the interface and was interpreted as an interfacial slip velocity. They observed significant strain hardening and enhanced transient extensional viscosity during extensional flows. This behavior was anticipated using a model based on force summation and interfacial tension as a fitting parameter.

In the work reported here, we aim to understand the role of interfacial polymer physics and the triggered interfaces/interphases in shear and extensional rheology, as well as polymer processing. Using the forced-assembly layer multilayer coextrusion process, various micro to nano-structured multilayer structures with stable flow and layered architecture were then formed with varying macromolecular architecture. Their shear and extensional rheological properties were investigated. Small amplitude oscillatory shear data

were fitted with the Palierne model to determine the interfacial tension of the matrix/droplet blends of each of the pairs. Meanwhile, the Macosko model was used to predict the interfacial tension under extensional flows. The estimated interfacial tensions will be compared to those obtained from emulsion model like Palierne with the equivalent blends. The main challenge is to check the validation of this recent model with high mismatched viscoelastic polymers. The evaluation of interfacial properties is essential for establishing the structure-dynamics-property relationship.

2. Experimental section

2.1. Materials and sample preparation

For the sake of clarity, only two polyethylenes will be presented in the rest of this manuscript: an LDPE-L1 and an LLDPE-LL2. These materials were chosen owing their high thermal stability and to investigate the effect of their macromolecular properties when they are combined with a glassy amorphous polymer such as PC and PS, acting as confining systems on PE (i.e., confined polymer). As shown by a schematic in **Figure 3.1**, these polymers were investigated throughout the thesis from symmetrical to immiscible and asymmetrical systems in terms of three categories: (i) LDPE-L1/LLDPE-LL2 pair, (ii) an immiscible LDPE-L1/PS pair, and (iii) an immiscible LDPE-L1/PC pair.

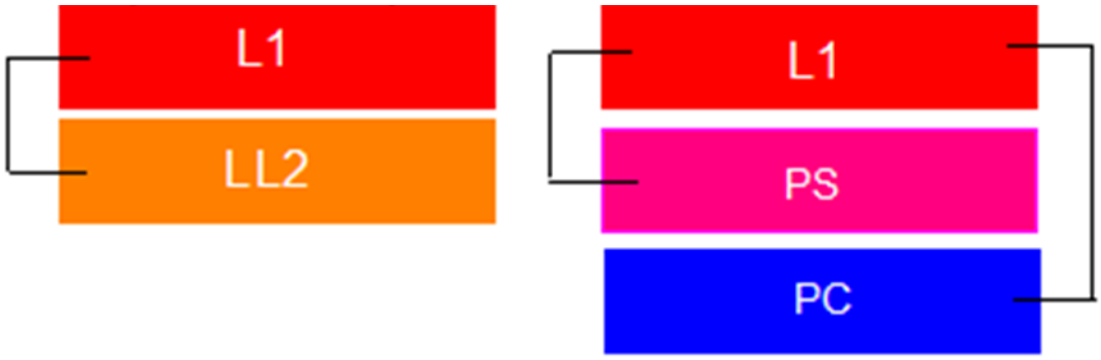

Figure 3.1 Types of polymer materials and pairs that have been investigated in this part.

The main characteristics of these materials are listed in **Table 3-1.** The weight average molar mass (Mw) and polydispersity index (Đ) were determined by high-temperature Steric

Exclusion chromatography at 150°C using 1,2,4-trichlorobenzene as the eluent for PEs and tetrahydrofuran (THF) for PS and PC. The activation energy (Ea) was determined from Arrhenius law by plotting the $\log\eta_0$ versus 1/T within a temperature range of 150°C<T<250°C.

Table 3-1 Characteristics of the investigated polymers.

Sample	M_w	Đ	η_0 (Carreau)	η^*(0,01rad/s) at 190°C	Ea	ρ	LCB
	[kg/mol]		[Pa.s]	[Pa.s]	[kJ/mol]	[g/cm3]	
LDPE-L1	238.6	9.0	38459	35169	53.5	0.922	2
LLDPE-LL2	93.7	2.5	9845	9232	31.0	0.918	0.9
PS	448.2	3.0	5429	4901	133.0	1.05	-
PC	22.9	2.5	111831	97583	152.0	1.2	-

The most important point that we have carefully considered is the positioning of the glass transition temperature of confining PS and PC materials against the crystallization temperature of the confined LDPE. As observed from **Figure 3.2** and summarized in **Table 3-2**, the glass transition temperature of confined PS is below 94°C and lies close to the crystallization temperature of the LDPE (93°C), while the PC had a Tg of 150°C, which is roughly 57°C higher than the LDPE crystallization temperature. By changing the confining polymer to PC instead of PS, we hope to understand the effect of rheological and Tg-Tc thermal contrast on interfacial stability when going from microlayers to nanolayers.

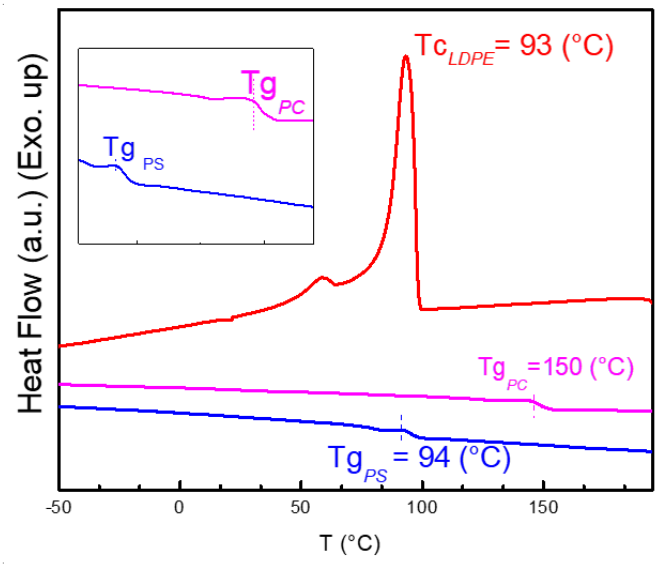

Figure 3.2 An example of DSC thermographs of cooling scans for neat polymers (LDPE-L1, PS, PC).

Table 3-2 Summary of the thermal analysis of the investigated polymers.

Sample	Thermal characterization		
	Tg (°C)	**Tm (°C)**	**Tc (°C)**
LDPE-L1	<-80	112	93
LLDPE-LL2	<-80	107-118	100
PS	94	----	-----
PC	150	----	-----

2.2. Sample preparation - Processing of multilayers

In this project, multilayer structures of micro/nanolayers were produced using a homemade multilayer coextrusion setup, as shown in **Figure 3.3**. From the feedblock, the initial two layers flow through a series of home made layer multiplication dies. These layer multiplication dies split the melt vertically and spread it horizontally to its original width

before stacking the layers, keeping a constant melt thickness [13]. In our work, two kind of home design multiplier elements have been used. In the first one, we keep the section constant, but we move from rectangle to rectangle by the intermediate of squares during dividing the flow. In the second, we keep the section constant but with rectangle in different zones. The final number of layers is determined as a function of the number of multiplications dies, which are placed in series between the feed block and final film, or sheet exit dies **Figure 3.3**. During the coextrusion process, the melt temperature was set at 240°C for the extruders, multipliers, and die. The chill roll temperature was then adjusted to 60°C with a drawing speed of 1.27 m/min for the three systems, to obtain a film thickness of 200±50 µm. The stretching ratio was kept lower, and we were focusing on what is happening during coextrusion step. The feed block configuration used for the systems was a B/A configuration, where A and B correspond to the extruders displayed in **Figure 3.3**. A set of n multipliers leads to a film of $2x2^n$, since a two-layered feed block was used for the LDPE-L1/ (LLDPE-LL2, PS, or PC) systems. The immiscible systems were obtained with volumetric flows of 50/50 and 10/90, keeping the total thickness of the film constant at around 200 µm. Only 50/50 volumetric flows were used in the LDPE-L1/LLDPE-LL2 systems.

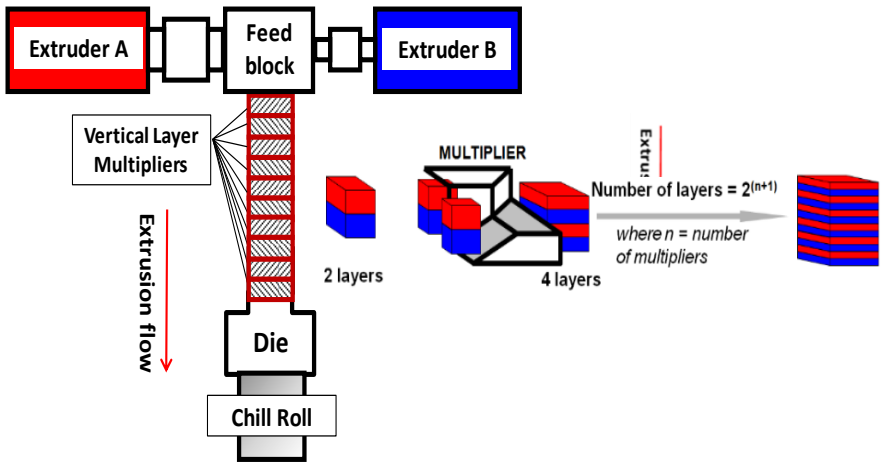

Figure 3.3 Schematic illustration of layer multiplication in the homemade multilayer coextrusion setup.

All multilayer films investigated are listed in **Table 3-3** for LDPE-L1 /LLDPE-LL2 systems and **Table 3-4** for LDPE-L1 against PC and PS, where n is the number of multipliers and N the corresponding number of layers. The estimated nominal layer thickness for each layer with a B/A film configuration was calculated using Eq. 50, for both A and B components with different volume fractions (50/50 and 10/90 for A/B, respectively).

$$h_{nomA,B} = \varphi_{A,B} \frac{h_{total}}{2^n} \quad (50)$$

where φ_A and φ_B represent the volume fraction of A and B, respectively, h_{total} the total film thickness and n the number of multipliers.

Table 3-3 Characteristics of the multilayered L1/LL2 films investigated.

Feed Block	Polymer systems (wt%)		LDPE-L1 /LLDPE-LL2 50/50	
	no. of layers (N)	no. of multipliers (n)	h_T (μm)	h_N
BA	32 L	4	200	6 μm
	256 L	7	200	781 nm
	1024 L	9	200	195 nm
	2048 L	10	200	97 nm
	16380 L	13	200	12 nm

Table 3-4 Characteristics of the multilayered LDPE-L1/(PS and PC) films.

Feed Block	Polymer systems (wt%)		LDPE-L1/PS				LDPE-L1/PC			
			50/50		10/90		50/50		10/90	
	no. of layers (N)	no. of multipliers (n)	h_T (μm)	h_N	h_T (μm)	h_N	h_T (μm)	h_N	h_T (μm)	h_N
BA	32L	4	160	5 μm	200	1 μm	200	6μm	170	1 μm
	256L	7	175	683 nm	200	136 nm	250	1 μm	200	156 nm
	1024L	9	200	195 nm	250	39 nm	200	195 nm	190	37 nm
	2048L	10	195	95 nm	200	19 nm	170	83 nm	180	18 nm
	16380L	10	200	12 nm	200	3 nm	200	12 nm	180	2 nm

2.1. Palierne model

Generally, the Palierne rheological model [126] has been extensively utilized to investigate the linear viscoelastic properties, as well as the interfacial properties of polymer blends [127]. This model, though, is only applicable to systems with spherical shape and no droplet–droplet interactions at low concentrations [128][129]. Blends of 20/80 for LDPE-L1/PS and 10/90 for LDPE-L1/PC were prepared in a corotating twin-screw extruder with a screw diameter of 16 mm (Thermo Electron PolyLab System Rheocord RC400P) at 240°C with a screw speed of 30 rpm. The as-prepared blends were compression molded into disks (25 mm diam. x 1 mm) at 200°C under a pressure of 200 bar prior to cooling under ambient conditions. The frequency sweep test was conducted at 240°C at frequencies varying from 628 rad/s to 0.01 rad/s to obtain the complex modulus for neat polymers and their blend.

According to the Palierne model, the complex shear modulus ($G^*(\omega)$) of an immiscible blend can be expressed as follows:

$$G^*_{blend} = G^*_m\left(\frac{1+3\Phi H^*}{1-2\Phi H^*}\right) \tag{51}$$

$$H^* = \frac{[(G^*_d - G^*_m)(19G^*_d + 16G^*_m)] + 4\frac{G}{Rv}(5G^*_d + 2G^*_m)}{\left[(2G^*_d + 3G^*_m)(19G^*_d + 16G^*_m)\right] + 40\frac{G}{Rv}(G^*_d + G^*_m)} \tag{52}$$

Where G_b^*, G_m^*, and G_d^* are the complex shear moduli of the blend, matrix, and dispersed phase (in this case, PE), respectively. ϕ is the volume fraction of the droplets with a radius R, Γ is the interfacial tension at the polymer/polymer interface obtained from fitting the experimental data and R_V is the volume average radius of droplet size of the dispersed phase, given by:

$$R_V = \frac{\sum_i (R_i f_i)}{\sum_i f_i} = \frac{\sum_i R_i^4}{\sum_i R_i^3} \tag{53}$$

where Ri is the radius of i particles calculated from the SEM micrographs.

The average number of cell radius Rn is defined as follows:

$$R_n = \frac{\sum_i R_i}{n} \tag{54}$$

where n is the number of droplets in a total area.

This model requires a narrow particle size distribution with a Rv/Rn ratio smaller than 2 [130]. In the case where Rv / Rn ratio exceeds 2, each radius and volume fraction must be taken into account individually, resulting in a considerably more complex expression of G*(ω).

The morphology of the LDPE-L1/PS and LDPE-L1/PC blends was observed by an FEI QUANTA 250 FEG microscope in high vacuum mode. Samples were fractured in liquid nitrogen at a temperature above the glass transition temperature (Tg), and then the surface of the blends was directly observed without any preparation. Both R_n and R_v were determined according to Eqs. (49) and (5454), where the size of dispersed phase particles for each blend was analyzed with ImageJ image analysis software using at least 100 droplets.

2.2. Macosko model

According to recent study, the Macosko model [126] was used to estimate the tensile stress growth coefficient of each layered pair $\eta^+_{E,M}$ versus time. This model is based on the summation of the contributions from each homopolymer and interfacial tension as a fitting parameter, and may be written as follows:

$$\eta^+_{E,M}(t) = \left(\frac{\phi}{\phi+1}\right)\eta^+_{E,PE}(t) + \left(\frac{1}{\phi+1}\right)\eta^+_{E,PS\ or\ PC}(t) + \frac{\Gamma(N-1)}{\dot{\varepsilon}H_0 e^{\left(-\frac{\dot{\varepsilon}t}{2}\right)}} \tag{55}$$

$$X = \frac{{H_{PE}}^{298K}}{{H_{PS\ or\ PC}}^{298K}} \tag{56}$$

$$Y = \frac{\left(\frac{{\rho_{PE}}^{298K}}{{\rho_{PE}}^{T}}\right)^{\frac{1}{3}}}{\left(\frac{{\rho_{PP}}^{298K}}{{\rho_{PS\ or\ PC}}^{T}}\right)^{\frac{1}{3}}} \tag{57}$$

$$\phi = XY \quad (58)$$

H_{PE}^{298K} : Nominal thickness at 25°C
ρ_{PE}^{298K}: Density of PE at 25°C
ρ_{PE}^{T}: Density of PE in the molten state
$\eta^{+}_{E,M}(t)$: Tensile stress growth coefficient
$\dot{\varepsilon}$: Strain rate
H_0: Total film thickness
N : Number of layers in the film
Γ : Interfacial tension between layers

One of the assumptions of the Macosko model is that the interfacial tension between layers is constant in the multilayer. This implies that the total volume of interfaces is also constant in practice. One of the main advantages of this model is that the tensile stress growth coefficient is directly dependent on the interfacial tension. Another assumption of the Macosko model is that there is homogeneous extensional deformation to stretch each constituent. This model could be fit to the experimental data obtained in extensional rheology.

3. Results and discussion

3.1. Melt Rheological study of selected polymers

3.1.1. Thermal stability study of the neat polymers

The viscoelastic properties of polymeric materials are very sensitive to structural modifications that can occur with temperature and time. In this chapter, dynamic time sweep measurements were performed to probe the healing process of neat polymers under conditions simulating the coextrusion process (high temperatures, longer times for high number of layers…). **Figure 3.4** depicts the normalized storage modulus G'(t)/G'(t=0) and complex viscosity η*(t)/η*(t=0) versus time for the neat polymers at a reference temperature of 240°C with an angular frequency of 0.1 rad/s for 30 min. This time corresponds to the maximum residence time of the polymers when they pass through the multiplier elements during the coextrusion. As observed, the neat polymers were thermally stable for t=30 min, except for the LLDPE (LL2), for which a significant increase in normalized G'(t)/G'(t=0) and η*(t)/η*(t=0) was seen, especially for t>1260 s. This can be

explained by crosslinking among the LLDPE chains or degradation mechanisms over a long period.

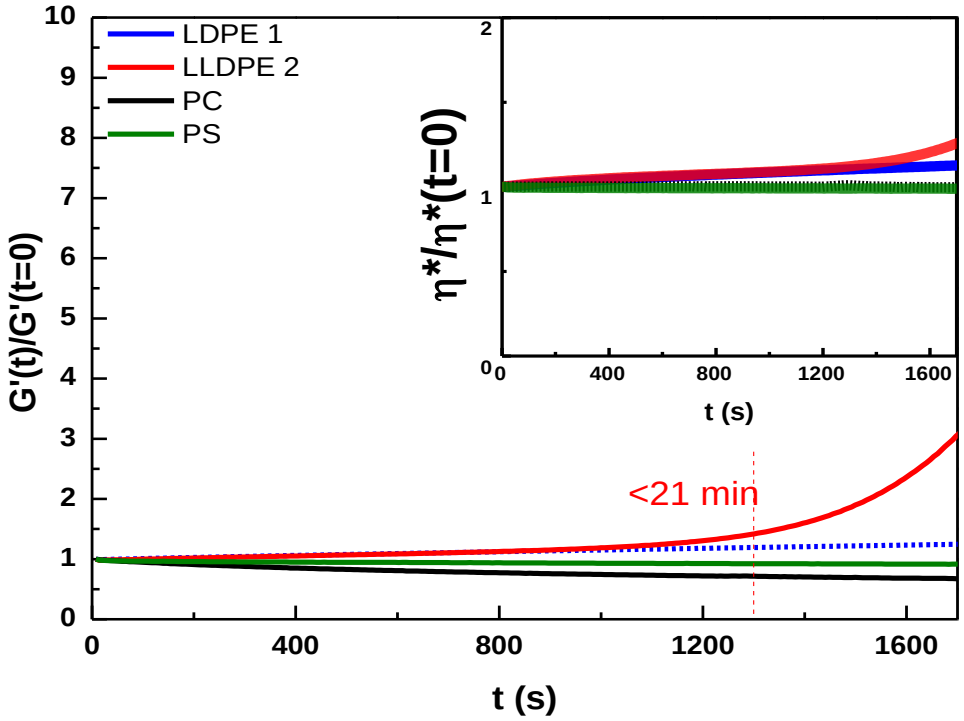

Figure 3.4 Comparison of the evolution of the normalized G′(t)/G′(t=0) and η*(t)/η*(t=0) as a function of healing time at 240°C with an angular frequency of 0.1 rad/s for neat polymers.

3.1.2. Dynamic shear viscoelasticity of the neat polymers

The master curves of the complex viscosity for all neat polymers at 240°C are shown in **Figure 3.5**. It can be observed that all the studied polymers showed a shear-frequency/thinning behavior that is more pronounced beyond 10 rad/s. Their zero-shear viscosity can be simply deduced as the $\lim_{\omega \to 0} \eta^* = \eta_0$ in the Newtonian regime, except for LDPE, for which the zero-shear viscosity values were not reached experimentally. Moreover, it can be clearly seen that the LDPE is more viscous compared to the other polymers at lower frequencies. This can be explained by the molecular structure of LDPE. As we demonstrated in the previous chapter, the presence of long-chain branching with high

molar masses created more entanglements, giving rise to higher viscosities at lower frequencies.

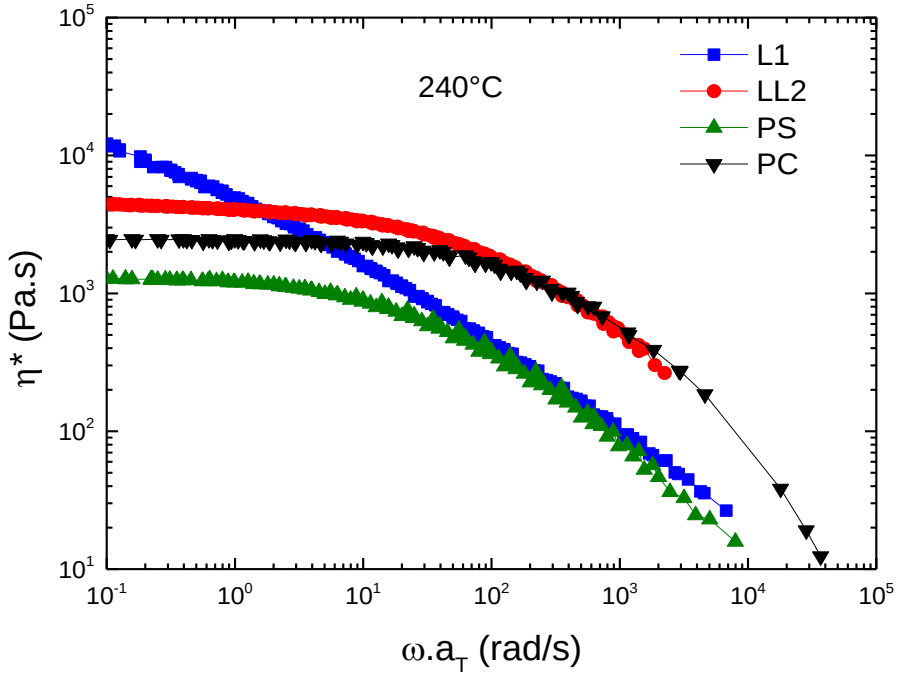

Figure 3.5 Master curves of complex viscosity versus angular frequency for L1, LL, PS and PC at 240°C.

The master curves and Cole–Cole diagrams of all of the neat polymers are given in **Figure 3.6** at a reference temperature of 240°C. The temperature dependence of the shift factors follows an Arrhenius-type equation for the PEs and the WLF (Ferry 1980) equation for PC and PS. The rheology at the terminal zone is observed to follow the typical relation $G' \sim \omega^2$ for the neat polymers. In the low angular frequencies, the storage moduli are highest for LDPE-L1. This result underlines a higher elasticity of LDPE-L1 than of LLDPE-LL2, PS, and PC. Moreover, the LDPE displays an interesting window for checking the effect of its long relaxation process in comparison to linear LLDPE, PS, and PC. A semicircular shape was obtained for all neat polymers except for the low-density polyethylene, with no arc shape being seen even at low frequencies, indicating a very long relaxation time for this polymer. These differences can be explained by the presence of long-chain branching in

LDPE and by its molecular weight distribution. The presence of LCB has a more pronounced effect on viscoelastic properties.

Zero shear viscosity was estimated with the Carreau-Yasuda model. The activation energy values (Ea) were obtained from the $\log\eta_0$ plotted versus 1/T within a temperature range of 190°C<T<240°C. The results of the activation energies in the molten state are listed in **Table 3-1 .**The activation energy of LDPE is higher than that of the LLDPE. This could be related to the presence of LCB branching or to the ultrahigh Đ values, which can be reflected in the activation energy, Ea. The value of the LDPE activation energy is around 50 kJ/mol, a typical value for an LDPE, while the activation energy value is 31 kJ/mol for LL2, a typical value for an LLDPE.

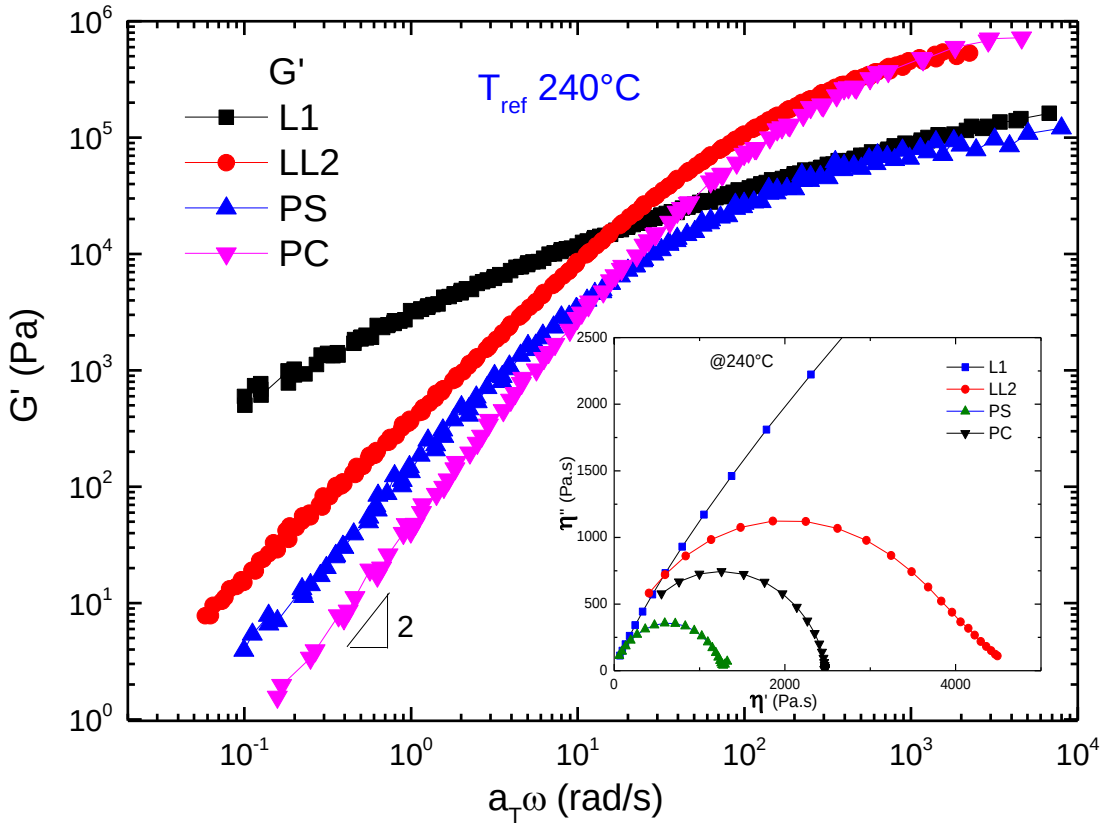

Figure 3.6 G′ Master curves and Cole-Cole diagram of the neat polymers shifted to a reference temperature of 240°C.

3.2. Application: Processing of multi-micro/nanolayers

Based on these results, both viscosity and elasticity ratios were obtained, as seen in **Figure 3.7**. The viscoelastic mismatch was highlighted in the hatched zone corresponding to the flow processing shear region. The zero-shear viscosity ratio and elasticity ratio of the studied materials at different temperatures are very important for understanding the flow behavior and the stress relaxation process during coextrusion. The different systems were studied and chosen to change the viscosity and elasticity ratios.

3.2.1. Viscosity and elasticity ratios of the neat polymers

It is well known that the melt viscosity and/or elasticity ratio between the components are very important for determining the layer structure and uniformity of the multilayer polymer structure. To determine the viscoelasticity ratio, the linear viscoelasticity of LDPE-L1, LLDPE-LL2, PS, and PC were studied using SAOS at a processing temperature of 240°C. **Figure 3.7** shows that the viscosity and elasticity ratios for the partially miscible pair LDPE-L1/LLDPE-LL2, which we have check it in both rheology and morphological investigations, are well-matched in the shear-rate range of the coextrusion process and differ significantly for immiscible systems LDPE-L1/PS and LDPE-L1/PC. Note that the LDPE-L1/LLDPE-LL2system was used as a reference in this thesis. The viscosity ratio and elasticity ratio are designated by M and M_λ, respectively. The hatched rectangle in grey represents the shear-rate range occurring in the feed block and hanger die (1–100 s^{-1}) [131] and the zone hatched in blue indicates the shear-rate range taking place in the multipliers (1–10 s^{-1}) [13]. The viscosity ratio of immiscible pairs is quite higher and can reach a value of 4 for LDPE-L1/PS and a value of 2 for LDPE-L1/PC, while the viscosity ratio for the LDPE-L1/LLDPE-LL2 system was close to 1. It is interesting to note that the LDPE-L1/PC system represents a high elasticity ratio at least three times higher than that of LDPE-L1/PS in the shear-rate range taking place in the multipliers. These values are also summarized in **Table 3-5.**

Table 3-5 Values of viscosity ratios and elasticity ratios of the studied polymer couples.

Shear rates (s^{-1}) assuming Cox-Merz rule	Viscosity ratios M_{η^*}			Elasticity ratios M_λ		
	L1/PS	L1/PC	L1/LL2	L1/PS	L1/PC	L1/LL2
1	4.0	2.0	1.2	7.2	49	9
10	1.7	0.6	0.5	2.6	8.6	4
100	1.0	0.3	0.3	1.3	2.8	1.8

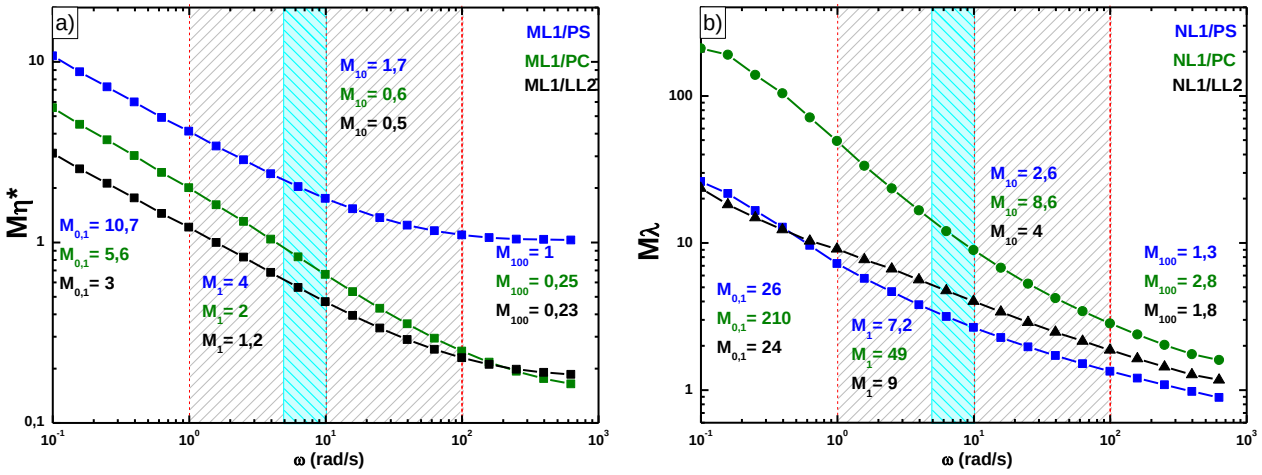

Figure 3.7 Viscosity ratios (a) and elasticity ratios (b) versus the flow rate for symmetrical and asymmetrical systems: LDPE-L1/LLDPE-LL2(black curve), LDPE-L1/PS (blue curve), and LDPE-L1/PC (green curve).

3.2.2. Estimation of contact time and nominal thickness in multilayer coextrusion with various numbers of layers (N)

The contact time between neighboring layers is required to quantitatively characterize the polymer-polymer adhesion and to keep the interface stable throughout the coextrusion process. The contact time is defined as the period required for the polymer to flow sequentially through the confluent zone of the manifold system, the series of multipliers (LME), and the die. In this study, the contact time for all multilayered films was determined as a function of the number of multipliers (n) as follows:

$$t_{cont} = \frac{V_{conf} + nV_{LME} + V_{die}}{Q_{mass}}\rho \quad (59)$$

where V_{conf}, V_{LME}, and V_{die} denote the volume of the confluent area in the feed-block, one-layer multiplying element, and die, respectively; and n represents the number of multipliers used. Q_{mass} refers to the mass flow rate and ρ denotes the apparent density of confluent melts at the extrusion temperature. The corresponding values are summarized in **Table 3-6**. The estimated contact time and the theoretical thickness for LDPE-L1/PC, LDPE-L1/PS, and LDPE-L1/LLDPE-LL2 are plotted in **Figure 3.8** as a function of the number of layers (the number of multipliers n). It is noticeable that the contact time of these multilayered structures increased with the increase in the number of layers or the number of multipliers (n), especially for immiscible pairs, accompanied by a decrease in nominal thickness. This was as expected, since each time that layers are multiplied through coextrusion, a new interface is produced, resulting in a longer melt contact time and a thinner layer in the order of several nanometers for nanolayered structures.

Table 3-6 Values of the confluent area in the feed-block, one-layer multiplying element, die and volume flow

V_{conf} (cm^3)	$V_{LME}(cm^3)$	V_{die} (cm^3)	Q_V (m^3/s)
1.952	7.748	43.891	26.6

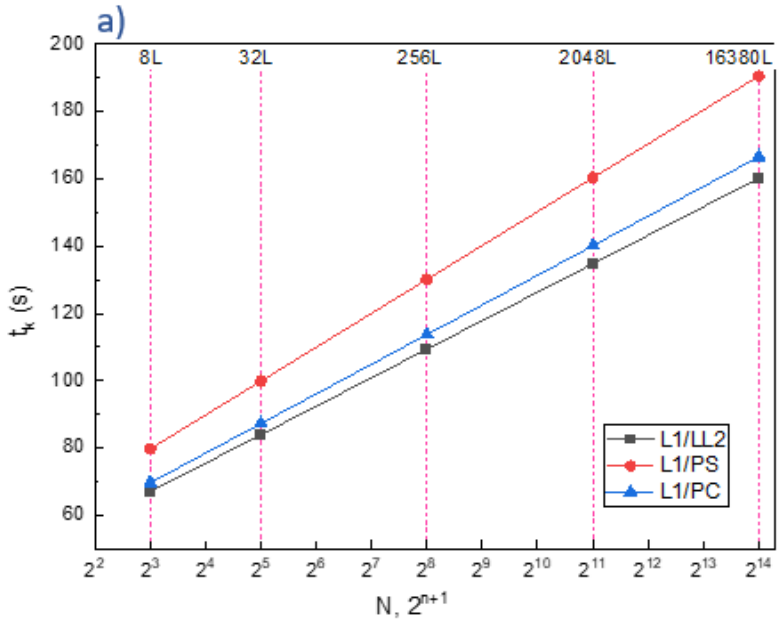

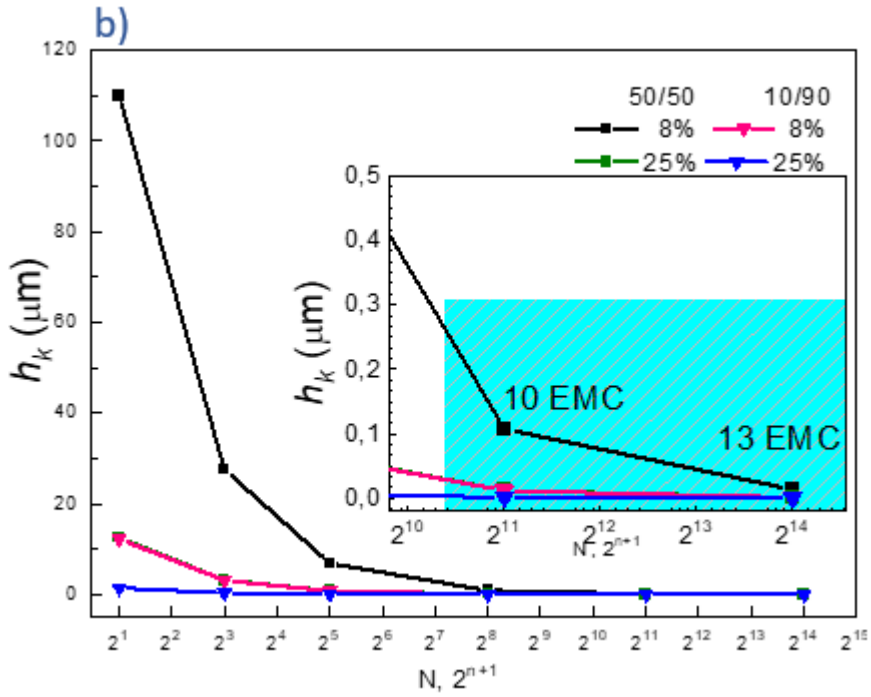

Figure 3.8 Calculated contact time (a) and theoretical thickness (b), for partially miscible and immiscible multilayer films with various numbers of layers (N) or the number of multipliers (n) ($N=2^{n+1}$).

3.3. Rheological study of multi/micro-nanolayered polymers and blend

3.3.1. Linear viscoelasticity of multilayer polymers and blend

3.3.1.1. Partially miscible LLDPE-L2/LDPE-L1 configuration

Dynamic frequency sweep tests were performed under a fixed strain amplitude of 5%, which lies in the linear viscoelastic regime, and an angular frequency of 628 to 0.01 rad/s, at a temperature of 240°C. **Figure 3.9.a** depicts the dynamic complex viscosity (η*) against angular frequency (ω) for neat polymers, their 50/50 blend, and multilayer structures of partially miscible systems at 240°C (for the sake of clarity, we have validated this partial miscibility by checking the morphology at different compositions of this PE based blends). It can be observed, in the frequency range (shear rate assuming cox-Merz rule) of our tests, that the rheological behavior of both linear and branched PEs is different from some shear-thinning behaviors in correlation with their structures (see chapter 2). Since the viscosity modulus of the two neat polymers are different, the multilayer structures reveal an

intermediate behavior between linear and low-density polyethylene, and close viscosity to their equivalent blend whatever the layer number. Indeed, the viscosity of multilayer structures is quite similar for all numbers of layers and shows a behavior rather similar to that of the LDPE-L1, while the zero-shear viscosity value was not reached experimentally due to our inability to make the measurement at sufficiently low frequencies with a thermally stable specimen (longer times). Moreover, no negative deviation of viscosity was observed in **Figure 3.9(a)**, even at high frequencies, for the LDPE-L1 and LLDPE-LL2 pairs, which explains, once again, the existence of a partial miscibility/compatibility. These results imply that there was no interfacial slippage produced between adjacent layers during the dynamic shear measurements for this system [64]. Then a good adhesion between neighboring polymer layers in the multilayer structures is created (results of SEM not shown here for the sake of clarity).

The same trend is observed for the storage modulus of neat polymers LDPE-L1 and LLDPE-LL2, the 50/50 blend, and multilayered polymers at 240°C, as can be seen in **Figure 3.9.(b)**. It can be noted that the multilayer structures and blend showed an intermediate behavior between the neat polymers. At low frequency, the G' of LDPE-L1 was higher than that of its equivalent blend and micro/nanolayered structures, which is possibly due to its higher molecular weight and the presence of LCB.

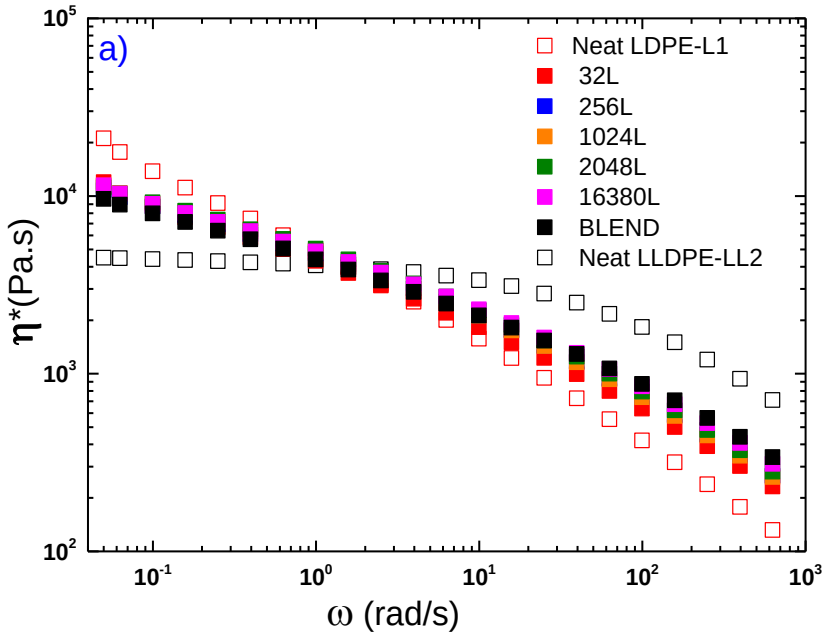

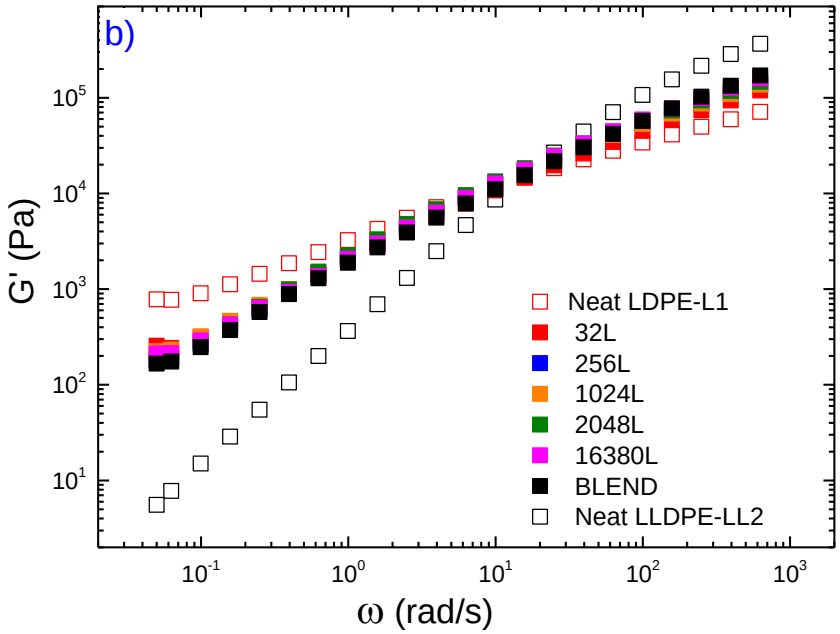

Figure 3.9 Complex viscosity and storage modulus versus angular frequency for neat LDPE-L1 and LLDPE-LL2, the (50/50) multilayer films, and their equivalent blend at 240°C.

3.3.1.2. Immiscible LDPE-L1/PS configuration

The complex viscosity of the samples plotted against angular frequency for various LDPE-L1/PS compositions with volume ratios of 50/50 and 10/90 are shown in **Figure 3.10**. For the films with a 50/50 composition, the complex viscosity curves of the multilayer structures and 50/50 blend lie between those of the neat LDPE (L1) and PS polymers and exhibit quite similar behavior to that of LDPE (L1), except for the 256-layer blue curve.

Indeed, the negative deviation of viscosity in 256 films is possibly caused when the increase in the number of layers greatly enhances the interfacial contribution, and then reduces entanglements between LDPE chains, leading to the appearance of interfacial slip at their interface.

Furthermore, and for the films with a highly asymmetric 10/90 composition of LDPE (L1)/PS, the viscosity of multilayer structures is quite similar for all numbers of layers, showing an intermediate behavior between the neat polymers LDPE-L1 and PS. Moreover, as observed in **Figure 3.10**, the viscosity of multilayer structures decreases by increasing the number of layers and presents a Newtonian plateau as well as the PS, due to the lack of entanglements in the interfacial region. This explains why PS, when present as the main component, truly confines LDPE-L1 layers during coextrusion, contrary to the film with a symmetric 50/50 LDPE-L1/PS composition that allows entanglement in LDPE-L1, leading to higher viscosities. Surprisingly, the 10 L1/90 blend shown a lower viscosity than the equivalent multilayer and neat PS, suggesting a great negative deviation and pronounced interfacial slippage.

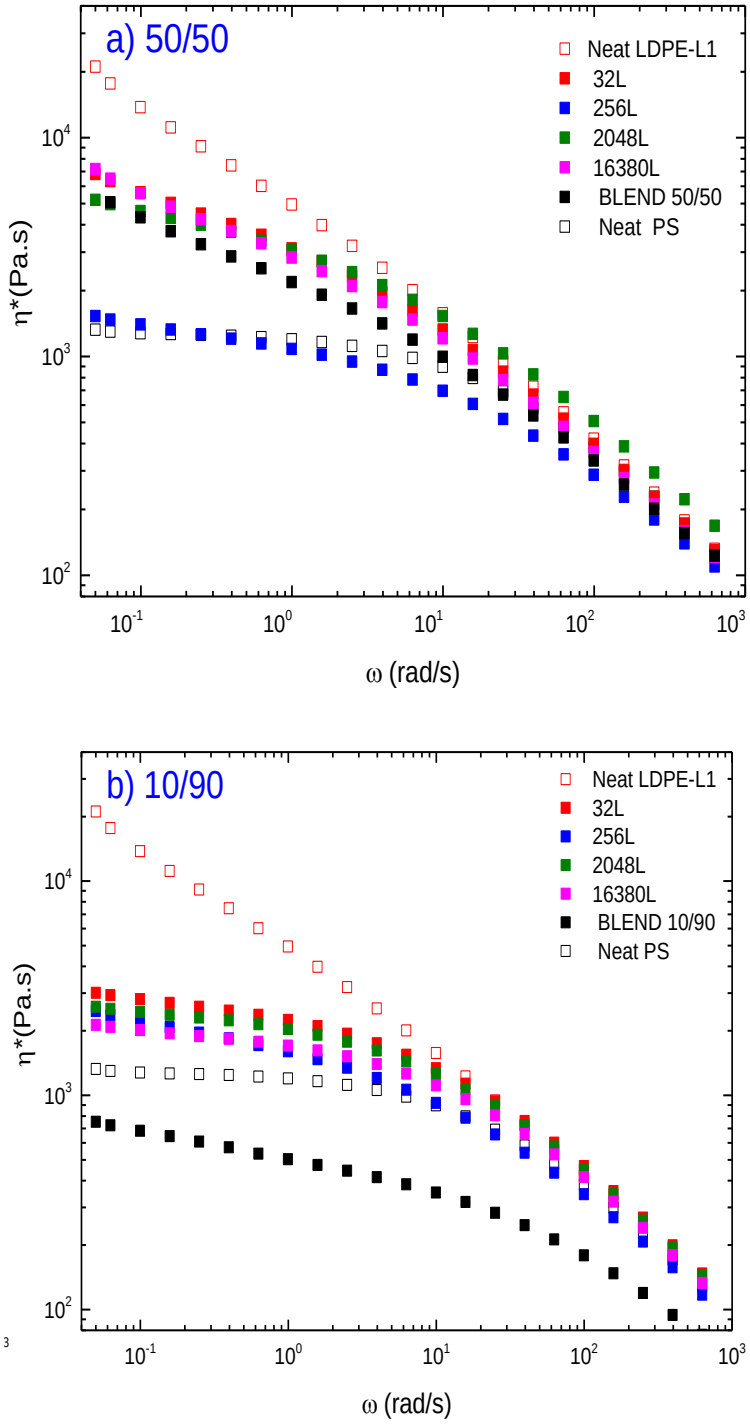

Figure 3.10 Complex viscosity versus angular frequency for LDPE-L1/PS multilayer films, blends ((a)50/50 and (b) 10/90), and neat polymers at 240°C.

3.3.1.1. Immiscible LDPE-L1/PC configuration

Additionally, LDPE-L1/PC films with the same compositions as the LDPE-L1/PS pair (50/50 and 10/90),were used for comparison (**Figure 3.11**). Both sets of LDPE-L1/PC films showed a negative deviation of the viscosity, demonstrating poor layer adhesion between neighboring polymer layers in coextrusion with weaker inter-chain entanglements in the interfacial region, leading to significant interfacial slip from the weak interfacial adhesion, and also inducing layer-interface instabilities during processing, which deteriorate the layer integrity and architecture (results of SEM in the next chapter)[3][4]. The PC chains display a higher monomeric friction and rigidity which they hinder the LDPE-L1 chain dynamics. Owing the higher activation energy of PC (152 kJ/mol), the initially geometrical confinement during processing makes difficult the continuity of stress across the interfaces during measurements. The PC chains restricts molecular mobility and hinders the cooperative motions of LDPE chains, which seems to be the origin of the decrease of the multilayer's shear viscosity and consequently the interfacial slip between adjacent layers. On this basis, the increase in the number of layers was responsible for enhancing the interfacial contributions with high interfacial area.

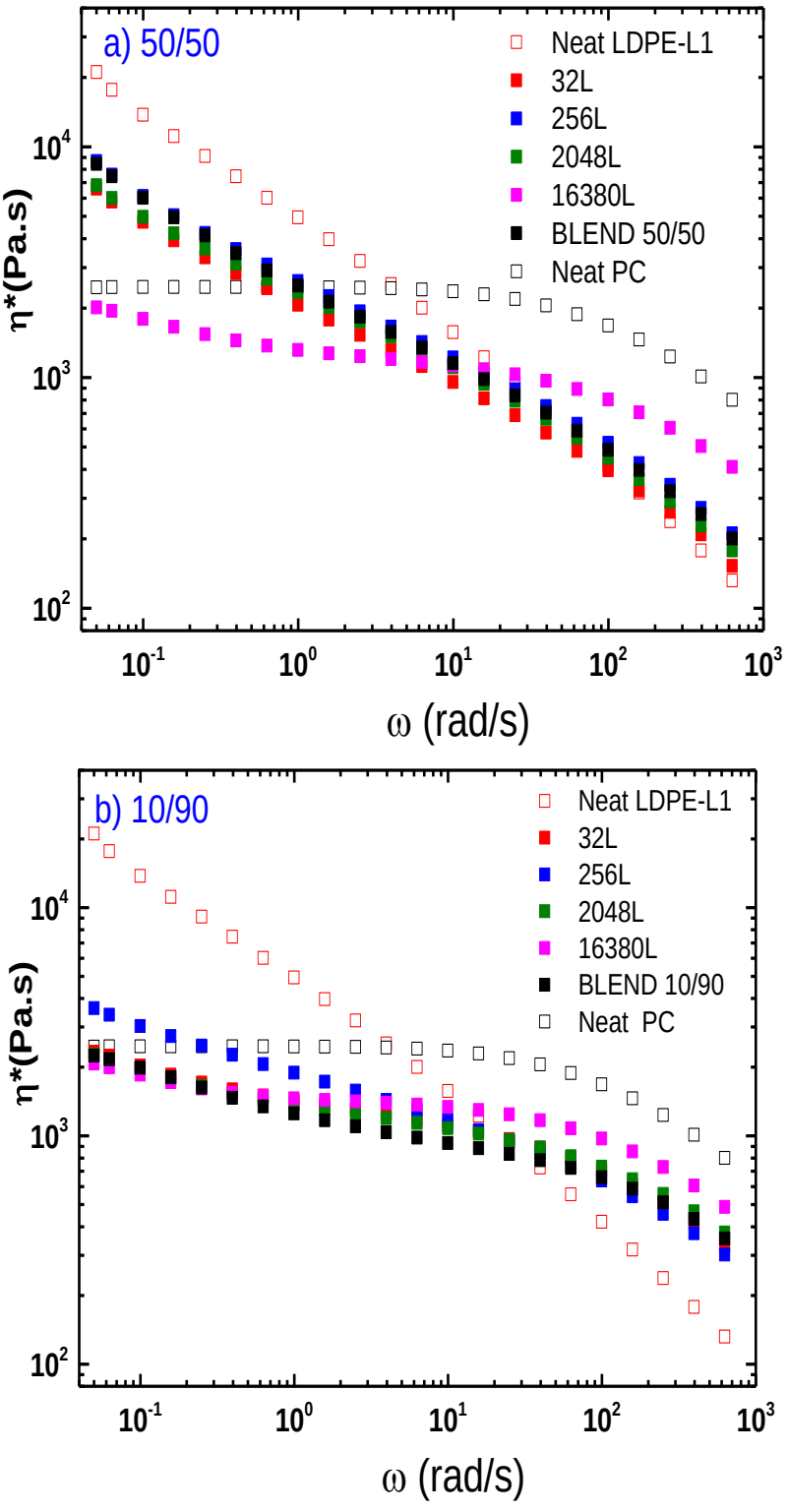

Figure 3.11 Complex viscosity and storage modulus versus angular frequency for L1/PC multilayer films, blends (50/50 and 10/90), and neat polymers at 240°C.

3.3.2. Extensional rheology of multilayered structures and blend

The strain validation and continuous visual access were first performed during the measurements by a built-in camera to monitor the evolution of a specimen's width dimension at the constant Hencky rate of 0.1 s^{-1}, as shown in **Figure 3.12**.

The **Figure 3.13a-b** depicts the evolution of the width ratio of LDPE-L1/PS at Hencky strain rates of 0.1 s^{-1} and 10 s^{-1} for the different numbers of layers ranging from 32 to 2048-layer films. Excellent superposition of actual and theoretical width evolution values is obtained for coextruded multilayer films, thereby illustrating the agreement between actual and applied strain with the SER over a broad range of extensional rates (0.1 s^{-1} and 10 s^{-1}) and for different numbers of layers, which further ensures a truly uniform extensional deformation during uniaxial extension experiments in the whole range of Hencky amplitudes (from 0 to 3.8).

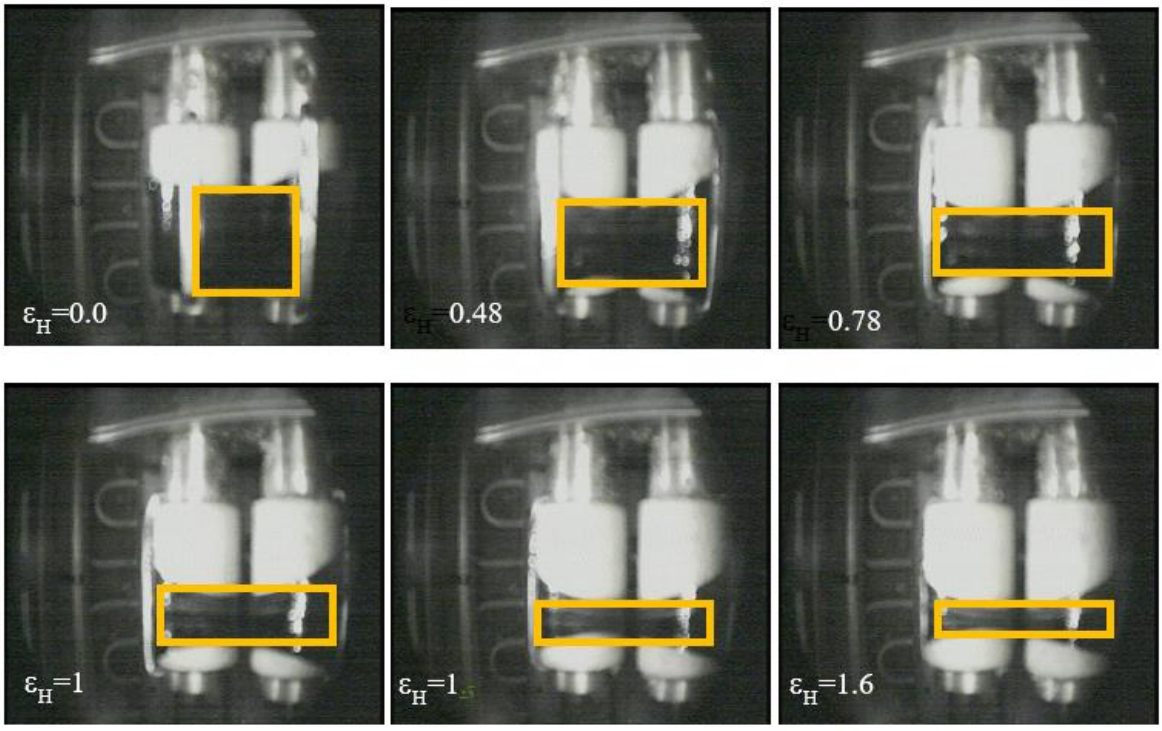

Figure 3.12 Sequential images recorded by a built-in camera to show the evolution of the actual width dimension of a coextruded LDPE-L1/PS (50/50) multilayer undergoing stretching at a constant Hencky strain rate of 0.1 s^{-1}. Example for 32 layers.

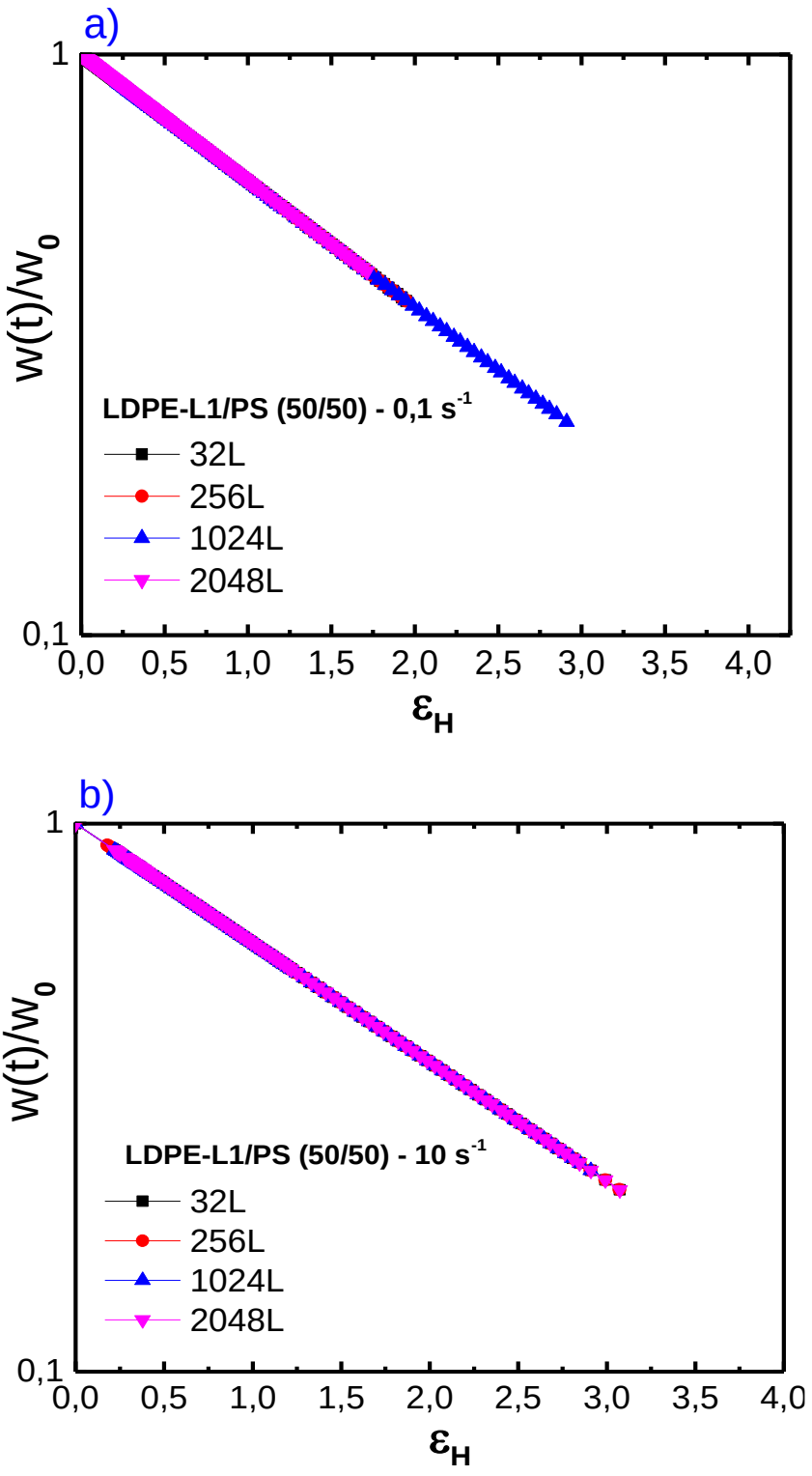

Figure 3.13 An example of the theoretical width dimension of coextruded LDPE-L1/PS (50/50) films at constant Hencky strain rates of (a) 0.1 s^{-1} and (b) 10 s^{-1}.

Figure 3.14, Figure 3.15, Figure 3.16, Figure 3.17, and **Figure 3.18** present the evolution of the transient tensile stress growth coefficient $\eta_E^+(t)$ as a function of extension time for both partially miscible and immiscible multilayer systems at 240°C from 0.1 to 10 s^{-1} of Hencky strain rates. For each polymer, the linear viscoelastic (LVE) envelopes were displayed by the solid line in black and determined independently by fitting the oscillatory shear data with a multi-mode Maxwell discrete relaxation spectrum (details in chapter 2). However, the theoretical LVE envelope of multilayers and their equivalent blend were determined by the following equation on the zero-shear viscosity of each polymer multiplied by its corresponding volume fraction.

$$log\,\eta_0 = f_i log\,\eta_{0,i} + f_i log\,\eta_{0,i} \quad (60)$$

where f_i and $\eta_{0,i}$ (i=A,B) are the volume fraction and zero-shear viscosities of the constituent components for neat polymers.

The predicted extensional viscosity (shown by red lines) for multilayer structures was determined by the additivity rule as follows:

$$\eta_E^+(t) = f_1\,\eta_{E,1}^+(t) + (1 - f_1)\,\eta_{E,2}^+(t) \quad (61)$$

where $\eta_E^+(t)$ is the transient extensional viscosity and depends on the volume fraction and the transient viscosity of each constituent of a multilayer structure.

3.3.2.1. Partially miscible LLDPE-L2/LDPE-L1 configuration

From **Figure 3.14**, the transient extensional viscosities of 32, 1024, 2048, and 16380-layered films deviate significantly from the LVE envelope, indicating strain-hardening behavior. This is attributed to the presence of a high amount of long-chain branching in LDPE-L1 (2 LCB/1000C) (details in chapter 2). For the 256-layered film, however, the system is clearly lower than the LVE regime at lower strains due to the interfacial failure of the LDPE-L1/LLDPE-LL2 micro layered system. The melt extensional behavior of the 256-layered film is therefore dominated by the structure of the bulk layers. Another interesting fact to note is the continuous increase in the degree of strain hardening with increasing numbers of layers up to 16 380 layers. Specifically, the 2048L seems to exhibit the strongest strain hardening among the tested multilayered films. The observed extensional rheological behaviors, which are highly dependent on the number of layers, can be explained by invoking the physical process of stretching a sample with a multilayered structure. When all layer thicknesses are reduced by a large extensional deformation, the extensional process would involve stretching the layer−layer interphases. Multilayer films with a larger number of layers would thus display the extensional behavior of polymer chains within the interphases. Herein, the polymer-polymer interfaces are composed of chain ends/arms stitched in their bulk layers by entanglements. Understandably, when the chain entanglements of polymer-polymer interfaces are completely stretched at the larger strain deformation, the interfacial stretching would unfasten their multiple branches from entanglements with segments in neighboring layers. The branched chains at the interface lead to interfacial stitching among layers, which acts as an elastic membrane. A larger proportion of interfaces would thus provide this stronger resistance to the stretching process, thereby manifesting as increased interfacial stress, as evidenced by enhanced strain hardening with an increasing number of layers [32]. The results show that the uniaxial elongation flow of the multilayered films seems to be more dominated by the LDPE behavior. The coextrusion of partially miscible LDPE-L1/LLDPE-LL2 pairs appears to be more stable. This would be attributable to the presence of the interphases generated from interdiffusion and favored by convective mixing.

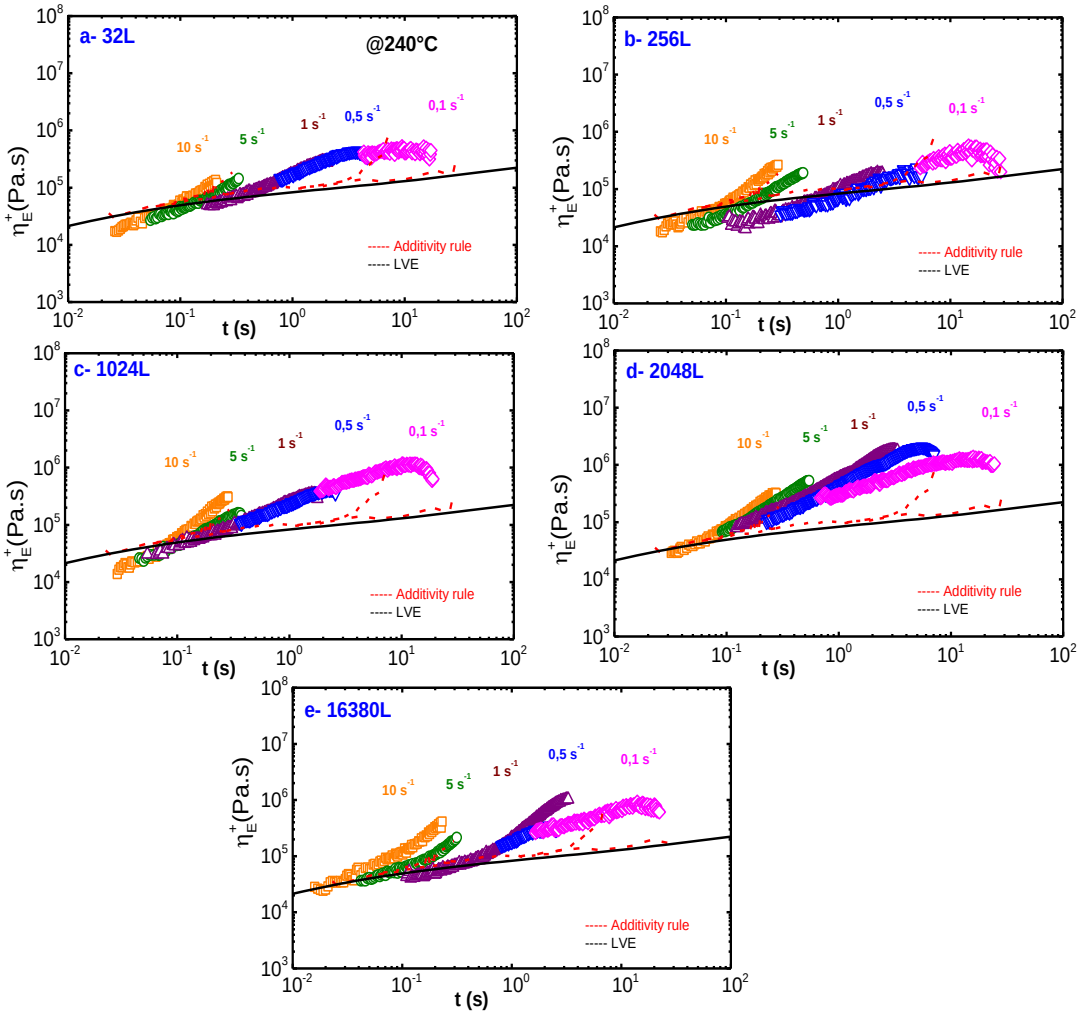

Figure 3.14 Stress growth coefficient-Extensional viscosity versus extension time at 240°C with extension rates varying from 0.1 to 10 s^{-1} for LDPE-L1/LLDPE-LL2 (50/50) multilayer films: (a) 32L, (b) 256L, (c) 1024L, (d) 2048L, and (e) 16384L. The dashed lines in (a) - (e) are predicted transient viscosities obtained by the additivity rule, and solid lines in (a) - (e) are LVE predictions with the equilibrium equivalent LDPE-L1/LLDPE-LL2 (50/50).

3.3.2.2. Immiscible LDPE-L1/PC configuration

In addition to the partially miscible LDPE-L1/LLDPE-LL2 configuration, the immiscible LDPE-L1/PC layered films were also investigated under extensional flows in the same conditions. The transient tensile stress growth coefficient $\eta_E^+(t)$ of the micro layered system (32L to 1024L), agree well with the LVE envelope (solid lines in black) and the predicted viscosities obtained by the additivity rule (dashed lines in red). This clearly indicates the good adhesion between adjacent layers, which is confirmed by SEM micrographs (see tiny images in **Figure 3.15 (a)-(b)**). The micro layered films present continuous and regular structures with a flat, smooth interface between LDPE and PC (more details in chapter 4).

In contrast, when the number of layers is increased up to (2048L-16380L), a negative deviation in η_E^+ from the LVE envelope and the additivity rule values was observed from 0.1 to 10 s^{-1} of Hencky strain rates. This is a characteristic of immiscible systems and may be related to an improperly matched elastic ratio. Note that the elasticity ratio of the LDPE-L1/PC system reached a value of 8.6 in the shear rate range of multipliers (1-10 s^{-1}), which explains the negative deviation that results in interfacial failures (e.g., interfacial slip).

However, despite the presence of long-chain branching in LDPE-L1, no strain hardening was observed in any of the coextruded micro/nanolayers. This may be related to the higher monomeric friction and chain rigidity of PC chains. Owing the higher activation energy of PC (152 kJ/mol), this restricts molecular mobility and hinders the cooperative motions of LDPE-L1 chains, which seems to be the origin of the lack of strain hardening in extension rheology. Similar results were observed for the micro/nanolayered films with a 10/90 composition in LDPE-L1/PC (**Figure 3.16**).

It is concluded that as the number of layer interfaces increases, the PC tends to gradually reduce the LDPE-L1 chain mobility, which explains the lack of strain hardening accompanied by interfacial distortions (layer breakup) resulting from the interfacial slip during processing.

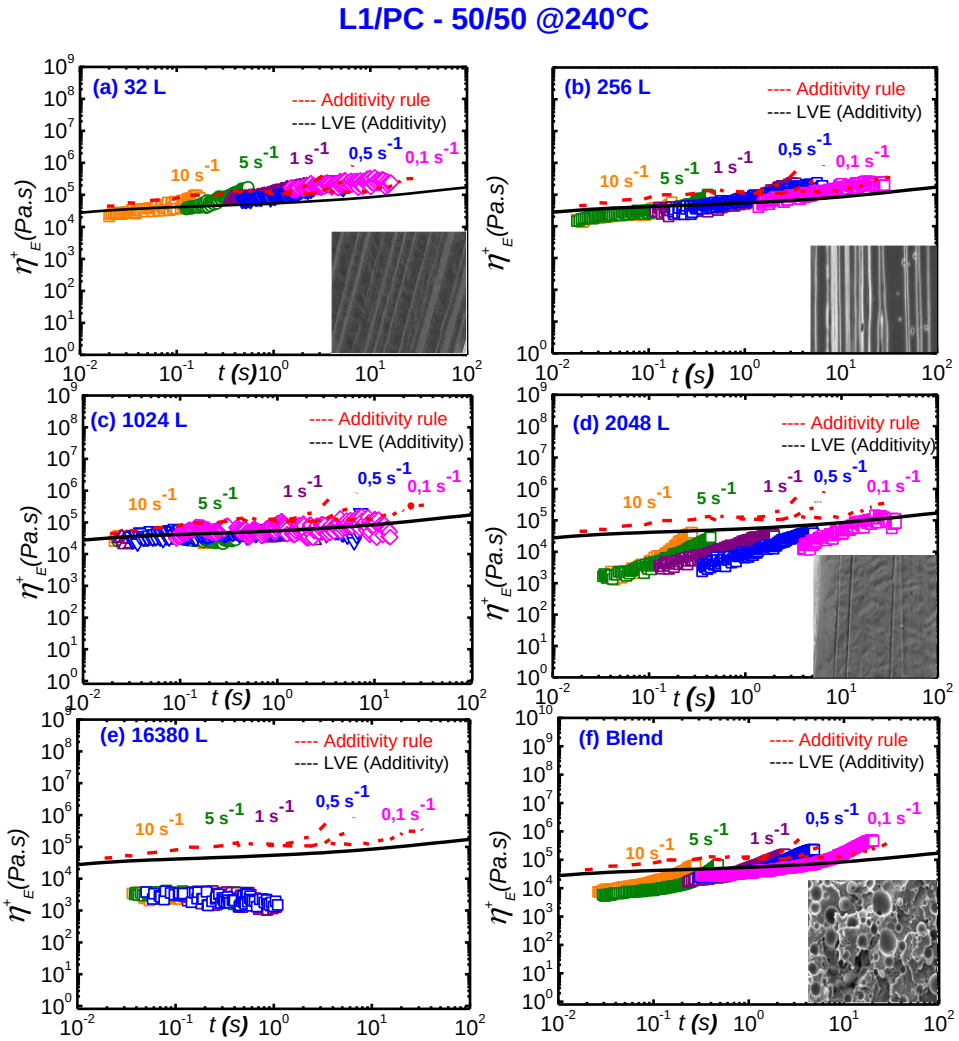

Figure 3.15 Extensional viscosity versus extension time at 240°C with Hencky strain rates varying from 0.1 to 10 s^{-1} for LDPE-L1/PC (50/50) multilayer films and their equivalent blend: (a) 32L, (b) 256L, (c) 1024L, (d) 2048L, (e) 16384L, and (f) blend. The dashed lines in (a) - (f) are predicted viscosities obtained by the additivity rule, and the solid lines are LVE predictions with the equilibrium equivalent LDPE-L1/PC (50/50) blend.

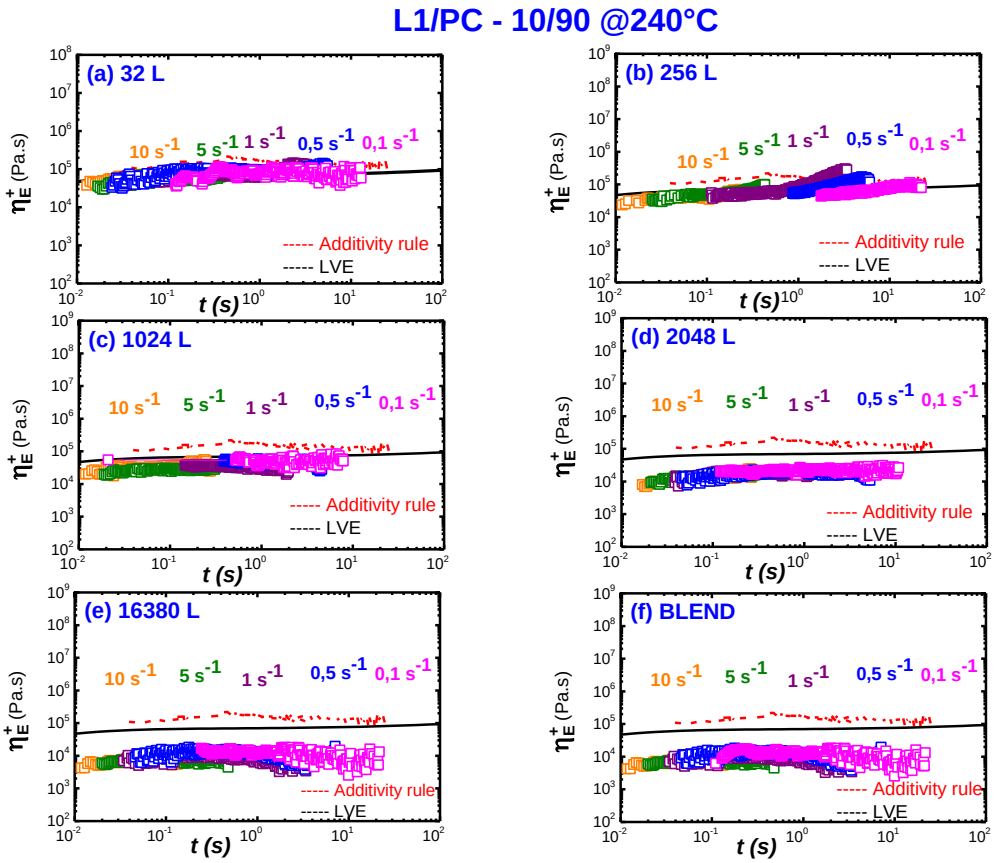

Figure 3.16 Extensional viscosity versus extension time at 240°C with extension rates varying from 0.1 to 10 s^{-1} for LDPE-L1/PC (10/90) multilayer films and their equivalent blend: (a) 32L, (b) 256L, (c) 1024L, (d) 2048L, (e) 16384L, and (f) blend. The dashed lines in (a) - (f) are predicted viscosities obtained by the additivity rule, and the solid lines are LVE predictions with the equilibrium equivalent LDPE-L1/PC (10/90) blend.

3.3.2.3. Immiscible LDPE-L1/PS configuration

Following the same protocol, the immiscible multilayered LDPE-L1/PS films were also measured in the same condition as others. From **Figure 3.17**, the transient extensional viscosities of 32, 1024, 2048, and 16380-layered films deviate significantly from the LVE envelope, indicating strain-hardening behavior. The strain hardening in a nanolayered structure was even stronger than that of its equivalent blend. In contrast to the LDPE-L1/PC multilayered films **Figure 3.15**, no strain hardening behavior was observed. This is possibly due to the elasticity ratio of LDPE-L1/PS, which is lower than that of L1/PC and which may

improve the interfacial stability of coextrusion. Similar behavior was found when we change the volume fraction of the LDPE-L1/PS 10/90 (see **Figure 3.18)**.

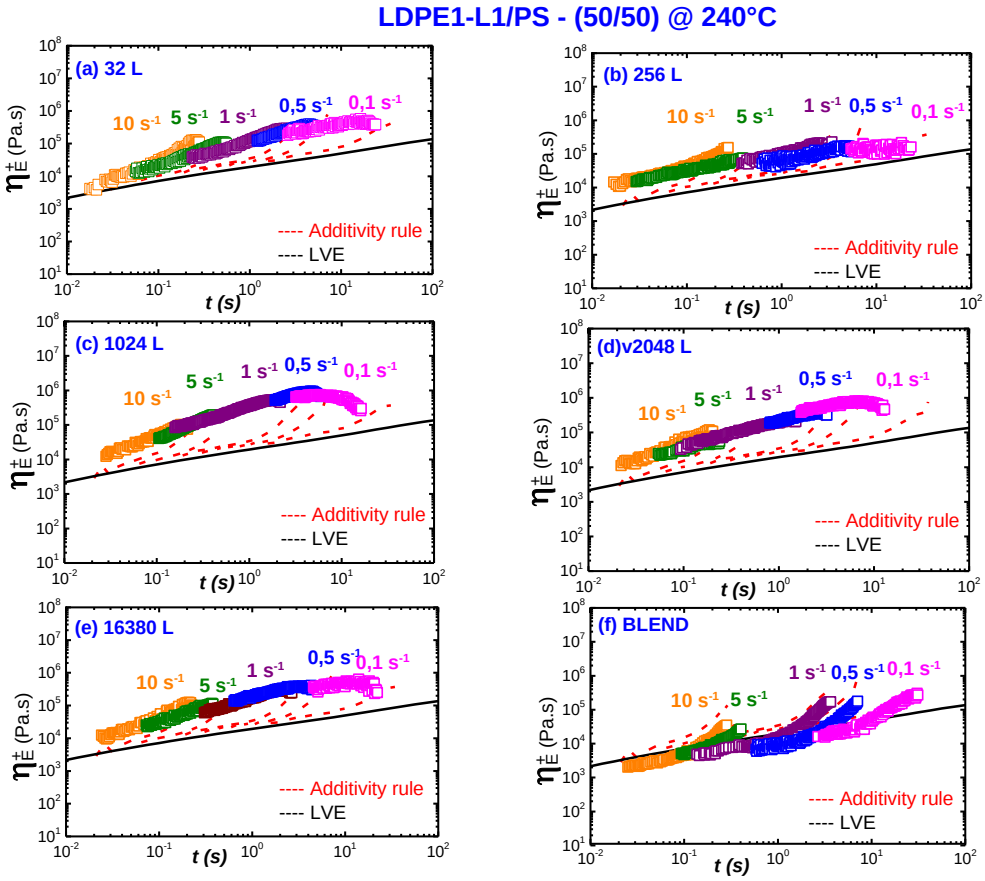

Figure 3.17 Extensional viscosity versus extension time at 240°C with extension rates varying from 0.1 to 10 s^{-1} for LDPE-L1/PS (50/50) multilayer films and their equivalent blend: (a) 32L, (b) 256L, (c) 1024L, (d) 2048L, (e) 16384L, and (f) blend. The dashed lines in (a) - (f) are predicted viscosities obtained by the additivity rule, and the solid lines are LVE predictions with the equilibrium equivalent LDPE-L1/PS (50/50) blend.

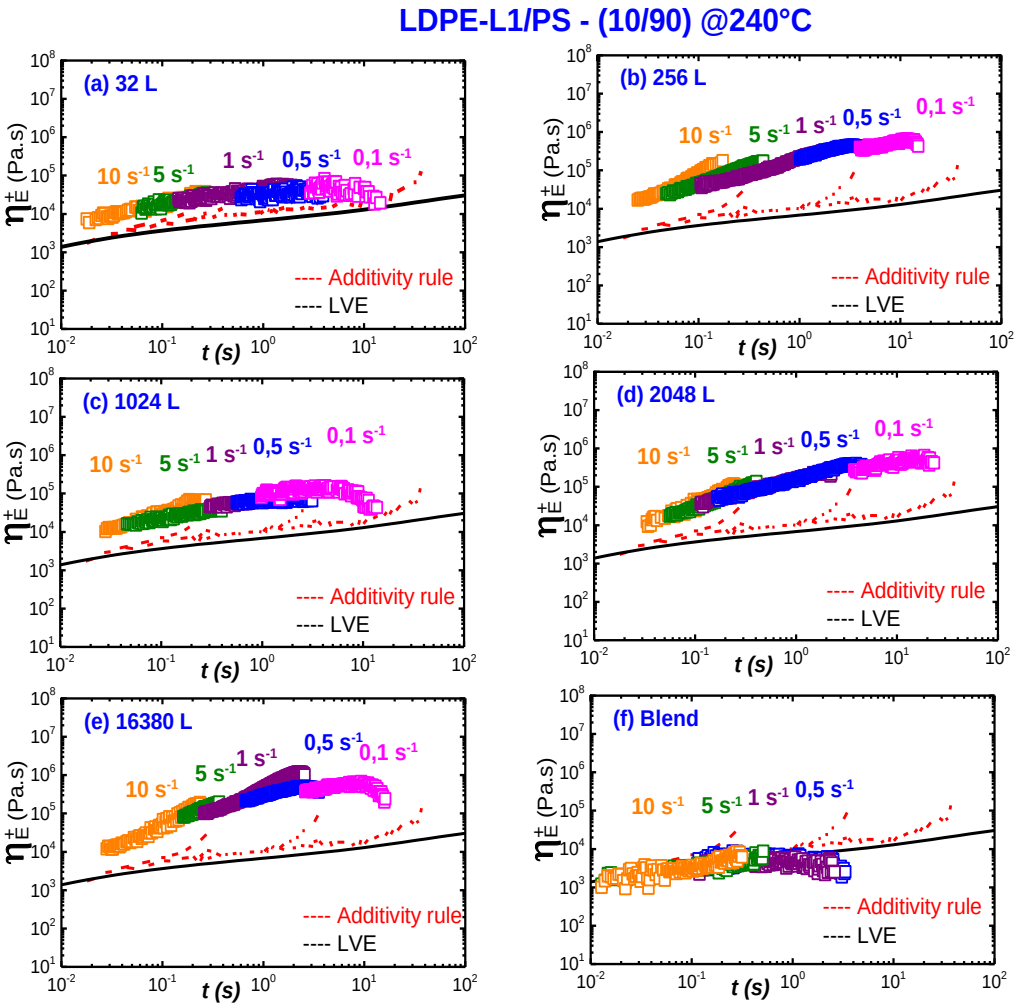

Figure 3.18 Extensional viscosity versus extension time at 240°C with extension rates varying from 0.1 to 10 s^{-1} for L1/PS (10/90) multilayer films and LDPE-L1/PS (10/90) blend: (a) 32L, (b) 256L, (c) 1024L, (d) 2048L, (e) 16384L, and (f) blend. The dashed lines in (a) - (f) are predicted viscosities obtained by the additivity rule, and the solid lines are LVE predictions with the equilibrium equivalent LDPE-L1/PS (10/90) blend.

3.4. Modelling the interfacial tension of immiscible systems

3.4.1. Palierne model

In order to predict the interfacial tension between dispersed phase LDPE and matrix (i.e., PS or PC), the Palierne rheological model was used. The SEM images of the LDPE-L1 droplets in the PC and PS matrix are shown in **Figure 3.19** to calculate the volume average droplet radius in a) LDPE-L1 /PC and b) LDPE-L1 /PS. The volume average diameter of the dispersed domains was calculated to be 3 μm and 7.7 μm for the LDPE-L1 /PS and LDPE-L1 /PC systems, respectively.

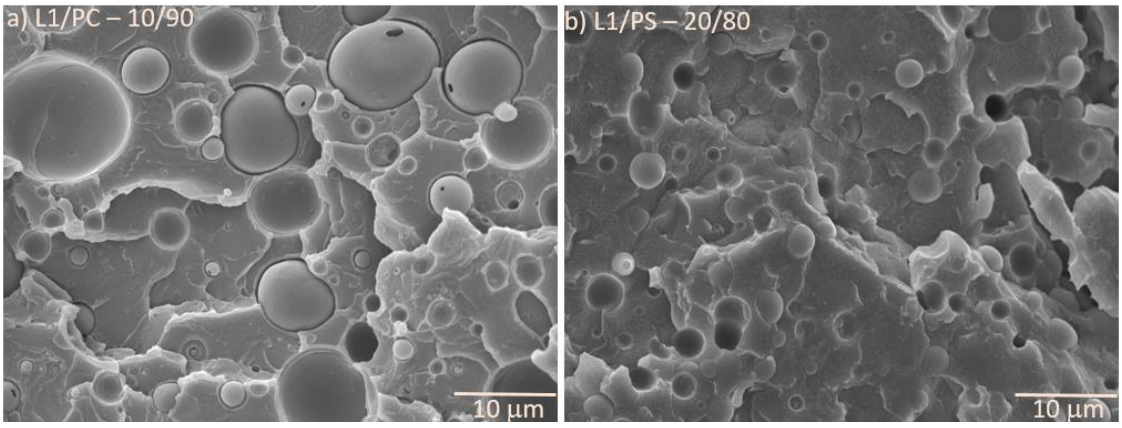

Figure 3.19 LDPE-L1 droplets in the PC and PS matrix imaged to determine volume average droplet radius in a) LDPE-L1 /PC and b) LDPE-L1 /PS.

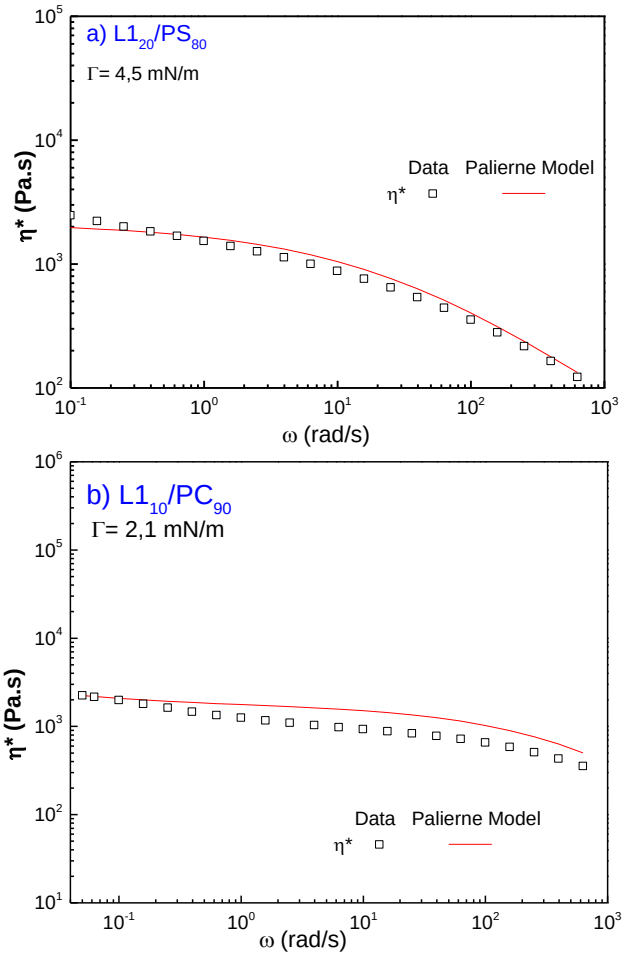

Figure 3.20 Experimental η* with the fitted Palierne model (solid lines) for L1/PS and L1/PC multilayers at 240 °C ,respectively

As illustrated in **Figure 3.20**, the η^* values predicted by the model agree very well with experimental data for LDPE-L1/PS and match less well with for LDPE-L1/PC. For the (20/80) LDPE-L1/PS blend the best fit of the model with the experimental data was achieved for Γ/R = 1500 Pa, while for (10/90) LDPE-L1/PC blend, the best fit was obtained for α/R = 270 Pa. A value of the interfacial tension equal to 4,5mN/m for L1/PS and 2,5mN/m for LDPE-L1/PC was obtained and is in good agreement with results observed in literature for the same systems[133][130][134].

3.4.2. Macosko model

To predict the tensile stress growth coefficient ($\eta^{+}_{E,M}$) against time, the Macosko model [124] was used. The evolution of the tensile stress growth coefficient versus time at constant Hencky strain rates of 0.1 s^{-1} and 10 s^{-1} is illustrated in **Figure 3.21** and **Figure 3.22** for LDPE-L1/PS multilayered structures with different numbers of layers ranging from 32 to 2048 layers and with the volume fraction of 10/90 for LDPE-L1/PS. It must be remembered that the selected multilayered LDPE-L1/PS structures present high viscosity and elasticity ratios and show relatively continuous, regular structures over the different numbers of layers. A model prediction of the stress growth coefficient for multilayer structures was given by the sum of each LDPE-L1, PS homopolymer, and interfacial contribution. The solid red line represents the model, and the green line depicts the interfacial contribution.

It can be observed that the low-density polyethylene L1 shows observable strain hardening, while the PS homopolymer does not produce any strain hardening. However, for multilayer films, a significant strain hardening is observed, at a Hencky strain deformation higher than 1 at 0.1 s^{-1} as a strain rate. This is due to the molecular structure of LDPE, which contains long-chain branches that promote strain hardening behavior, and it is less pronounced at a higher strain rate of 10 s^{-1}, as seen in **Figure 3.22**.

Moreover, for micro-layered films with fewer than 1024 layers (**Figure 3.21**), the Macosko model does not properly predict the experimental data and provides an unreasonable interfacial value. This is because for a weak number of interfaces, it is principally the bulk that is solicited. In contrast, as we increase the number of layers to 1024, the experimental data agree very closely with the prediction. These differences could be attributed to the number of interfaces, which means that the more we increase the number of interfaces the more the surface-to-volume fraction increases and systematically amplifies the interfacial contribution [124]. Then, we mainly solicit the interfaces/interphases formed for nanolayered structures. The value of the interfacial tension for 1024 layers is around 4 mN/m, in good agreement with the experimentally computed value of 4,5± mN/m using the Palierne model. Additionally, similar results are obtained when these same multilayer structures are stretched at a higher strain rate of 10 s^{-1}.

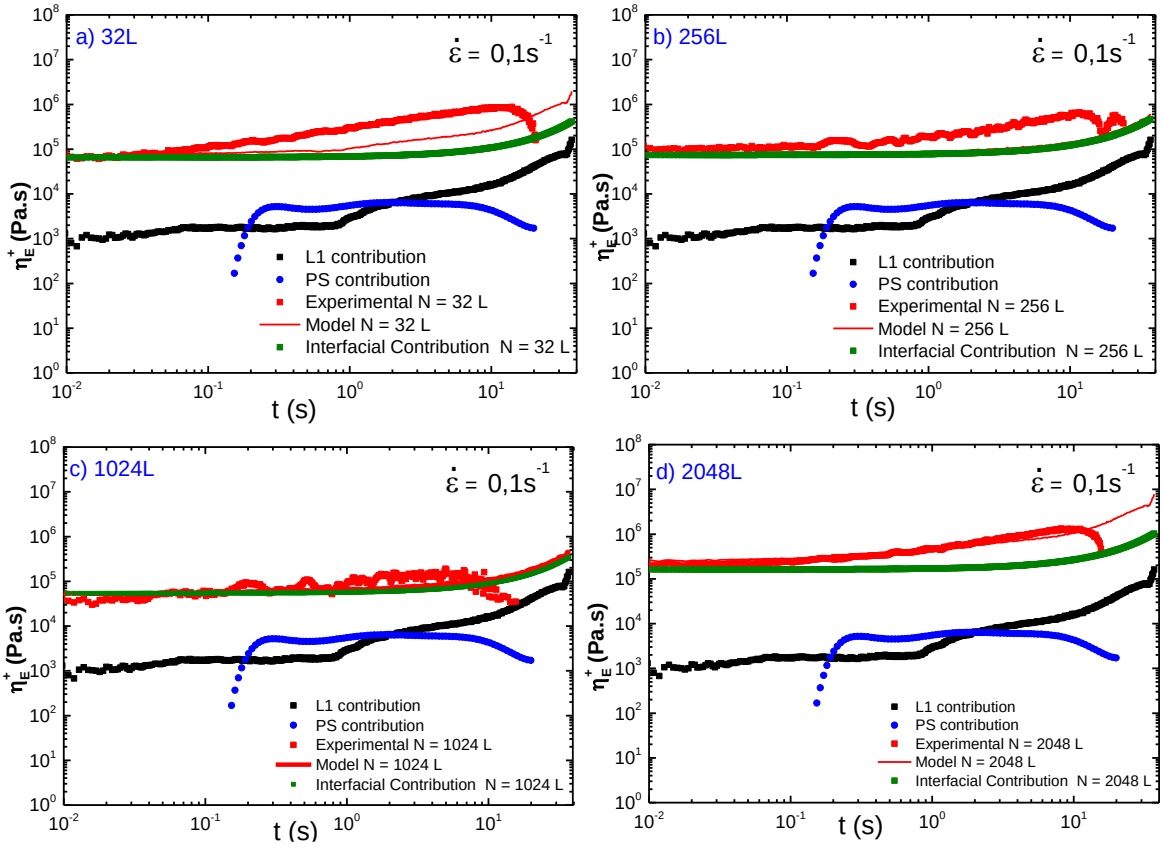

Figure 3.21 Contributions from L1 layers, PS layers, and interface summed to show the multilayer tensile stress growth coefficient predicted by Eq. (55) overlaid with experimental data at 0.1 s^{-1}.

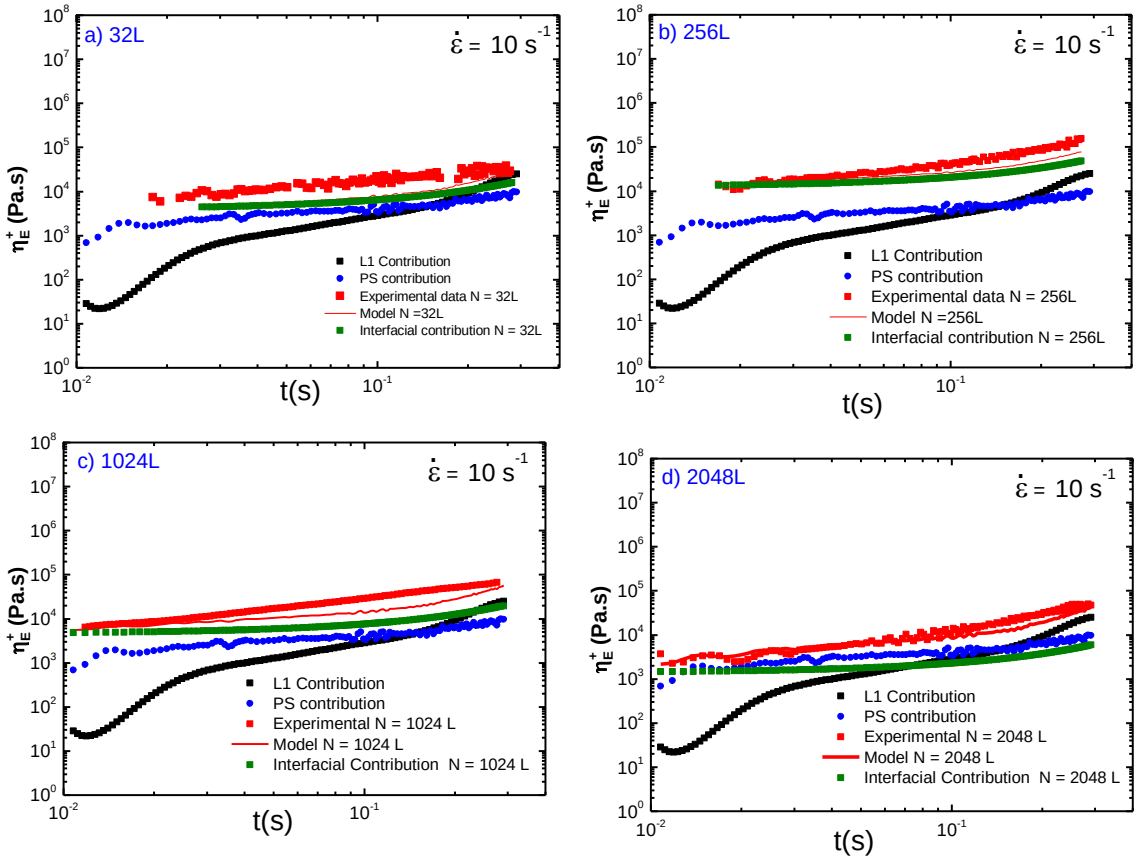

Figure 3.22 Contributions from L1 layers, PS layers, and interface summed to show the multilayer tensile stress growth coefficient predicted Eq. (55) overlaid with experimental data at 10 s^{-1}.

In addition, the same approach was applied to LDPE-L1/PC structures with the volume fraction of 10/90 to investigate the effect of the confining polymer on the contribution of interfacial tension and then compare it with the previous system, LDPE-L1/PS (see **Figure 3.23**). As a reminder, both systems have high viscosity and elasticity ratios in which the softening polymer (PC or PS) confines the strain hardening polyethylene. By changing the confining polymer to PC instead of PS, we hope to understand the effect of stratified flow on the interfacial stability when going from 32 to 2048 layers. We can clearly see that the experimental and predicted values are not in good agreement for micro-layered films with fewer than 1024 layers but match well for nanolayered films. This result corresponds well to previous studies of LDPE-L1/ PS in which the Macosko model fails to predict the interfacial tension for the micro layered films containing some interfaces. We speculate that

this might be due to the solicitation of the bulk for microlayered films, and as we increase the number of interfaces up to 1024, we mainly solicit the interface/interphases formed for nanolayered structures.

Therefore, it can be observed that the interfacial contribution plateau remains unchanged even when we continue to increase the number of layers and decrease their nominal thickness, which indicates that the interfacial contribution was less impacted by the confinement effect. Using the model described above the interfacial tension between PC and LDPE was found to be around 2.5 mN/m for 1024 and 2048 layers. This result shows good agreement with the one obtained with the Palierne model, which is 2.5 mN/m at 0.1 s^{-1}. The same trend was also observed for LDPE-L1/PC (10/90) at a higher strain rate of 10 s^{-1} , as shown in Figure 3.24.

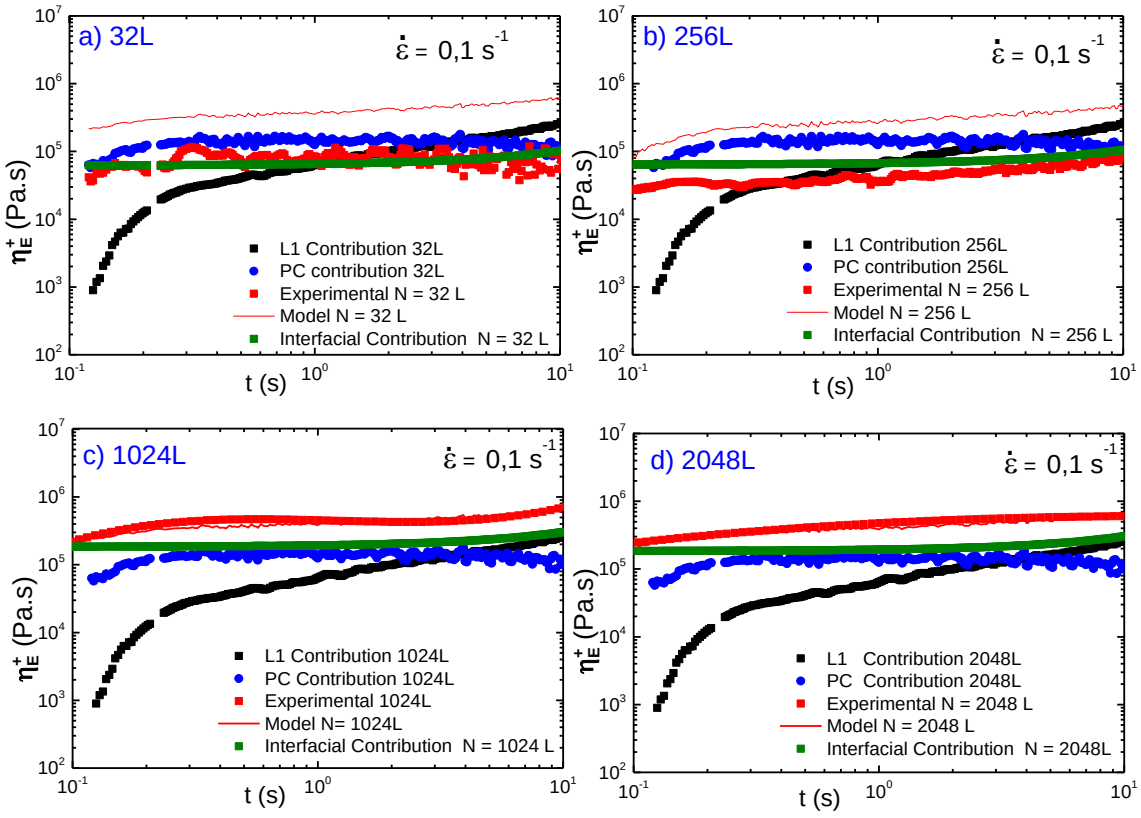

Figure 3.23 Contributions from L1 layers, PC layers, and interface summed to show the multilayer tensile stress growth coefficient predicted by Eq. (55) overlaid with experimental data at 0.1 s^{-1}.

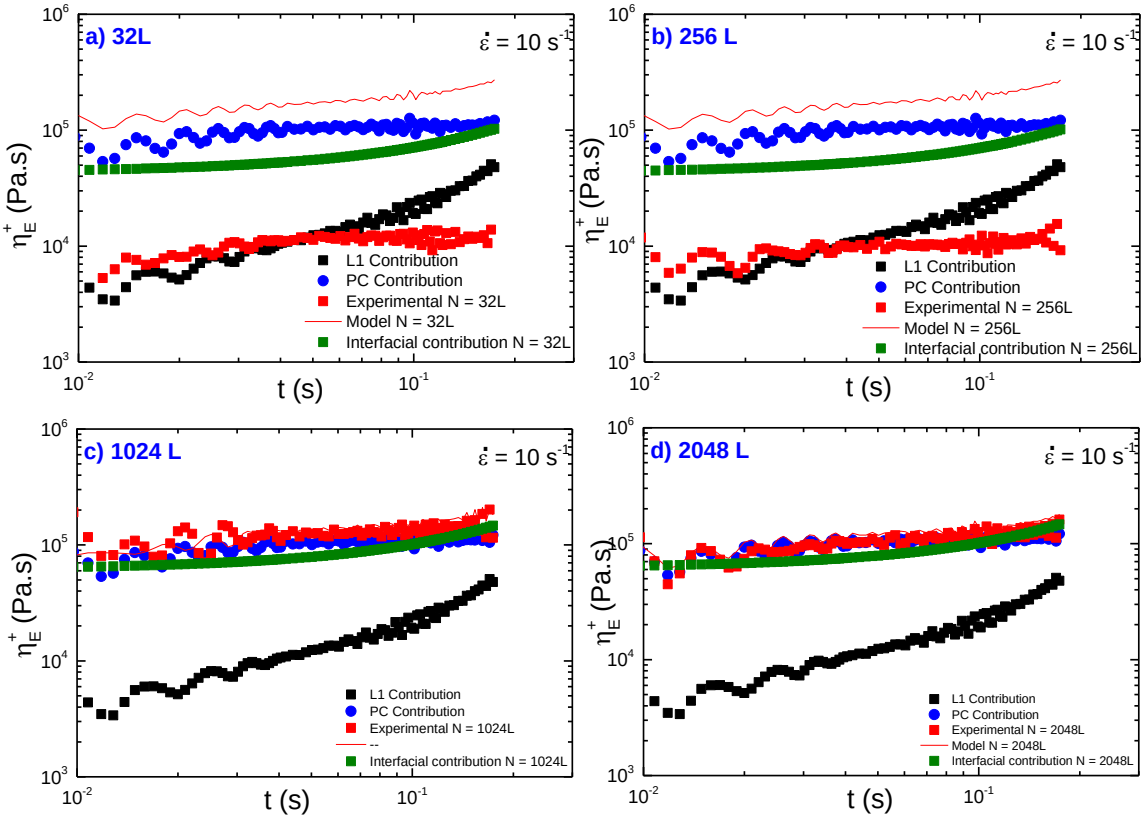

Figure 3.24 Contributions from L1 layers, PC layers, and interface summed to show the multilayer tensile stress growth coefficient predicted by Eq. (55) overlaid with experimental data at 10 s-1.

Figure 3.25 and **Figure 3.26** illustrate the extensional data for both immiscible systems at all three extension rates from 0.1 s^{-1} to 10 s^{-1}. It can be seen that the LDPE/PS exhibits strain hardening behavior over the strain rate range tested, and seems to be more dominated by the LDPE behavior. In contrast, no strain hardening is observed for the LDPE-L1/PC pair showing a strain-softening behavior, which seems to be more dominated by the PC behavior. However, the predicted tensile stress growth coefficients fail to describe 32 layered films for both LDPE/PC and LDPE/PS with significant upward deviation at all strain rates, possibly related to the number of interfaces and the extension rate. In contrast, the Macosko model accurately describes the 1024 layered films for both immiscible systems.

This result suggests that interfacial contribution depends on the extension rate, rises with a higher deformation rate, and significantly increases by increasing the number of layers.

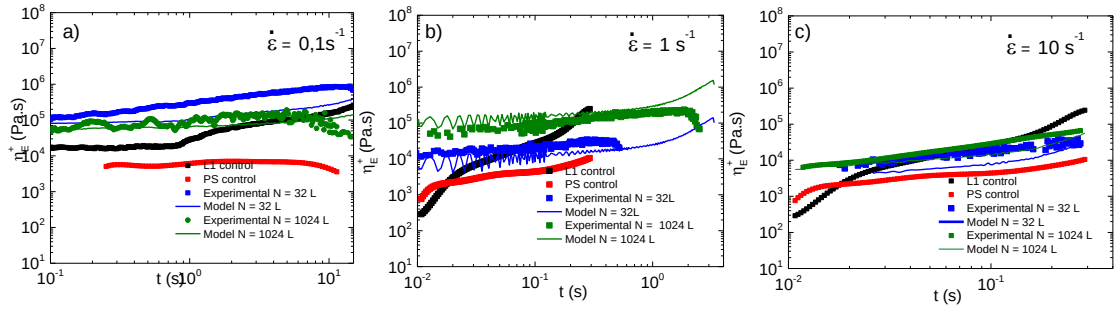

Figure 3.25 Tensile stress growth coefficients of LDPE-L1 (black squares) and PS (red circles) homopolymers, in addition to LDPE-L1/PS 32 layer and 1024 layer films coupled with solid lines representing model fitting at (a) 0.1 s^{-1}, (b) 1 s^{-1}, and (c) 10 s^{-1} strain rates.

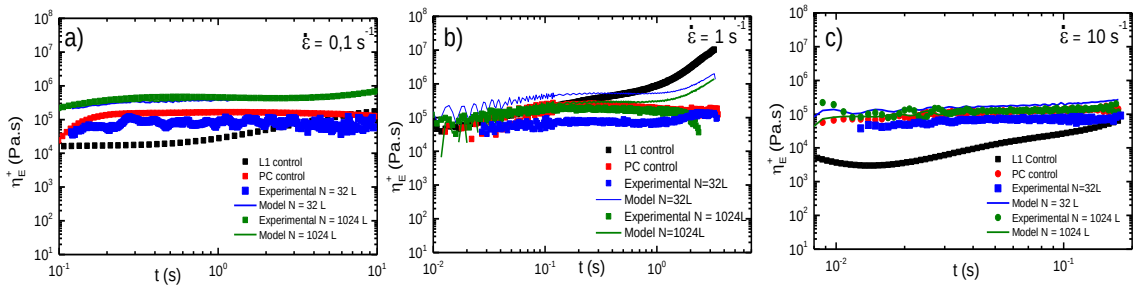

Figure 3.26 Tensile stress growth coefficients of LDPE-L1 (black squares) and PC (red circles) homopolymers, in addition to LDPE-L1/PC 32 layer and 1024 layer films coupled with solid lines representing model fitting at (a) 0.1 s^{-1}, (b) 1 s^{-1}, and (c) 10 s^{-1} strain rates.

Therefore, the Weissenberg number $W_i = \dot{\varepsilon}\lambda_i$ was determined for each homopolymer to indicate when chains get oriented into melt flow. From small amplitude oscillatory shear (SAOS) measurements, the relaxation time λ was determined by using the crossover modulus G' and G". The λ values of each homopolymer are recapitulated in **Table 3-7**. In the case of LDPE, the orientation of chains will occur for a strain rate higher than 3.9 s^{-1}, which means at $\dot{\varepsilon} = 10\ s^{-1}$ we will also have the effect of orientation and interfacial contribution.

Table 3-7 Relaxation time λ of each homopolymer.

Homopolymers	λ (s)	1/λ (s^{-1})
LDPE – L1	0.256	3.9
PS	0.01014074	98
PC	0.00147099	679

To understand the effect of interfacial contribution, we measure a parameter (Z) using the relation reported in Eq. (63) [135] for a different number of layers ranging from 32 up to 2048 layered films.

$$Z = \frac{\eta^{+}_{E,M}}{\left(\frac{\phi}{\phi+1}\right)\eta^{+}_{E,LDPE} + \left(\frac{1}{\phi+1}\right)\eta^{+}_{E,PS\ or\ PC}} \tag{62}$$

From **Figure 3.27**, the contribution of $\eta^{+}_{E,M}$ increases obviously when the z parameter is higher than unity. Moreover, it is worth noting that for a lower strain rate we obtain higher values of Z, and this was verified for all layered films. Our results are in agreement with the work of Macosko et al. [135]. Indeed, very similar results were obtained for lower strain at 10 s^{-1} and 1 s^{-1} and are independent of strain except for 1 s^{-1} when the strain approaches 3, with a significant increase of z-values being observed. This indicates that we have the effect of orientation in addition to the interfacial contribution. From Eq. (63), we deduce that the more we decrease the strain rate, the more we amplify the interfacial contribution.

$$\sigma^{+}_{E,i} = \dot{\varepsilon}\,\eta^{+}_{E,i} \tag{63}$$

$$z = \frac{\sigma^{+}_{E,M}}{\dot{\varepsilon}\,\left[\left(\frac{\phi}{\phi+1}\right)\eta^{+}_{E,LDPE} + \left(\frac{1}{\phi+1}\right)\eta^{+}_{E,PS\ or\ PC}\right]} \tag{64}$$

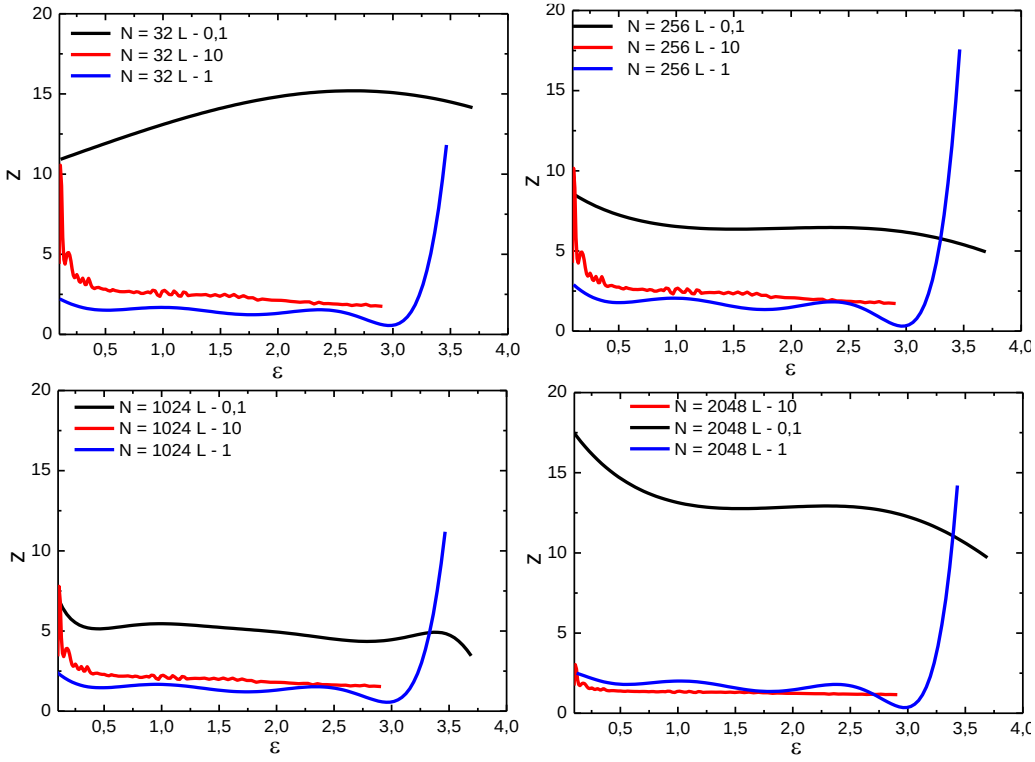

Figure 3.27 Dimensionless Z-value vs dimensionless strain for LDPE-L1/PS multilayers from 32 layers to 2048 layers at 0.1 s^{-1}, 1 s^{-1} and 10 s^{-1} strain rates.

Moving now for the LDPE-L1/PC pair and keeping the same composition of 10/90 (see **Figure 3.28**). It can be observed that the interfacial contribution is independent of strain.

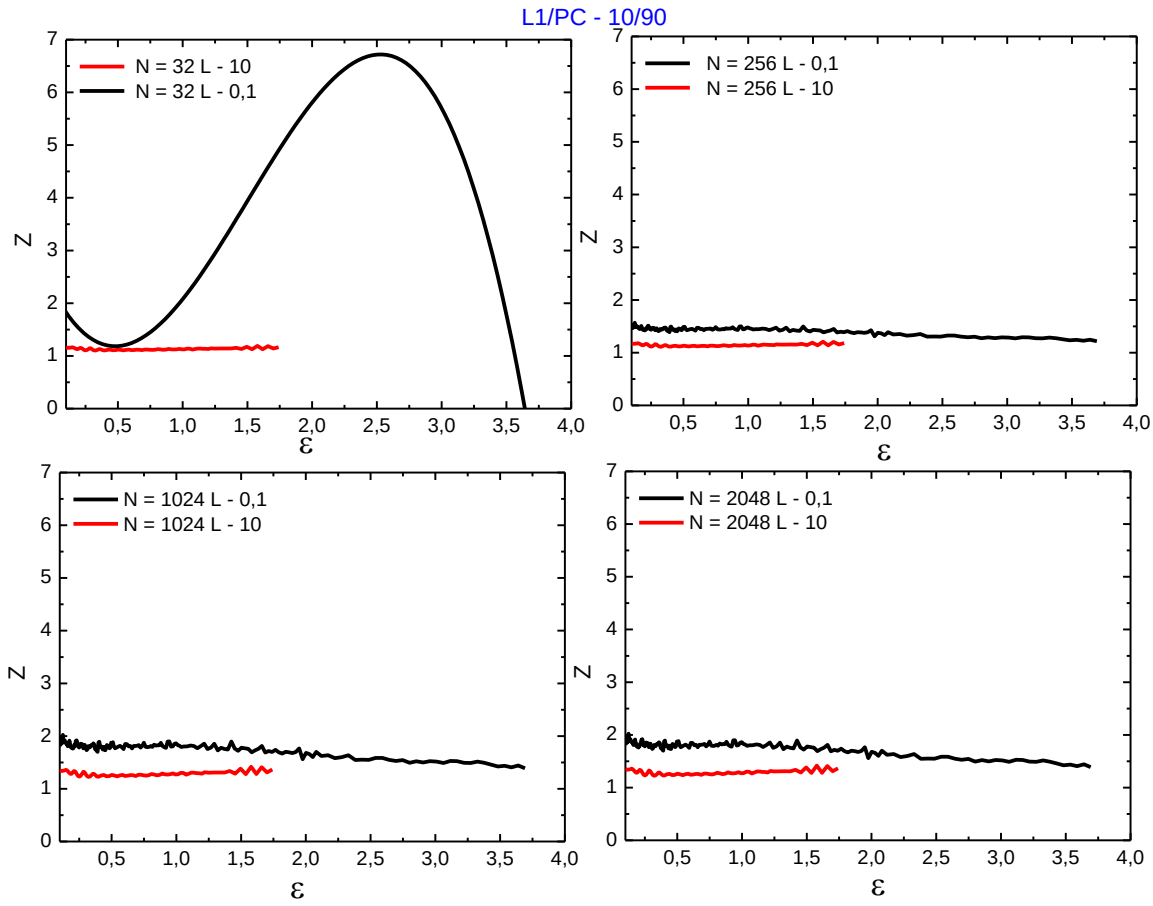

Figure 3.28 Dimensionless Z-value vs dimensionless strain for LDPE-L1/PC multilayers at 0.1 s^{-1} and 10 s^{-1} strain rates.

The results presented in **Figure 3.29** suggest that for micro layered films containing few interfaces, unreasonable values of interfacial tension are obtained from fitting the model to the experimental data, and the more we increase the number of interfaces using multipliers, the more logical a value of interfacial tension is achieved, thus corroborating the values found in the literature (4.5 mN/m for LDPE-L1/PS pair and 2.5 mN/m for LDPE-L1/PC).

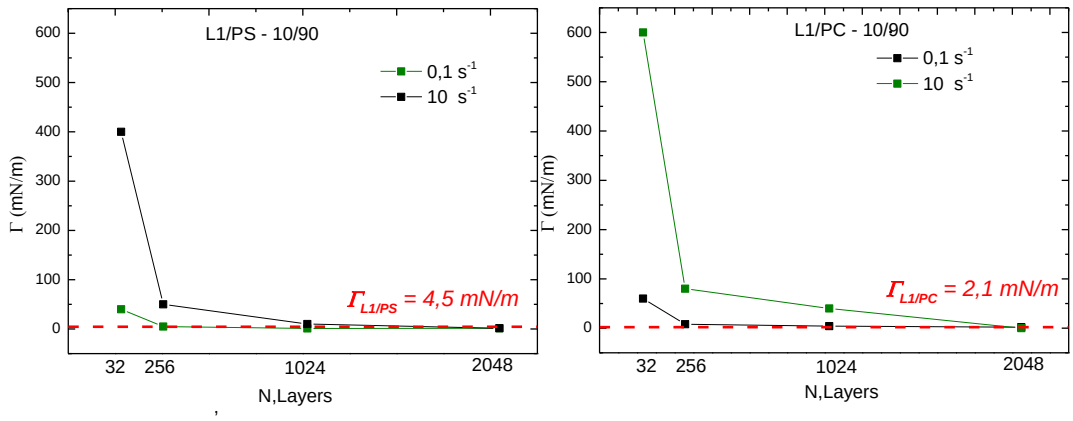

Figure 3.29 The fitted interfacial tension value obtained from the model versus the number of layers for the LDPE-L1/PS and LDPE-L1/PC pairs.

4. Conclusion

In the work reported here, we aim to understand the role of interfacial polymer physics and the triggered interfaces/interphases in shear and extensional rheology, as well as polymer processing. The three systems chosen in this work varied from a partially miscible system (LDPE-L1/LLDPE-LL2) to immiscible system (LDPE-L1/PC and LDPE-L1/PS).

This chapter is structured as follows:

Initially, the rheological properties of each sample were studied in the linear viscoelastic regime in order to choose the appropriate parameters to fabricate films under the most stable conditions. The melt viscosity and/or elasticity ratio between the components at different temperatures were then obtained to understand the flow during coextrusion despite their high mismatched viscoelastic properties. The viscosity ratio of immiscible pairs is around 2 for LDPE-L1/PS and a value of 0.6 for LDPE-L1/PC. However, the elasticity ratio of the LDPE-L1/PC system reached a value of 8.6, which was greater than the value found in the LDPE-L1/PS (2.6) system in the shear rate range of multipliers (1-10 s^{-1}). The rheological tool is important for determining the layer structure and uniformity of the multilayer polymer structure.

Second, various nanostructured multilayer structures with relatively stable flow and layered architecture were elaborated. The contact time between neighboring layers and the theoretical thickness of these multilayered structures were obtained to quantitatively characterize the polymer-polymer adhesion and to keep the interface stable throughout the coextrusion process. As we increase the number of layers through the coextrusion process, a new interface is produced, resulting in a longer melt contact time and a thinner layer in the order of several nanometers for nanolayered structures. Then, their shear and extensional rheological properties were investigated. Small amplitude oscillatory shear data were fitted with the Palierne model to determine the interfacial tension of the matrix/droplet blends of each of the pairs. The chains in the N-1 interfaces/interphases were disentangled during shear deformation, resulting in a decrease in total shear viscosity, which is taken as a direct sign of interfacial slip velocity and, thus, agrees with our previous investigations. The

evaluation of interfacial properties is essential for establishing the structure-dynamics-property relationship.

Under extensional flows, the LDPE-L1/LLDPE-LL2 and LDPE-L1/PS multilayers exhibited an increased transient extensional viscosity and pronounced strain hardening. In contrast to the LDPE-L1/PC multilayered films, no strain hardening behavior was observed. This behavior was anticipated using a Macosko model, which is based on force summation and interfacial tension as a fitting parameter. The estimated interfacial tension was compared to those obtained from emulsion model like Palierne with the equivalent blends. The main challenge is to check the validation of this recent model with high mismatched viscoelastic polymers.

According to our modeling from Palierne and Macosko model, the interfacial tension between the LDPE-L1 and the PS is on the order of 4.5 mN/m, and around 2.5 mN/m for LDPE-L1/PC. The estimated interfacial tensions with Palierne corroborate those of Macosko model.

Chapter 4. Structure-morphology processing properties relationships of multi micro-/nanolayered polymers

1. Introduction

The layer-multiplying coextrusion technology has attracted more interest in the last decade, this new technology allows us to discover a new world that goes from microscale to nanoscale structure and achieve new properties. When the layer thickness goes to the nanoscale, the crystalline morphology changed from spherulite (3D) to truncated spherulites (2D) and to a highly oriented lamellar morphology (1D) [19]. This change in crystalline morphology will impact the properties of the multilayer films. The main context of the present chapter is to get a better understanding of the effect of confinement on the structural and morphological properties in their multi-layered systems fabricated by the forced-assembly multilayer coextrusion process. Various micro to nano-structured multilayer structures with stable flow and layered architecture were elaborated in the previous chapter. The main focus is to demonstrate that there is a processing window to fabricate a well architectured and continuous mismatched rheological LDPE-L1/(PS or PC) systems. The obtained multilayers were characterized through various techniques such as wide X-ray scattering (WAXS) and electron microscopy (SEM, TEM…).

2. Experimental

2.1. Materials and sample preparation

The same materials as in the previous chapter were be utilized in this chapter, the properties of each material, including LDPE-L1, LLDPE-LL2, PC, and PS, are listed in Table 3-1 (Chapter 3).

2.2. Morphological properties

2.2.1. Scanning electron microscopy

The morphology of the multilayered LDPE-L1/PC and LDPE-L1/PS films was observed by scanning electron microscopy (SEM) using an FEI QUANTA 250 FEG microscope in high-vacuum mode. The samples were stained by ruthenium tetraoxide vapor (RuO_4) for two days and then placed between two epoxy resin plaques until consolidation. The samples were sectioned normal to extrusion direction via a cryo-ultramicrotome (LEICA EM UC7) at room temperature using a diamond knife. To have sufficient contrast, it is important not to exceed 1 to 2 µm of cut. It is noted that for the SEM observation we imaged the remaining blocks of samples, while for TEM it is necessary to obtain ultrathin sections.

2.2.2. Transmission electron microscopy (TEM)

The morphology of the LDPE-L1/PS multilayer film was also characterized by transmission electron microscopy (TEM). Extremely thin sections of about 80 nm were microtomed from specimens perpendicular to the extrusion direction using an ultramicrotome.

2.2.3. Atomic force microscopy (AFM)

Atomic force microscopy (AFM, Multimode 8, Bruker) was used to analyze the layered structure in the LDPE-L1/PS multilayer films. The measurements were performed under ambient conditions. The tapping mode was executed at a scan rate of 0.5 Hz with uncoated silicon probes. A smooth, flat cross-section of the film was obtained by cryo ultramicrotomy at room temperature. Layer continuity and uniformity of the films were characterized. Phase and height images of the cross-sections were recorded [2].

2.2.4. X-ray characterizations

An Oxford Diffraction Gemini A Ultra diffractometer equipped with a molybdenum (Mo) source, as well as a high-intensity, Enhance Ultra Cu X-ray (Cu K) source was used to analyze the crystal structure of multilayered films. These measurements were carried out at the Henri Longchambon diffractometry center in Lyon. A small portion of multilayer films was examined in all three orientations after being placed on a sample holder (perpendicular, transverse, and in the direction of flow). The diffractometers are equipped with a CCD camera and controlled by CrysAlisPro software. The measurements were performed under a continuous nitrogen flow and at constant temperature.

3. Results and discussion

3.1. Architecture and morphology of coextruded multi-miro/nanolayers

3.1.1. Stability map analysis

Owing the notes of films quality given during coextrusion, stability maps for all coextruded films with stable and unstable domains were constructed (see **Figure 4.1**) The appearance of the films is shown schematically according to the ratio of viscosity against volumetric flows of 50/50 at 240°C. For the partially miscible LDPE-L1/LLDPE-LL2 pair, the films obtained were stable, and no defects or instability were observed regardless of the number of layers. On the other hand, for an immiscible system such as LDPE-L1/PS, the viscosity and elasticity ratio are around 2 and 3 at ω=10 rad/s (Table 3-5). The resulting films appear to be more stable, especially for a number of microlayers going from 32 layers to 1024 layers. In contrast, as we increase the number of layers up to 16380, some defects appear in the film. For the LDPE-L1/PC system with a viscosity ratio of 0.6 and an elasticity ratio below 9, the films obtained seem to be relatively stable for a number of micrometric layers lower than 256L. As the number of layers increases to 16380, however, severe instability is observed, along with somewhat chaotic interfacial defects. To conclude, the LDPE-L1/PS system is more stable than the LDPE-L1/PC system. This is possibly due to the elasticity ratio of LDPE-L1/PS, which is lower than that of L1/PC and which may improve the interfacial stability of coextrusion. It is important to note that in both immiscible systems (LDPE-L1/PS and LDPE-L1/PC), delamination was possible only for a low number of layers (i.e multi-microlayers) because of insufficient adhesion. between the layers.

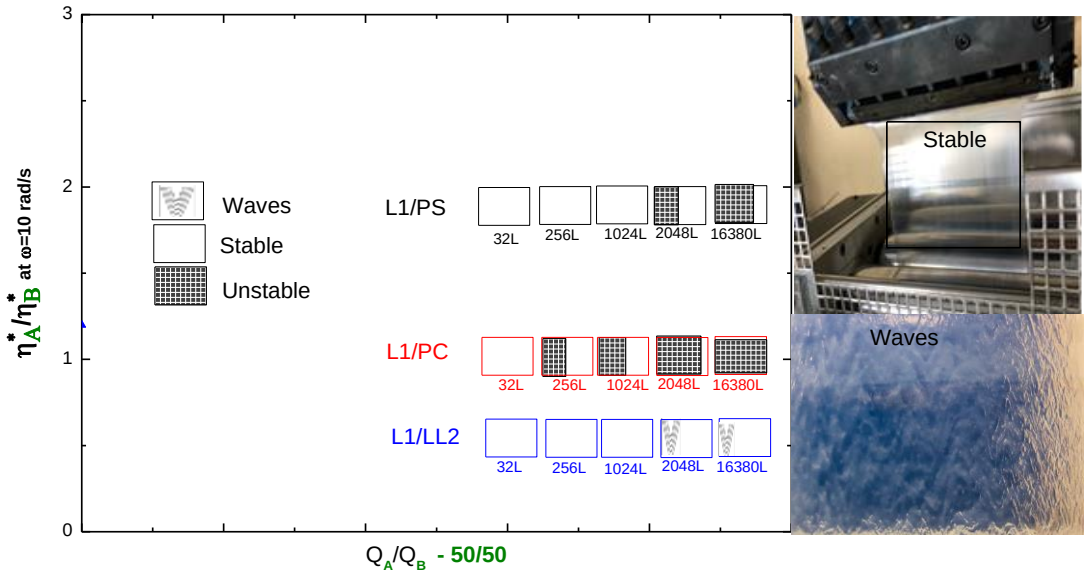

Figure 4.1 Chart of stability/instability observed experimentally for different couples of coextruded films with the plot of viscosity ratios at ω=10 rad/s versus composition using a reference temperature of 240°C.

3.1.2. Transparency of the coextruded multi-micro/nanolayered films

Different photographs of the coextruded LDPE-L1/PS and LDPE-L1/PC films were taken as a function of the number of layers to highlight the transparency and homogeneity of the films, as depicted in **Figure 4.2.** The multilayer films are viewed as transparent films, and this transparency was maintained whatever the architecture and number of layers. Interestingly, the transparency seems to be more important with multi-nanolayered films keeping flexible quality of the final structures despite the association of rigid confined polymers with LDPE-L1.

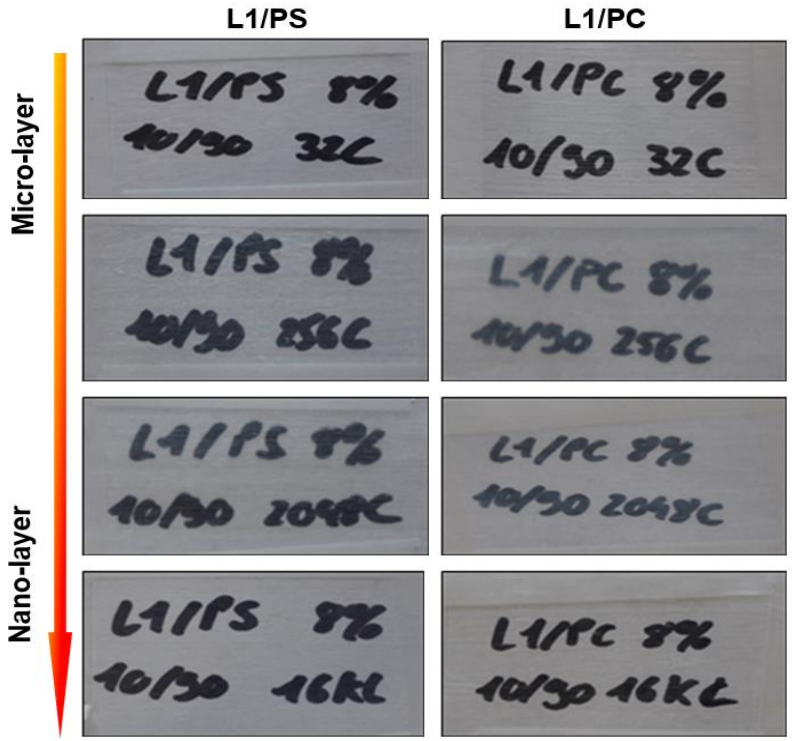

Figure 4.2 Photographs of the coextruded LDPE-L1/PS and LDPE-L1/PC films to highlight their transparency.

3.1.3. Layer architecture/structure

In this section, PS and PC are used to confine the semicrystalline LDPE-L1 layers from the microscale to the nanoscale in order to study the effect of the number of layers on the multilayered film morphologies**. Figure 4.3** and **Figure 4.4** show the SEM micrographs of the multilayer LDPE-L1 /PS and LDPE-L1 /PC mismatched systems with a volume fraction of 50/50 and an identical total thickness of ± 200 μm. Here, the low-density polyethylene (LDPE-L1) layers are grey, and the polycarbonate (PC) and the polystyrene appear darker than the LDPE phase. This good contrast is due to the use of different staining between LDPE-L1, PC, and PS by utilizing ruthenium tetroxide (RuO_4), which can promote the visualization of the internal structure. Note that scanning electron microscopy technology (SEM) allows us to examine a wide area in a short time. The larger the area, the more the structure found is representative of the entire sample. Additionally and at the opposite of some literature, only small areas can be imaged with TEM or AFM, so there is a risk that

typical structures cannot be imaged [68]. Depending on the system studied, the multilayer films can have a continuous, uniform layered structure.

As imaged by SEM (see **Figure 4.3**), uniform and continuous LDPE-L1 and PS layers are clearly seen, with sharp interfaces and continuous structure for films ranging from 32 to 1024 layers. However, as the layer thickness decreases from microscale to nanoscale, some layers remain continuous and some layers begin, in places, to break up into nanosheets and nanodroplets (i.e., 2048L, **Figure 4.3 (d)**). The onset of the breakup layer in the LDPE-L1 /PS system was determined in 2048L with nominal thicknesses of 95 nm (**Table 3-4**), which is slightly around the gyration radius of the studies polymers.

In **Figure 4.4 (a),** for the micro-layered 32L film, it can be seen that all of the LDPE-L1 and PC layers are clearly distinguished and continuous, and the thickness of the layers is noticeably irregular. The layer thickness measured differs from the actual layer thickness (**Table 3-4**). When the number of layers is increased to 256L (h_N=1μm) (**Figure 4.4 (b))**, the film is divided into two areas, one with continuous layers and the other with break-up layers. It is also worth noting that compared with the 2048L and 16380L LDPE-L1 /PS films, the layers of LDPE-L1 and PC can no longer be distinguished.

The breakup behavior of the LDPE-L1 /PS system was different from that of the LDPE-L1 /PC system. Note that the elasticity ratio of the LDPE-L1 /PC system reached a value of 9 at ω=10 rad/s, which was greater than that of the LDPE-L1 /PS system, with a value around 3 in the shear rate range of the multipliers (1-10 s^{-1}). Viscoelastic mismatched properties between the polymers may be the reason for the nonuniformity across the layers, contrary to the LDPE-L1 /PS system, which displayed stable and continuous layers despite to not matched viscoelastic properties but lower elastic ratio. The LDPE-L1 /PC films with a composition of 50/50 have more defects than the LDPE-L1 /PS.

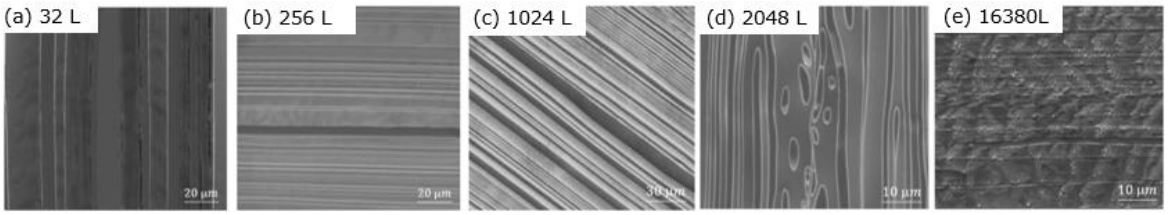

Figure 4.3 SEM micrographs of the multilayer LDPE-L1/PS system ranging from 32L to 16380L.

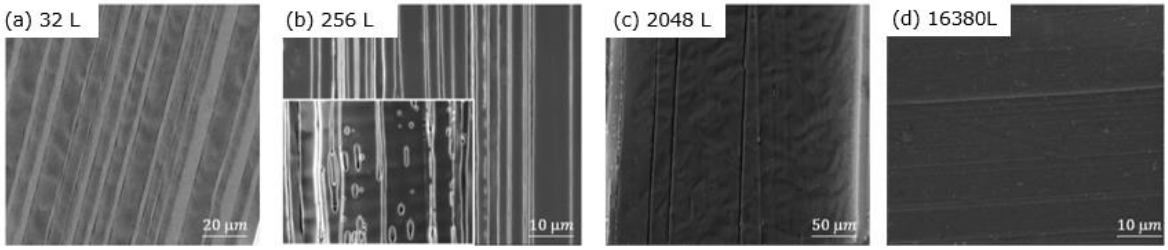

Figure 4.4 SEM micrographs of the multilayer LDPE-L1/PC system.

Figure 4.5 and **Figure 4.6** shows morphology features imaged by a TEM microscope in the multilayered LDPE-L1/PS films with the number of layers 2048L and 16380L, respectively. Clearly, these multilayered films are mostly continuous, with more or less uniform thickness and some local areas with interfacial distortions such as layer breakup and droplet formation. We can also see that the interface area between LDPE-L1 and PS is visibly sharp.

Our findings reveal that for the LDPE-L1/PS system, lamellar morphologies are still observed in films with a higher number of layers and a nominal layer thickness of 95 nm (i.e., 2048-layer film) with only some layers that tend to split into droplets, keeping the other areas uniform and interfaces sharp and clear. It is assumed that this is related to the interfacial contribution that dominates the flow. According to the literature and our modelling in the previous chapter, the interfacial tension between the LDPE-L1 and the PS is of the order of 4.5 mN/m, which makes it possible to stabilize the flow up to a certain critical number of layers. In other words, the capillary forces (interfacial force) outweigh the elastic forces and subsequently make it possible to stabilize the nanometric layers. In contrast, the interfacial tension of LDPE-L1/PC is around 2.5 mN/m, which is significantly lower than that of LDPE-L1/PS, implying that volume contribution will dominate the flow

and outweighs the interfacial contribution. Thermodynamically, the interphase thickness developed at this case seems be lower than the case of LDPE-L1 /PS system. By increasing the number of layers, the nanolayered system become more dominated by the interfaces/interphases created since the nominal layer thickness decrease drastically at less the gyration radius. As a result, the layers break up into small droplets to stabilize those interfaces. Owing their high viscoelastic mismatched properties, and depending on the immiscible system chosen, and on the critical thickness reached generally for nanometric thicknesses, the rate of breakup increases dramatically. Furthermore, crystallization properties in LDPE-L1 changes from micro to nanolayers which make the stabilization mechanisms more complex. Hereto, we have demonstrated that it is possible to prepare some nanolayer structures with 16380-PS/LDPE-L1 (**Figure 4.6**) systems despite their high mismatched properties. We demonstrated also that lower elastic contrast is a key to stabilize their flow structure in nanolayered systems.

Instead, the LDPE-L1 crystals appear as bright stripes and tend to be organized into flattened spherulites (2D) (see **Figure 4.5(e)** and **Figure 4.6(b**)). It should be recalled that the LDPE-L1 layer thickness is about 100 nm, which is significantly less than the dimension of the LDPE spherulites (100 μm). It is assumed that as the number of layers increases, the spherulites transform from 3D spherulites to somewhat compressed 2D spherulites, or even to strongly oriented lamellae arranged unidirectionally (1D). This hypothesis will be investigated in the next section by analyzing the crystalline structure of LDPE-L1.

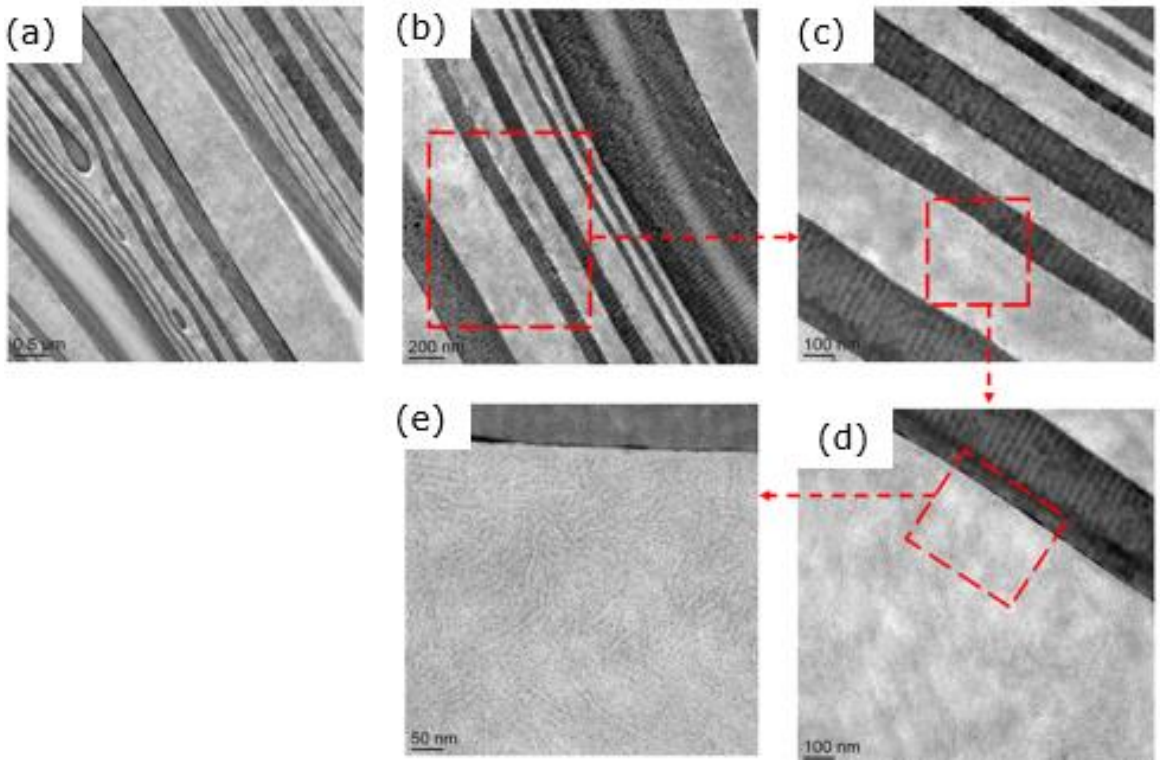

Figure 4.5 TEM micrographs of 2048 LDPE-L1/PS multilayered structures.

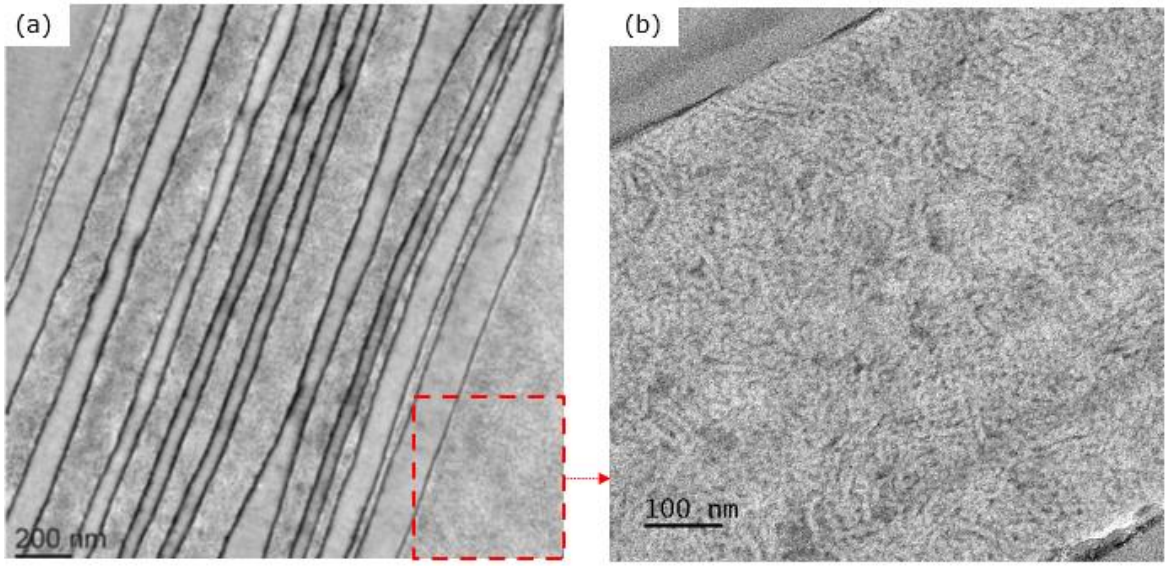

Figure 4.6 TEM micrographs of 16380 LDPE-L1/PS multilayered structures. Crystalline and homogeneous structure is highlighted from left to right.

This concern will be further verified by the following AFM investigations to provide additional evidence of the crystalline lamellae develop in the LDPE-L1/PS 1024 and 16380

multilayered materials. It can be observed in **Figure 4.7** and **Figure 4.8** that the LDPE-L1 and PS layers are continuous and parallel among all AFM images. According to MEB, TEM, and AFM findings, some nanolayer structures can be created with PS/LDPE-L1 systems despite their mismatched properties.

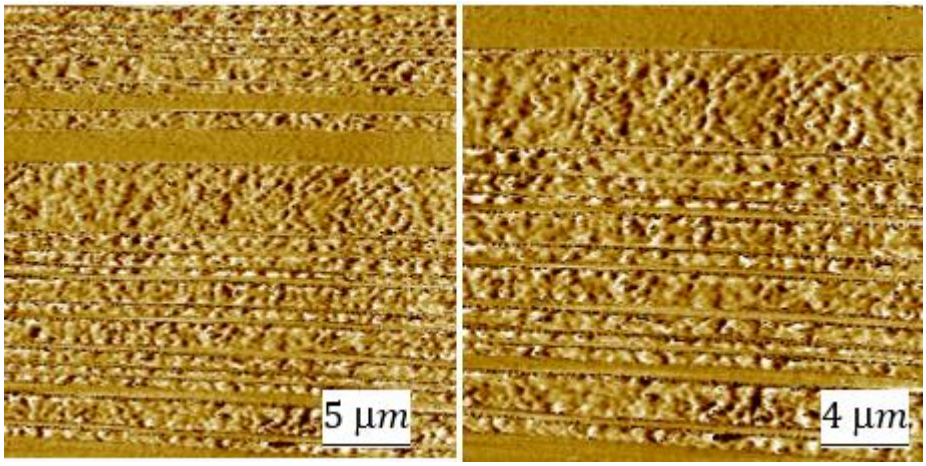

Figure 4.7 Extruded-direction AFM phase morphologies of 1024 layer LDPE-L1/PS as-extruded film. The light color phase in the **figure** is PS and the dark color phase is the LDPE-L1.

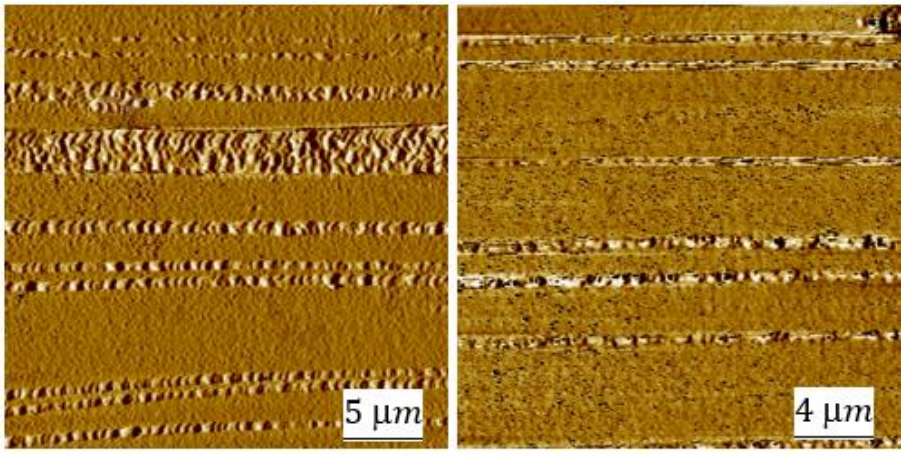

Figure 4.8 AFM micrographs showing the flow direction of 16380L layer LDPE-L1/PS as-extruded film.

3.1.4. Crystalline structure

The orientation and crystalline structure of LDPE-L1 in multilayered LDPE-L1/(PS and PC) films were characterized by the 2D-WAXS patterns with an X-ray incident beam in the extruded (ED) and normal (ND) directions to the film plane (see Figure 4.9 and **Figure 4.10)**. The LDPE-L1 control exhibit two isotropic rings (Figure 4.9 **(e**)). The first ring at (2θ =21.33°) and the second ring at (2θ =23.66°), corresponding to (110) and (200) from the orthorhombic crystal structure of polyethylene [18], which implied that the LDPE-L1 lamellae were randomly oriented [136]. Figure 4.11 depict the 1D profiles for coextruded LDPE-L1/PS, and LDPE-L1/PC multilayers, respectively. In all multilayer films prepared, the reflections from the (110) and (200) planes were visible in the 1D profile superposed with the wide amorphous halo of PS (**Figure 4.11 (a**)), and the amorphous halo of PC (Figure 4.11 **(b**)).

It can be seen from **Figure 4.9 a-d**, that the (110) plane appeared as an isotropic ring in the ED direction for all multilayers with only a slight equatorial concentration in the 16380L-ND direction. This suggests that the LDPE-L1 chains were slightly oriented in the extrusion direction [137]. For the 16380 layered films **(Figure 4.9 (d**)), a strong equatorial concentration of the (200) plane was observed in ED direction. This orientation was attributed to the effect of the geometric constraint from the nanoscale confinement caused by the glassy PS on the melt flow. It is assumed that by increasing the number of layers from 32 to 16380L or decreasing the individual LDPE-L1 thickness from 5 μm to 12 nm, the LDPE-L1 spherulites transform from (3D) to flattened (2D) spherulites, and then to stacked in-plane lamellae. This finding was consistent with the TEM result (**Figure 4.5(e)** and **Figure 4.6(b))**.

However, for the coextruded LDPE-L1/PC films an amorphous halo with no distinctive reflection rings is shown in **Figure 4.10.(a-c**). This is confirmed by the 1D profile. The rigid PC segments (Tg=150°C) impede the molecular mobility of LDPE-L1 segments during crystallization and consequently suppress the crystallization process of LDPE-L1, resulting in an amorphous film. This concern will be further verified by DSC.

To sum, the confinement effect of LDPE-L1 chains against amorphous PS in the extruded (ED) direction gives rise to an in-plane orientation, in which the LDPE crystals are set

perpendicular to the film plane, whereas in the normal direction (ND) the in-plane oriented chains are stretched and extended along the equator during the coextrusion process.

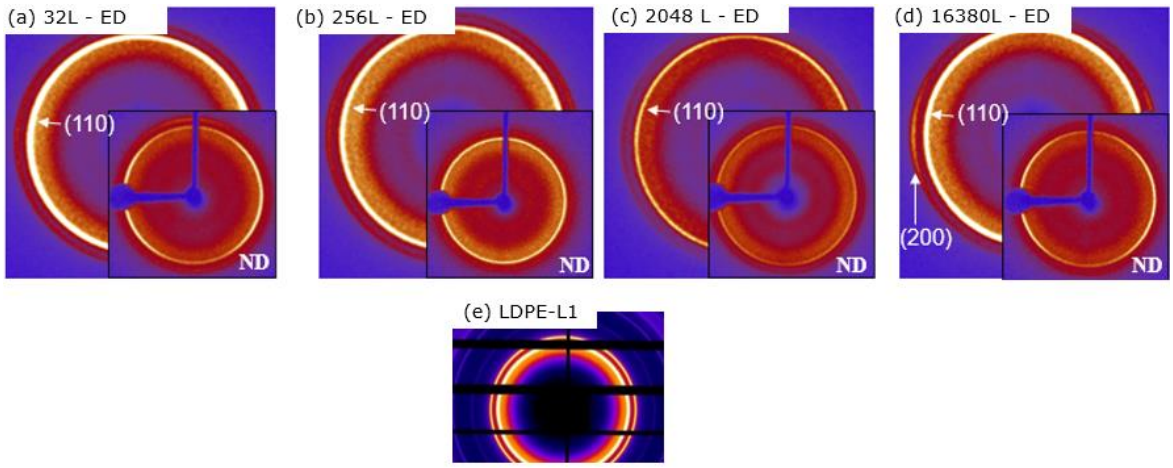

Figure 4.9 2D-WAXS profiles recorded with an X-ray beam in the extruded and normal directions to the film plane for neat LDPE-L1 and LDPE-L1/PS multilayers: a) 32L, b) 256L, c) 2048L, d) 16380L, and e) LDPE-L1 control.

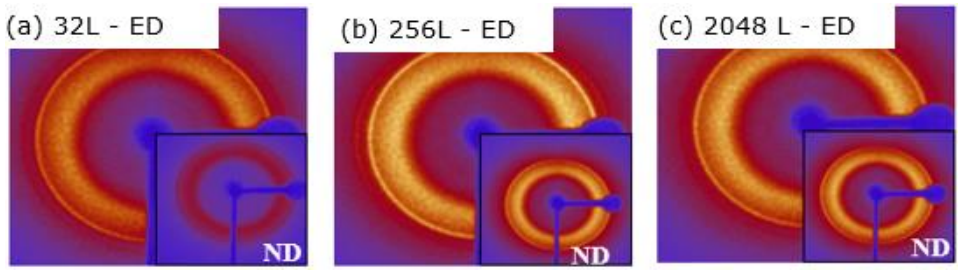

Figure 4.10 2D-WAXS profiles recorded with an X-ray beam in the extruded and normal directions to the film plane for LDPE-L1/PC multilayers: a) 32L, b) 256L, and c) 2048L.

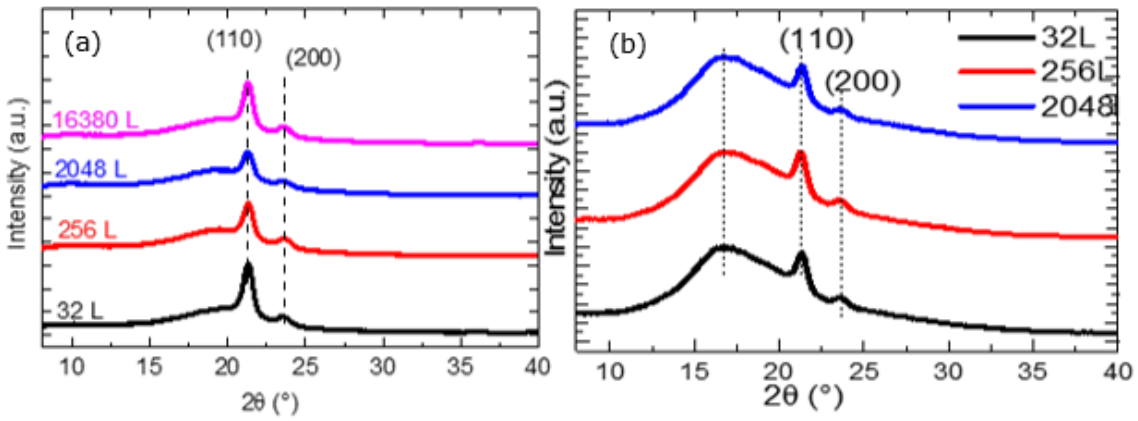

Figure 4.11 1D-WAXS profiles for coextruded (a) LDPE-L1/PS and (b) LDPE-L1/PC multilayers. The intensity was normalized with the thickness of the studied films. The scattering angle is denoted as 2θ.

The DSC thermographs of heating scan for LDPE-L1/PS and LDPE-L1/PC multilayers and their blend with a weight fraction of 50/50 are shown in **Figure 4.12**. The DSC parameters are summarized in **Table 4.1**. We can note a negligible change in the melting temperature, crystallinity and lamellar thickness for all coextruded films and present a similar behavior as a blend. Additionally, we note that the crystallinity of the coextruded LDPE-L1/PC films is negligible around 1%, confirming the amorphous behavior observed in WAXS. This suggests that the geometrical confinement from the nanolayer did not affect the thermal crystalline properties of LDPE-L1 systems, but their morphology as demonstrated by WAXS, TEM, MEB.

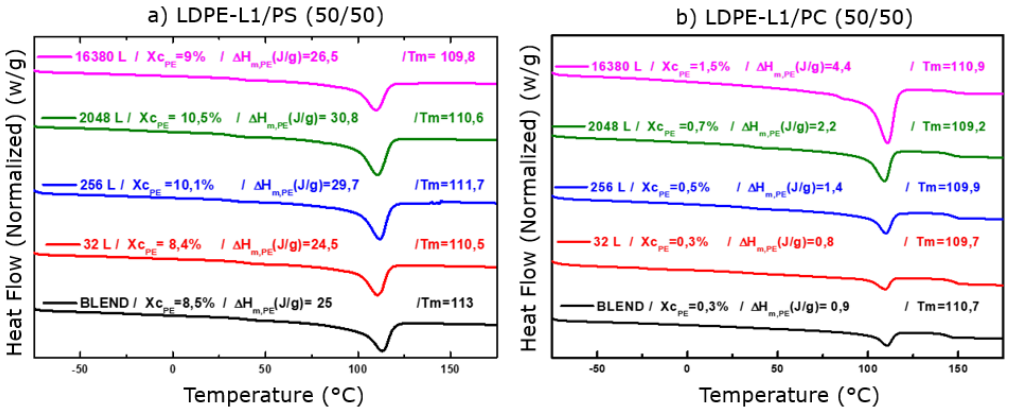

Figure 4.12 DSC thermographs of heating scan for a) LDPE-L1/PS and b) LDPE-L1/PC multilayers and blend (50/50).

Table 4.1 DSC parameters for a) LDPE-L1/PS and b) LDPE-L1/PC multilayers, blend (50/50), and neat LDPE-L1

	a) LDPE-L1/PS			
	Tm (°C)	ΔH_m (J/g)	$X_{c,DSC}$ (%)	L_c (nm)
L1	112	117	40	9.47
32L	110.5	24.5	8.4	9.01
256L	111.7	29.7	10	9.38
2048L	110.6	30.8	10.5	9.04
16380L	109.8	26.5	9	8.81
Blend	113	25	8.5	9.81

	b) LDPE-L1/PC			
	Tm (°C)	ΔHm (J/g)	$Xc_{,DSC}$ (%)	Lc (nm)
L1	112	117	40	9.47
32L	110.7	0.8	0.3	9.4
256L	109.7	1.4	0.5	9
2048L	109.9	2.2	0.7	9.47
16380L	109.2	4.4	1.5	9
Blend	110.7	0.9	0.3	-

4. Conclusion

The present chapter aimed to understand the effect of confinement on the structural and morphological properties in their multi-layered systems fabricated by the forced-assembly multilayer coextrusion process. The main focus is to demonstrate that there is a processing window to fabricate a well architectured and continuous mismatched rheological LDPE-L1/(PS or PC) systems. The obtained multilayers were characterized through various techniques such as wide X-ray scattering (2D-WAXS) and electron microscopy (SEM, TEM…).

Initially, stability maps for all coextruded films with stable and unstable domains were constructed. We found that LDPE-L1/PS system is more stable than the LDPE-L1/PC system. This is possibly due to the elasticity ratio of LDPE-L1/PS, which is lower than that of L1/PC and which may improve the interfacial stability of coextrusion. Then, the transparency and homogeneity of the coextruded films were obtained. The multilayer films are viewed as transparent films, and this transparency was maintained whatever the architecture and number of layers. Interestingly, the transparency seems to be more important with multi-nanolayered films keeping flexible quality of the final structures despite the association of rigid confined polymers with LDPE-L1.

Therefore, the morphology/microstructure of the coextruded films was analyzed by SEM, TEM and AFM. Owing their high viscoelastic mismatched properties, and depending on the immiscible system chosen, and on the critical thickness reached generally for nanometric thicknesses, the rate of breakup increases dramatically. The onset of the breakup layer in the LDPE-L1 /PS system was determined in 2048L, and in the LDPE-L1 /PC in 256L. This is due to the viscoelastic mismatched properties between the polymers and may be the reason for the nonuniformity across the layers. Interestingly, we have demonstrated that it is possible to prepare some nanolayer structures with 16380-PS/LDPE-L1 systems despite their high mismatched viscoelastic properties. We demonstrated also that lower elastic contrast is a key to stabilize their flow structure in nanolayered systems. Finally, the orientation and crystalline structure of the coextruded films were characterized by the 2D-WAXS. The confinement effect of LDPE-L1 chains against amorphous PS direction gives

rise to stacked in-plane lamellae. Moreover, we found that the geometrical confinement from the nanolayer did not affect the thermal crystalline properties of LDPE-L1 chains, but their morphology as demonstrated by WAXS, TEM, SEM and AFM.

Chapter 5. Multi-micro/nanolayer films based on polyolefins: New approach from Eco-design to recycling

1. Introduction

Since the discovery of Polyethylene in the 1950s, polymers have been reaching all the areas of our daily life. Europe's plastic production currently varies around 60 million tonnes [138]. The largest end-use markets for plastics are packaging (39%) and building sector (19.7%). Meanwhile, agricultural plastic demand accounts for 3.3% of the total [138]. Flexible films have become extremely popular among all plastic material applications due to their versatility, lightness, resistance, and printability. At the moment, multilayer films account for 17% of global flexible film production [139]. These multilayer structures are created through coextrusion, an industrial process widely used to create films suitable for a variety of applications, including food packaging, medical applications, and, more recently, microelectronics and nonlinear optics [140], [13]. Multilayer polymer systems are manufactured to satisfy the expectation of high-value-added applications such as gas barrier films, mechanically robust systems, and optical applications[141]. For example, the most frequently used polymers in the consumer packaging sector are low-density polyethylene (LDPE) and high-density polyethylene (HDPE), followed by polyethylene terephthalate (PET), polypropylene (PP), and polystyrene (PS). LDPE and LLDPE are the most frequently used materials in agricultural applications and other non-consumer packaging. [142].

However, the rising generation and accumulation of non-biodegradable waste is becoming a widely discussed topic, since a large number of plastic packaging products are now designed to have a short service life because of the low cost and ease of production [2]. Every year, roughly 25 million tonnes of post-consumer plastic waste are generated in the European Union. The total volume of flexible consumer packaging is expected to rise from 27.4 million tonnes in 2017 to 33.5 million tonnes in 2020 [139],[142]. Most consumers perceive plastic packaging in negative way because of the considerable high amount of waste produced in their everyday lives. All things considered, finding new solutions for the multilayered films valorization is critical.

Therefore, if mechanical recycling is assumed, a new approach from eco-design to multilayer structure recycling should be considered as an alternative.

In the context of the Circular Economy, the European Union has been actively promoting recycling design in recent years [7]. The strategy consists on the development of new products so they can be recycled at their End-of life. Recyclability and the degree to which they can incorporate recycled materials are heavily influenced by the design of polymers flexible films. The implementation of Extended Producer Responsibility (EPR) schemes, in which the End-of-life cost becomes an economic motivation for the producers encourages design for recycling [8].

The circular economy relies heavily on recycling to close the loop. However, since the multilayer films are made of different types of polymers, their recycling becomes more challenging. Considering that complex blends are created as a result of the recycling process, compatibilizers must be added into the blends, which can develop new problematics that need to be further solved. Using strategies as structure simplification and eco-design are key factors to increase the recyclability of the materials [139].

The secondary raw material obtained from recycled polymer waste serves as the starting point for the eco-design dynamic, coming from a previous product End-of life. However, as Ragaert et al. 2017 have explained, design for recycling must take into account a variety of factors. To begin, a thorough characterization of the recycling polymers was performed in order to determine their strengths and weaknesses. Finding potential new or existing products in which the recycled materials can be incorporated. Then, adapt the new products design for the manufacturing using recycled materials. In addition, for some product requirements, cost- effective strategies can be applied in order to upgrade the recycled material quality. This can involve the addition of small amounts of additives including compatibilizers or stabilizers.

The majority of European's recycling companies deal with two sorts of waste streams: Polyethylene and Polyethylene terephthalate (PET) based streams. Though, the presence of other types of films comprising polypropylene and polystyrene (PS) can contaminate the waste stream of PE based films. In light of the latter, multilayered polyethylene (PE)/polystyrene (PS) systems were investigated and discussed for this study, as these polymer combinations are typically encountered in recycling companies' waste streams. They are frequently utilized together in the manufacturing of products and are difficult to separate. Optical, ballistic densitometer and infrared sorting are used after the waste is

received. However, none of these automatic sorting can reliably separate polyethylene from polystyrene and polypropylene. PS is found in a variety of waste streams, ranging from 5 wt% to 10 wt%. In general, one of the major issues in processing mixed plastic wastes is property degradation induced by incompatibility between PE/PS.

The PE/PS systems as blends are not miscible from a thermodynamic point of view. Indeed, combining immiscible polymer pairings like this usually produces materials with poor mechanical characteristics and a heterogeneous morphology. Multilayer coextrusion has been used to combine several systems with semicrystalline polymers as restricted materials versus amorphous polymers with layer thicknesses ranging from 100 nm to 10nm to improve the final properties of immiscible blends such as PE/PS without the presence of compatibilizers [143], [137]. The crystalline morphology of the system gradually evolves from three-dimensional (3D) spherulite morphology to one-dimensional (1D) lamellar morphology as the thickness of a layer is reduced.

Previous research [11] looked into the effects of HDPE nanolayers sandwiched between thicker polystyrene (PS) in multilayer coextruded systems. Surprisingly, when the layer thickness of HDPE decreased from microscale to nanoscale, the crystallinity reduced from 60 to 33%. This result was related to microscale discoidal morphologies (>100nm) that changed into long bundles of edge-on lamellae in HDPE nanolayers (<100 nm). In multilayer systems, confined crystallization of polypropylene (PP) against hard polymer (PS) with variable layer thickness and composition has also been investigated [12]. The mechanical properties and morphology of the multilayered film are strongly influenced by changes in layer thickness and composition of the component polymers. However, when the film thickness is reduced, the morphology changes from continuous and homogeneous to irregular structure, and the mechanical properties ,particularly the elongation at break are significantly affected [68].

The main focus of this chapter is to study the complex PE/PS systems with a new approach from eco-design to recycling. For this purpose, the coextruded multilayer LDPE-L1/PS films were recycled with two different recycling processes. The impact of the number of layers and the LDPE-L1/PS composition on mechanical properties and morphology was then investigated.

2. Experimental section

2.1. Materials and sample preparation

The coextruded LDPE-L1/PS films with compositions of 50/50 and 10/90, as well as films with different number of layers ranging from 32 to 16380 layers were studied in detail in chapter 3 and their properties are listed in **Table 3-4**.

2.2. Mechanical recycling process

The multimicro/nanolayer films used in this study were recycled at the laboratory scale utilizing two different mechanical recycling methods.

1) The first mechanical recycling method (M1) was grinding, followed by mini-Twin-screw extrusion and injection molding as the final step.
2) The second mechanical recycling method (M2) was grinding, followed by injection molding.

The grinding process is a common step in both methods of mechanical recycling. This industrial process involves deconstructing multilayer films and converting them into small flakes by using a blade grinder. With regards to the first mechanical recycling method (M1), the flakes produced during the grinding of multilayer films will be utilized as raw material to feed the mini-Twin-screw extrusion. The resultant compounds were pelletized using a cutting machine. The extrusion process was conducted at 240°C utilizing a Thermoscientific mini CTW co-rotating twin-screw HAAKE machine. Finally, the pellets produced by a mini twin-screw extruder were employed as raw material to feed the injection-molding process. The HAAKETM-Mini-jet piston injection molding system was utilized to produce flat rectangular specimens for tensile testing. The samples had a thickness and width of 2x4 mm, respectively. Temperature and pressure were maintained at 220°C and 550 bar for 8 seconds, respectively, throughout the injection process. After that, a packing pressure of 450 bars was applied for 8 seconds.

With regards to the second mechanical recycling method (M2), the flakes produced during the grinding of multilayer films will be utilized as raw to feed the injection-molding process. The flakes obtained from grinding were employed as raw material to feed the injection-molding process.

2.3. Mechanical and morphology characterization

2.3.1. Tensile Test

The INSTRON electromechanical measuring machine were used to perform the tensile test. The samples tested were rectangular in shape. The cross section was 50 mm in length and 4 mm in width, respectively. One end of the specimen was attached to the machine while the other was displaced at a steady rate of 50mm/min via a 100N load cell. The data was obtained by tracking the force as a function of displacement using a map. Moreover, utilizing calibrated equipment to measure cross-sectional area improvements during deformation is inadequately accurate for thin films such as the multilayers examined in this study. As a consequence, our study focused only on engineering stresses and strains.

The engineering stress on the samples was calculated using Eq. (65), where F denotes the force needed to produce a certain deformation and A denotes the area. The engineering strain was then computed using Eq. (66) where l_o signifies the initial length and Δl represents the length change. The elongation and tensile strength at break were determined using the stress-strain plot. The tests were conducted in the direction of the machine.

$$\sigma_{eng} = \frac{F}{A} \ (\frac{N}{m^2}) \tag{65}$$

$$\varepsilon_{eng} = \frac{\Delta l}{l_o} \times 100 \tag{66}$$

2.3.2. Scanning Electron Microscopy

The effect of the mechanical recycling method on the morphology of LDPE-L1/PS multilayers was investigated in this section. The morphology of neat and recycled LDPE-L1/PS multilayered films was observed by scanning electron microscopy (SEM) using FEI QUANTA 250 FEG microscope in high-vacuum mode. The SEM observations were

conducted on LDPE-L1/PS specimens obtained from both mechanical recycling process. The recycled LDPE-L1/PS multilayer systems were fractured in liquid nitrogen at a temperature below Tg. Direct observation was conducted with no further treatment. In contrast to the observation made for the recycled films, the neat LDPE-L1/PS multilayer systems (see chapter 4) were first stained for two days with ruthenium tetraoxide vapor (RuO4) and then sandwiched between two epoxy resin plaques till solidification. The specimens were sectioned normal to extrusion direction via a cryo-ultramicrotome (LEICA EM UC7) at room temperature using a diamond knife.

3. Results and discussion

3.1. Study of the mechanical properties

3.1.1. Effect of number of layers and composition

In this part, the effect of layer thickness and composition on the mechanical properties were investigated. For these LDPE-L1/PS multilayer systems, the thickness of each component and number of layers was varied going from microscale to nanometric scale. with a nominal thickness around 95 nm for the 50/50 composition, which is very close to its scale of lamellae thickness.

Figure 5.1 illustrates the stress-strain curves for multilayer LDPE-L1/PS 50/50 films. As can be shown, the tensile strength at yield of the multimicro-nanolayer structures was similar to that of PS and remain constant over 22 MPa. Nevertheless, the number of layers has an influence on the elongation at break of the multilayered films, as shown in **Figure 5.1** and Table 5-1. For example, the LDPE-L1/PS-32L structure, with a nominal thickness of 5μm, exhibit an intermediate behavior between the LDPE-L1 and PS. The LDPE-L1/PS-32L mechanical behavior is brittle and comparable to the neat PS. However, for the LDPE-L1/PS-16380L, with a nominal thickness of 12 nm, the mechanical response of the multilayer film is more ductile, which indicates that the brittle behavior observed with the LDPE-L1/PS-32L is due to the poor adhesion between the LDPE-L1 and PS interfaces at the microscale. Hence, as we increase the number of layers the adhesion at the LDPE-L1/PS interface is improved due to the layer's geometric confinement, which explains the increases in film's ductility. These results relate with previous studies of multilayered immiscible PP/PS films with different compositions (from 90/10 to 10/90) reported by Scholtyssek et

al. 2010 [68]. They found that the elongation at break increases significantly with the decrease of nominal layer's thickness at constant composition, which correspond to the observations previously discussed with the LDPE-L1/PS-163280L film.

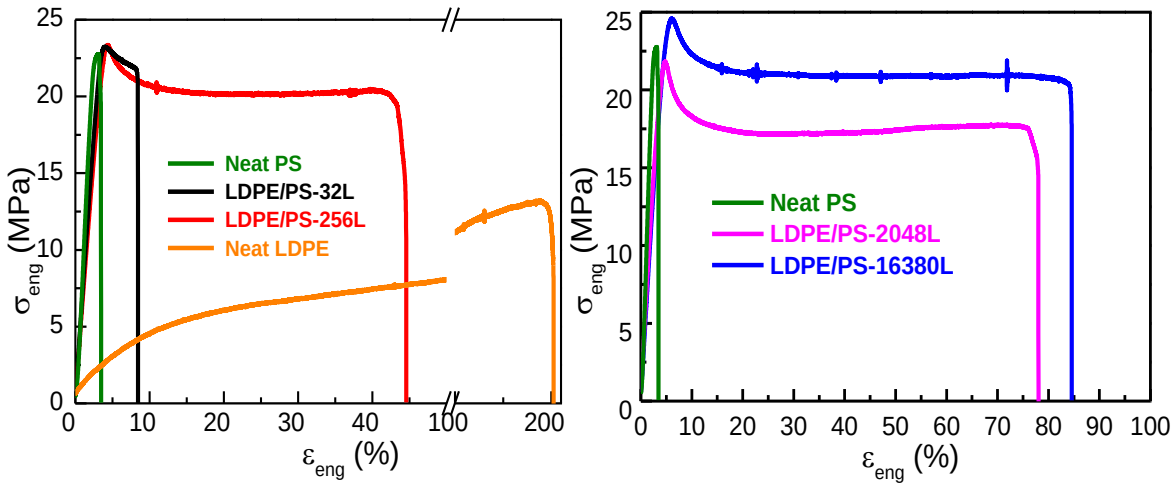

Figure 5.1 Engineering stress-strain plot of LDPE-L1/PS multilayer 50/50 (wt/wt) films with different numbers of layers in machine direction.

Table 5-1 Mechanical properties of the LDPE-L1/PS 50/50 (wt/wt) films with various number of layers.

Films	Tensile strength at yield (MPa)	Tensile strength at break (MPa)	Elongation at break (%)
LDPE-L1/PS-32L	22± 2.8	22± 22	8± 2.4
LDPE-L1/PS-256L	22± 6	20± 2	45± 18
LDPE-L1/PS-2048L	22± 2.6	18± 2.6	78± 27
LDPE-L1/PS-16380L	24± 2.2	20± 2	84± 20

In case of the multilayered structures with 90/10 composition, the samples showed an intermediate behavior between the neat LDPE-L1 and PS, as seen in **Figure 5.2** and **Table 5-2**. However, for the LDPE-L1/PS-16380L film with a nominal layer thickness less than 10 nm, we can observe an increase of the tensile strength and elongation at break. This may

be explained by the impact of geometric confinement of LDPE-L1 crystals against the amorphous PS during the coextrusion process, which is discussed in depth in Chapter 3 of this manuscript.

Regarding the effect of the LDPE-L1/PS composition, clear differences were found between the LDPE-L1/PS films with 50/50 and 10/90 composition as shown in **Figure 5.1** and **Figure 5.2**. The sample with LDPE-L1/PS 50/50 composition shows higher elongation at break for all number of layers, compared with the LDPE-L1/PS 10/90 composition. These results demonstrate that the film's ductility is not only influenced by the nominal layer thickness but also by the composition. A similar conclusion was observed by Scholtyssek et al. [68] showing that composition has a significant effect on the ductility of the multilayered films.

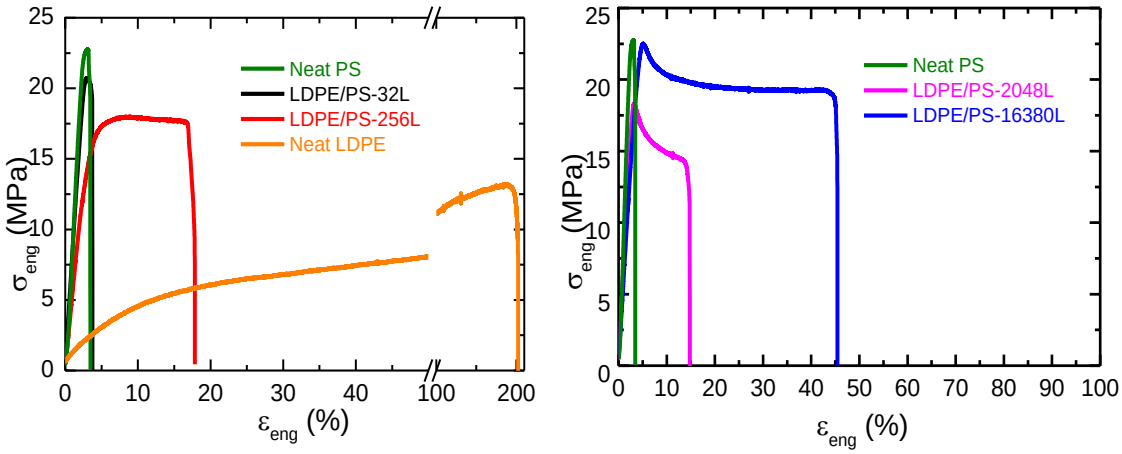

Figure 5.2 Engineering stress-strain plot of multilayered LDPE-L1/PS 10/90 films with different number of layers in machine direction.

Table 5-2 Mechanical properties of the LDPE-L1/PS 10/90 (wt/wt) films with different number of layers.

Films	Tensile strength at yield (MPa)	Tensile strength at break (MPa)	Elongation at break (%)
LDPE-L1/PS-32L	20± 3.2	20± 3	4± 0.5
LDPE-L1/PS-256L	18± 0.5	17.5± 1	16± 14
LDPE-L1/PS-2048L	18± 1.1	14± 1.5	14± 3
LDPE-L1/PS-16380L	22± 2.6	19± 2	45± 14

3.1.2. Influence of the recycling process system on the mechanical properties

In this section we analyzed the effect of the different recycling process (described previously in the experimental section) on the mechanical properties of the multilayer films. In Erreur ! Source du renvoi introuvable. **(a)**, the effect of the number of layers with recycled films LDPE-L1/PS (10/90) obtained from the second mechanical recycling method (M2) is shown. An important reduction of the elongation at break of the recycled multilayer film with 2048 layers compared with the 256 layer's film was observed. This was expected, since the nominal thickness of the LDPE-L1/PS-2048L (10/90) film are thinner (~19nm) than the multilayer film with 256 layers (~136nm), which reflects the fragility of the layers during the grinding and injection steps of the recycling process M2. Nevertheless, in terms of tensile strength at yield and break we observe the opposite effect with the number of layers. This can be explained due to the effect of geometric confinement of LDPE-L1 crystals against the amorphous PS, even after the recycling process M2.

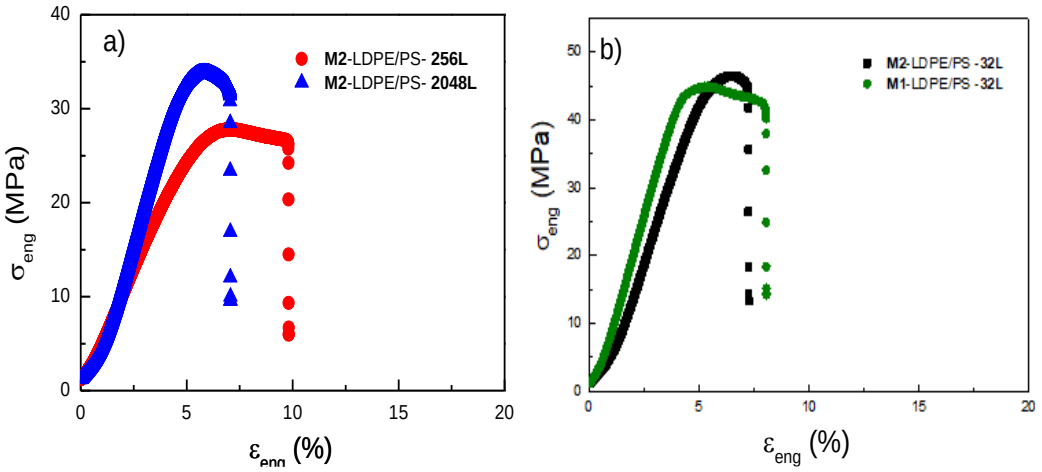

Figure 5.3 Engineering stress-strain plot of the recycled a) M2-LDPE-L1/PS (10/90) with different number of layers. b) LDPE-L1/PS (10/90)-32L multilayer films (MD direction) with the M1 and M2 recycling systems.

Then in **Figure 5.3 (b)** we compare the effect of the recycling process M1 and M2 on the mechanical properties of the LDPE-L1/PS (90/10) with 32 layers. As a reminder, the difference between the recycling process M1 and M2 is the additional step of twin-screw extrusion between the grinding and the injection molding steps. As displayed, both recycled films showed equivalent strength at yield and break, as well as the elongation at break. These

results indicate that the additional step of twin-screw extruder for the M1 recycling process did not degrade the multilayer films.

3.1.3. Morphology characterization of the Recycled and virgin LDPE-L1/PS films

SEM micrographs of virgin and recycled LDPE-L1/PS-256L with 50/50 volume fraction are displayed in **Figure 5.4.** These structures were observed and analyzed over a cross-section in the machine direction with the aim of studying the effect of the recycling system on the morphology of the multilayered structure.

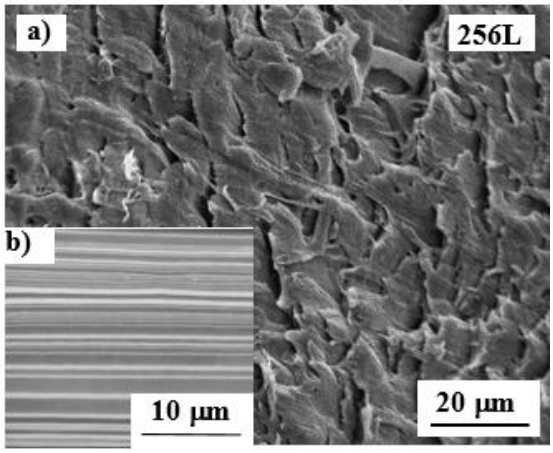

Figure 5.4 SEM images of the recycled M2-LDPE-L1/PS-256L multilayer film (a); and virgin LDPE-L1/PS-256L multilayer film (b) with 50/50 composition.

As observed in **Figure 5.4 (b)**, the virgin LDPE-L1/PS-256L exhibits a continuous and regular structure morphology. It is noteworthy to note that the the continuity as well as the uniformity of the multilayered films was greatly impacted by the film thickness and composition, which relate with the results obtained by Scholtyssek et al. 2010[68]. However, with the recycled M2-LDPE-L1/PS-256L film (**Figure 5.4 (a)**) we can no longer differentiate the layers from each other. These results prove that only the grinding and injection molding step were sufficient to brake the layered structure presented by the virgin LDPE-L1/PS-256L morphology.

4. Conclusion

In this work, a new approach from design to recycling is studied. In order to improve the manufacturing of new products using recycled materials and simplify their own recyclability, we proposed a design of multi-micro/nanolayer films with different number of layers.

As a reminder, the multimicro/nanolayer LDPE-L1/PS films were prepared in the previous chapter by coextrusion process at laboratory scale, with varying the number of layers and compositions (10/90) and (50/50). These films were recycled using two different mechanical recycling methods. To begin, we investigated the influence of the number of layers and compositions on the mechanical properties. For the symmetrical composition LDPE-L1/PS (50/50), the multilayered films presented a brittle behavior with nominal thickness at the microscale. However, as we decreased the nominal layers thickness down to the nanoscale, the mechanical behavior of the multilayer films was more ductile, as the elongation at break was increased. This relates to the geometrical confinement and the orientation of LDPE-L1 chains during the coextrusion process. Additionally, the same trend was found for asymmetrical composition (10/90), which suggests that the ductility of the films is not only influenced by the nominal thickness but also by the composition of the blends. Then, a morphology with a continuous and regular structure of the virgin multilayers films was observed with SEM analysis. But after the second mechanical recycling method, the layered structure could no longer been observed, which indicates that only the grinding and injection molding step were sufficient to brake the layered structure presented by the virgin multilayer film.

In this chapter, we demonstrated the design of multi-micro/nanolayer films as a very promising solution for the industrial problematics that comes with the valorization of recycled materials, without the use of compatibilizers. Although, it is important to mention that this study was performed only at the laboratory scale with cast film coextrusion. The translation of micro/nanolayered technologies into the cast film processing at commercial scale and a deep understanding the involved nanostructure mechanisms, will need further studies in the future.

Conclusions and perspectives

General conclusions

The objective of this research is to understand the role of confinement on the rheology and molecular dynamics in multilayer polymeric structures fabricated by the forced-assembly multilayer coextrusion of high mismatched viscoelastic systems polyethylenes (PE) and confined polymers (PS and PC). This thesis elaborated systematically the influence of the interfacial properties to control the interface/interphases in the micro-nanostructured model multilayers polymers, as well as their recyclability for advanced applications.

The main conclusions that are specific to each part of the thesis can be summarized as following:

In the **Chapter 1,** we presented an overview of multilayered polymers basics, including common preparation methods, rheological, interfacial, and confinement phenomena, as well as their excellent properties for applications using the multilayer coextrusion. The applications of multilayer coextruded polymers were summarized, including dielectric, optical properties, and gas barrier, etc. Additionally, Interfacial phenomena occurring in multilayer coextruded polymers were explained, involving the interfacial diffusion, as well as relevant theoretical aspects. Flow instabilities and interfacial defects were used to describe rheological phenomena in multilayer coextruded polymers.

In the **Chapter 2,** the physicochemical, thermal, and rheological properties for the four kinds of polyethylenes (LDPEs and LLDPEs) were studied. The main objective is to gain a better understanding of the structure and architecture properties of these PE in relationship with their shear and elongation properties. For the clarity of this manuscript, the rheological properties of the confined polymers will be given, for comparison, in chapter 3.

Initially, the structure of each sample was obtained from various physicochemical characterization techniques such as nuclear magnetic resonance spectroscopy (^{13}C-NMR), size exclusion chromatography and multi-angle laser light scattering (SEC-MALLS), and crystallization elution fractionation (CEF). It was found by SEC and ^{13}C-NMR that LDPEs of high molecular weight contain a great amount of LCB in comparison with linear ones,

which is in good agreement with the dispersity of each sample. The reason for this differences is related to the complex LDPE molecular structure, which is formed via free-radical polymerization and at high pressure. Moreover, the CEF findings were of the same order of magnitude as those obtained using the ^{13}C-NMR analysis, indicating the reliability of both methods.

Second, the linear and nonlinear rheology were used to probe the structure of the branched and linear polyethylene. The rheological results were strongly influenced by the presence of long-chain branching (LCB). It was found that LDPEs with a higher amount of LCB (2 LCB/1000C) created more entanglements density thus resulting in higher molecular weights giving rise to higher viscosities at lower frequencies and exhibit a significant shear thinning at higher frequencies.

Indeed, the presence of long-chain branching (LCB) leads to more pronounced strain hardening behavior in the elongational flow. Surprisingly, in terms of LLDPE-LL2, a positive deviation in extensional viscosity from the LVE envelope at larger strains was observed. This result was not expected since this polymer has lower molecular weight and negligible long chain branching (0.5 LCB/1000C). It can be said that extensional rheology is extremely sensitive to even trace amounts of LCB and the homogeneity of its distribution per chain. Whereas this find does not seem to be valid for LLDPE1 which it is more polydisperse. The presence of two distributions in relaxation spectrum can be another key to explain this difference. Lastly, a comparison between the predictions of the HMMSF model and Extensional rheology data was done. A good agreement was found between the HMMSF model and the extensional viscosity data. These findings lead to a better understanding of the relationships between the molecular structure of linear and branched PEs with rheological properties.

In **chapter 3**, we aim to understand the role of interfacial polymer physics and the triggered interfaces/interphases in shear and extensional rheology, as well as polymer processing. First, the rheological properties of each sample were studied in the linear viscoelastic regime in order to choose the appropriate parameters to fabricate films under the most stable conditions. The melt viscosity and/or elasticity ratio between the components at different temperatures were then obtained to understand the flow during coextrusion despite their high mismatched viscoelastic properties. Second, various nanostructured multilayer

structures with relatively stable flow and layered architecture were elaborated The contact time between neighboring layers and the theoretical thickness of these multilayered structures were obtained to quantitatively characterize the polymer-polymer adhesion and to keep the interface stable throughout the coextrusion process. As we increase the number of layers through the coextrusion process, a new interface is produced, resulting in a longer melt contact time and a thinner layer in the order of several nanometers for nanolayered structures. Then, their shear and extensional rheological properties were investigated. Small amplitude oscillatory shear data were fitted with the Palierne model to determine the interfacial tension of the matrix/droplet blends of each of the pairs. The estimated interfacial tension between the LDPE-L1 and the PS is on the order of 4.5 mN/m, and around 2.5 mN/m for LDPE-L1/PC.

Under extensional flows, the LDPE-L1/LLDPE-LL2 and LDPE-L1/PS multilayers exhibited an increased transient extensional viscosity and pronounced strain hardening. In contrast to the LDPE-L1/PC multilayered films, no strain hardening behavior was observed. This behavior was anticipated using a Macosko model, which is based on force summation and interfacial tension as a fitting parameter. The main challenge is to check the validation of this recent model with high mismatched viscoelastic polymers. The estimated interfacial tension was compared to those obtained from emulsion model like Palierne with the equivalent blends. The estimated interfacial tensions with Palierne corroborate those of Macosko model. The evaluation of interfacial properties is essential for establishing the structure-dynamics-property relationship.

In **chapter 4**, we aim to understand the effect of confinement on the structural and morphological properties in their multi-layered systems fabricated by the forced-assembly multilayer coextrusion process. The main focus is to demonstrate that there is a processing window to fabricate a well architectured and continuous mismatched rheological LDPE-L1/(PS or PC) systems. The obtained multilayers were characterized through various techniques such as wide X-ray scattering (2D-WAXS) and electron microscopy (SEM, TEM…).

Initially, stability maps for all coextruded films with stable and unstable domains were constructed. We found that LDPE-L1/PS system is more stable than the LDPE-L1/PC system. This is possibly due to the elasticity ratio of LDPE-L1/PS, which is lower than that

of LDPE-L1/PC and which may improve the interfacial stability of coextrusion. Then, the transparency and homogeneity of the coextruded films were obtained. The multilayer films are viewed as transparent films, and this transparency was maintained whatever the architecture and number of layers. Interestingly, the transparency seems to be more important with multi-nanolayered films keeping flexible quality of the final structures despite the association of rigid confined polymers with LDPE-L1.

Therefore, the morphology/microstructure of the coextruded films was analyzed by SEM, TEM and AFM. Owing their high viscoelastic mismatched properties, and depending on the immiscible system chosen, and on the critical thickness reached generally for nanometric thicknesses, the rate of breakup increases dramatically. The onset of the breakup layer in the LDPE-L1 /PS system was determined in 2048L, and in the LDPE-L1 /PC in 256L. This is due to the viscoelastic mismatched properties between the polymers and may be the reason for the nonuniformity across the layers. Interestingly, we have demonstrated that it is possible to prepare some nanolayer structures with 16380-PS/LDPE-L1 systems despite their high mismatched viscoelastic properties. We demonstrated also that lower elastic contrast is a key to stabilize their flow structure in nanolayered systems. Finally, the orientation and crystalline structure of the coextruded films were characterized by the 2D-WAXS. The confinement effect of LDPE-L1 chains against amorphous PS direction gives rise to stacked in-plane lamellae. Moreover, we found that the geometrical confinement from the nanolayer did not affect the thermal crystalline properties of LDPE-L1 chains, but their morphology as demonstrated by WAXS, TEM, SEM and AFM.

Finally, **in chapter 5** and in the context of circular economy, a future-oriented approach from eco-design to a recycling strategy of the studied multi-micro/nanolayered systems was investigated. Therefore, a novel route is purposed to decrease the number of constituents, control the thickness of the layers, avoid using tie layers, and enhance the recyclability of the studied systems. The morphological and mechanical properties are tuned depending on the initial architectures.

Although, it is important to mention that this study was performed only at the laboratory scale with cast film coextrusion. The translation of micro/nanolayered technologies into the cast film processing at commercial scale and a deep understanding the involved nanostructure mechanisms, will need further studies in the future. Based on the interesting

results about “Eco-design by recycling” from micro/nanolayered polymers, another perspective will deal to continue the present investigation with complex multicomponent multilayer systems with or without tie or barrier layers.

Perspectives

There are still some perspectives in the current work that can be developed further in the future, as listed below:

1) Future work can be done using different model couples with mismatched viscoelastic highly filled polymers. Special attention will be given to the effect of alignment/dispersion and confinement during coextrusion on shear and elongation rheological behavior.

2) In our study, we examined the morphology and microstructure of coextruded films using only branching LDPE-L1 in a 50/50 composition with PS and PC. Additional study should be done to investigate the influence of confinement on the crystallization morphology of multimicro/nanolayer films by varying the composition and also the multilayer pairings (2D to 1D crystalline structures). Effect of stretching will be also examined.

3) In the context of circular economy, it is important to mention that this study was performed only at the laboratory scale with cast film coextrusion. The translation of micro/nanolayered technologies and their mechanical recycling approach into the cast film processing at a industrial scale and a deep understanding the involved nanostructure mechanisms will need further studies in the future.

4) Another challenging work is to study the influence of recycling on the evolutive crystalline morphology of the multi micro/nanolayer films.

Appendix

1. ^{13}C NMR Spectrum of polyethylenes with different macromolecular architecture

- LDPE – L1:

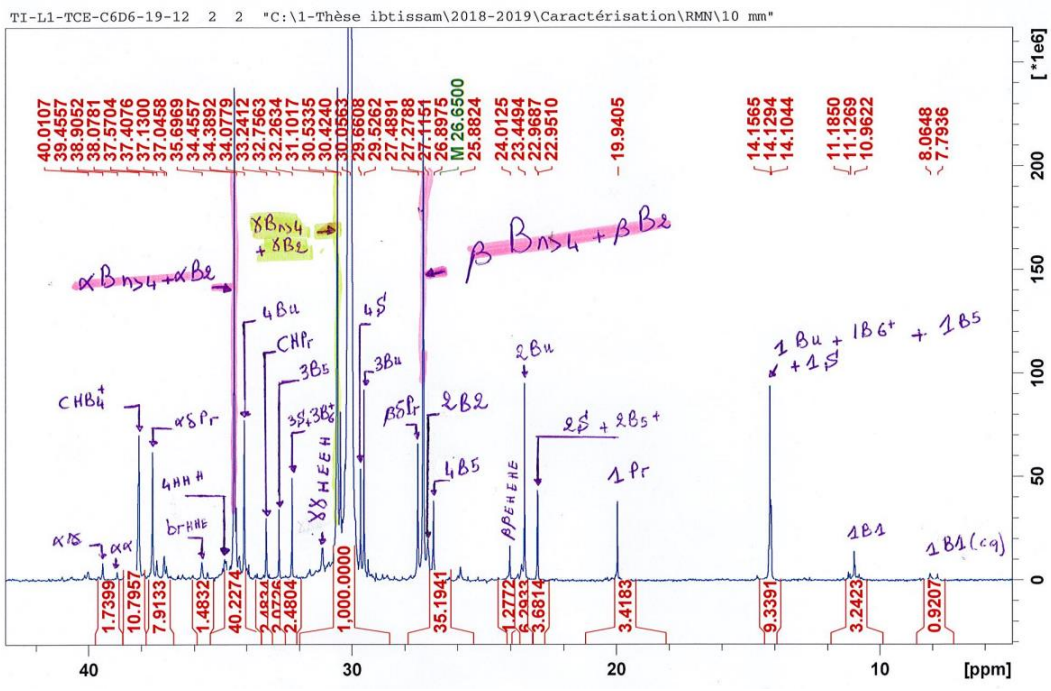

- LDPE – L2:

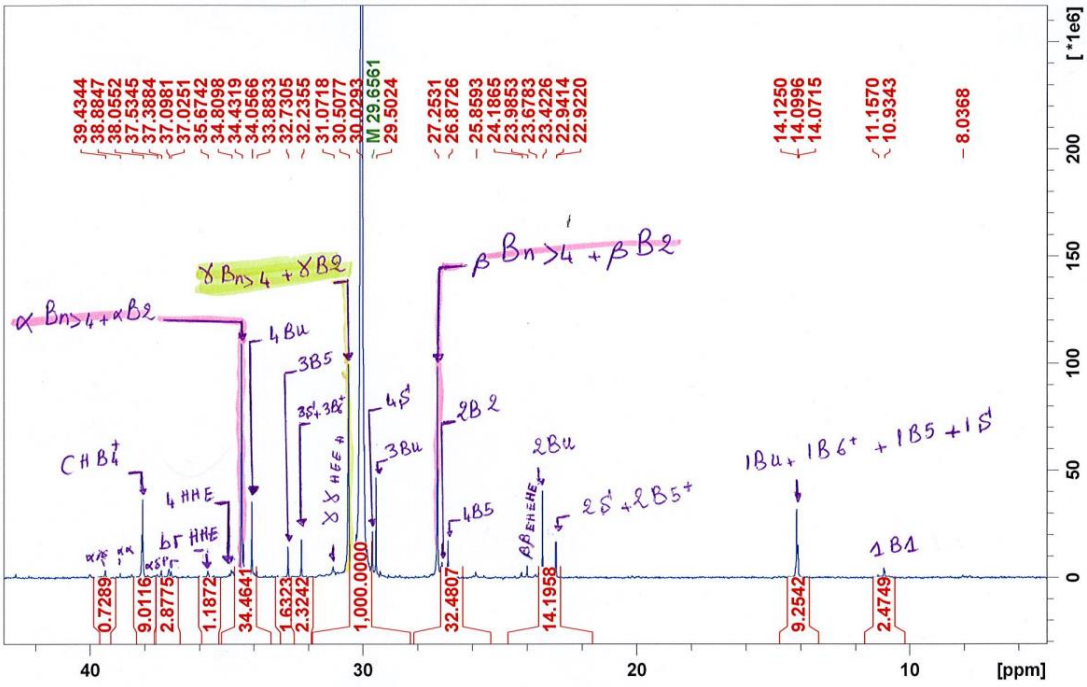

- LLDPE – LL1:

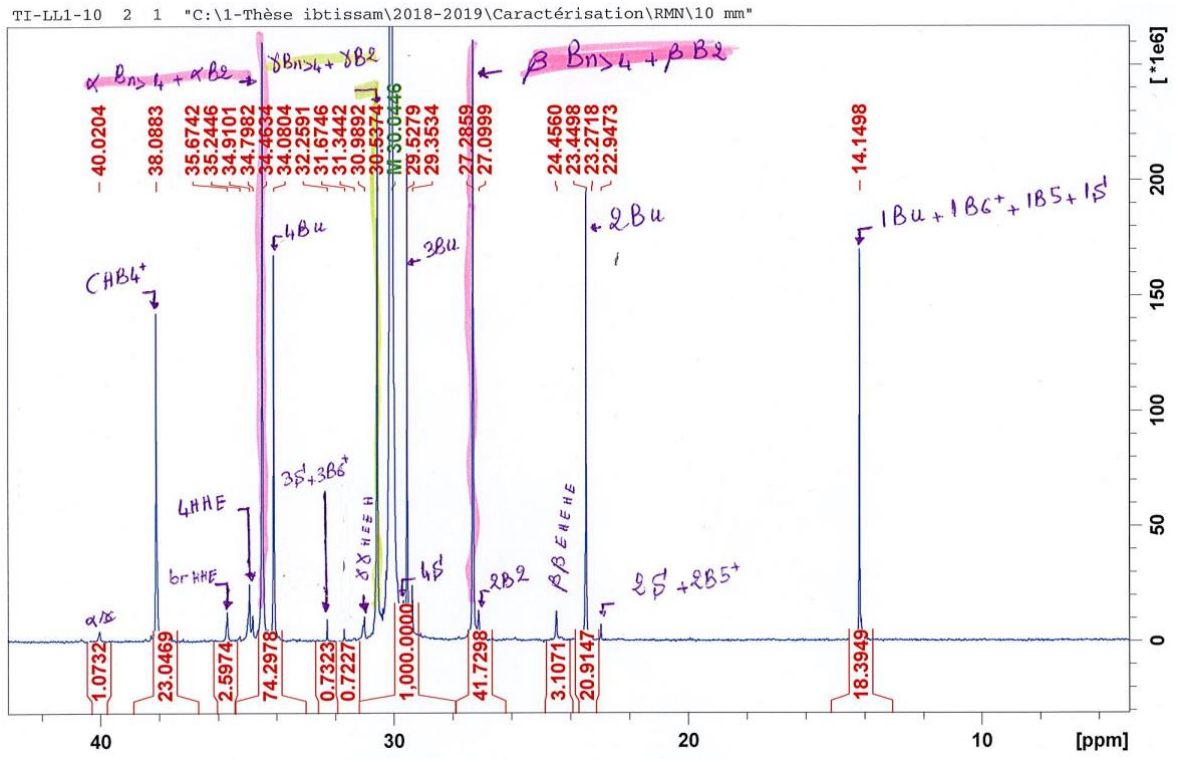

- LLDPE – LL2:

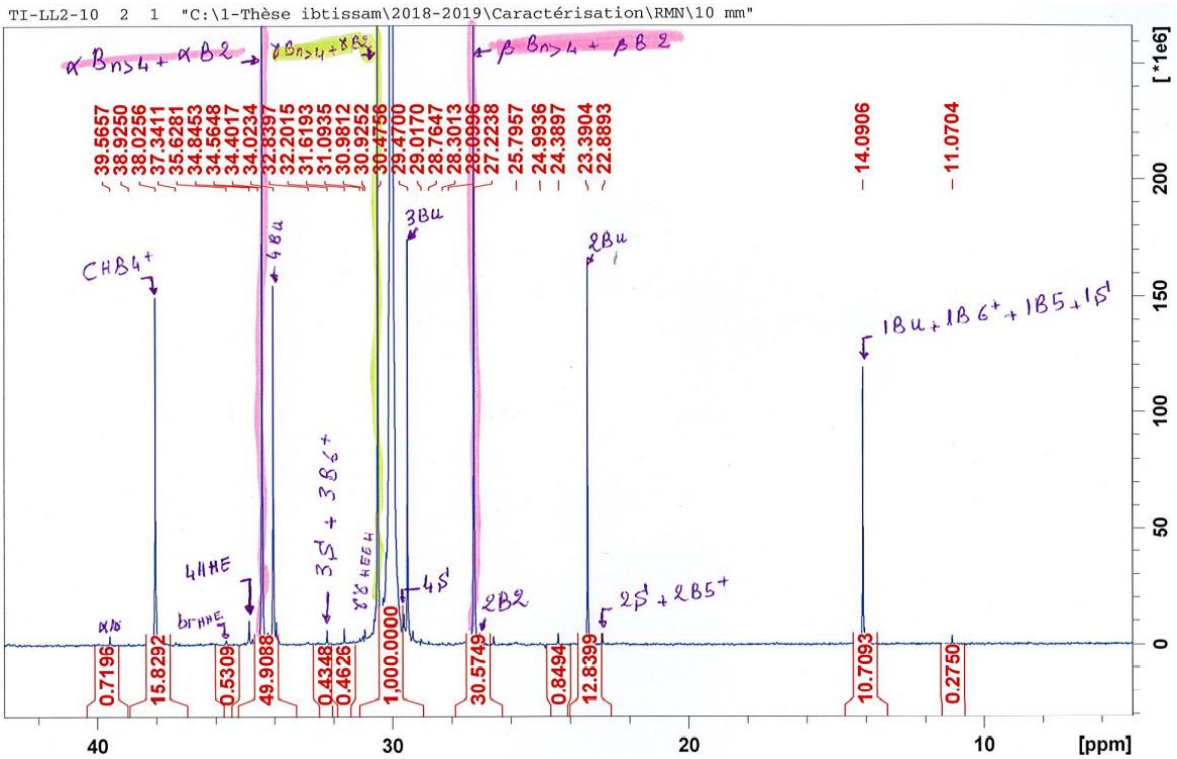

References

[1] X. Zhang *et al.*, "Progress on the layer-by-layer assembly of multilayered polymer composites: Strategy, structural control and applications," *Prog. Polym. Sci.*, vol. 89, pp. 76–107, 2019.

[2] J. J. Richardson, M. Björnmalm, and F. Caruso, "Technology-driven layer-by-layer assembly of nanofilms," *Science (80-.).*, vol. 348, no. 6233, 2015.

[3] B. S. Yilbas, A. Al-Sharafi, and H. Ali, *Surfaces for Self-Cleaning*. 2019.

[4] Z. Li, A. Olah, and E. Baer, "Micro- and nano-layered processing of new polymeric systems," *Prog. Polym. Sci.*, vol. 102, p. 101210, 2020.

[5] T. Kazmierczak, H. Song, A. Hiltner, and E. Baer, "Polymeric one-dimensional photonic crystals by continuous coextrusion," *Macromol. Rapid Commun.*, vol. 28, no. 23, pp. 2210–2216, Dec. 2007.

[6] J. Y., T. H., H. A., B. E., and J. S. Shirk, "New Class of Bioinspired Lenses with a Gradient Refractive Index," *J. Appl. Polym. Sci.*, vol. 103, no. 3, pp. 1834–1841, 2007.

[7] C. Y. Lai, A. Hiltner, E. Baer, and L. T. J. Korley, "Deformation of confined poly(ethylene oxide) in multilayer films," *ACS Appl. Mater. Interfaces*, vol. 4, no. 4, pp. 2218–2227, Apr. 2012.

[8] M. Gupta, Y. Lin, T. Deans, E. Baer, A. Hiltner, and D. A. Schiraldi, "Structure and gas barrier properties of poly(propylene- graft -maleic anhydride)/phosphate glass composites prepared by microlayer coextrusion," *Macromolecules*, vol. 43, no. 9, pp. 4230–4239, 2010.

[9] Z. Li, A. Olah, and E. Baer, "Micro- and nano-layered processing of new

polymeric systems," *Prog. Polym. Sci.*, vol. 102, no. xxxx, p. 101210, 2020.

[10] K. Lamnawar, H. Zhang, and A. Maazouz, "Coextrusion of Multilayer Structures, Interfacial Phenomena," *of Polymer Science and Technology (4th edition, John Wiley & Sons Inc, 2013)*. 2013.

[11] W. alterJ Schrenk, "Method for multilayer coextrusion," pp. 1–5, 1973.

[12] M. Ponting, A. Hiltner, and E. Baer, "Polymer nanostructures by forced assembly: Process, structure, and properties," *Macromol. Symp.*, vol. 294, no. 1, pp. 19–32, 2010.

[13] B. Lu *et al.*, "Unveiling the Effects of In Situ Layer–Layer Interfacial Reaction in Multilayer Polymer Films via Multilayered Assembly: From Microlayers to Nanolayers," *Macromol. Mater. Eng.*, 2020.

[14] H. Wang, J. K. Keum, A. Hiltner, and E. Baer, "Confined crystallization of peo in nanolayered films impacting structure and oxygen permeability," *Macromolecules*, vol. 42, no. 18, pp. 7055–7066, 2009.

[15] M. Ponting, Y. Lin, J. K. Keum, A. Hiltner, and E. Baer, "Effect of substrate on the isothermal crystallization kinetics of confined poly(ε-caprolactone) nanolayers," *Macromolecules*, vol. 43, no. 20, pp. 8619–8627, 2010.

[16] G. Zhang, P. C. Lee, S. Jenkins, J. Dooley, and E. Baer, "The effect of confined crystallization on high-density poly(ethylene) lamellar morphology," *Polymer (Guildf).*, vol. 55, no. 2, pp. 663–672, 2014.

[17] T. E. Bernal-Lara, R. Masirek, A. Hiltner, E. Baer, E. Piorkowska, and A. Galeski, "Morphology studies of multilayered HDPE/PS systems," *J. Appl. Polym. Sci.*, vol. 99, no. 2, pp. 597–612, 2006.

[18] T. E. Bernal-Lara, R. Y. F. Liu, A. Hiltner, and E. Baer, "Structure and thermal

stability of polyethylene nanolayers," *Polymer (Guildf).*, vol. 46, no. 9, pp. 3043–3055, 2005.

[19] L. Deepak and M. Ponting, "Gas Transport, Mechanical, Interphase, and Interdiffusion Properties in Coextruded- Multilayered Films," in *Manufacturing and Novel Applications of Multilayer Polymer Films*, 2016.

[20] K. Arabeche *et al.*, "Study of the cooperativity at the glass transition temperature in PC/PMMA multilayered films: Influence of thickness reduction from macro- to nanoscale," *Polymer (Guildf).*, vol. 53, no. 6, pp. 1355–1361, 2012.

[21] R. Casalini, L. Zhu, E. Baer, and C. M. Roland, "Segmental dynamics and the correlation length in nanoconfined PMMA," *Polymer (Guildf).*, vol. 88, pp. 133–136, 2016.

[22] M. A. Priolo, K. M. Holder, T. Guin, and J. C. Grunlan, "Recent advances in gas barrier thin films via layer-by-layer assembly of polymers and platelets," *Macromol. Rapid Commun.*, vol. 36, no. 10, pp. 866–879, 2015.

[23] H. Wang *et al.*, "Confined crystallization of polyethylene oxide in nanolayer assemblies," *Science (80-.).*, vol. 323, no. 5915, pp. 757–760, 2009.

[24] W. J. Koros, "Barrier Polymers and Structures," *Anal. Chem.*, vol. 62, no. 13, p. 737A, 1990.

[25] J. M. Carr, D. S. Langhe, M. T. Ponting, A. Hiltner, and E. Baer, "Confined crystallization in polymer nanolayered films: A review," *J. Mater. Res.*, vol. 27, no. 10, pp. 1326–1350, May 2012.

[26] C. Lai, R. Ayyer, A. Hiltner, and E. Baer, "Effect of confinement on the relaxation behavior of poly(ethylene oxide)," *Polymer (Guildf).*, vol. 51, no. 8, pp. 1820–1829, 2010.

[27] E. Baer and L. Zhu, “50th Anniversary Perspective: Dielectric Phenomena in Polymers and Multilayered Dielectric Films,” *Macromolecules*, vol. 50, no. 6, pp. 2239–2256, 2017.

[28] E. Baer, A. Hiltner, J. Shirk, and M. A. Wolak, “MULTILAYER POLYMER DIELECTRIC FILM,” *US 2010/0172066A1*, 2010.

[29] M. A. Wolak *et al.*, “Dielectric response of structured multilayered polymer films fabricated by forced assembly,” *Appl. Phys. Lett.*, vol. 92, no. 11, pp. 10–13, 2008.

[30] M. Mackey *et al.*, “Reduction of dielectric hysteresis in multilayered films via nanoconfinement,” *Macromolecules*, vol. 45, no. 4, pp. 1954–1962, 2012.

[31] B. Lu, H. Zhang, A. Maazouz, and K. Lamnawar, “Interfacial Phenomena in Multi-Micro-_Nanolayered Polymer Coextrusion_ A Review of Fundamental and Engineering Aspects _ Enhanced Reader,” *Polymers (Basel).*, vol. 13, no. 417, 2021.

[32] B. Lu *et al.*, “Role of the macromolecular architecture of copolymers at layer-layer interfaces of multilayered polymer films: A combined morphological and rheological investigation,” *Ind. Eng. Chem. Res.*, vol. 59, no. 51, pp. 22144–22154, 2020.

[33] B. Lu, K. Lamnawar, A. Maazouz, and G. Sudre, “Critical Role of Interfacial Diffusion and Diffuse Interphases Formed in Multi-Micro-/Nanolayered Polymer Films Based on Poly(vinylidene fluoride) and Poly(methyl methacrylate),” *ACS Appl. Mater. Interfaces*, vol. 10, no. 34, pp. 29019–29037, 2018.

[34] J. K. Tseng *et al.*, “Interfacial polarization and layer thickness effect on electrical insulation in multilayered polysulfone/poly(vinylidene fluoride)

films," *Polymer (Guildf).*, vol. 55, no. 1, pp. 8–14, 2014.

[35] M. MacKey, A. Hiltner, E. Baer, L. Flandin, M. A. Wolak, and J. S. Shirk, "Enhanced breakdown strength of multilayered films fabricated by forced assembly microlayer coextrusion," *J. Phys. D. Appl. Phys.*, vol. 42, no. 17, 2009.

[36] K. Yin, Z. Zhou, D. E. Schuele, M. Wolak, L. Zhu, and E. Baer, "Effects of Interphase Modification and Biaxial Orientation on Dielectric Properties of Poly(ethylene terephthalate)/Poly(vinylidene fluoride-co-hexafluoropropylene) Multilayer Films," *ACS Appl. Mater. Interfaces*, vol. 8, no. 21, pp. 13555–13566, 2016.

[37] J. Dooley, K. S. Hyun, and K. Hughes, "An experimental study on the effect of polymer viscoelasticity on layer rearrangement in coextruded structures," *Polym. Eng. Sci.*, vol. 38, no. 7, pp. 1060–1071, 1998.

[38] P. D. Anderson, J. Dooley, and H. E. H. Meijer, "Viscoelastic effects in multilayer polymer extrusion," *Appl. Rheol.*, vol. 16, no. 4, pp. 198–205, 2006.

[39] E. Baer, A. Hiltner, and J. S. Shirk, "POLYMER 1D PHOTONIC CRYSTALS," *US 6,696,142 B2*, 2004.

[40] B. C. Fong, K. Keith M. Kotchick, S. Cobb, and R. . Miller, "BRIGHTNESSENHANCEMENT ARTICLE," *USOO628OO63B1*, 2001.

[41] E. Helfand and Y. Tagami, "Theory of the interface between immiscible polymers," *J. Polym. Sci. Part B Polym. Lett.*, vol. 9, no. 10, pp. 741–746, 1971.

[42] E. Helfand and Y. Tagami, "Theory of the interface between immiscible polymers. II," *J. Chem. Phys.*, vol. 56, no. 7, pp. 3592–3601, 1972.

[43] B. Lu, “Rheology and Dynamics at the Interface of Multi Micro-/Nanolayered Polymers,” 2017.

[44] D. Brosetav, G. H. Fredrickson, E. Helfand, and L. Leibler, “Molecular Weight and Polydispersity Effects at Polymer-Polymer Interfaces,” *Macromolecules*, vol. 23, no. 1, pp. 132–139, 1990.

[45] R. J. Composto, E. J. Kramer, and D. M. White, “Mutual Diffusion in the Miscible Polymer Blend Polystyrene/Poly(xylenyl ether),” *Macromolecules*, vol. 21, no. 8, pp. 2580–2588, 1988.

[46] B. Lu, K. Lamnawar, and A. Maazouz, “Rheological and dynamic insights into an in situ reactive interphase with graft copolymers in multilayered polymer systems,” *Soft Matter*, vol. 13, no. 13, pp. 2523–2535, 2017.

[47] C. D. Mueller, S. Nazarenko, T. Ebeling, T. L. Schuman, A. Hiltner, and E. Baer, “Novel structures by microlayer coextrusion - Talc-filled PP, PC/SAN, and HDPE/LLDPE,” *Polym. Eng. Sci.*, vol. 37, no. 2, pp. 355–362, 1997.

[48] F. Brochard, J. Jouffroy, and P. Levinson, “Polymer-Polymer Diffusion in Melts,” *Macromolecules*, vol. 16, no. 10, pp. 1638–1641, 1983.

[49] E. J. Kramer, P. Green, and C. J. Palmstrøm, “Interdiffusion and marker movements in concentrated polymer-polymer diffusion couples,” *Polymer (Guildf).*, vol. 25, no. 4, pp. 473–480, 1984.

[50] G. Pollock, S. Nazarenko, A. Hiltner, and E. Baer, “Interdiffusion in microlayered polymer composites of polycarbonate and a copolyester,” *J. Appl. Polym. Sci.*, vol. 52, no. 2, pp. 163–176, 1994.

[51] Devang Khariwala, “STRUCTURE-PROPERTY RELATIONSHIPS IN MULTILAYERED POLYMERIC SYSTEM AND OLEFINIC BLOCK COPOLYMERS,” 2011.

[52] H. Qiu and M. Bousmina, “Determination of mutual diffusion coefficients at nonsymmetric polymer/polymer interfaces from rheometry,” *Macromolecules*, vol. 33, no. 17, pp. 6588–6594, 2000.

[53] H. Zhang, K. Lamnawar, and A. Maazouz, “Rheological modeling of the mutual diffusion and the interphase development for an asymmetrical bilayer based on PMMA and PVDF model compatible polymers,” *Macromolecules*, vol. 46, no. 1, pp. 276–299, 2013.

[54] H. Zhang, K. Lamnawar, and A. Maazouz, “Fundamental studies of interfacial rheology at multilayered model polymers for coextrusion proceb,” *AIP Conf. Proc.*, vol. 1664, no. May, pp. 1–6, 2015.

[55] H. Zhang, K. Lamnawar, A. Maazouz, and J. M. Maia, “A nonlinear shear and elongation rheological study of interfacial failure in compatible bilayer systems,” *J. Rheol. (N. Y. N. Y).*, vol. 60, no. 1, pp. 1–23, 2016.

[56] R. Y. F. Liu, T. E. Bernal-Lara, A. Hiltner, and E. Baer, “Interphase materials by forced assembly of glassy polymers,” *Macromolecules*, vol. 37, no. 18, pp. 6972–6979, 2004.

[57] R. Y. F. Liu, A. P. Ranade, H. P. Wang, T. E. Bernal-Lara, A. Hiltner, and E. Baer, “Forced assembly of polymer nanolayers thinner than the interphase,” *Macromolecules*, vol. 38, no. 26, pp. 10721–10727, 2005.

[58] R. Y. F. Liu, Y. Jin, A. Hiltner, and E. Baer, “Probing Nanoscale Polymer Interactions by Forced-Assembly,” *Macromol. Rapid Commun.*, vol. 24, no. 16, pp. 943–948, 2003.

[59] B. Lu, K. Lamnawar, A. Maazouz, and G. Sudre, “Critical Role of Interfacial Diffusion and Diffuse Interphases Formed in Multi-Micro-/Nanolayered Polymer Films Based on Poly(vinylidene fluoride) and Poly(methyl

methacrylate),” *ACS Appl. Mater. Interfaces*, vol. 10, no. 34, pp. 29019–29037, 2018.

[60] B. Lu, K. Lamnawar, and A. Maazouz, “Influence of in situ reactive interphase with graft copolymer on shear and extensional rheology in a model bilayered polymer system,” *Polym. Test.*, vol. 61, pp. 289–299, 2017.

[61] D. Langhe and M. Ponting, “Coextrusion Processing of Multilayered Films,” in *Manufacturing and Novel Applications of Multilayer Polymer Films 1st Edition*, William Andrew, 2016, pp. 16–45.

[62] B. Debbaut and J. Dooley, “Secondary motions in straight and tapered channels: Experiments and three-dimensional finite element simulation with a multimode differential viscoelastic model,” *J. Rheol. (N. Y. N. Y).*, vol. 43, no. 6, pp. 1525–1545, 1999.

[63] J. Dooley and L. Rudolph, “Viscous and elastic effects in polymer coextrusion,” *J. Plast. Film Sheeting*, vol. 19, no. 2, pp. 111–122, 2003.

[64] R. Zhao and C. W. Macosko, “Slip at polymer–polymer interfaces: Rheological measurements on coextruded multilayers,” *J. Rheol. (N. Y. N. Y).*, vol. 46, no. 1, pp. 145–167, 2002.

[65] P. C. Lee, H. E. Park, D. C. Morse, and C. W. Macosko, “Polymer-polymer interfacial slip in multilayered films,” *J. Rheol. (N. Y. N. Y).*, vol. 53, no. 4, pp. 893–915, 2009.

[66] P. C. Lee and C. W. Macosko, “Polymer-polymer interfacial slip by direct visualization and by stress reduction,” *J. Rheol. (N. Y. N. Y).*, vol. 54, no. 6, pp. 1207–1218, 2010.

[67] A. Bironeau *et al.*, “Existence of a Critical Layer Thickness in PS / PMMA Nanolayered Films,” *Macromolecules*, vol. 50, no. 10, pp. 4064–4073, 2017.

[68] S. Scholtyssek, R. Adhikari, V. Seydewitz, G. H. Michler, E. Baer, and A. Hiltner, “Evaluation of morphology and deformation micromechanisms in multilayered PP/PS films: An electron microscopy study,” *Macromol. Symp.*, vol. 294, no. 1, pp. 33–44, 2010.

[69] K. Ho, J. S. Lee, N. Viriyabanthorn, C. Sung, C. M. F. Barry, and J. L. Mead, “Interfacial instabilities in multilayer extrusion,” *2004 NSTI Nanotechnol. Conf. Trade Show - NSTI Nanotech 2004*, vol. 3, pp. 468–471, 2004.

[70] Y. Lin, A. Hiltner, and E. Baer, “A new method for achieving nanoscale reinforcement of biaxially oriented polypropylene film,” *Polymer (Guildf).*, vol. 51, no. 18, pp. 4218–4224, 2010.

[71] P. Agrawal *et al.*, “Rheological properties of high-density polyethylene/linear low-density polyethylene and high-density polyethylene/low-density polyethylene blends,” *Polymer Bulletin*. 2021.

[72] G. B. Galland, R. F. De Souza, R. S. Mauler, and F. F. Nunes, “13C NMR Determination of the Composition of Linear Low-Density Polyethylene Obtained with [η3-Methallyl-nickel-diimine]PF6 Complex,” *Macromolecules*, vol. 32, no. 5, pp. 1620–1625, 1999.

[73] U. Kessner, J. Kaschta, F. J. Stadler, C. S. Le Duff, X. Drooghaag, and H. Münstedt, “Thermorheological behavior of various short-and long-chain branched polyethylenes and their correlations with the molecular structure,” *Macromolecules*, vol. 43, no. 17, pp. 7341–7350, 2010.

[74] J. M. Dealy, R. G. Larson, J. M. Dealy, and R. G. Larson, *Structure and Rheology of Molten Polymers*. 2006.

[75] V. Bourg, R. Valette, N. Le Moigne, P. Ienny, V. Guillard, and A. Bergeret, “Shear and extensional rheology of linear and branched polybutylene succinate

blends," *Polymers (Basel).*, vol. 13, no. 4, pp. 1–19, 2021.

[76] X. Liang, Z. Luo, L. Yang, J. Wei, X. Yuan, and Q. Zheng, "Rheological properties and crystallization behaviors of long chain branched polyethylene prepared by melt branching reaction," 2017.

[77] H. Münstedt, S. Kurzbeck, and L. Egersdörfer, "Influence of molecular structure on rheological properties of polyethylenes," *Rheol. Acta*, vol. 29, pp. 21–29, 1998.

[78] G. Cabrera, I. Touil, E. Masghouni, A. Maazouz, and K. Lamnawar, "Multi-Micro/Nanolayer Films Based on Polyolefins: New Approaches from Eco-Design to Recycling," *Polymers (Basel).*, vol. 13, p. 413, 2021.

[79] Y. Yu, P. J. Deslauriers, and D. C. Rohlfing, "SEC-MALS method for the determination of long-chain branching and long-chain branching distribution in polyethylene," *Polymer (Guildf).*, vol. 46, no. 14, pp. 5165–5182, 2005.

[80] J. A. Langsten, R. H. Colby, T. C. M. Chung, F. Shimizu, T. Suzuki, and M. Aoki, "Synthesis and characterization of long chain branched isotactic polypropylene via metallocene catalyst and T-reagent," *Macromolecules*, vol. 40, no. 8, pp. 2712–2720, 2007.

[81] C. B. Gell, W. W. Graessley, V. Efstratiadis, M. Pitsikalis, and N. Hadjichristidis, "Viscoelasticity and Self-Diffusion in Melts of Entangled," *J Polym Sci Pol Phys*, vol. 35, pp. 1943–1954, 1997.

[82] Z. Zhou *et al.*, "Long Chain Branching Detection and Quantification in LDPE with Special Solvents, Polarization Transfer Techniques, and Inverse Gated 13C NMR Spectroscopy," *Macromolecules*, vol. 51, no. 21, pp. 8443–8454, 2018.

[83] E. Narimissa and M. H. Wagner, "From linear viscoelasticity to elongational

flow of polydisperse linear and branched polymer melts: The hierarchical multi-mode molecular stress function model," *Polymer (Guildf).*, vol. 104, no. November 2016, pp. 204–214, 2016.

[84] B. H. Zimm and W. H. Stockmayer, "The dimensions of chain molecules containing branches and rings," *J. Chem. Phys.*, vol. 17, no. 12, pp. 1301–1314, 1949.

[85] L. P. Lindeman and J. Q. Adams, "Carbon-13 Nuclear Magnetic Resonance Spectrometry: Chemical Shifts for the Paraffins through C9," *Anal. Chem.*, vol. 43, no. 10, pp. 1245–1252, 1971.

[86] B. Monrabal, J. Sancho-Tello, N. Mayo, and L. Romero, "Crystallization elution fractionation. A new separation process for polyolefin resins," *Macromol. Symp.*, vol. 257, pp. 71–79, 2007.

[87] A. A. Alghyamah and J. B. P. Soares, "Crystallization Elution Fractionation of LLDPEs Made with Metallocene Catalysts," *Macromol. Symp.*, vol. 312, no. 1, pp. 43–50, 2012.

[88] B. Monrabal and P. Del Hierro, "Characterization of polypropylene-polyethylene blends by temperature rising elution and crystallization analysis fractionation," *Anal. Bioanal. Chem.*, vol. 399, no. 4, pp. 1557–1561, 2011.

[89] S. Anantawaraskul, J. B. P. Soares, and P. M. Wood-Adams, "Fractionation of semicrystalline polymers by crystallization analysis fractionation and temperature rising elution fractionation," *Adv. Polym. Sci.*, vol. 182, no. August, pp. 1–54, 2005.

[90] H. Pasch and M. I. Malik, *Crystallization-Based Fractionation Techniques*. 2014.

[91] G. Cabrera, "THESE de DOCTORAT DE L ' UNIVERSITE DE LYON

opérée au sein de," 2020.

[92] C. M. Small, G. M. McNally, W. R. Murphy, and A. Marks, "The manufacture and performance of polyethylene-polyisobutylene films for cling applications," *Dev. Chem. Eng. Miner. Process.*, vol. 11, no. 1–2, pp. 169–184, 2003.

[93] H. Pasch and M. I. Malik, *Advanced Separation Techniques for Polyolefins*. .

[94] F. Brunel, O. Boyron, A. Clement, and C. Boisson, "Molecular Dynamics Simulation of Ethylene/Hexene Copolymer Adsorption onto Graphene: New Insight into Thermal Gradient Interaction Chromatography," *Macromol. Chem. Phys.*, vol. 220, no. 8, pp. 1–9, 2019.

[95] F. M. Mirabella and E. A. Ford, "Characterization of Linear Low-Density Polyethylene: Cross-Fractionation According to Copolymer Composition and Molecular Weight," vol. 25, pp. 777–790, 1987.

[96] D. Yan, W. Wang, and S. Zhu, "Effect of long chain branching on rheological properties of metallocene polyethylene," *Polymer (Guildf).*, 1994.

[97] J. C. Randall, "A REVIEW OF HIGH RESOLUTION LIQUID 13CARBON NUCLEAR MAGNETIC RESONANCE CHARACTERIZATIONS OF ETHYLENE-BASED POLYMERS," *Jounral Macromol. Sci. Part C Polym. Rev.*, vol. 29, no. 2–3, pp. 201–317, 1989.

[98] T. Usami and S. Takayama, "Fine-Branching Structure in High-Pressure, Low-Density Polyethylenes by 50.10-MHz 13C NMR Analysis," *Macromolecules*, vol. 17, no. 9, pp. 1756–1761, 1984.

[99] M. Mohammadi, A. A. Yousefi, and M. Ehsani, "Thermorheological analysis of blend of high-and low-density polyethylenes," *J. Polym. Res.*, vol. 19, no. 2, pp. 24–29, 2012.

[100] P. Micic and S. N. Bhattacharya, “Rheology of LLDPE, LDPE and LLDPE/LDPE blends and its relevance to the film blowing process,” *Polym. Int.*, vol. 49, no. 12, pp. 1580–1589, 2000.

[101] O. Delgadillo-Velázquez, S. G. Hatzikiriakos, and M. Sentmanat, “Thermorheological properties of LLDPE/LDPE blends,” *Rheol. Acta*, vol. 47, no. 1, pp. 19–31, 2008.

[102] M. H. Wagner and H. M. Laun, “Nonlinear shear creep and constrained elastic recovery of a LDPE melt,” *Rheologica Acta*, vol. 17, no. 2. pp. 138–148, 1978.

[103] A. Malmberg, E. Kokko, P. Lehmus, B. Löfgren, and J. V. Seppälä, “Long-chain branched polyethene polymerized by metallocene catalysts Et[Ind]2ZrCl2/MAO and Et[IndH4]2ZrCl2/MAO,” *Macromolecules*, vol. 31, no. 24, pp. 8448–8454, 1998.

[104] H. Zhang, K. Lamnawar, and A. Maazouz, “Fundamental studies of interfacial rheology at multilayered model polymers for coextrusion process,” 2013.

[105] S. L. Wingstrand, M. Van Drongelen, K. Mortensen, R. S. Graham, Q. Huang, and O. Hassager, “Influence of Extensional Stress Overshoot on Crystallization of LDPE,” *Macromolecules*, vol. 50, no. 3, pp. 1134–1140, 2017.

[106] M. H. Wagner, S. Kheirandish, and M. Yamaguchi, “Quantitative analysis of melt elongational behavior of LLDPE/LDPE blends,” *Rheol. Acta*, vol. 44, no. 2, pp. 198–218, 2004.

[107] B. Bernstein, E. A. Kearsley, and L. J. Zapas, “A Study of Stress Relaxation with Finite Strain,” *Rubber Chem. Technol.*, vol. 38, no. 1, pp. 76–89, 1965.

[108] A. Kaye, “NON-NEWTONIAN FLOW IN INCOMPRESSIBLE FLUIDS P a r t I A general rheological equation of state P a r t II Some problems in steady

flow by," *Aerosp. Eng. reports, Tech. Univ. Delft*, no. 134, pp. 1–20, 1962.

[109] R. I. Tanner, "From A to (BK)Z in Constitutive Relations," *J. Rheol. (N. Y. N. Y).*, vol. 32, no. 7, pp. 673–702, 1988.

[110] T. Samurkas, J. M. Dealy, and R. G. Larson, "Strong Extensional and Shearing Flows of a Branched Polyethylene," *J. Rheol. (N. Y. N. Y).*, vol. 33, no. 4, pp. 559–578, 1989.

[111] M. H. Wagner, H. Bastian, P. Ehrecke, P. Hachmann, and J. Meissner, "A Constitutive Analysis of Uniaxial, Equibiaxial and Planar Extension of Linear and Branched Polyethylene Melts," *Prog. Trends Rheol. V*, pp. 4–7, 1998.

[112] E. S. Doi M, "The theory of polymer dynamics," *Oxford Univ. Press. Oxford*, 1986.

[113] M. H. Wagner and J. Schaeffer, "Nonlinear strain measures for general biaxial extension of polymer melts," *J. Rheol. (N. Y. N. Y).*, vol. 36, no. 1, pp. 1–26, 1992.

[114] M. H. Wagner and J. Schaeffer, "Rubbers and polymer melts: Universal aspects of nonlinear stress–strain relations," *J. Rheol. (N. Y. N. Y).*, vol. 37, no. 4, pp. 643–661, 1993.

[115] M. H. Wagner, P. Rubio, and H. Bastian, "The molecular stress function model for polydisperse polymer melts with dissipative convective constraint release," *J. Rheol. (N. Y. N. Y).*, vol. 45, no. 6, pp. 1387–1412, 2001.

[116] M. H. Wagner, M. Yamaguchi, and M. Takahashi, "Quantitative assessment of strain hardening of low-density polyethylene melts by the molecular stress function model," *J. Rheol. (N. Y. N. Y).*, vol. 47, no. 3, pp. 779–793, 2003.

[117] M. H. Wagner, J. Hepperle, and H. Münstedt, "Relating rheology and

molecular structure of model branched polystyrene melts by molecular stress function theory," *J. Rheol. (N. Y. N. Y).*, vol. 48, no. 3, pp. 489–503, 2004.

[118] Y. Masubuchi, Y. Matsumiya, H. Watanabe, G. Marrucci, and G. Ianniruberto, "Primitive chain network simulations for Pom-Pom polymers in uniaxial elongational flows," *Macromolecules*, vol. 47, no. 10, pp. 3511–3519, 2014.

[119] E. Narimissa, V. H. Rolón-Garrido, and M. H. Wagner, "A hierarchical multi-mode MSF model for long-chain branched polymer melts part I: elongational flow," *Rheol. Acta*, vol. 54, no. 9–10, pp. 779–791, 2015.

[120] E. Narimissa and M. H. Wagner, "A hierarchical multimode molecular stress function model for linear polymer melts in extensional flows," *J. Rheol. (N. Y. N. Y).*, vol. 60, no. 4, pp. 625–636, 2016.

[121] E. Narimissa and M. H. Wagner, "Review of the hierarchical multi-mode molecular stress function model for broadly distributed linear and LCB polymer melts," *Polym. Eng. Sci.*, vol. 59, no. 3, pp. 573–583, 2019.

[122] L. Poh, E. Narimissa, and M. H. Wagner, "Modelling of elongational flow of hdpe melts by hierarchical multi-mode molecular stress function model," *Polymers*, vol. 13, no. 19. 2021.

[123] J. Zhang, T. P. Lodge, and C. W. Macosko, "Interfacial slip reduces polymer-polymer adhesion during coextrusion," *J. Rheol. (N. Y. N. Y).*, vol. 50, no. 1, pp. 41–57, 2006.

[124] A. M. Jordan *et al.*, "Rheology of polymer multilayers: Slip in shear, hardening in extension," *J. Rheol. (N. Y. N. Y).*, vol. 63, no. 5, pp. 751–761, Sep. 2019.

[125] L. Levitt, C. W. Macosko, T. Schweizer, and J. Meissner, "Extensional rheometry of polymer multilayers: A sensitive probe of interfaces," *J. Rheol. (N. Y. N. Y).*, vol. 41, no. 3, pp. 671–685, 1997.

[126] J. F. Palierne, “Linear rheology of viscoelastic emulsions with interfacial tension,” *Rheol. Acta*, vol. 29, no. 3, pp. 204–214, 1990.

[127] D. Shi, G. H. Hu, Z. Ke, R. K. Y. Li, and J. Yin, “Relaxation behavior of polymer blends with complex morphologies: Palierne emulsion model for uncompatibilized and compatibilized PP/PA6 blends,” *Polymer (Guildf).*, vol. 47, no. 13, pp. 4659–4666, 2006.

[128] A. Maani, B. Blais, M.-C. Heuzey, and P. J. Carreau, “Rheological and morphological properties of reactively compatibilized thermoplastic olefin (TPO) blends,” *J. Rheol. (N. Y. N. Y).*, vol. 56, no. 3, pp. 625–647, 2012.

[129] R. Salehiyan, S. Ray, F. Stadler, and V. Ojijo, “Rheology–Microstructure Relationships in Melt-Processed Polylactide/Poly(vinylidene Fluoride) Blends,” *Materials (Basel).*, vol. 11, no. 12, p. 2450, Dec. 2018.

[130] K. Lamnawar, A. Maazouz, G. Cabrera, and R. Al-Itry, “Interfacial tension properties in biopolymer blends: From deformed drop retraction method (DDRM) to shear and elongation rheology-application to blown film extrusion,” *Int. Polym. Process.*, vol. 33, no. 3, pp. 411–424, 2018.

[131] T. Messin *et al.*, “Impact of water and thermal induced crystallizations in a PC/MXD6 multilayer film on barrier properties,” *Eur. Polym. J.*, vol. 111, no. May 2018, pp. 152–160, 2019.

[132] A. M. Jordan, P. Lee, C. Thurber, and C. W. Macosko, “Adapting a Capillary Rheometer for Research on Polymer Melt Interfaces,” *Ind. Eng. Chem. Res.*, vol. 57, no. 42, pp. 14106–14113, 2018.

[133] C. J. Carriere, G. Biresaw, and R. L. Sammler, “Temperature dependence of the interfacial tension of PS/PMMA, PS/PE, and PMMA/PE blends,” *Rheol. Acta*, vol. 39, no. 5, pp. 476–482, 2000.

[134] H. T. Pham and C. J. Carriere, “The effect of temperature on the interfacial tension of polycarbonate/polyethylene blends,” *Polym. Eng. Sci.*, vol. 37, no. 3, pp. 636–639, 1997.

[135] A. M. Jordan *et al.*, “Rheology of Polymer Multilayers: Slip in Shear, Hardening in Extension.”

[136] G. Zhang, P. C. Lee, S. Jenkins, J. Dooley, and E. Baer, “The effect of confined spherulite morphology of high-density polyethylene and polypropylene on their gas barrier properties in multilayered film systems,” *Polymer (Guildf).*, vol. 55, no. 17, pp. 4521–4530, 2014.

[137] H. Wang *et al.*, “Confined Crystallization of Polyethylene Oxide in Nanolayer Assemblies,” *Science (80-.).*, vol. 323, no. 5915, pp. 757–760, Feb. 2009.

[138] Plastics Europe and EPRO, “Plastics – the Facts 2016,” *Plast. – Facts 2016*, p. 37, 2016.

[139] O. Horodytska, F. J. Valdés, and A. Fullana, “Plastic flexible films waste management – A state of art review,” *Waste Manag.*, vol. 77, pp. 413–425, 2015.

[140] A. Bondon, K. Lamnawar, and A. Maazouz, “Experimental investigation of a new type of interfacial instability in a reactive coextrusion process,” *Polym. Eng. Sci.*, vol. 55, no. 11, pp. 2542–2552, Nov. 2015.

[141] M. Ponting, T. M. Burt, L. T. J. Korley, J. Andrews, A. Hiltner, and E. Baer, “Gradient multilayer films by forced assembly coextrusion,” *Ind. Eng. Chem. Res.*, vol. 49, no. 23, pp. 12111–12118, 2010.

[142] G. Cabrera, J. Charbonnier, G. Pichon, A. Maazouz, and K. Lamnawar, “Bulk rheology and surface tribo-rheometry toward the investigation of polyisobutylene migration in model and recycled multilayer agricultural

films," *Rheol. Acta*, vol. 59, no. 11, pp. 821–847, 2020.

[143] G. T. Offord, S. R. Armstrong, B. D. Freeman, E. Baer, A. Hiltner, and D. R. Paul, "Gas transport in coextruded multilayered membranes with alternating dense and porous polymeric layers," *Polymer (Guildf).*, vol. 55, no. 5, pp. 1259–1266, 2014.

Publications and oral presentations at scientific conferences

Publications

G. Cabrera, I. Touil, E.Masghouni, A.Maazouz and K.Lamnawar, Multi-Micro/Nanolayer Films Based on Polyolefins: New Approaches from Eco-Design to Recycling, Polymers, 13, 413, 2021, https://doi.org/10.3390/polym13030413.

B. Lu, A. Bondon, I.Touil, H. Zhang, A.Maazouz and K.Lamnawar, Industrial and Engineering Chemistry Research, 59, 22144-22154, 2020, https://dx.doi.org/10.1021/acs.iecr.0c04731.

Additionally, we have two articles that will be submitted soon:

I.TOUIL, A. MAAZOUZ, K. LAMNAWAR, Structure-rheology properties of polyethylene's with varying macromolecular architectures.

I.TOUIL, A. MAAZOUZ, K. LAMNAWAR, Interfacial shear and elongation rheology of immiscible micro-nanolayered polymers with varying macromolecular architectures and high mismatched viscoelastic properties: New insight on the nano structuration effects and modeling of interfacial properties.

Oral presentations at scientific conferences

International conferences

I. TOUIL, A. MAAZOUZ, K. LAMNAWAR, Multi-Micro-Nanolayers polymers based on polyethylene with varying macromolecular architectures : Structure, shear and elongation rheology and processing, Rotomolding Thermoforming and Blow-molding, du 10 au 12 juillet 2019, Paris, France.

I. TOUIL, A. MAAZOUZ, K. LAMNAWAR, Multi-Micro-Nanolayers polymers based on polyethylene with varying macromolecular architectures : Structure, shear and elongation rheology and processing , Annual European Rheology Conference, du 7 au 8 avril 2019, Portoroz, Slovenia.

French national conferences

I. TOUIL, , A. MAAZOUZ, K. LAMNAWAR Multi-Micro-Nanolayers polymers based on polyethylene with varying macromolecular architectures : Structure, shear and elongation rheology and processing , Journées IMPact, du 1 au 2 juillet 2019, Saint Etienne, France.

I. TOUIL, , A. MAAZOUZ, K. LAMNAWAR Etude multi-échelle des structures polymères nano-confinées et stratifiées par le procédé de coextrusion - Matériaux multifonctionnels pour des applications de hautes valeurs ajoutées, 53ème Congrès du Groupe Français de Rhéologie, du 29 au 31 octobre 2018, Brest, France.

FOLIO ADMINISTRATIF

THESE DE L'UNIVERSITE DE LYON OPEREE AU SEIN DE L'INSA LYON

NOM : TOUIL **DATE de SOUTENANCE :** 17/12/2021
Prénoms : Ibtissam
TITRE : Multi-micro/nanolayers of highly mismatched viscoelastic polymers based on polyethylene with varying macromolecular architectures: Multiscale investigations towards better control of their structuration and recycling by coextrusion.

NATURE : Doctorat **Numéro d'ordre** : 2021LYSEI111
Ecole doctorale : Matériaux de Lyon
Spécialité : Matériaux Polymères

RESUME This study aims to understand the effects of confinement on the rheology and molecular dynamics in multilayer polymeric structures fabricated by the forced-assembly multilayer coextrusion of polyethylenes (PE) and confined polymers (PS and PC). The originality of our approach deals with coextrusion of these high mismatched viscoelastic systems. Through this work, PEs with varying macromolecular architectures, with short-chain branching (SCB) and long-chain branching (LCB), were used. Various nano-structured multilayer structures with stable flow and layered architecture were then obtained. Hitherto, various characterization techniques such as WAXS, SEM or TEM, and rheology were used to probe the structure and molecular dynamics of the PE chains. Micro and nanolayered instabilities were observed depending on the viscoelastic mismatched properties and interfacial tensions. The layer multiplication strongly affects the crystallization microstructure/morphology and molecular orientations of PEs. Interestingly, we found that macromolecular and geometrical confinements further influence the final morphology. Subsequently, they remarkably influence the rheology and molecular dynamics of PEs depending on the amount of LCB. From micro- to nanolayers, strain hardening properties in the extensional measurements are strongly dependent on the number of layers, architecture, compositions and confinement. Relevant mechanisms involving molecular rheology theories are proposed to elucidate the reasons underlying the changes. Meanwhile, we were able to model interfacial tension properties especially in the case of nanolayered polymeric systems. Hence, this work clearly demonstrates how the multiscale structural evolution during the micro-/nano-layer coextrusion process can control the final properties of multilayered products. Our findings are aimed at a better understanding of the interfacial properties towards controlling the interface/interphases in the present micro-nanostructured model multilayers polymers including their recyclability for advanced applications ranging from ultra-barrier films from cast extrusion to flexible and high transparency sheets for thermoforming process. Finally, and in the context of circular economy, a future-oriented approach from eco-design to a recycling strategy of the studied multi-micro/nanolayered systems was investigated. Therefore, a novel route is purposed to decrease the number of constituents, control the thickness of the layers, avoid using tie layers, and enhance the recyclability of the studied systems.

MOTS-CLÉS: Multi micro-/nanolayered polymers, interface, coextrusion, instabilities, rheology, recycling, eco-design, polymer blends, morphology, elongation rheology, modelling.

Laboratoire de recherche : Ingénierie des Matériaux Polymères (IMP), CNRS UMR 5223
MOTS-CLÉS : Multi micro-/nanolayered polymers, interface ; coextrusion, instabilities, rheology, recycling, eco-design, polymer blends, morphology.
Laboratoire de recherche : Ingénierie des Matériaux Polymères (IMP), CNRS UMR 5223

Directeurs de thèse : Khalid LAMNAWAR ; Abderrahim MAAZOUZ

Composition du jury :

DUQUESNE Sophi	Professeur (Université de Lille)	Rapporteur
AJJI Abdellah	Professeur (École Polytechnique de Montréal)	Rapporteur
EL KISSI Nadia	Directrice de Recherche CNRS (Université Grenoble Alpes)	Examinateur
DUCHET Jannick	Professeur (INSA-LYON)	Examinateur
LAMNAWAR Khalid,	Professeur (Associate, HDR) (INSA Lyon)	Directeur
MAAZOUZ Abderrahim	Professeur (INSA Lyon)	Directeur
DA CRUZ-BOISSON Fernande	Ingénieure de Recherche CNRS (INSA Lyon)	Invitée
LU Bo	Docteur (Université de Zhengzhou, Chine)	Invité